RAPHAEL MARSCHALL

INNER GAS AND DUST COMAE OF COMETS

BUILDING A 3D SIMULATION PIPELINE TO UNDERSTAND MULTI-INSTRUMENT RESULTS FROM THE ROSETTA MISSION TO COMET 67P/CHURYUMOV-GERASIMENKO

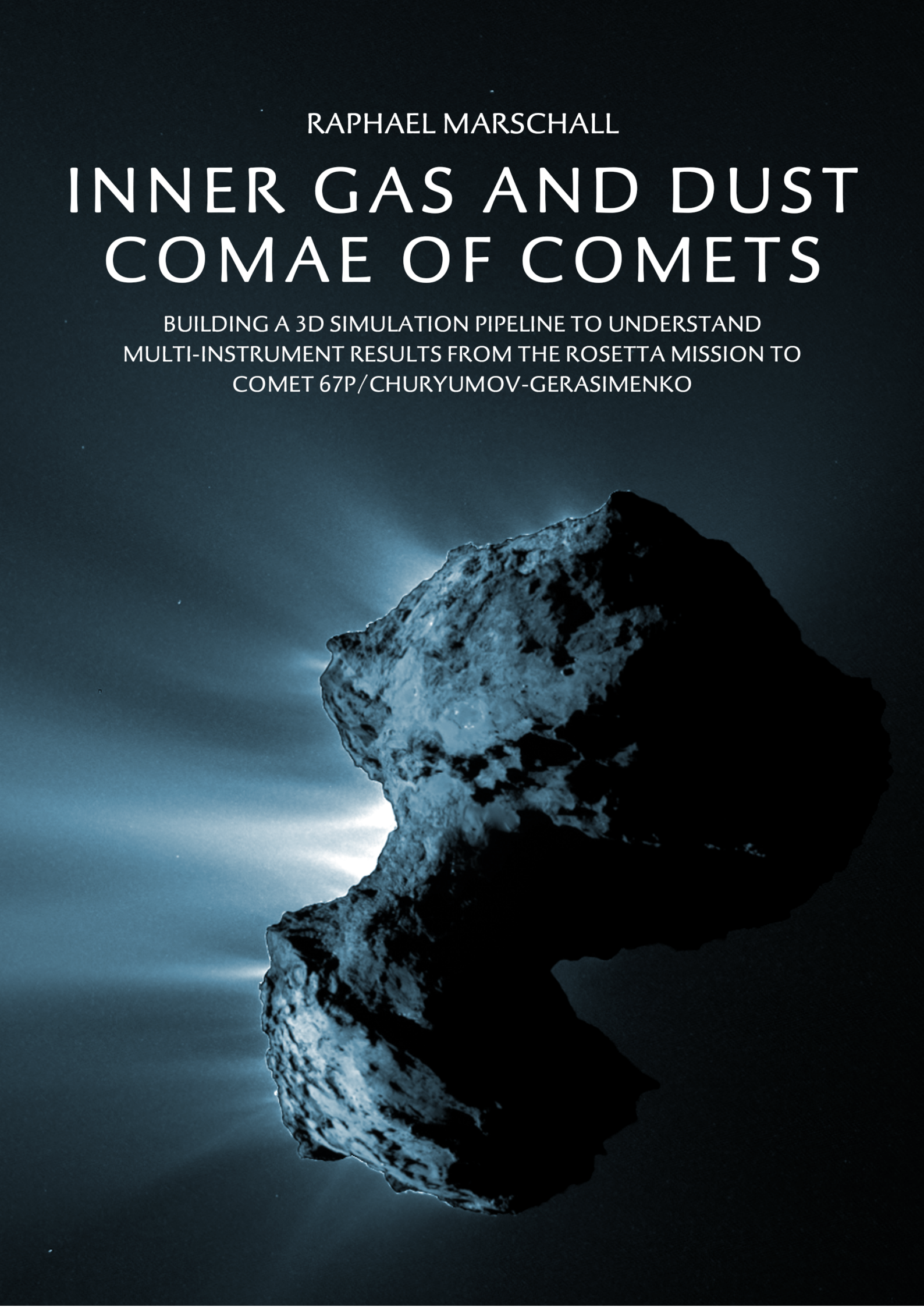

Cover image: NAC_2015-08-20T00.14.28.415Z_IDB0_1397549000_F22
Copyright: ESA/Rosetta/MPS for OSIRIS Team MPS/UPD/LAM/IAA/SSO/INTA/UPM/DASP/IDA
Scaling and colours: Pixels which are on nucleus are scaled to $[0.00; 0.10]$, pixels that are off nucleus are scaled to $[0.00, 0.01]$. A back/blue/white colour palette was used.

INNER GAS AND DUST COMAE OF COMET

Building a 3D simulation pipeline to understand multi-instrument results from the Rosetta mission to comet 67P/Churyumov-Gerasimenko

Inaugural Doctoral Dissertation
of the Faculty of Science
of the University of Bern

by
Raphael Marschall

Advisor:
Prof. Dr. Nicolas Thomas
Physics Institute, University of Bern

Accepted by the Faculty of Science

Bern, 28.07.2017

The Dean
Prof. Dr. G. Colangelo

LICENSE

ABSTRACT

In this thesis we present a self consistent simulation pipeline to investigate and model the innermost gas and dust comae of comets, in particular the ones of comet 67P/Churyumov-Gerasimenko (CG). The model uses a previously developed shape model of the nucleus. From this the water sublimation rates and gas temperatures at the surface are computed. The gas expansion is modelled with a 3D Direct Simulation Monte Carlo algorithm. A dust drag algorithm is then used to compute dust volume number densities in the coma, which are then converted to brightnesses using Mie theory and a line-of-sight integration.

We present results for a spherical nucleus to understand the fundamental properties of the gas and dust dynamics of cometary comae. Amongst others we will show how the competing forces of gravity and gas drag act on dust particles of various sizes. The resulting effects - such as gravitationally bound particles - are important processes in the context of comet CG.

The ultimate aim of this work is to interpret data acquired in the time frame of August 2014 to January 2015 from the European Space Agency's Rosetta spacecraft when it was in close proximity to the nucleus of comet CG. By constraining our models from the Rosetta Orbiter Spectrometer for Ion and Neutral Analysis (ROSINA) and Optical, Spectroscopic, and Infrared Remote Imaging System (OSIRIS) instruments we can determine the gas and dust emission distribution and further parameters of the gas and dust activity, such as the dust size distribution as well as the dust to gas ratio.

We show that a model assuming purely-insolation-driven outgassing from the surface does not produce a reasonable fit to ROSINA/COPS data. A stronger source in the «Neck» region of the nucleus (Hapi region) is needed to match the observed modulation of the gas density in detail. This agrees with OSIRIS data of the same time span, which shows that the dust emission from the «Neck»was dominant in August to September 2014. The current model matches this observation reasonably if a power index of $2-3$ for the dust size distribution is used. A better match to the OSIRIS data is seen by using a single large particle size for the coma. Furthermore, we show that gas activity from cliff areas only produces a statistically equally good fit to the ROSINA/COPS data as a the purely-insolation-driven model. In contrast, pure cliff activity does not reproduce the dust brightness

observed by OSIRIS and can thus be ruled out. Additionally, we will present analysis showing that topographic re-radiation does not contribute significantly to the sublimation behaviour of H_2O but plays an important role in how the gas flux interacts with the irregular shape of the nucleus. We demonstrate that fits to the observations are non-unique. However we can conclude that gas and dust activity from cliffs and the Hapi region is consistent with the ROSINA/COPS and OSIRIS data sets for the considered time span and is thus a plausible solution. Finally, we present an outlook on extending our analysis to further instruments such as the Microwave Instrument for the Rosetta Orbiter (MIRO), and the Visible and Infrared Thermal Imaging Spectrometer (VIRTIS) instruments.

PUBLICATIONS

Some of the ideas and figures in this thesis have already appeared previously in the following publications:

Papers as First Author

Marschall, R., S. Mottola, C.C. Su, Y. Liao, M. Rubin, J.S. Wu, N. Thomas, K. Altwegg, H. Sierks, W.-H. Ip, H.U. Keller, J. Knollenberg, E. Kührt, I.L. Lai, Y. Skorov, L. Jorda, F. Preusker, F. Scholten, J.-B. Vincent (2017), Cliffs vs. Plains: Can ROSINA/COPS and OSIRIS data of comet 67P/Churyumov-Gerasimenko in autumn 2014 constrain inhomogeneous outgassing?, Astronomy and Astrophysics, 605, A112, doi:10.1051/0004-6361/201730849.

Marschall, R., C.C. Su, Y. Liao, N. Thomas, K. Altwegg, H. Sierks, W.-H. Ip, H.U. Keller, J. Knollenberg, E. Kührt, I.L. Lai, M. Rubin, Y. Skorov, J.S. Wu, L. Jorda, F. Preusker, F. Scholten, A. Gracia Berná, A. Gicquel, G. Naletto, X. Shi, and J.-B. Vincent, (2016), Modelling observations of the inner gas and dust coma of comet 67P/Churyumov-Gerasimenko – First results, Astronomy and Astrophysics, 589, A90, doi:10.1051/0004-6361/201628085.

Papers as Co-Author

Liao Y., C.C. Su, R. Marschall, J.S. Wu, M. Rubin, I.L. Lai, W.-H. Ip, H.U. Keller, J. Knollenberg, E. Kührt, Y. Skorov, and N. Thomas, (2016), 3D Direct Simulation Monte Carlo Modelling of the Inner Gas Coma of Comet 67P/Churyumov-Gerasimenko: A Parameter Study, Earth, Moon, and Planets, 117, 41-64, doi:10.1007/s11038-016-9486-1.

El-Maarry, M. R., N. Thomas, A. Gracia-Berná, R. Marschall, A.-T. Auger, O. Groussin, S. Mottola, M. Pajola, M. Massironi, S. Marchi, S. Höfner, F. Preusker, F. Scholten, L. Jorda, E. Kührt, H. U. Keller, H. Sierks, M. F. A'Hearn, C. Barbieri, M. A. Barucci, J.-L. Bertaux, I. Bertini, G. Cremonese, V. Da Deppo, B. Davidsson, S. Debei, M. De Cecco, J. Deller, C. Güttler, S. Fornasier, M. Fulle, P. J. Gutierrez, M. Hofmann, S. F. Hviid, W.-H. Ip, J. Knollenberg, D. Koschny, G. Kovacs, J.-R. Kramm, M. Küppers, P. L. Lamy, L. M. Lara, M. Lazzarin, J. J. Lopez Moreno, F. Marzari, H. Michalik, G. Naletto, N. Oklay, A. Pommerol, H. Rickman, R. Rodrigo, C. Tubiana, J.-B. Vincent, (2015), Fractures on comet 67P/Churyumov-Gerasimenko observed by the Rosetta/OSIRIS, Geophys. Res. Lett., 42, 5170-5178, doi:10.1002/2015GL064500.

Thomas, N., B. Davidsson, M.R. El-Maarry, S. Fornasier, L. Giacomini, A.G. Gracia Berna, S.F. Hviid, W.-H. Ip, L. Jorda, H.U. Keller, J. Knollenberg, E. Kührt, F. La Forgia, I.L. Lai, Y. Liao, R. Marschall, M. Massironi, S. Mottola, M. Pajola, O. Poch, A. Pommerol, F. Preusker, F. Scholten, C.C. Su, J.S. Wu, J.-B. Vincent, H. Sierks, C. Barbieri, P.L. Lamy, R. Rodrigo, H. Rickman, D. Koschny, M.F. A'Hearn, M.A. Barucci, J-L. Bertaux, I. Bertini, G. Cremonese, V. Da Deppo, S. Debei, M. Fulle, O. Groussin, P.J. Gutierrez, J.-R. Kramm, M. Küppers, L. M. Lara, M. Lazzarin, J. J. Lopez Moreno, F. Marzari, H. Michalik, G. Naletto, and C. Güttler, (2015), Re-distribution of particles across the nucleus of comet 67P/Churyumov-Gerasimenko, Astron. Astrophys., 583, A17, doi:10.1051/0004-6361/201526049.

Pommerol, A., N. Thomas, M. R. El-Maarry, M. Pajola, O. Groussin, A. -T. Auger, N. Oklay, S. Fornasier, C. Feller, B. Davidsson, A. Gracia, B. Jost, R. Marschall, O. Poch, M. A. Barucci, J. -L. Bertaux, F. La Forgia, H. U. Keller, E. Kuehrt, S. C. Lowry, S. Mottola, G. Naletto, H. Sierks, C. Barbieri, P. L. Lamy, R. Rodrigo, H. Rickman, D. Koschny, J. Agarwal, M. F. A'Hearn, I. Bertini, G. Cremonese, V. Da Deppo, M. De Cecco, S. Debei, C. Guettler, M. Fulle, P. J. Gutierrez, S. F. Hviid, W. -H. Ip, L. Jorda, J. Knollenberg, G. Kovacs, J. -R. Kramm, M. Küppers, L. Lara, M. Lazzarin, J. L. Lopez Moreno, F. Marzari, H. Michalik, F. Preusker, F. Scholten, C. Tubiana, and J. -B. Vincent, (2015) , OSIRIS observations of metre-size exposures of H2O ice at the surface of 67P/Churyumov-Gerasimenko and interpretation using laboratory experiments, Astron. Astrophys., 583, A25, doi:10.1051/0004-6361/201525977.

ACKNOWLEDGEMENTS

This work would not have been possible without the help and support of so many people over the past four years and beyond. This is my attempt to acknowledge them.

I would like to thank my Ph.D. advisor Prof. Dr. Nicolas Thomas for giving me the opportunity to join his group and work in this immensely interesting field. The experiences of the past years are invaluable to me. I would like to especially thank you for providing such a great working environment with an exceptionally interdisciplinary and international research group that truly and profoundly expanded my horizon. I very much appreciate the scientific support and guidance you have always provided me with, something I have never taken for granted. You have given me space to explore own ideas and brought me back to focus at the right moments.

Then I would like to thank my parents Yvonne and Franz Marschall, my sister Salome Marschall, and my girlfriend Cilia Julen for their support. You all have supported my life and career decisions and have been my rock to lean on in difficult times and you were there to share the happy moments and celebrate achievements.

I am also very fortunate to have had the opportunity to work with a number of great people. Especially I want to thank Susanne Finklenburg, and Ying Liao for their input to my work. I have also enjoyed the more recent work with Selina-Barbara Gerig and Olga Pinzón very much, the next generation of cometary modellers in the Planetary Imaging Group (PIG) here in Bern.

Furthermore, I would like to thank Martin Rubin, Yuri Skorov, Stefano Mottola, Ekkehard Kührt, David Kappel, Ladislav Rezac, and Horst Uwe Keller for all the insightful discussions and inputs to my work and understanding of cometary physics.

Working in an interdisciplinary international group as the PIG has made work incredibly enjoyable. In «historical» order thanks go out to Susanne Finklenburg, Antoine Pommerol, Mohamed Ramy El-Maarry, Ying Liao, Xavier Diot, Bernhard Jost, Julien Gouman, Zuriñe Yoldi, Olivier Poch, Victoria Roloff, Antonio Gracia de Berná, Yann Brouet, Luca Guallini, Alireza Hosseini, Selina-Barbara Gerig, Clémence Herny, Panagiotis Theologou, Olga Pinzón, Patricio Becerra, and Romain Cerubini.

Special thank go to Stefan Lerch, Selina-Barbara Gerig, Zuriñe Yoldi, and Salome Marschall for proofreading parts of this thesis.

During the ten years studying physics at the University of Bern, I was fortunate to have some truly wonderful people around me that have turned from fellow students to great friends. Studying together, learning together, debating the smaller and larger issues of physics and beyond has made my world so much richer. Thank you Siegfried Achermann, Alexander Läderach, Stefan Lerch, Erik Nygren, Manuel Unternährer, and Michael von Grünigen.

Finally, I would like to thank Ruth and Hans Zoss for being incredible intellectual role models to me. It is always such a pleasure discussing with both of you. Because of all these profound discussions you have shaped my philosophy of life and view of the world more than you possibly know. Merci du fond du cœur pour tout.

CONTENTS

LIST OF FIGURES

ACRONYMS

AU	astronomical unit
BCS	bi-spherical coordinate system
CG	67P/Churyumov-Gerasimenko
cd	comet day
COPS	COmet Pressure Sensor
CLT	comet local time
COSIMA	Cometary Secondary Ion Mass Analyser
eaf	effective active fraction
ESA	European Space Agency
GIADA	Grain Impact Analyser and Dust Accumulator
DFMS	Double Focusing magnetic Mass Spectrometer
DLR	*Deutsche Zentrum für Luft- und Raumfahrt*
DSMC	Direct Simulation Monte Carlo
LTE	local thermodynamic equilibrium
mcs	mean collisional separation
mfp	mean free path
MiARD	Multi-instrument Analysis of Rosetta Data
MIDAS	Micro-Imaging Dust Analysis System
MIRO	Microwave Instrument for the Rosetta Orbiter
MPS	*Max-Planck-Institut für Sonnensystemforschung*
NAC	narrow angle camera
NG	Nude Gauge
OSIRIS	Optical, Spectroscopic, and Infrared Remote Imaging System
PPMCC	Pearson product-moment correlation coefficient
ROSINA	Rosetta Orbiter Spectrometer for Ion and Neutral Analysis

RTOF	Reflectron type Time Of Flight mass spectrometer
SNR	signal-to-noise ratio
VIRTIS	Visible and Infrared Thermal Imaging Spectrometer
WAC	wide angle camera
VDF	velocity distribution function

Part I

INTRODUCTION & MOTIVATION

1 INTRODUCTION

Comets are kilometre to tens of kilometre sized solar system bodies. In contrast to the planets and other larger objects that are orbiting the Sun, the typical comet moves on a highly elliptical orbit with substantial inclination. The two main families of periodic comets are Halley type comets and Jupiter family comets. Comets are often classified according to their orbital periods and Tisserand's parameter with respect to Jupiter[1], T_J. Halley type comets have orbital periods of less than 200 years and $T_J < 2$. This family of comets owes its name to the most famous member of the family, comet 1P/Halley (Halley, 1705). Jupiter family comets are characterised with $2 < T_J < 3$ and typically have their aphelion close to Jupiter's orbit while their small perihelion takes them far into the inner solar system and close to the Sun. Comet 67P/Churyumov-Gerasimenko (CG) - which will be the main focus of this work - is a member of this family. Comet CG, discovered by Klim Ivanovich Churyumov and Svetlana Ivanovna Gerasimenko in 1969, has an orbital period of 6.44 years during which it is taken out to a maximum distance of 5.68 astronomical units (AU) and in to a minimum distance of 1.24 AU. The two major reservoirs of comets in our solar system are considered to be the Oort Cloud and the Kuiper Belt. Gravitational interactions with other stars or planets of our solar system are thought to scatter the comets of these reservoirs into the inner solar system. Comets are widely regarded to have retained their pristine composition from the formation of our solar system. Often referred to as dusty-ice-balls, comets heat up when they approach the Sun such that the ice begins to sublimate and ejects dust particles into space with it. This produces their characteristic ion and dust tails which can be hundreds of millions of kilometres long and which can, in some cases, be seen by the naked eye. Figure 1 shows an image taken 1997 of comet Hale-Bopp exposing its ion (faint blueish) and dust tail (bright whitish).

Until recently, comets were only observable with ground based telescopes and due to the small size of their nuclei they were never resolved with these techniques. Only in 1986 with the fly-by of comet 1P/Halley by six spacecrafts - two each from Japan (Suisei & Sakigake) and the Soviet Union (Vega 1 & 2), and one each from the United States of America (ICE) and Europe (Giotto) - did we enter the

1 $T_J = \frac{a_J}{a_c} + \sqrt{\frac{a_c}{a_J}(1-e^2)}\cos(i)$, where a_J and a_c are the semi-major axes of Jupiter and the comet, e is the comet's eccentricity, and i the comet's inclination.

Figure 1: Image with comet Hale-Bopp taken in 1997. The image shows the ion (faint blueish) and dust tails (bright whitish) of the comet. © John Tewell, released under CC BY-NC 2.0, https://creativecommons.org/ licenses/by-nc/2.0/

era of close in-situ observations of cometary nuclei. Even until today only a small number of cometary nuclei have ever been resolved by spacecraft and later by ground based telescopes (Figure 2). Giotto was the spacecraft passing 1P/Halley the closest and the mission's success prompted the European Space Agency (ESA) to initiate the next cometary mission. Rosetta was born: A mission with the aim to not merely fly by but to catch a comet, escort it along its orbit, and observe it in close vicinity as the comet approaches its perihelion and beyond. Furthermore ESA added the lander Philae to descend for the first time, in a controlled way, to a cometary surface and gather actual ground truths on its physical properties. Rosetta was launched on 2004-03-02 from the Guiana Space Centre in French Guiana on board an Ariane 5G+ V-158 rocket and set course for its target comet CG. After the more than ten year journey Rosetta arrived at comet CG on 2014-08-06 and began its two year science phase to study the cometary surface as well as the dust and gas comae and plasma environment. On 2014-11-12 Philae touched down on the surface. Unfortunately the harpoons - designed to hold Philae to the surface after touchdown - malfunctioned and therefore Philae rebounded from the surface and touched down hundreds of metres from the intended landing site in a almost permanently shadowed area. Its exact position was only determined by OSIRIS close to the end of the mission. The Rosetta mission finally ended with the planned spacecraft crash of the orbiter on the surface on 2016-09-30.

How different comets look on different scales is illustrated with Figure 3 and Figure 4 both showing comet CG. The first figure shows comet CG from the ground based Subaru Telescope and highlights

the roughly 7 million kilometres long dust tail. The second image, taken with the OSIRIS-NAC, shows the resolved nucleus up close.

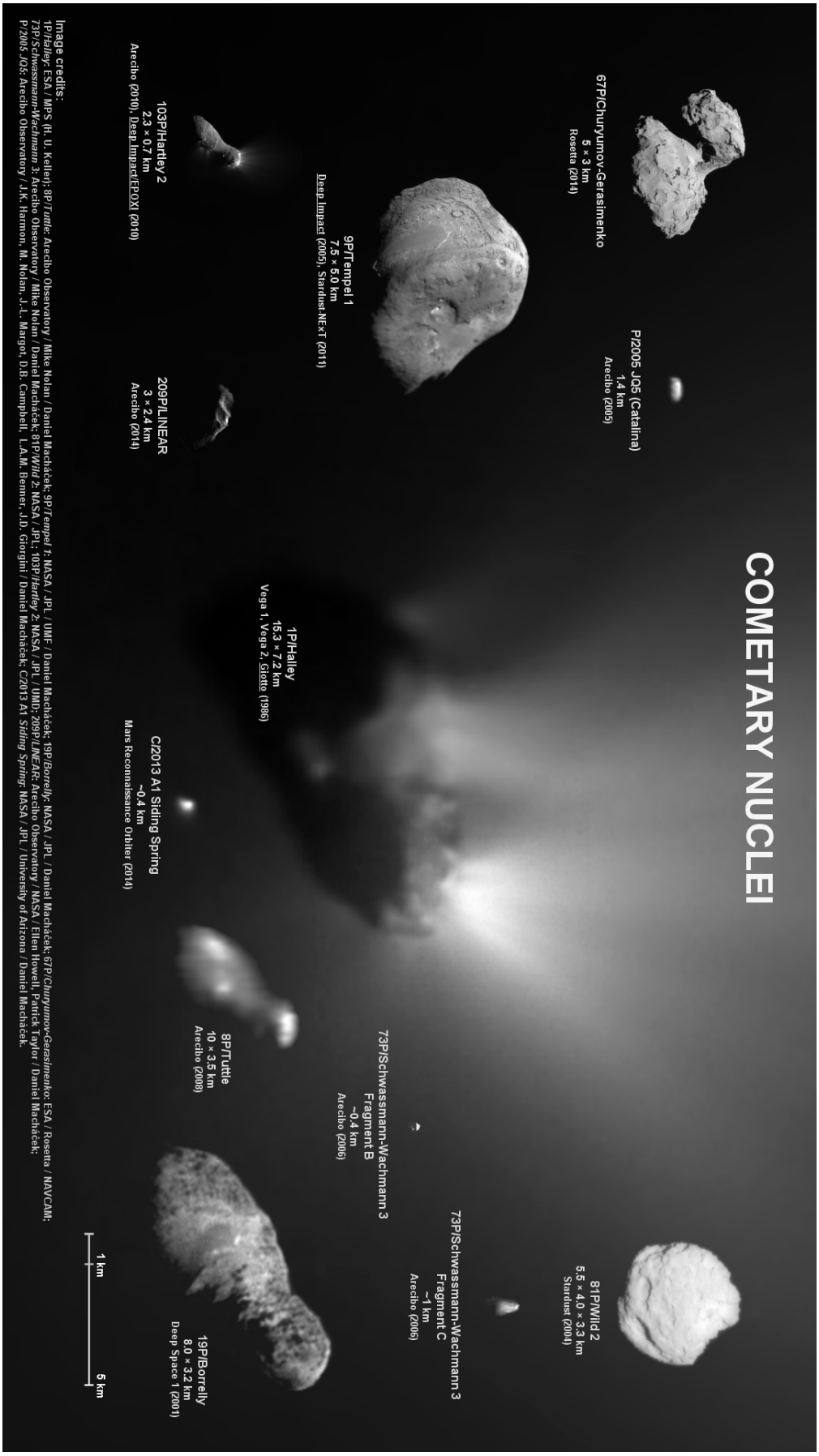

Figure 2: Collage of resolved cometary nuclei to date. The comets are displayed to scale. © Daniel Machacek, released under CC BY-NC-SA 2.0, https://creativecommons.org/ licenses/by-nc-sa/2.0/

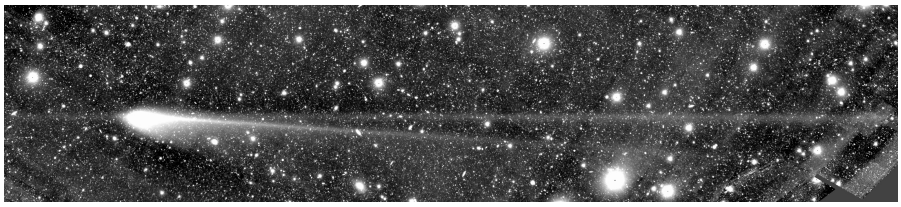

Figure 3: Comet CG as seen through the Subaru Telescope's Hyper Suprime Cam's wide field of view. The image was taken between 2:40-3:50 on 2016-03-08 (Hawaii Time). A broad-band filter (g-band, 480 nm) was used. The image is composed of ten 6-minute exposure images, stuck with respect to the background star positions. The comet itself is blurred due to its movement during the exposure. The dust tail is estimated to be more than 7 million kilometres long. © National Astronomical Observatory of Japan (NAOJ) image and text. https://www.subarutelescope.org/ Topic/2016/05/12/

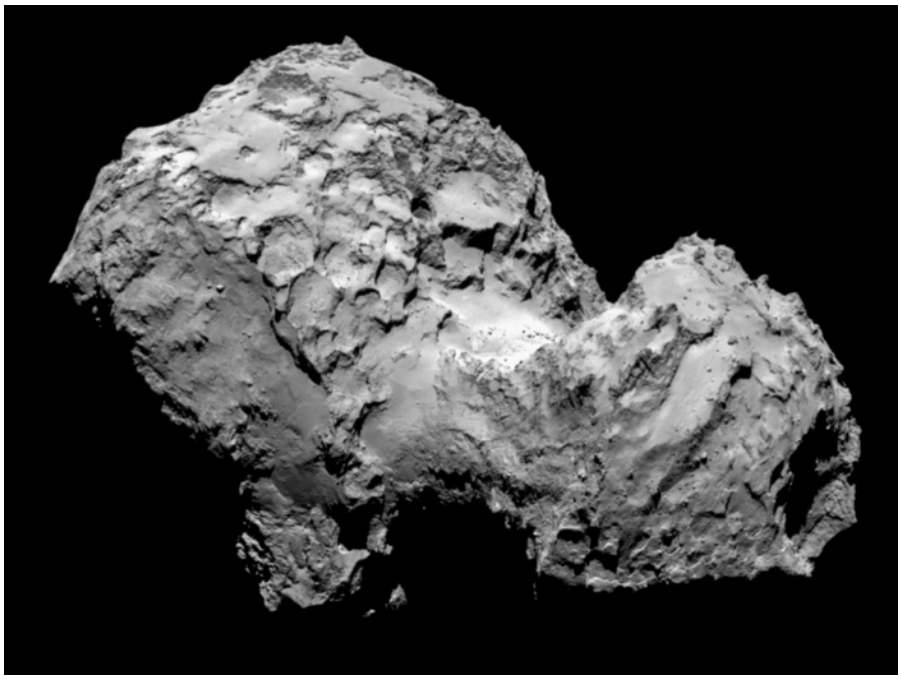

Figure 4: Comet CG by Rosetta's OSIRIS-NAC on 2014-08-03 from a distance of 285 km. The image resolution is 5.3 metres/pixel. © ESA/Rosetta/MPS for OSIRIS Team MPS/UPD/LAM/IAA/SSO/INTA/UPM/DASP/IDA/

2 MOTIVATION

Rosetta's payload was designed to comprehensively investigate the gas and dust emission from the nucleus (Glassmeier et al., 2007; Schulz, 2010) as the comet approached the Sun. In this work, the ultimate goal is to interpret observations by the Optical, Spectroscopic, and Infrared Remote Imaging System (OSIRIS) of the innermost dust coma and observations by the Rosetta Orbiter Spectrometer for Ion and Neutral Analysis (ROSINA) of the spacecraft in-situ gas density. We will use the observations to constrain the outgassing distribution on the nucleus surface and provide a preliminary model of the innermost gas and dust coma of the comet when it was between 3.4 and 2.8 AU pre-perihelion from the Sun. In particular, we are looking for models in support of the supposed inhomogeneous surface ice distribution inferred from data from the Microwave Instrument for the Rosetta Orbiter (MIRO) (Biver et al., 2015; Lee et al., 2015; Gulkis et al., 2015), the Ultraviolet Imaging Spectrometer (ALICE) (Feldman et al., 2015), the Visible and Infrared Thermal Imaging Spectrometer (VIRTIS) (Bockelée-Morvan et al., 2015), and ROSINA (Bieler et al., 2015) for the gas and reproducing the dust jet features observed by OSIRIS (Lara et al., 2015; Lin et al., 2015).

Because of the limited amount of data of the inner dust coma of comets pre-Rosetta and the relative abundance of dust coma/tail observations from ground based techniques most modelling efforts were targeted to simulate the large scale dust tail as e.g. in Agarwal et al., (2006), Agarwal, Müller, and Grün, (2007), and more recently Moreno et al., (2016). In contrast to this we are interested in building a model for the innermost dust coma, i.e. the first few kilometres above the surface. As far as we know Szegö et al., (2002) were the first to present a dust model for the inner dust coma and were able to produce reasonable results to interpreter Vega and Giotto observations of comet 1P/Halley.

To constrain the dust and gas emission we intend to show the importance of multi-instrument analysis. Intuitively, this can be understood from the illustration in Figure 5. A low local gas density measured by ROSINA at the spacecraft position can be consistent with a high gas column density as inferred by a line of sight measurement from e.g. MIRO. The sublimation of surface ices leads to the production of the gas and dust comae of comets (e.g. Huebner et al., (2006)). Due to the complex shape the expansion of gas from the surface

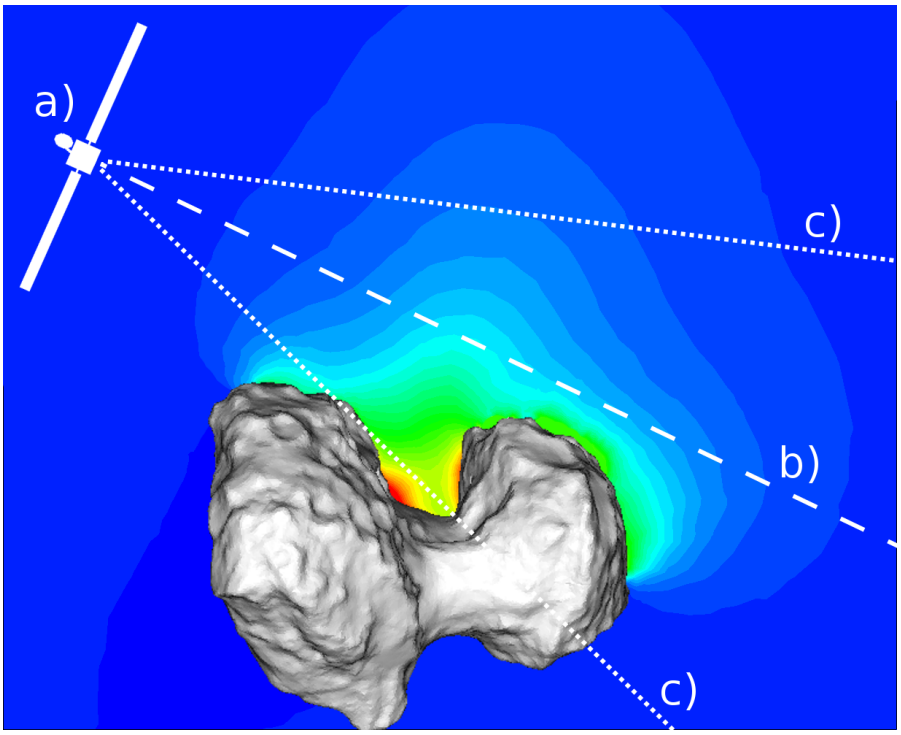

Figure 5: Illustration of the gas/dust coma (red color indicates high, and blue low local number density) and possible data gathering by different instruments: a) measurements at the spacecraft position (e.g. gas density as measured by ROSINA or dust collection by GIADA, COSIMA, and MIDAS), b) line of sight measurements as indicated by the dashed line (e.g. spectra as measured by VIRTIS-H or MIRO), c) field of view imaging as indicated by the dotted lines (e.g. surface and dust coma brightness as measured by OSIRIS or gas spectra as mapped by VIRTIS-M)

into space is complex in itself. Thus there is a need for models to understand data from different instruments in a self consistent manner. Furthermore, the question to which degree outgassing from cometary surfaces is inhomogeneous has been the subject of intense debate for many years (Keller et al., 1987; Crifo et al., 2002). The Rosetta data from autumn and winter 2014 - which we have chosen to focus on in this work - are particularly suited to the task of searching for inhomogeneity of outgassing because the spacecraft was relatively close to the nucleus at this time. Expansion of the gas (both radially and laterally) into the inner coma tends to smooth out inhomogeneities at larger distances. We will show in Section 7.3 that ROSINA cannot differentiate between certain kinds of inhomogeneous gas emission distributions on the surface. By adding data from other instruments (e.g. OSIRIS) such a degeneracy can be lifted to some degree. This realisation has motivated us to design a comprehensive modelling pipeline to simulate the inner gas and dust comae that will allow us to make comparisons with multiple instruments. This will

help us to constrain the emission from the surface to a higher degree than with just a single instrument. Though we must emphasise that the possible solutions we present are likely still non-unique.

Hence, we are interested to study possible inhomogeneities of the cometary gas and dust activity and whether the emission distribution can be linked to surface morphology or topography. To determine the local gas production rate on the surface as a function of time is another goal that is implicitly linked to the first. In addition, we strive to determine or constrain such parameters as the dust to gas production rate ratio and the dust size distribution. Our modelling pipeline allows us to study the complex dynamics of the gas and dust flow and its effects on measurable quantities. Determining the gas and dust emission rate and further parameters - ultimately for a longer period or even the entirety of the mission - is of great importance for the understanding of various processes linked to the ice sublimation. Some of these processes are e.g. the understanding of the surface erosion and mass loss; the understanding of dust transport and re-deposition; or the study of non-gravitational forces acting on the comet's orbit. We will show how the data and model can make constraints on e.g. the surface ice distribution for the first part of the mission in 2014. This will also highlight potential of the modelling pipeline we have set up.

In Part ii we will first describe the Rosetta instruments relevant for the work we present here. Then we will outline our modelling approach and describe in detail all of our models involved in understanding Rosetta data (Chapter 4). We dedicate Part iii to understanding spherical models and adding layers of complexity by introducing different emission distributions and the non-spherical shape of comet CG. We are in particular interested in how certain initial conditions such as the emission distribution on the surface, or the global gas production rate influence the properties of the gas and dust flow fields in 3D space (i.e. number density, speed, and temperature). Furthermore, we seek to understand how the complex shape of comet CG alters the gas and dust results. Finally Part iv presents our results to understand ROSINA and OSIRIS data and how they primarily constrain the emission distribution, dust size distribution, and dust to gas production rate ratio.

Part II

INSTRUMENTS & MODELS

3

ROSETTA INSTRUMENTS

This chapter gives a brief introduction to the instruments most important to this thesis. We will be discussing results of these instruments and compare them to our models in Part iv. Figure 6 shows an illustration of ESA's Rosetta spacecraft and its eleven scientific instruments. In the following three section we are going to focus only on ROSINA (Section 3.1), OSIRIS (Section 3.2), MIRO (Section 3.3), and VIRTIS (Section 3.4). The main focus in this thesis lays on ROSINA and OSIRIS as we have performed detailed comparisons with these two instruments (Part iv). The other two instruments have become part of our work done within the European Union's Horizon 2020 research and innovation programme project called Multi-instrument Analysis of Rosetta Data (MiARD). This project is still ongoing and no detailed comparisons and conclusions will be presented in this thesis. But we will show simulation results illustrating progress towards a comprehensive comparison with the MIRO and VIRTIS data in Chapter 12.

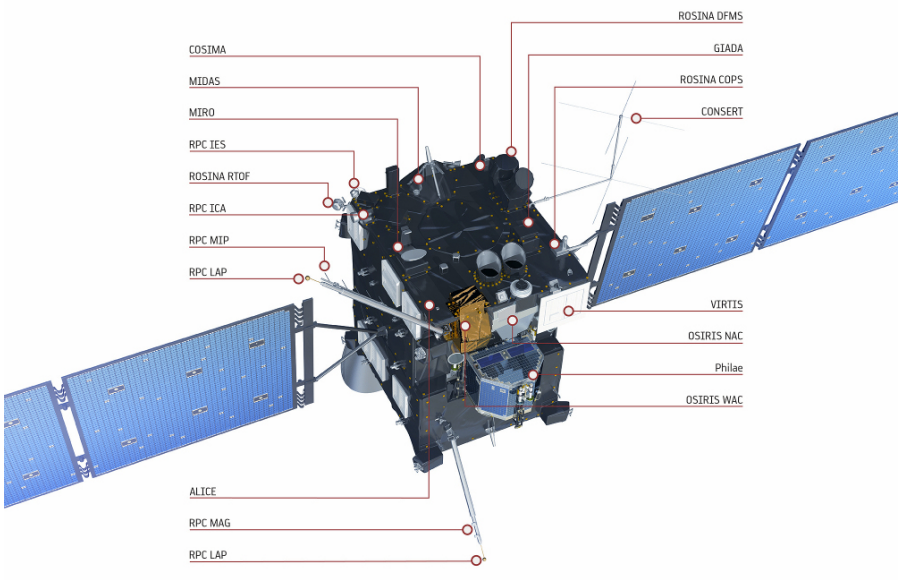

Figure 6: Illustration of ESA's Rosetta spacecraft with its eleven scientific instruments and their position and orientation on the spacecraft. *Copyright: ESA/ATG medialab*

3.1 ROSINA

The Rosetta Orbiter Spectrometer for Ion and Neutral Analysis (ROSINA) instrument is actually a suite of three instruments targeted to characterise to high precision the in-situ gas environment of comet CG at the spacecraft position. ROSINA is comprised of:

- A Double Focusing magnetic Mass Spectrometer (DFMS)
- A Reflectron type Time Of Flight mass spectrometer (RTOF)
- Two pressure gauges providing total pressure and ram pressure, the COmet Pressure Sensor (COPS)

We will only be comparing the COPS data to gas simulation of molecular water. Thus, the background signal has been subtracted from the data and the gas number densities have been scaled to reflect the H_2O signal according to the bulk gas compositions measured by DFMS. Furthermore, data within 30 minutes of thruster firings for attitude changes and other orbital manoeuvres of the spacecraft have been omitted. The choice of 30 minutes has been taken in accordance with the common practice within the ROSINA team.

The data set we use was obtained between 2014-08-20 and 2015-03-01 when the comet was between 3.51 and 2.2 AU from the Sun pre-perihelion. Hässig et al., (2015) have shown large variations in the gas composition with sub-spacecraft latitude. H_2O is the most dominant gas when the spacecraft is over the summer hemisphere (corresponding to equatorial to high sub-spacecraft latitudes at that time). This is the reason for us to perform simulations with H_2O as the sole gas species. For high negative sub-spacecraft latitudes (winter hemisphere at that time) the $CO_2$and CO signal become equally high or higher than that of the H_2O signal. As we have only performed single species simulations with H_2O we must thus be very cautious comparing the COPS data with our simulation results for high negative sub-spacecraft latitudes. For regions that are permanently shadowed we would not expect our simulations to reproduce the data. Other studies as e.g. Bieler et al., (2015) and Fougere et al., (2016a) artificially introduce night side emission on the order of 2% to further enhance the fits to the ROSINA data. This will be discussed in Section 4.6.

3.2 OSIRIS

The Optical, Spectroscopic, and Infrared Remote Imaging System (OSIRIS) consists of two high-resolution optical cameras, a narrow angle camera (NAC) with an angular resolution of 18.6 µrad px^{-1} and a field of view of $2.20 \times 2.22°$, and a wide angle camera (WAC) with 100 µrad px^{-1} angular resolution and a field of view of $11.35 \times 12.11°$ (Keller et al., 2007). Both cameras operate in the optical wavelength regime (250–1000 nm) with 12 spectral filters for the NAC and 14 spectral filters for the WAC. The images used for comparison in this work were acquired with the WAC using a «dust continuum» filter with a central wavelength of 612.6 nm and a bandwidth of 9.8 nm.

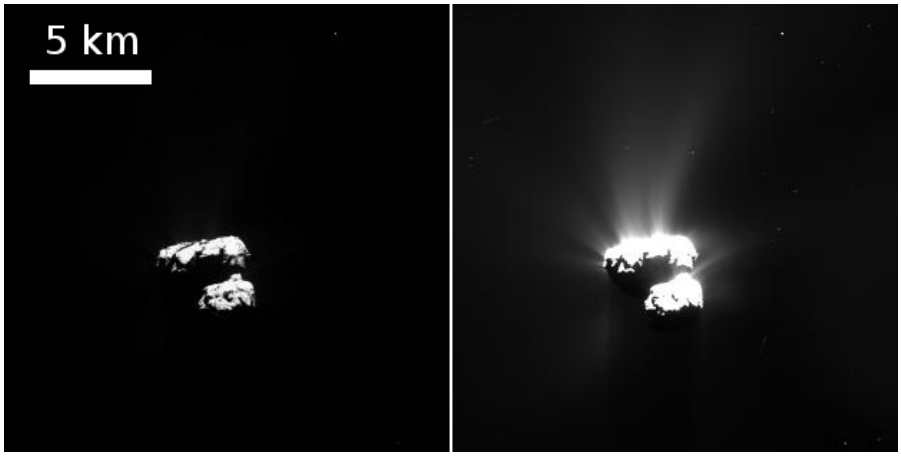

Figure 7: WAC_2015-05-11T14.08.25.827Z_IDB0_139754950_F13.IMG stretched to two different ranges illustrating the high dynamic range of the OSIRIS cameras and exposing the dust coma.

OSIRIS image files have the format (text in braces and italics indicate the changing values for each image): *{camera identifier}_{date (format: YYYY-MM-DD)}*T*{time (format: hh.mm.ss)}*ZID*{level id}* *_{spacecraft clock count}* _F*{filter id}*.IMG where:

- *{camera identifier}* is either «WAC» or «NAC».
- *{level id}* is «00», «01», «02», «03», or «B0». Each indicating a different level of post processing of the image, the last indicating level «3B». This is described in more detail in Tubiana et al., (2015). E.g. level «03» gives for each pixel the radiance, I, in W m^{-2} nm^{-1} sr^{-1}. For the highest Level («3B») each pixels contains the reflectance, R (R = I/F, where F is the solar flux) which is unit-less.
- *{filter id}* is made up of two single digit integer numbers, each for the filter wheel position on each of the two filter wheels. E.g. «18» is to be read as «one eight» (not «eighteen») thus corresponding to filter wheel one being at position 1 and filter wheel two being at position 8.

Thus e.g. the file «WAC_2015-05-11T14.08.25.827Z_IDB0 _139754950 _F13.IMG» corresponds to the level «3B» data of an image taken by the wide angle camera on 2015-05-11 at 14:08:25.827 UTC with filter 13. Figure 7 shows this image on two scales, illustrating the high dynamic range of the OSIRIS cameras. The left panel shows the image scaled such that the nucleus is well exposed and the right panel shows the same image stretched in a manner that the dust coma is visible. In the latter case the nucleus becomes over exposed. Both the comet nucleus and the much fainter dust coma can be simultaneously imaged.

3.3 MIRO

The Microwave Instrument for the Rosetta Orbiter (MIRO) consists of a 30 cm telescope and two heterodyne receivers operating at frequencies of 190 GHz (wavelength of 1.6 mm; millimetre receiver) and 562 GHz (wavelength of 0.5 mm; sub-millimetre receiver) (Gulkis et al., 2007). The continuum channels of MIRO are designed to measure the temperature of the cometary surface and sub-surface and thus the temperature gradient close to the surface. MIRO can thus estimate thermal properties such as the thermal inertia (Gulkis et al., 2015), which is important for our modelling work. Additionally, MIRO is equipped with a 4096 channel CTS (Chirp Transform Spectrometer) (Gulkis et al., 2007) which is connected to the sub-millimetre receiver and can thus be used to measure absorption and emission spectra. The Spectrometer is tuned to measure the spectra of CO, CH_3OH, NH_3 as well as the following three isotopologues of water, $H_2^{16}O$, $H_2^{17}O$, and $H_2^{18}O$. Here we are especially interested in the spectra of the water isotopologues. These spectra can either be used to infer the H_2O column density, as well as the H_2O number density, speed, and temperature along the line of sight of MIRO. These profiles along the MIRO line of sight can be compared to the corresponding extracted profiles of our simulations as we will show in Chapter 12. Conversely, extracted profiles from our simulations can be used to produce predictions for spectra which can then be compared to the actual spectra measured by MIRO. This is work still ongoing in the context of the MiARD project and in particular in collaboration with David Marshall, Ladislav Rezac, and Paul Hartogh from the *Max-Planck-Institut für Sonnensystemforschung* (MPS).

3.4 VIRTIS

The Visible and Infrared Thermal Imaging Spectrometer (VIRTIS) is an imaging spectrometer on board of Rosetta that operates in the visible and infrared regime of the electromagnetic spectrum (Coradini et al., 2007).

«The VIRTIS instrument combines a double capability: (1) high-resolution visible and infrared imaging in the 0.25-5 μm range at moderate spectral resolution (VIRTIS-M channel) and (2) high-resolution spectroscopy in the 2-5 μm range (VIRTIS-H channel).» (Coradini et al., 1999)

VIRTIS is of importance to us to understand the thermal properties of the nucleus surface in complement to MIRO. As with MIRO we can use profiles of our simulations to convert these into spectra which can be compared to VIRTIS-H data. Furthermore, VIRTIS-M can be used to produce spatially resolved gas column density maps. This is ongoing work (see Chapter 12) in the context of the MiARD project and in particular in collaboration with David Kappel from the *Deutsche Zentrum für Luft- und Raumfahrt* (DLR) in Berlin. The main challenge we face here is the long exposure/integration times needed for a high signal-to-noise ratio. These long observation times result in large changes in the viewing geometry of the comet due to its rotation and the movement of the spacecraft, though the latter contributes much less to the change in geometry in most cases as the relative speed of the spacecraft to the comet is quite low (less than a few meters per second).

4

MODELS AND INPUT PARAMETERS

In this chapter we describe in detail the different models involved in our modelling pipeline and how they intersect with Rosetta data. Additionally, we will describe the different input parameters used in the models and how they are varied and influence the results. In Section 4.1 we discuss the modelling approach we have taken, which is illustrated in Figure 8. Each subsequent section is dedicated to the one of our steps in the modelling pipeline, from the shape model (Section 4.2) to the production of artificial dust images (Section 4.10). We conclude with a summary of the involved input parameters and constants in Section 4.11.

4.1 MODELLING APPROACH

Our guiding principle was to set up a pipeline of models that will enable us to comprehensively study in a self consistent way the dynamics of the inner dust and gas comae of comet 67P/Churyumov-Gerasimenko (CG) in full 3D. The various models should contain all dominant physical processes while using the least amount of free parameters. This is to ensure that the parameter space is kept as small as possible while not neglecting any significant physics involved. According to these principle we were evidently forced to make some decisions as to which effects can be neglected. E.g. we chose to omit some secondary effects due to scientific arguments but also because of the available computational power. Hence, including all physical processes involved would simply not be computationally feasible. We are interested in studying the effects of the dominant physical processes. The nature of secondary effects can be studied in a later step. We will point out these decisions and their justification wherever they come up. It is important not only to understand the included physics but also the limitations of the respective models. These limitations can be of fundamental nature as to the physical processes implemented or in the applicability to specific conditions of the considered comet. Furthermore, we will highlight possible extensions to the models which could be implemented in the future.

Figure 8 illustrates our modelling approach schematically. It shows how our model interacts with data from different Rosetta instruments. Each blue arrow box represents an independent model or procedure, relying solely on the results of the preceding box, global input parameters common to all models, and individual input

parameters solely necessary for that model. Though the schematic illustrates the modelling pipeline in the context of Rosetta and its target comet CG it is not constrained to it. The same models can in principle be applied to any comet and in particular be used to investigate some simpler spherical cases as discussed in Part iii.

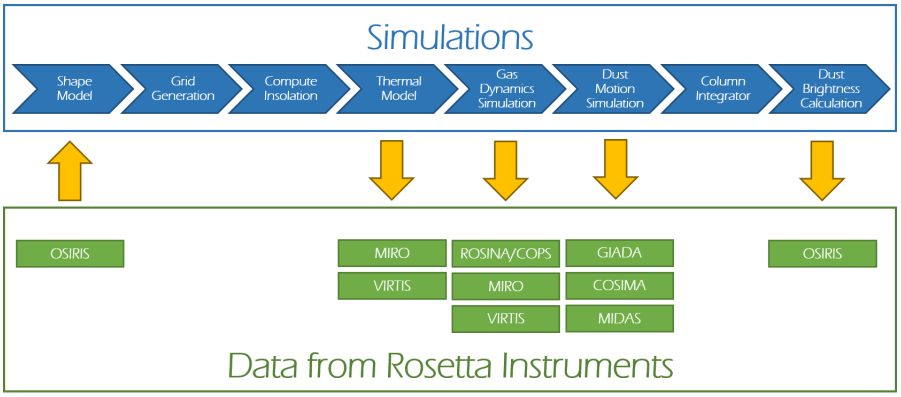

Figure 8: Schematic illustration of our modelling pipeline. Each blue arrow box stands for a model or procedure building on the prior model by using its results. The green boxes indicate the instruments of Rosetta with which we can compare the results of the respective model with.

One important decision we have made, which needs to be justified right at the beginning, is the fact that we are not simulating the gas and dust comae at the same time within the same code, but rather in sequence. First the gas coma is simulated with a Direct Simulation Monte Carlo (DSMC) approach (Section 4.7) the result of which is used in a next step to model the dust coma with a test particle approach (Section 4.8). This can only be done when one assumes that the gas flow is independent of the presence of the dust. Two conditions need to be fulfilled for this to be true.

1. **The cometary coma is gas dominated:** The dust motion is driven by the gas and thus gains in kinetic energy by extracting it from the gas flow. If the energy transferred from the gas to the dust is a significant fraction of gas energy, the presence of the dust has a non-negligible back-reaction on the gas flow and influences its dynamical properties and must thus be taken into account. For all models considered in this work we are dealing with a gas dominated coma as the energy in the dust coma is only a few percent of the energy within the gas coma (Marschall et al., 2016, and Part iv).

2. **No significant extended/distributed source:** The gas of cometary comae can have two origins. Either it comes directly from the nucleus (sub-)surface or icy dust grains are dragged out into space where their ice content sublimates producing

what is referred to an extended or distributed source (e.g. Ahearn et al., (1986) and Eberhardt et al., (1987) for comet 1P/Halley). In such a case additional gas is injected into the coma which not only has an impact on the gas but also on the size distribution of the dust (Vaisberg, Smirnov, and Omelchenko, 1986). For comet CG there is no evidence for such an extended water gas source (Fulle et al., 2016a).

Thus, simulating the gas and dust dynamics in sequence can only be applied to comae dominated by gas and comae that lack any significant extended gas source coming from icy dust particles. Because both of these conditions are met for comet CG it is unproblematic to simulate the gas and the dust dynamics in sequence. Simulating both, dust and gas, within the same code results in much longer simulation times (especially in a non-fluid approach as ours). This is due to the very different time scales that gas and dust particles inhabit. Gas molecules accelerate very fast to speeds of hundreds of meters per second whereas very large particles only move at a few meters per second (e.g. Marschall et al., (2016) and Skorov et al., (2016)). This results in very different time steps and time scales which need to be implemented within one code making it inefficient. There are approaches that treat the gas and dust as fluids. But these approaches have some drawbacks, the main one being that dust streams cannot cross through each other. But in a rarefied dust environment this does happen and needs to be accounted for, especially when studying the first kilometres above the nucleus surface.

The main assumptions for the work presented here are:

1. We are dealing with a rarefied gas and dust environment.
2. The gas coma is dominated by a single species (H_2O) to the extent that we can neglect the minor gas species (Hässig et al., 2015).
3. The gravitational field of the comet (mass according to (Sierks et al., 2015)) is too weak to affect the gas dynamics and must only be considered for the dust dynamics, in particular for large particles.
4. Both the gas and dust speeds are high enough that the rotation of the comet can be neglected and thus time dependent simulations are not necessary (Part iv). For very large dust particles this will no longer be true, hence our solutions need to be considered with great care and time dependent solutions will ultimately be needed.

In the following sections we will be discussing each model and procedure involved. The starting point of any of our simulations is a

3D shape model of the cometary surface (Section 4.2). This surface model - in principle any closed 3D surface made up of triangles (or surface facets) - is the basis for constructing a 3D grid (Section 4.4) filling in the volume from the cometary surface out to a certain distance. We will also refer to the grid as our simulation domain. The cells - comprising the grid - are the units within which all of the properties of the 3D gas and dust flows are calculated. Knowing the position of the Sun at a specific time allows the calculation of the angle of incidence of the solar light with regard to the surface facets (Section 4.5) and subsequently the surface temperature and gas production rate (Section 4.6). The surface temperature and gas production rate allow the simulation of the 3D gas flow field (Section 4.7) and thereafter the dust flow field (Section 4.8) within the simulation domain. For the latter the gravity field (Section 4.3) of the comet needs to be accounted for. For a determined viewing geometry the dust result will be used to calculate dust column densities along the line of sight (Section 4.9) which can be converted to brightness values using a particle scattering model (Section 4.10).

Once a shape model has been selected and the desired resolution of the simulation domain has been chosen the first three parts of the simulation pipeline (shape model, gravity field, and the grid) are not altered and remain fixed. At that point variations of the models occur solely in subsequent parts of the pipeline starting with the thermal model (Section 4.6).

4.2 THE COMET'S SHAPE AND SURFACE

4.2.1 *3D shape models*

The foundation of our simulations is the adequate cometary 3D surface shape model. We can use arbitrary shapes as input as long as the surface is closed. For this work we will present results for two shapes, a sphere and the actual shape of comet CG. These shape models are built of triangles, which we refer to as surface facets. This triangulation can be seen in Figure 9.

We have been using two versions of CG shape models. Firstly, we have used the model called SHAP4S of Preusker et al., (2015), which is based on a stereophotogrammetric technique and is based on OSIRIS-NAC images acquired between 2014-08-19 and 2014-09-03. It was made available to us in February 2015. The model has a horizontal spacing of 2 m and a vertical accuracy on the decimetre scale. The model has over 16 million facets. This shape model is beyond our computation capacity. Hence we used a decimated version of this model where the number of facets has been reduced to 50'000,

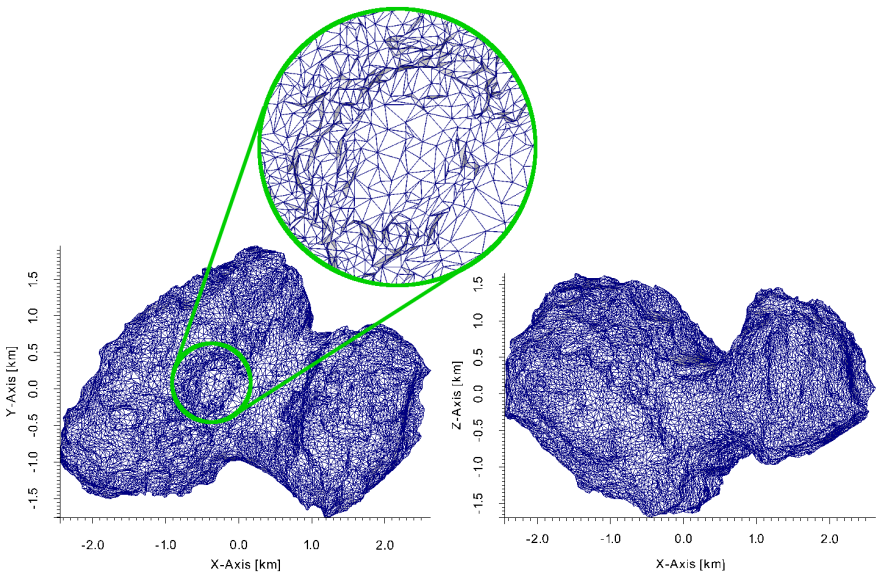

Figure 9: The 3D surface of CG (decimated 50'000 facets version of SHAP7) illustrating the surface triangulation, the Cartesian coordinate system and scale of the comet. The left panel shows a north polar view and the right panel a side view with the observer positioned on the negative y-axis.

providing a resolution of roughly 32 m.

The second model we have used is called SHAP7 which was also produced by the DLR group that produced SHAP4S. It's final version was made available to us in December 2016. Its made up of more than 44 million surface facets and has a spacing of 1-2 m and a vertical accuracy of 0.2-0.3 m. Again images from the OSIRIS-NAC camera have been used. In particular the images of the imaging sequences SHAP4S (for the northern hemisphere), SHAP5 & SHAP6 (for equatorial latitudes), and SHAP7 (for the southern hemisphere). Again the full resolution shape model cannot be directly used for our models due to hardware restrictions but thanks to an upgrade of our cluster with a resulting increase in computing power we have been using the decimated version of SHAP7 where the number of surface facets has been reduced to 125'000 facets.

The data that was used to construct the SHAP4S model was acquired during the time when the mid to high southern latitudes were in permanent shadow. Thus, these areas could not be imaged and are hence not included in the model. SHAP7 covers the entire cometary surface to a much higher precision. The main differences between the SHAP4S and SHAP7 are illustrated in Figure 11. In addition to the lack of the southern hemisphere SHAP4S is also much smoother than SHAP7, which provides a much more detailed surface description.

We consider SHAP7 the final shape model of CG to be used for the kind of modelling work we are performing.

4.2.2 *Coordinate systems of comet CG*

Figure 9 shows the decimated version of SHAP7 with 50'000 facets in two views. The figure also shows the coordinate system referred to as the Cheops frame, which has been agreed upon to be the coordinate system of comet CG. The comet measures approximately 4.5x3.5x3 km in the x-y-z-directions.

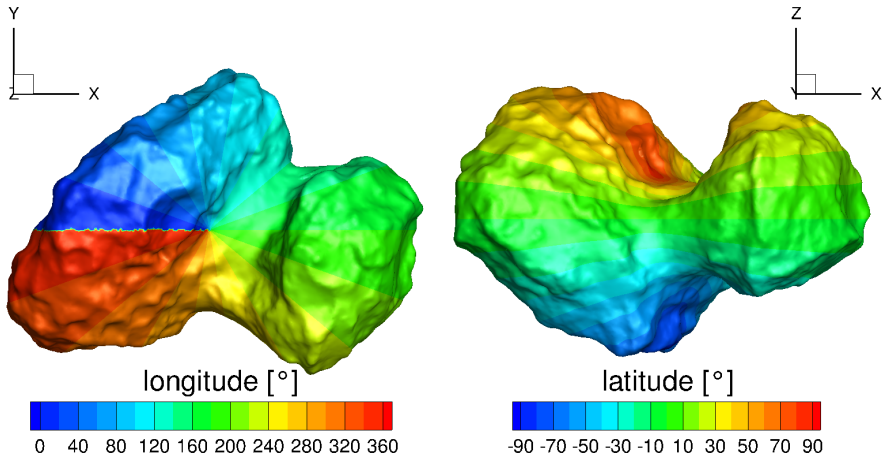

Figure 10: Two perspectives of the comet as in Figure 9 showing the longitude/latitude coordinate system used in this work. The left panel shows the north polar view and the longitude plotted on the surface while the right panel shows a side view of the comet with the latitude.

In the Cheops frame the z-axis is aligned with the rotation axis of the comet with a right handed rotational sense. The positive z-axis defining the north pole and the negative z-axis defining the south pole. In this coordinate system each facet position can be converted from Cartesian coordinates into spherical coordinates. The resulting longitudes and latitudes are visualised in Figure 10. We are dealing with a very concave shape the longitude/latitude system does not map out the comet unambiguously as can be seen in Figure 10. More than one position on the comet can have the same longitude and latitude. Furthermore, the 0° meridian can in principle be set arbitrarily. We have decided to align it with the negative x-axis. This results in the zero longitude zero latitude point to be positioned in the Imhotep region (we will define these regions in Section 4.2.4) where the Cheops boulder - giving the reference frame its name - is located.

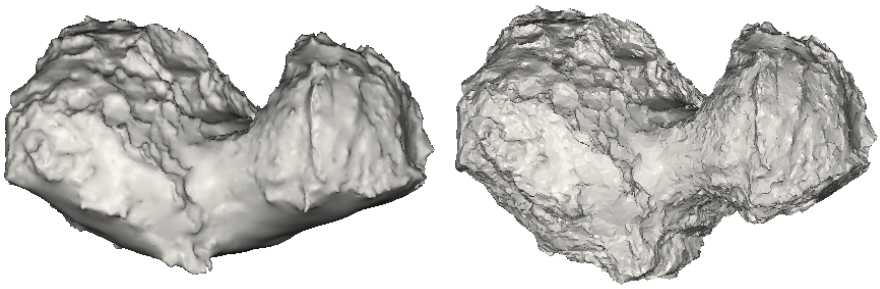

Figure 11: Comparison view of the two shape models used in this work. SHAP4S on the left and SHAP7 on the right illustrating especially the additional coverage of the southern hemisphere in the SHAP7 model. Both models are decimated versions with 50'000 facets.

4.2.3 *Orbital and rotational parameters of comet CG*

Comet CG has quite a stable rotation axis which is tilted by 52.3° with respect to its orbital plane. The orientation of the rotation axis and rotation period was determined with OSIRIS images (Mottola et al., 2014; Sierks et al., 2015; Preusker et al., 2015). The orientation of the axis is RA = 9.54°, Dec = 64.11° (in J2000 equatorial coordinates) and the rotation period upon arrival at the comet was (12.4043 ± 0.0007) h. The comet shows only a very weak precession within a half cone of 0.14° and a precession period of 10.7 days (Preusker et al., 2015). Due to the gas activity the rotation period was observed to slow down in the course of the escort phase of the Rosetta mission (Keller, H. U. et al., 2015).
Due to the stable rotation axis the illumination conditions can be fully characterised by the heliocentric distance, the sub-solar latitude, and subsequent rotation around the rotation axis (z-axis in the Cheops frame). Figure 12 shows the first two of these parameters as a function of time for the period of Rosetta's mission at the comet. The figure is also annotated with the two equinox passings, perihelion, the arrival of Rosetta at CG, and the end of the Rosetta mission. The heliocentric distance primarily controls the energy flux to the surface while the sub-solar latitude (and longitude) controls the part of the comet where this energy is deposited on. Figure 12 illustrates that the northern hemisphere of comet CG experiences cold summers (high sub-solar latitudes at large heliocentric distances) while the southern hemisphere sees hot summers (high negative sub-solar latitudes at small heliocentric distances) and thus the exact opposite of the northern hemisphere. This is important for the understanding of the long time evolution of the comet. In addition, the south summer solstice does not align perfectly with the perihelion passage but occurred on the 2015-09-04 which is 22 days post-perihelion. This results in the fact that during the Rosetta mission at the comet a larger range of sub-solar latitudes was covered in the inbound orbit compared to the

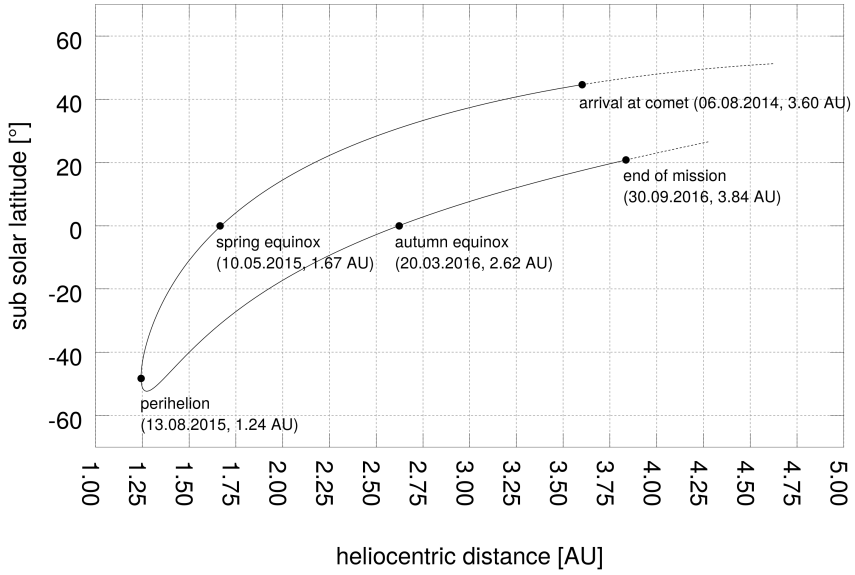

Figure 12: Heliocentric distance and sub-solar latitude of comet CG for the period of ESA's Rosetta mission. The plot is annotated with the two equinox passings, perihelion, the arrival of Rosetta at CG, and the end of the Rosetta mission.

outbound orbit of CG. Due to the very elliptical orbit (perihelion at 1.24 AU and aphelion at 5.69 AU) and according to Kepler's 2nd law of planetary motion (Kepler, 1609; Kepler, 1622) the temporal change in heliocentric distance ($\frac{dR_h}{dt}$) is small when close to aphelion and large when close to perihelion. Due to the configuration of the rotation axis in conjunction to the elliptical orbit the temporal variation of the sub-solar latitude ($\frac{d\ lat}{dt}$) is highest at perihelion and smallest at aphelion. This needs to be kept in mind when simulating the outgassing of the comet in discrete time steps.

4.2.4 *The surface morphology of comet CG*

The nucleus of comet CG is commonly divided into two lobes - the bigger one usually referred to as the «Body» and the smaller one referred to as the «Head» lobe. The two lobes are connected by what is referred to as the comet's «Neck». The surface exhibits a vast variety of surface morphologies (Thomas et al., 2015b). This has been used to define 26 morphological regions (Thomas et al., 2015b; El-Maarry et al., 2015; El-Maarry et al., 2016; El-Maarry et al., 2017). Figure 13 shows the northern regions, which will be the ones mainly used in this work.
There are regions which are strongly consolidated (e.g. Hathor), others are fully or partially covered by dust (e.g. Hapi in the «Neck», Ma'at on the «Head» lobe, or Ash on the «Body» lobe), others are large depressions (e.g. Aten on the «Body» lobe, or Hatmehit on the

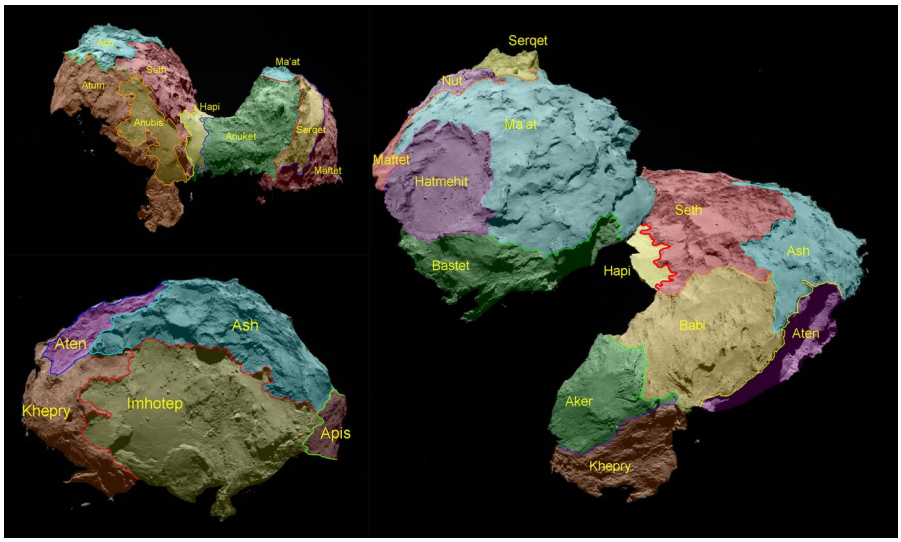

Figure 13: Figure taken from Thomas et al., (2015b) showing the defined morphological regions on the northern hemisphere and equatorial regions of comet CG.

«Head» lobe). All 26 regions as defined by El-Maarry et al., (2015) and El-Maarry et al., (2016) are listed in Table 3 which also includes a classification of each region.

4.3 GRAVITATIONAL MODEL

The gravity field of comet CG differs substantially from that of a sphere. It is therefore necessary to calculate the real gravitational field of the comet to accurately asses its effect on dust particles (described later in Section 4.8). We determine the gravity field of this complex by employing a simple model. The gravitational acceleration of an arbitrary object exhibited at any point in space can be written as

$$\vec{a}_G(\vec{y}) = G \int_V \rho \frac{\vec{r}}{|\vec{r}|^3} dV \tag{1}$$

where $\vec{r}$ is the vector of point $\vec{y}$ to the volume element dV, G is the gravitational constant, and ρ is the local mass density of the body.

Since this integral only has an analytic solution for the homogeneous sphere, homogeneous spherical shells, or a point source, the value of $\vec{a}_G$ must be determined numerically in our case. This was achieved by discretising the volume of the shape model SHAP4S (Preusker et al., 2015) with a resolution of 30 m resulting in $\sim$ 800'000 volume elements ΔV and assuming a constant density of 462 kg m^{-3}, which results in a total mass of $9.9 \cdot 10^{12}$ kg (Sierks et al., 2015). The integral in Equation 1 thus reduces to a sum over all these elements:

$$\vec{a}_G(\vec{y}) = G\rho\Delta V \sum_n \frac{\vec{r}}{|\vec{r}|^3} \quad , \tag{2}$$

Region name	Region type
«Body» lobe	
Aker	Strongly consolidated
Anhur	Weakly consolidated
Anubis	Non-consolidated: Smooth
Apis	Strongly consolidated
Ash	Non-consolidated: Dust-covered
Aten	Depression
Atum	Strongly consolidated
Babi	Dust-covered/Brittle
Bes	Consolidated
Geb	Consolidated
Imhotep	Non-consolidated: Smooth
Khepry	Strongly consolidated
Khonsu	Consolidated/mixed
Seth	Weakly consolidated/Brittle
«Neck»	
Hapi	Non-consolidated: Smooth
Sobek	Consolidated
«Head» lobe	
Anuket	Strongly consolidated
Bastet	Strongly consolidated
Hathor	Strongly consolidated
Hatmehit	Depression
Ma'at	Non-consolidated: Dust-covered
Maftet	Strongly consolidated
Neith	Consolidated
Nut	Depression
Serqet	Strongly consolidated
Wosret	Consolidated

Table 3: Table taken and combined from El-Maarry et al., (2015) and El-Maarry et al., (2016) listing and describing the 26 defined morphological regions on comet CG.

This has been done for over 21 million points of a cubical grid up to a distance of 10 km from the centre of the nucleus. The resolution of the cubical grid is 30 m up to a distance of 3 km, 50 m between 3 and 5 km, and 100 m beyond 5 km distance to the nucleus centre.

Figure 14 and Figure 15 show the results from this calculation. First we see in Figure 14 that the surface acceleration has a global minimum in the «Neck» in the Hathor region towards the Hapi region. Gravitational maxima are in the Imhotep region on the «Body» lobe and the Hatmehit depression on the «Head» lobe. The maximum gravitational acceleration is $\sim 2 \cdot 10^{-4}$ m s^{-2} which is five orders of magnitude lower than the gravitational acceleration on the Earth. Due to the complex shape it is not intuitive what the local gravitational slopes look like. The Hathor cliff is in some places almost vertical but other slopes e.g. in the Seth region seem very much steeper than they actually are ($35 - 60°$).

Figure 15 shows two slices ($x = 0$ m and $y = 0$ m) for the full 3D gravity field. The panels on the left show the gravitational field strength with the same trends that we have already seen in Figure 14 (gravitational low in the «Neck» and gravitational high over Hatmehit and Imhotep). It is immediately apparent that the gravity field close to the surface differs substantially from a point source gravity field. We have thus compared CG's gravity field with point source gravity. The middle panels show the ratio of the field strengths of CG to point gravity. We can see that we massively overestimate the gravitational field strength in the «Neck» regions were we to assume point gravity and on the contrary underestimate the gravitational acceleration especially above Hatmehit and Ash. But point gravity is not only failing to estimate the field strength correctly but also the direction of the field. This is shown in the right panels where we plot the angle between the direction of point source and CG's gravity. Due to the concave shape the larges deviations are as expected in the «Neck» regions where they can be up to 60° (Hathor). These calculations also show that the field strength and direction of the field come close to each other (ratio $= 1$ and angle $= 0°$) between $5 - 10$ km. It is thus quite safe to assume that beyond 10 km from the centre of the nucleus the point source approximation is valid. We can also calculate the escape velocity with

$$v_e = \sqrt{\frac{2GM}{r}} \quad , \tag{3}$$

where M is the mass of the comet, and r is taken to be the effective radius of the nucleus (2 km). This results in an escape velocity of $v_e = 0.81$ m s^{-1}.

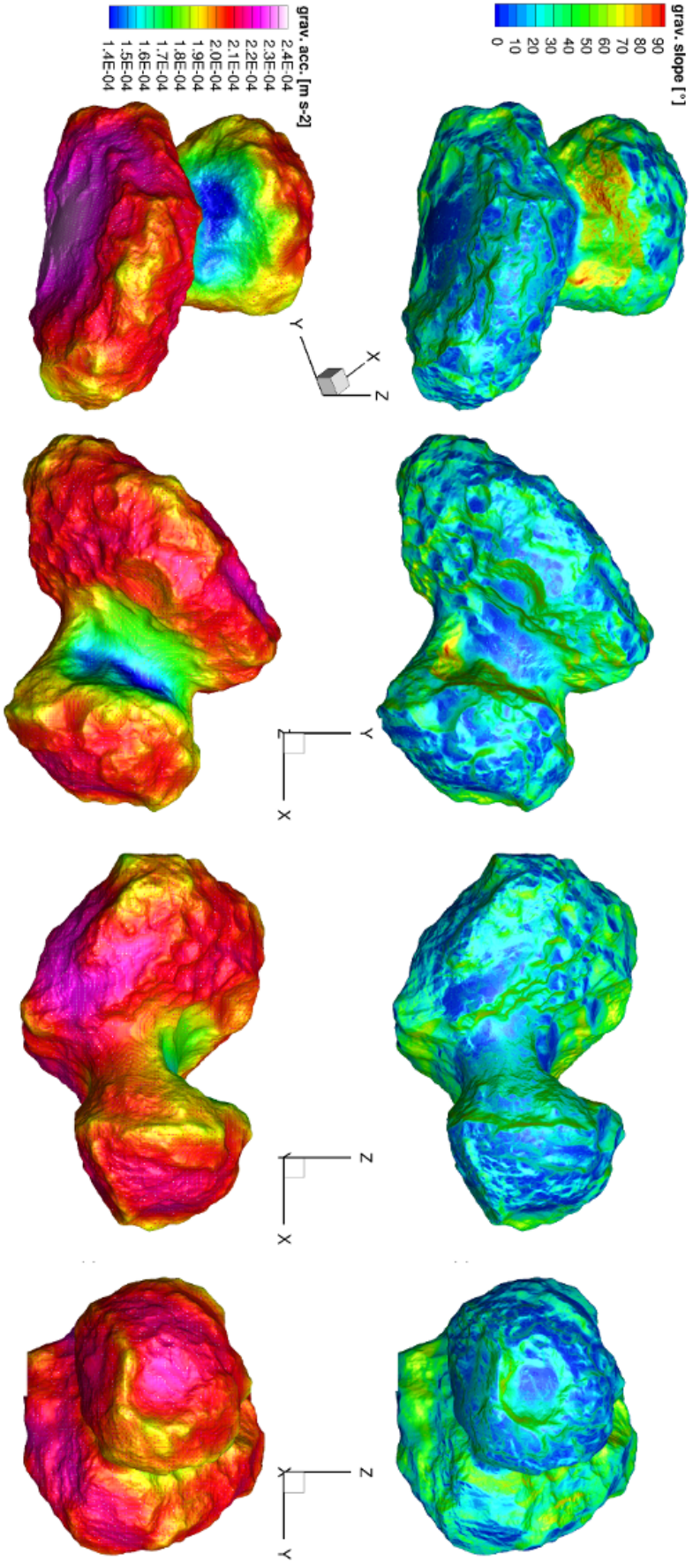

Figure 14: The local gravitational slope (top row) and surface acceleration (bottom) of comet CG for different viewing geometries

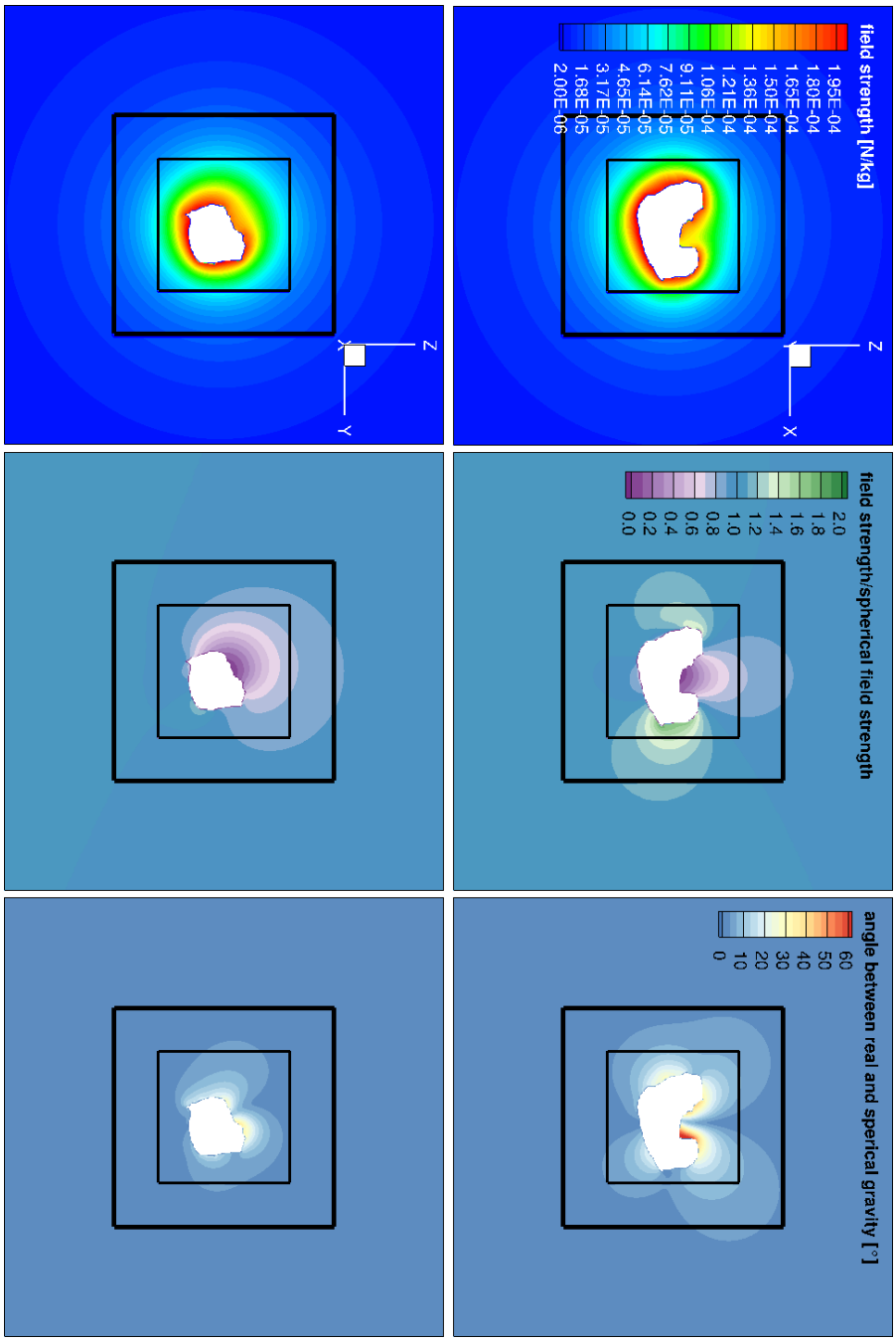

Figure 15: We show two different slices (top row: $y = 0$ m, bottom row: $x = 0$ m) through the solution of the gravity field. The two boxes show the boundary between the three sub-grids where the resolution changes. The gravitational field strength (left panels), ratio between the real and spherical gravitational field strength (centre panels), and angle between the real gravitational field and the spherical field (right panels) are shown for both slices.

4.4 GRID GENERATION

A substantial amount of time and understanding of the physics of gas flows goes into building a grid wherein its cells the actual calculations of the gas and dust comae are performed. The generation of our simulation grids has been performed in the most part by Ying Liao (Liao, 2017) and in the recent months additionally by Olga Pinzón.

On the basis of a shape model described in Section 4.2, we constructed an unstructured 3D grid with the software Gridgen™ by Pointwise (pointwise.com/gridgen/). The fundamental challenge posed here is expanding a complex 2D surface such as the one of comet CG with large scale concavities into 3D space.

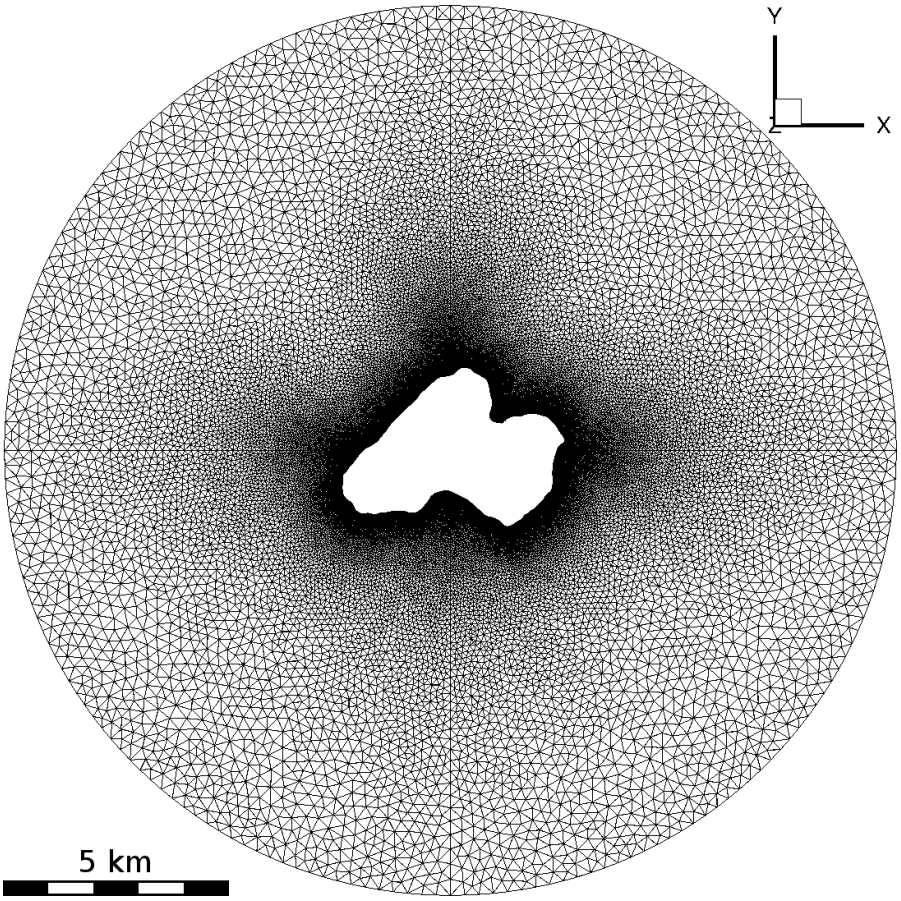

Figure 16: Slice with $z = 0$ m through the unstructured 3D grid illustrating the tetrahedron cells. The cells increase in size from the comet surface to the outlet surface which is located at 10 km from the nucleus centre. This grid is based on the 50′000 facet decimation of SHAP7 and is comprised of a total of 3′210′647 cells.

We are primarily interested in the gas and dust flow immediately above the surface, hence the simulation domain has been extended out to only 10 km from the centre of the nucleus. The unstructured grid uses tetrahedron cells. Figure 16 shows a slice through an example of an unstructured 3D grid illustrating the tetrahedron cells. The cell size must be adjusted to satisfy the condition that mcs/mfp < 1, which requires some experience. The mean collisional separation (mcs) is determined within the gas simulation and has no physical meaning but rather is the distance between two gas molecules that undergo a collision within the simulation. As the mean free path (mfp) depends on the local gas production rate the grid resolution is tightly linked to the level of gas activity. If mcs/mfp > 1 the errors of the results become larger. The construction of the grid takes a significant amount of time and thus it is not feasible to redo this step to make the perfect grid for every simulation. We have thus relaxed the above constraint slightly and will still consider a simulation result valid if mcs/mfp < 10 in a small volume of the simulation domain but does not exceed 10. This ensures that we can use our grids for more cases without compromising the validity of the result. In the process of the grid construction the surface is re-triangulated and thus slightly altered. One of the tasks during the grid construction is to ensure that this altering is kept as small as possible in order that the resulting surface of the grid still resembles the original shape model to a high degree. As the gas expands into the surrounding space the mfp increases as well. This allows for the cell size to increase with distance to the surface. For a radial gas flow with constant speed the number density of the gas decreases with the inverse square of the distance and thus the mfp increases with the square of the distance. In reality the mfp increases even stronger than in this simplified case due to the acceleration of the gas. This relative behaviour is taken into account in the increasing size of the grid cell as a function of distance to the nucleus. Anticipating all the properties of the physics involved in the subsequent gas simulation allows the grid to have as many cells as needed for an accurate simulation but not too many as to unnecessarily increasing the run-time of the code. Hence, the inclusion of knowledge about the physics at this point of the process ensures that later steps can be performed in a shorter time and thus much more efficiently. For this work we have used multiple grids for a spherical surface and the surface of comet CG. The grid used typically consist of a surface with 50′000 to 300′000 surface facets and 900′000 to 8′000′000 cells.

4.5 ILLUMINATION MODEL

The surface of the comet is illuminated by solar radiation which results in heating of the surface and subsequent sublimation of ices. To determine the rate of outgassing from the cometary surface it

is required to determine the energy input to that surface. This is proportional to the cosine of the angle of incidence of the Sun light to the surface (angle between the surface normal and the direction of the Sun). We calculate the angle of incidence for each surface facet of the nucleus. The situation is schematically shown in Figure 17. Our code calculates the incidence angle for each facet taking into account self shadowing. Self shadowing occurs if a part of the surface closer to the Sun blocks a part further away. This is especially important for this comet due to its concave shape.

Earlier, the calculation of the incidence angles was performed with another code that was written by Antonio Gracia Berná. That code was implemented in Unity3D by means of ray tracing. An internal function of Unity3D would count for a ray going from the Sun to every facet the number of intersections with the comet surface. Facets with more than one intersection (including the final striking of the surface at the target facet) would be shadowed. Unfortunately, this method was very time consuming and thus replaced at a later point with the following method. Calculating the incidence angles of a shape model with 50'000 facets took approximately 12 minutes while the method described below would get to the same result within only 20 seconds (in both cases a 3.2 GHz Intel® Core™ i5-3470 CPU was used).

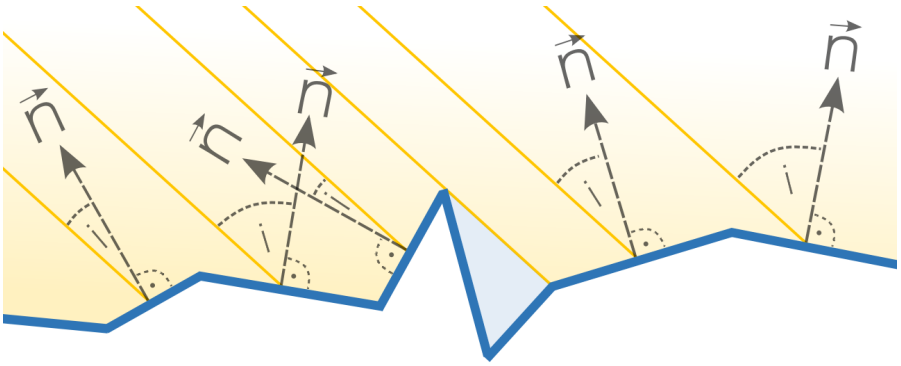

Figure 17: Illustration of the calculation of the incidence angle. For each surface facet the angle between the surface facet normal (dashed arrows) and the direction of the Sun (yellow lines) is calculated taking into account self shadowing.

The code treats this problem in two steps. The angle of incidence, i_k, of surface facet k is determined by the simple equation

$$\cos(i_k) = \frac{\vec{n_k} \cdot \vec{s}}{|\vec{n_k}| \cdot |\vec{s}|} \quad , \tag{4}$$

where $\vec{n_k}$ is the normal vector of surface facet k, and $\vec{s}$ is the vector pointing from the surface to the Sun. If $\cos(i) \geqslant \pi/2$ the respective facet is not facing the Sun and thus not illuminated. For facets where $0 \leqslant \cos(i) < \pi/2$ the facet is illuminated only if no other facet is

within the line of sight to the Sun blocking the Sun. Each facet has three corner points - we refer to these as vertices - each of which we check whether it is shadowed by another facet. For this we adopt a brute force method. In a fully brute force approach we would need to check every vertex against every facet which results in a problem of complexity $n_v \times n_f$, where n_v is the number of vertices and n_f is the number of surface facets. For shape models with a high number of surface facets this method becomes very slow. But this approach can be made more efficient using some geometrical tricks.

We rotate first the comet into a new coordinate system where the new z-axis is pointing in the direction of the Sun. The new coordinate basis is

$$\vec{x}' = \frac{1}{\sqrt{s_x^2 + s_y^2}} \begin{pmatrix} s_y \\ -s_x \\ 0 \end{pmatrix}, \tag{5}$$

$$\vec{y}' = \frac{1}{\sqrt{(s_x s_z)^2 + (s_y s_z)^2 + (s_x^2 + s_y^2)^2}} \begin{pmatrix} s_x s_z \\ s_y s_z \\ -(s_x^2 + s_y^2) \end{pmatrix}, \tag{6}$$

$$\vec{z}' = \frac{\vec{s}}{|\vec{s}|} \tag{7}$$

where $\vec{s} = (s_x, s_y, s_z)$ is the direction of the Sun. Any point with coordinates $\vec{p} = (p_x, p_y, p_z)$ in the original coordinate system can thus be rewritten in the new coordinates as

$$\vec{p}' = \alpha\vec{x}' + \beta\vec{y}' + \gamma\vec{z}', \tag{8}$$

where

$$\alpha = \vec{p} \cdot \vec{x}', \quad \beta = \vec{p} \cdot \vec{y}', \quad \gamma = \vec{p} \cdot \vec{z}', \tag{9}$$

or for short $\vec{p}' = (\alpha, \beta, \gamma)$. In this new coordinate system a vertex with γ_i can only be shadowed by facets k where $\gamma_k > \gamma_i$. Furthermore, the number of facets can be constrained by imposing that vertex i can only be shadowed by facets k where $|\alpha_i - \alpha_k| \leqslant \alpha_{th}$ and $|\beta_i - \beta_k| \leqslant \beta_{th}$. $(\alpha_{th}, \beta_{th})$ are threshold values as to how «close» a potential shadowing facet must be to be checked. The threshold values have been chosen to be the mean facet size plus five standard deviations of the facet size. For any facet that satisfies each of the following three conditions

$$\gamma_k \geqslant \gamma_i, \quad |\alpha_i - \alpha_k| \leqslant \alpha_{th}, \quad |\beta_i - \beta_k| \leqslant \beta_{th}, \tag{10}$$

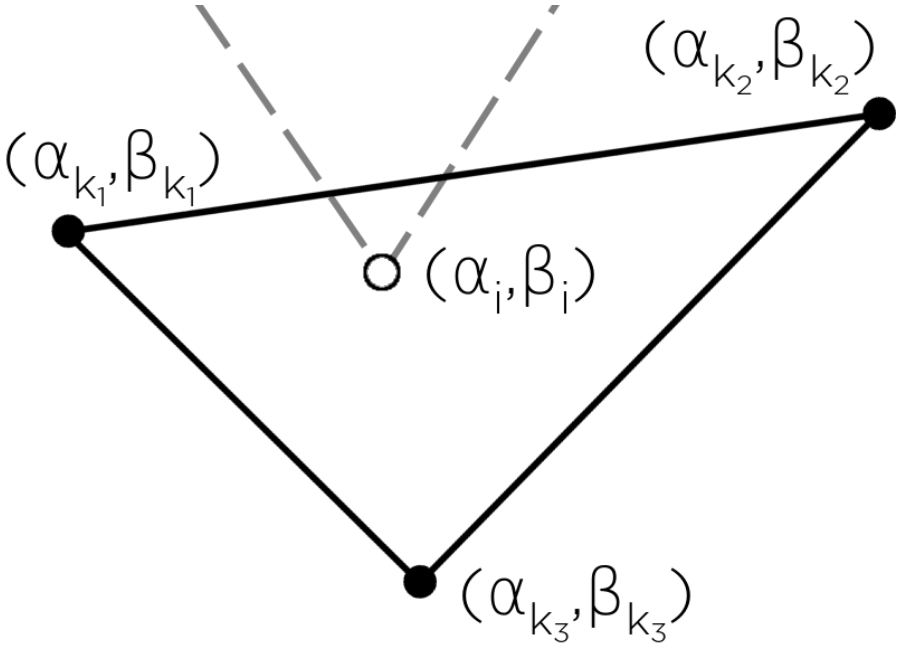

Figure 18: Schematic of a facet k (made up of its three vertices, filled black circles) shadowing vertex i (blank black circle) with the notation used in Equations (10) to (12).

we check if vertex i lies within the facet triangle k. By only checking facets that satisfy these conditions the number of comparisons can be dramatically reduced.

To determine whether facet k shadows vertex i we construct the following variables:

$$S = \frac{(\beta_{k_2} - \beta_{k_3})(\alpha_i - \alpha_{k_3}) + (\alpha_{k_3} - \alpha_{k_2})(\beta_i - \beta_{k_3})}{(\beta_{k_2} - \beta_{k_3})(\alpha_{k_1} - \alpha_{k_3}) + (\alpha_{k_3} - \alpha_{k_2})(\beta_{k_1} - \beta_{k_3})} \tag{11}$$

$$T = \frac{(\beta_{k_3} - \beta_{k_1})(\alpha_i - \alpha_{k_3}) + (\alpha_{k_1} - \alpha_{k_3})(\beta_i - \beta_{k_3})}{(\beta_{k_2} - \beta_{k_3})(\alpha_{k_1} - \alpha_{k_3}) + (\alpha_{k_3} - \alpha_{k_2})(\beta_{k_1} - \beta_{k_3})} \tag{12}$$

$$Q = 1 - S - T \tag{13}$$

A facet k satisfying $0 \leqslant S, T, Q \leqslant 1$ will shadow vertex i. Performing this for each vertex i this procedure can even capture partial shadowing of facets. The fraction that a facet is shadowed, F_s, can easily be calculated with

$$F_s = N_s/3 \quad , \tag{14}$$

where N_s is the number of vertices of the facet that are shadowed. If $F_s = 0$ the facet is fully illuminated and for $F_s = 1$ the facet is in full shadow. Note that this method is only an approximation of

the shadowed fraction of each facet. In this work we have not used partially shadowed facets but rather defined a shadowed facet when $N_s \geqslant 2$. It will become apparent in Chapter 9 that this approximation is sufficient at this point. For a more precise calculation of F_s one could calculate the area of the facet of interest being shadowed by all other facets. This could be implemented with a very similar method to the one described here.

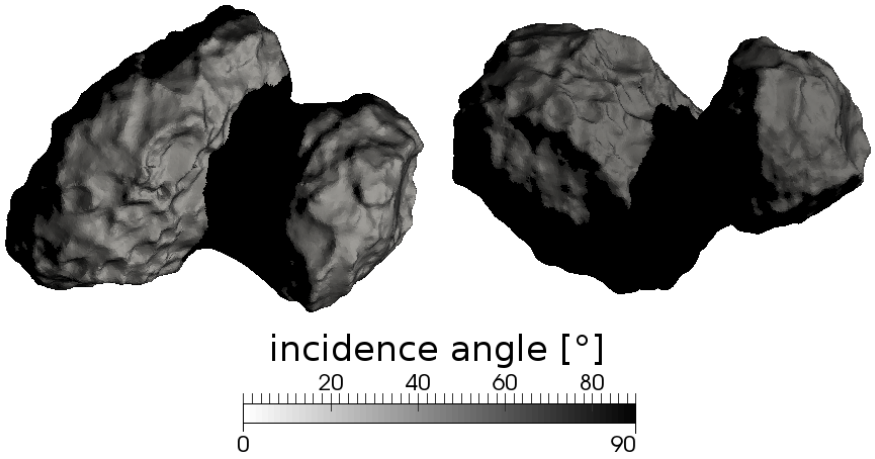

Figure 19: Visualisation of the result of the incidence angle calculation for sub-solar latitude of 35° and sub-solar longitude 200° realised on the 2014-12-01 when the comet was at a heliocentric distance of 2.86 AU pre-perihelion. Viewing geometries are as in Figure 9

Figure 19 visualises an example result of this calculation. It shows the incidence angle in degrees. Areas such as Hathor are fully shadowed because its surface facets are not facing the Sun. On the other hand most of Hapi is also shadowed but not because its facets are not facing the Sun but because the «Head» lobe is blocking the sunlight.

4.6 THERMAL MODEL

Now that we have calculated the incidence angle of the Sun light to the surface of the comet (Section 4.5) we can now use a thermal model to calculate the surface temperature and gas production rate.

We have decided to use a simple thermal model omitting thermal conductivity (i.e. the thermal inertia was set to zero. We note that Gulkis et al., (2015), Schloerb et al., (2015), and Choukroun et al., (2015) measured low values consistent with values seen at 9P/Tempel 1) but including sublimation of water ice. The sublimation coefficient, α_s, was set to 1 for simplicity. Kossacki et al., (1999) have shown that the sublimation coefficient can be up to an order of magnitude smaller than unity for a cometary environment. In that case the gas flux is only reduced by a maximum of 3% while the sublimation tempera-

ture increases by 10%. It is thus safe to neglect this effect at this point.

We note that Keller et al., (2015) presented a thermal model including topographic re-radiation (includes especially heating of shadowed facets by illuminated facets facing them). Topographic re-radiation in the visible part of the light spectrum as a source of additional energy will not be a significant effect due to the very low albedo of the surface. In Marschall et al., (2017) we have found no significant effect of topographic re-radiation on the water coma in the early phase of the mission at large heliocentric distances. This will be discussed further in Section 9.1.3. Topographic re-radiation in the visual part of the electromagnetic spectrum can safely be neglected because of the low albedo of the surface. We thus neglect topographic re-radiation effects.

The thermal balance for each surface facet was produced by

$$0 = \frac{S\,(1 - A_H)\cos(i)}{{R_h}^2} - \epsilon\sigma T^4 - L Q_{gas} \quad , \tag{15}$$

where A_H is the directional–hemispheric albedo (set to 0.04, Fornasier et al., (2015)), S the solar constant at 1 AU (taken to be 1384 W m^{-2}), i the angle of incidence, R_h the heliocentric distance of the comet in AU, ϵ the IR emissivity (set to 0.9), σ Stefan-Boltzmann's constant, L the latent heat of sublimation of water ice (2.84 MJ kg^{-1}; Huebner et al., (2006)), and Q_{gas} the sublimation rate (i.e. the gas mass loss rate per unit time and unit area). A preliminary test by Liao, 2017 with a thermal inertia of 50 J m^{-2} K^{-1} $s^{-1/2}$ has shown no significant effect on the gas dynamics result. It thus seems well justified to neglect thermal inertia effects at this point.

The sublimation rate was then computed from the surface temperature, T, using the equation

$$Q_{gas} = p_{evp}\sqrt{\frac{M_{H_2O}}{2\pi k T}} \quad , \tag{16}$$

where k is the Boltzmann constant, M_{H_2O} the molecular mass of water, and the equilibrium vapour pressure of water vapour (p_{evp}) was computed from values given by Huebner et al., (2006). This scheme provided a sublimation flux and a gas temperature for each facet and limits the number of free parameters. Essentially only ϵ is a free parameter because varying A_H within reasonable bounds has only a small effect. Equations (15) and (16) are functions of only Q_{gas}, and T, and can thus be solved analytically. When neglecting thermal conductivity unilluminated surfaces are not covered by Equations (15) and (16), thus the gas flux was set to zero and the nominal surface temperature to 100 K. The temperature calculated

here is the temperature of the sublimating surface which in the case of CG might actually lie below the physical surface temperature because no exposed surface ice has been observed apart from rather small scale patches (Pommerol et al., 2015). Either the surface ice is masked by dust with which it is mixed (Yoldi et al., 2015) or lies too deep to be detected by remote sensing instruments. In the first case, the surface temperature and the temperature of the subliming surface would be very similar. In the second case, the layer containing the ice is covered by a dusty layer which can be substantially hotter than the subliming surface. Thus the gas would flow through the dry top layer. The porosity and thickness determine how much the gas is heated by flowing through this surface layer. At this point we know almost nothing about this process so we assume that the surface temperature is equal to the subliming surface even though we are aware that this might in fact not be true.

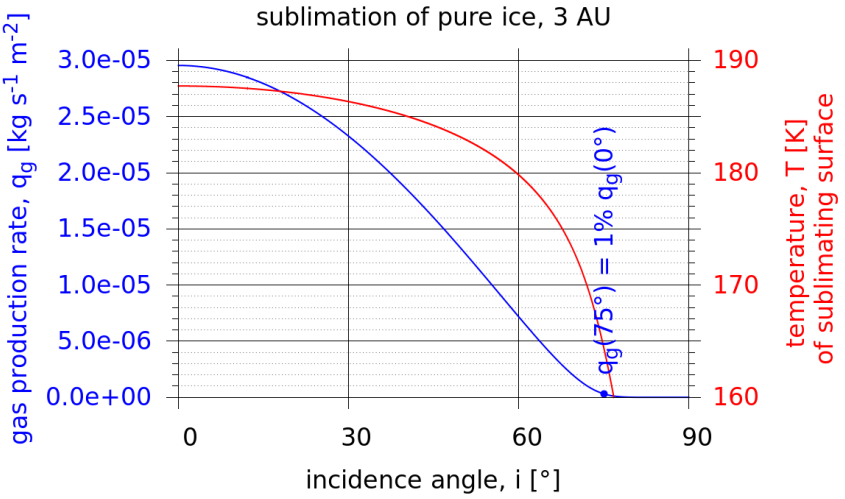

Figure 20: The gas production rate per unit area, and the temperature is shown as a function of the incidence angle. The values were calculated at a heliocentric distance of 3 AU for an eaf of 1%.

Figure 20 shows the gas production rate and surface temperature at 3 AU as a function of the incidence angle. We can clearly see the influence of the cosine of the incidence angle in the production rate for low incidence angles. On the other hand the surface temperature remains high for a large range of incidence angles. Within the incidence angle range of 0° to 60° the temperature varies by only 18 K whereas the production rate decreases by more than a factor of 4 within the same range. The reason for this is that once the temperature is high enough for sublimation most of the energy is going into sublimating the ice rather than heating it. At 75° incidence angle the surface temperature has dropped to 165 K and

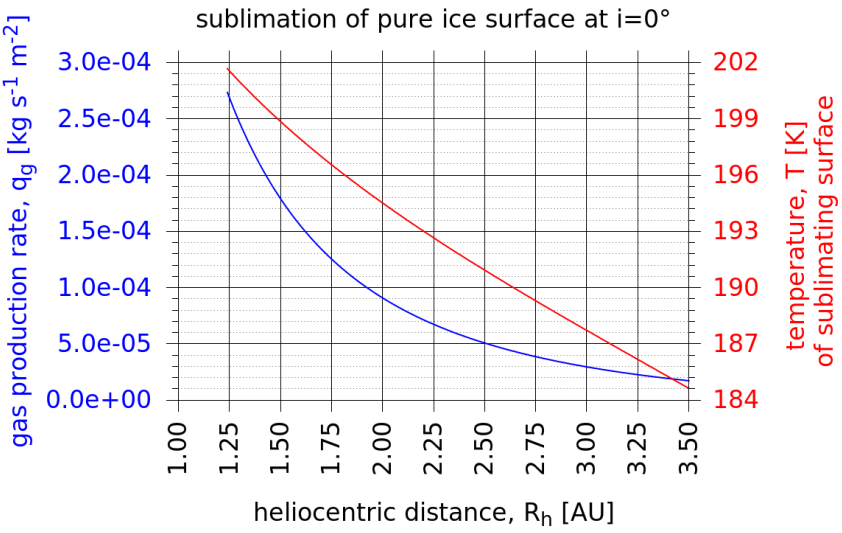

Figure 21: The gas production rate per unit area, and the temperature is shown as a function of the heliocentric distance. The values were calculate for an incidence angle of 0° and an eaf of 1%.

the production rate to 1% of the production rate at 0° incidence angle.

In Figure 21 we plot the gas production rate and surface temperature for 0° incidence angle as a function of the heliocentric distance range during the escort phase of the Rosetta mission. As in the previous figure we see that the temperature only increases by roughly 10% from 3.5 AU to 1.24 AU while the gas produce rate increases by a factor of approximately 16 within the same range. This again is due to the fact that most of the energy goes into sublimation rather than heating of the surface. In the gas production rate we also see the effect of the quadratic increase of the incoming solar energy due to the heliocentric distance.

Using this scheme would normally produce gas production rates far in excess of what is observed. We therefore scale the results of the production rates to produce values that are closer to those observed at comet CG. One can visualise this as being equivalent to only a fraction of each surface facet being active with the rest being inert (akin to a chessboard pattern; Keller et al., (2015)). We refer to this as the eaf with required values at this time of typically 1% (Gulkis et al., 2015) for the purely-insolation-driven models described later. The eaf is a free parameter of our model.

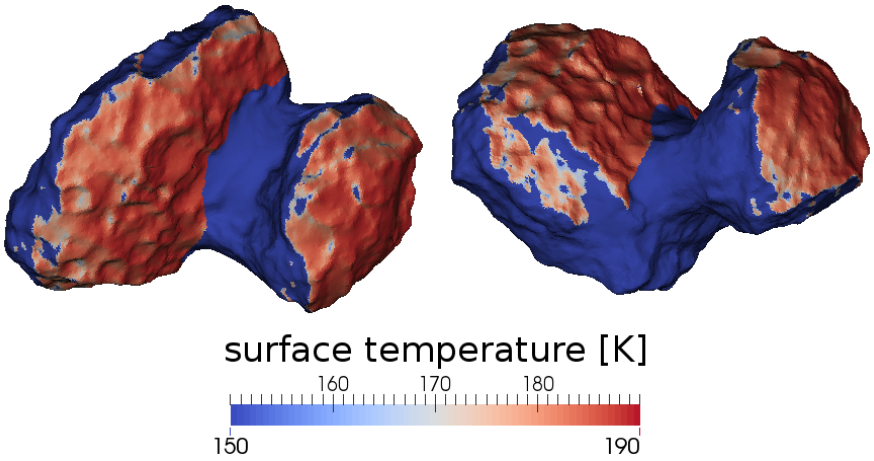

Figure 22: Visualisation of the surface temperature [K] for the same solar geometry as in Figure 19 and viewing geometries as in Figure 9

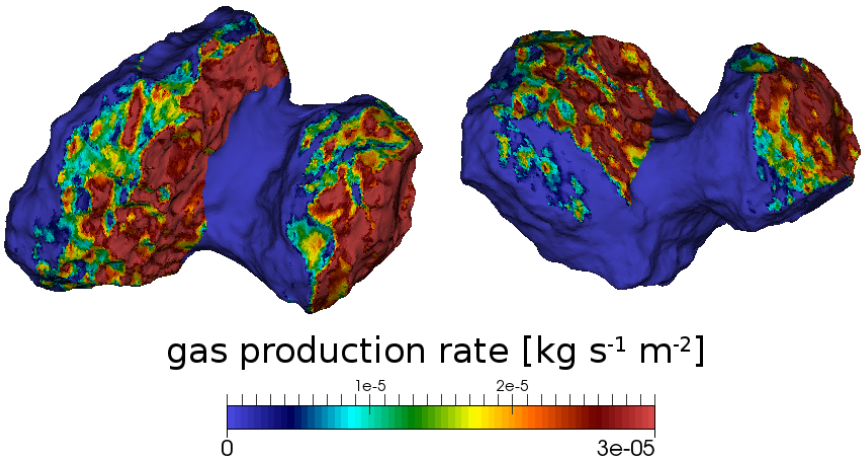

Figure 23: Visualisation of the gas production rate [kg s^{-1} m^{-2}] for an effective active fraction of 1% for the same solar geometry as in Figure 19 and viewing geometries as in Figure 9

Assuming a half Maxwellian velocity distribution at the surface, we can convert the production rate per unit area, Q_{gas}, to an initial number density at the surface. By using

$$v_g(T) = \sqrt{\frac{8kT}{\pi m_g}} \quad , \tag{17}$$

for the speed of the gas, v_g, with m_g being the molecular mass of the gas, we can convert the mass production rate to a number density n_g (Bird, 1994) due to flux conservation

$$Q_{gas} = \frac{1}{4} n_g m_g v_g \quad . \tag{18}$$

This scheme implies that surface temperatures where sublimation is occurring never exceed approximately 200 K (i.e. the free sublimation

temperature of water), which is formally inconsistent with measurements of the surface temperatures of comets (Emerich et al., 1987). However, the eaf has been shown to be small (as confirmed here), and this approach does not exclude a hotter surface being adjacent to our active surface. We interpret the eaf more as «areal mixing» and with dust, that can itself be much hotter, opposite to «intimate mixing» where the temperature of the dust and ice would be very similar.

For the simulations presented in this work, we assume that the gas equilibrates with the subliming surface temperature at the source. This is an intermediate assumption between two extremes. On the one hand, the energy in the gas may be lower than this assumption if the rotational degrees of freedom are in disequilibrium after emission from the icy surface. On the other hand, if the gas passes through a hot, inert surface layer, it will be heated above the sublimation temperature before leaving the surface.

There are some minor limitations to this model. Firstly, we are neglecting thermal inertia effects. Although current data suggests this is well justified even a small thermal inertia will have an influence on the result - though only in a minor way for the heliocentric distances we are examining in this work. But these effects are to some extent taken into account - albeit non-physically - implicitly in what we call the effective active fraction (eaf) (see Section 4.7). Secondly, due to the very concave shape of the nucleus, shadowed areas can be heated by illuminated facets facing them. We have examined this so called topographic re-radiation effect and will present our results in Part iv to show no significant effect for the considered heliocentric distances. But this effect can indeed become important for smaller heliocentric distances. Both of the two mentioned points also clarify, that non-illuminated facets in the model presented above do not have a defined temperature and are as mentioned set to the nominal value of 100 K while the gas production rate is set to zero. That this is a fair assumption for unilluminated and thus inert surfaces as illustrated in Figure 20 and discussed earlier.

The thermal model we are using does not result in gas emission from either diurnally or seasonally shadowed areas. Other studies as e.g. Bieler et al., (2015) and Fougere et al., (2016a) introduce night side emission on the order of 2% to further enhance the fits to the ROSINA data. But these models do not produce this kind of emission from a physical model but simply by adding emission artificially. Though there are undoubtedly physical processes present, that will result in emission after local Sun set, but we prefer not to introduce these effects without backing them up with a physical thermal model.

4.7 GAS DYNAMICS COMA MODEL

Simulating and studying the flow of gas from the cometary surface into 3D space is somewhat complex and depends on the scale at which the coma is to be studied. When ice sublimates into vacuum it forms a non-equilibrium boundary layer, the «Knudsen layer», with a scale height of ~ 10 to 100 mfp (λ) (Ytrehus, 1975; Davidsson, 2008). Within this layer the velocity distribution function (VDF) is strongly non-Maxwellian. This layer can become infinitely thick when the production rate is low. Gas flows can cover the fully collision-less free flow regime, in which $\lambda \sim \infty$, to the fluid regime with a very short mfp. To determine the flow regime of a specific case the Knudsen number, Kn, is defined as

$$\mathrm{Kn} = \frac{\lambda}{L} \quad , \tag{19}$$

where L is the characteristic size of the studied system, in our case a few kilometres. Irrespective of the flow regime the Boltzmann equations need to be satisfied but for certain regimes approximations can be made to more easily calculate the flow field. When the Knudsen number is small ($\mathrm{Kn} < 0.1$) the gas flow is in the fluid or continuum regime and the flow can be accounted for by solving the Euler equations or Navier–Stokes equations. Such (multi-)fluid models for comets with high production rates have been studied by Marconi and Mendis, (1982), Marconi and Mendis, (1983), Gombosi, Cravens, and Nagy, (1985), Kitamura, (1986), Kitamura, (1987), Crifo and Rodionov, (1997a), Crifo and Rodionov, (1997b), and Shou et al., (2016). On the other hand when the Knudsen number is very large ($\mathrm{Kn} \gg 100$) collisions can be neglected and we consider this the free molecular flow regime. Historically, these were the first models studied e.g. by Eddington, (1910), Haser, (1957), and Wallace, Miller, and Freeman, (1958) as they are the simplest models that can be considered. For the intermediate regime where $0.1 < \mathrm{Kn} < 3$ the Euler and Navier-Stokes equations are no longer valid and the kinetics of gas particle collisions need to be accounted for. First models using a statistical Monte Carlo approach were studied by Combi and Delsemme, (1980), Kitamura, (1986), Combi and Smyth, (1988), Hodges, (1990), Xie and Mumma, (1996a), and Xie and Mumma, (1996b) and comparisons with fluid models were performed e.g. by Crifo et al., (2002). The state of the art method for studying non-equilibrium though is Direct Simulation Monte Carlo first proposed by (Bird, 1994) and which has since been applied by many (Combi, 1996; Skorov and Rickman, 1999; Crifo et al., 2002; Crifo et al., 2003; Tenishev, Combi, and Davidsson, 2008; Tenishev, Combi, and Rubin, 2011; Davidsson, 2008; Zakharov et al., 2009; Fougere et al., 2013) especially as the computational power available

has significantly increased in the past decades.

Because the production rate at comet CG spans large ranges from low to high the gas flow in principle transitions from either fluid or collisional to a free adiabatic outflow. Thus our preferred method is DSMC because it intrinsically covers all of these regimes. For high production rates a fluid approach might be computationally more economical though. The code we are using, named PDSC^{++} (Su, 2013), has previously been used to model the water vapour distribution in the vicinity of comet 9P/Tempel 1 (Finklenburg et al., 2014) and is based on the PDSC code developed by Wu and co-workers (Wu and Lian, (2003); Wu, Tseng, and Wu, (2004); Wu and Tseng, (2005)). PDSC^{++} allows a simulation of 2D, 2D-axisymmetric, and 3D flows on hybrid unstructured grids. The code has been parallelised, allowing a much larger number of cells, and has been implemented on several clusters in Bern (Switzerland) and Taiwan. The code is especially useful because it is able to treat the large density gradients by implementation of a variable time step and a transient adaptive sub-cell technique to increase computational speed and accuracy in the regions of high density (Finklenburg et al., 2014; Finklenburg, 2014).

Within the DSMC code the real gas molecules are represented by a smaller number of simulation particles that are used to generate a statistical representation of the flow. The microscopic behaviour of the simulation molecules is separated into a translational step and a collision step. In the collision step, the collision pairs are chosen randomly from all the molecules that are within one cell at the time of the collision step. Macroscopic gas properties such as number density, velocity, and temperature are then calculated by averaging the appropriate quantity over all simulation molecules in the respective sampling cell.

Even though the code is fully capable to treat multi-species flows, in this work we consider H_2O only because, as mentioned earlier, it is the dominant species in the coma of CG (Hässig et al., 2015). In addition, we are interested in the dynamics within the first kilometres of the gas coma above the cometary surface and thus do not need to include any chemistry into our gas model. Processes such as photo-dissociation and ionisation occur on much longer time scales (Crovisier, 1989; Xie and Mumma, 1996a; Combi, Harris, and Smyth, 2004).

For each facet of the nucleus surface a gas reservoir density of each gas species and surface temperature is set as input for the code. Both of these quantities are taken from the previous thermal model

calculations in Section 4.6. The outlet surface at 10 km is set to a vacuum boundary condition while for the nucleus surface (inlet surface) each surface facet can be defined as an absorbing (vacuum), or reflecting surface. If the surface is chosen to be reflecting, any gas molecule hitting this surface will be reflected either specularly, diffusely, or a linear combination of the two. Whether we have specular or diffuse reflection can in principle be set for each surface facet. In the case of diffuse reflection a gas molecule hitting that surface is equilibrated to the respective surface temperature and then re-emitted with the corresponding VDF. In the case of specular reflection the gas molecule is reflected as on a mirror with the angle of incidence equal the angle of emission measured to the surface normal conserving the speed. Whenever using a reflecting surface we have chosen the diffuse reflecting surface because we consider it the more physical option. It is intuitive that a temperature-dependent behaviour of the surface reflectance seems the most physically plausible. Cold surfaces thermally trap gas and thus act as absorbing surfaces (Rubin et al., 2014). In contrast, hot surfaces would diffusely reflect any gas back-flux. Sandford and Allamandola, 1993 have determined residence times for different molecules on various icy surfaces for different temperatures which can be used in our model to determine the reflectivity of the surface. If the temperature of a specific surface facet is such that the residence time is a substantial fraction of the cometary rotation period we would assume that facet to be absorbing. On the contrary when the temperature is such that the residence time is short we would presume the respective facet to diffusely reflect any gas back-flux.

The thermal model of Section 4.6 results in global production rates which are two orders of magnitude higher than compatible with ROSINA/COPS data. To match ROSINA/COPS observations the production rate needs to be artificially reduced. We control the power of the emission from a specific area (individual surface facet) or region via the eaf. How this scaling arises at the surface cannot be determined at this stage. Whether it is due to a dust cover over the ice rich layer or actual inert areas interlaced with highly active ice patches cannot be disentangled at this point. An eaf of unity corresponds to the entire facet area emitting at a rate corresponding to the free sublimation rate. An eaf of zero on the other hand corresponds to an inert facet. If applied globally the eaf is usually on the order of a few percent and has been selected to match to the best extent possible, the observed gas densities at Rosetta. Though in principle the eaf can be set for each facet we have chosen to only vary it on a regional scale, when and if needed, to not artificially make the problem under-constrained by introducing essentially thousands of free parameters. In this sense only an additional $\sim 10-15$ free parameters are introduced, because

of the 27 regions only a fraction of them ever comes into Sun light at any heliocentric distance.

There are several further input parameters to the code such as the VDF (in this work always chosen to be half-Maxwellian), initial rotational temperature, rotational relaxation time (set to one in this work), or the collisional model (a standard variable soft sphere model is applied here). These parameters have not been varied in this work but the effects of varying them has been studied extensively by Liao et al., (2016) and Liao, (2017) who has found little effects on the gas dynamics result.

In order that the simulation yields reliable results it is crucial that in each cell, the mean collisional separation (mcs, i.e. the mean distance between the collision of two simulation particles) divided by the physical mfp be less than one as discussed in Section 4.4. Additionally, the total number of simulation particles per cell should be at least 10 to allow meaningful sampling of the gas properties. These constraints have been met with the simulations shown here. The only exceptions are some simulations with high production rates where the mcs/mfp can exceed one in a small volume of the simulation domain but still be smaller than 10.

We must also stress at this point that one DSMC simulation represents «only» a stationary solution of the gas flow at a specific solar geometry and is thus time independent. This is due to the fact that the gas is accelerated to $\sim$ 700 m s^{-1} which results in gas molecules leaving the simulation domain after seconds to tens of seconds. To study time dependent phenomena, such as a time sequence of ROSINA/COPS number density measurements, multiple solar geometries must be run (Marschall et al., 2016). Due to the pattern in ROSINA/COPS data we have chosen to run eight rotation phases of one cometary day to make a comprehensive comparison. In this way we get quasi time-dependent solutions. The details of the setups will be emphasised when the respective results are presented in Part iv.

As an output, the code provides the number density, velocity, and temperature of the gas flow field of each cell in the simulations domain. These values will be used as input for the dust dynamics model as described in Section 4.8. Not only do we use this output as an input for the dust dynamics simulation but it can directly be used to compare with three instruments on board of Rosetta (ROSINA, MIRO, and VIRTIS). Constraining the gas solution in this way ensures the further steps having a good foundation. By means of column integration (as explained in Section 4.10 for the dust) and profile

extraction along the line of sight while matching the illumination and viewing geometry at the time of the observations, comparisons with VIRTIS and MIRO data is possible. We will be presenting predictions for VIRTIS and MIRO from our models but have not yet used the data to constrain our gas model of the comet, though this is ongoing work. Our primary comparison of the gas coma with Rosetta data is with ROSINA/COPS which we shall use to constrain the surface emission distribution with (see Section 4.8). ROSINA/COPS measures the gas number density at the spacecraft position. For us to be able to compare our simulations to the data we need to match the illumination geometry during the time of the observations. Then we extract the corresponding number density at the spacecraft position from our simulation domain. As the cometocentric distance of Rosetta was always larger than 10 km - except for the final phase of the mission in fall 2016, during close fly-bys, and lander delivery - there is a need for extrapolation of our results. We will show in Part iii and Part iv that the gas has reached terminal velocity and moves radially outwards at the outer boundary of 10 km from the centre of the nucleus. This implies free radial outflow beyond 10 km meaning that the gas number density drops proportional to $1/r^2$ from that point onward - r being the distance to the cometocentre. For the comparison with the data we use SPICE (Acton, 1996) to determine the comet local time (CLT) of the observations, and subsequently filtering out the observations for which the CLT matches the CLT of one of our simulations. For these observations we calculate the spacecraft position in the comet frame (using again SPICE). Should the spacecraft be within our simulation domain, we directly extract the number density of the cell within which Rosetta is currently situated. If Rosetta is at cometocentric distances $D_c > 10$ km we extract the number density value at the edge of our domain as if Rosetta were at 10 km and scale the value with $(10\ \text{km}/D_c)^2$.

When we compare ROSINA/COPS number densities we require a quantitative measure as to how well our model reproduces the data. Here we pursue the approach taken by Bieler et al., 2015 and use the PPMCC. It is defined as

$$\text{ppmcc} = \frac{\Sigma_{i=1}^{n}(x_i - \bar{x})(y_i - \bar{y})}{\sqrt{(\Sigma_{i=1}^{n}(x_i - \bar{x})^2)}\sqrt{(\Sigma_{i=1}^{n}(y_i - \bar{y})^2)}} \quad , \tag{20}$$

where n is the number of data points that are being compared, x_i and y_i are the number density of the model and the data, and $\bar{x}$ and $\bar{y}$ is the mean value of the data and model values. This formula can be rearranged to be implemented in a single pass algorithm by using the form

$$\text{ppmcc} = \frac{n\Sigma_{i=1}^{n}x_i y_i - \Sigma_{i=1}^{n}x_i \Sigma_{i=1}^{n}y_i}{\sqrt{(n\Sigma_{i=1}^{n}x_i^2 - \left(\Sigma_{i=1}^{n}x_i\right)^2)}\sqrt{(n\Sigma_{i=1}^{n}y_i^2 - \left(\Sigma_{i=1}^{n}y_i\right)^2)}} \quad . \tag{21}$$

4.8 DUST DYNAMICS COMA MODEL

Given a gas flow field we can now study the motion of dust particles in this flow. The motion of the dust is governed by these two dominant forces: the force produced by the gas drag on the dust particles to accelerate them away from the surface (Gombosi, Cravens, and Nagy, 1985; Kitamura, 1986; Kitamura, 1987; Szegö et al., 2002), and the gravity of the nucleus as an opposing force. The dust follows, though in a complex way, the gas flow from the nucleus. If the gas flow is perpendicular to the surface so is the motion of the dust particles within the first meters above the surface. But lateral flows in areas with large gas production rate gradients (such as e.g. close to the terminator) are possible and thus also result in lateral dust flows close to the surface. Solar radiation pressure is assumed to be negligible this close to the nucleus (Tenishev, Combi, and Rubin, 2011) and is thus not included in the model. We treat the dust grains as test particles and consider them to be spherical, although there are strong indications that especially the larger dust grains are porous and fluffy aggregates (Kolokolova and Kimura, 2010; Schulz et al., 2015; Rotundi et al., 2015; Langevin et al., 2016; Bentley et al., 2016; Mannel et al., 2016). We justify our choice of treating the dust as spherical particles with the fact that the main parameters influencing the dust trajectory are the mass and cross-section. Hence our dust particles must be understood as effective spheres with the respective cross-section and mass of the dust particles they represent. At this point we still know little about the physical properties of dust particle (such as their shapes, density) and, perhaps more importantly, about how they orient themselves in the gas flow (Ivanovski et al., 2017).

The bulk density of the dust particles was assumed to be $440\,\mathrm{kg\,m^{-3}}$ for all dust sizes. Fulle et al., (2015) have estimated the dust density of very fluffy particles of sizes ranging between 0.2 to 2.5 mm detected with the GIADA to $< 1\,\mathrm{kg\,m^{-3}}$. The smaller compact particles, which dominate the coma have much higher density between 800 and $2'000\,\mathrm{kg\,m^{-3}}$ (Rotundi et al., 2015; Fulle et al., 2016b). We have considered smaller more compact particles in this study and thus chosen to assume a dust density that is close to the bulk density of the comet itself. Though we are aware that the bulk density of the dust particles will ultimately be a function of the size as e.g. described on p. 52 of Divine et al., (1986) for comet Halley.

We neglect any dust-dust interactions because we have seen that the mfp of the dust particles in our models for reasonable setups is at least 2 km and increases strongly towards the edge of our simulation domain. This condition is most probably not satisfied in outbursts when the dust brightness becomes of the order of the nucleus itself

or brighter and is thus optically thick. Whether the mfp of the dust is large enough in perihelion cases needs to be examined. When the mfp becomes too small such that collisions between particles are frequent this process needs to be included in a future model. Additionally, we assume that although the dust is accelerated by the gas, the back reaction of the dust onto the gas is negligible, allowing us to model the gas and dust dynamics separately and in series. The dust can in principle alter the gas flow in two ways: Firstly, the dust can be heated by the sunlight up to temperatures higher than the gas temperature. When the gas subsequently interacts with the hotter dust it is heated which alters the VDF. Secondly, when the dust to gas ratio is too large and therefore the kinetic energy needed to accelerate the dust is a non-negligible fraction of the kinetic energy of the gas the gas would need to loose energy and thus slow down. Tenishev, Combi, and Rubin, (2011) note that heating of the gas by collisions with the dust should be negligible and that kinetic back coupling of the dust in the coma does not affect the gas field in the case of comet CG. Our models show the total kinetic energy of the dust to be two orders of magnitude lower than that of the gas. We thus agree with this statement and can safely assume no back reaction of the dust flow on the gas. Again, this needs re-evaluation in cases of smaller heliocentric distances or when attempting to model outburst.

The alternate approach to the test particle approach is to treat the dust as an additional fluid in a fluid model. In such a model the interaction between gas and dust as well as dust with dust can be treated within the same code. Though this can be computationally more efficient it has some drawbacks. In the fluid approach the number of species that can be simulated is somewhat limited, whereas in our test particle approach the different dust sizes can be simulated individually and thus the code can be easily parallelised. The only constraint on the number of dust sizes that can be simulated is computational power. In our case an implementation of the code with up to 64 dust sizes is easily possible on our computer cluster. Additionally, the test particle approach has the physical advantage that flows can penetrate each other which is important in a rarefied environment as with comet CG. A fluid model cannot reflect that.

For the described approach (Finson and Probstein, (1968), Gombosi, Cravens, and Nagy, (1985), Gombosi, Nagy, and Cravens, (1986), Gombosi, (1987), and Sengers et al., (2014)) the equation of motion for each dust grain which has mass m_d, radius r_d, and geometric cross-section $\sigma_d = \pi r_d^2$ at position $\vec{x}$ and with velocity $\vec{v}_d = \frac{d\vec{x}}{dt}$ is

$$\begin{aligned} m_d \frac{d^2\vec{x}}{dt^2} &= \vec{F}_G + \vec{F}_D \\ &= \vec{F}_G + \frac{1}{2} C_D m_g n_g \sigma_d |\vec{v}_g - \vec{v}_d| (\vec{v}_g - \vec{v}_d) \quad , \end{aligned} \tag{22}$$

where $\vec{F}_G$ is the gravitational force, m_g the mass of the gas molecule considered (in our case molecular water), and n_g and $\vec{v}_g$ are the number density and velocity of the gas. If we assume an equilibrium gas flow where the mfp of the gas is much larger than the dust size (free molecular aerodynamics), the drag coefficient C_D is defined as

$$C_D = \frac{2\zeta^2+1}{\sqrt{\pi}\zeta^3} e^{-\zeta^2} + \frac{4\zeta^4+4\zeta^2-1}{2\zeta^4}\mathrm{erf}(\zeta) + \frac{2(1-\varepsilon)\sqrt{\pi}}{3\zeta}\sqrt{\frac{T_d}{T_g}} \quad , \quad (23)$$

with the gas temperature T_g, the dust temperature T_d (chosen to be equal to T_g), and ε is the fraction of specular reflection (set to 0), and

$$\zeta = \frac{|\vec{v}_g - \vec{v}_d|}{\sqrt{\frac{2kT_g}{m_g}}} \quad . \quad (24)$$

Figure 24 illustrates the drag coefficient as a function of ζ and illustrates that it converges to 2 when $\zeta \to \infty$. ζ becomes large when $|\vec{v}_g - \vec{v}_d| \approx |\vec{v}_g|$ and $|\vec{v}_g|$ is larger than the thermal velocity. ζ is small when $\vec{v}_g \approx \vec{v}_d$. The drag coefficient depends in principle on the exact shape and composition of the dust particles considered and is non-trivial to calculate. Skorov et al., (2016) have made calculation for the dynamical properties of complex dust aggregates in the context of cometary gas flows. The influence of non-spherical shapes on the dust dynamics has also been studied by Ivanovski et al., 2017 showing that spherical dust might underestimate the maximum liftable size. Moreover, non-spherical particles will also result in higher dispersal of the dust speeds. As we still have little information on the exact shape and composition of the dust particles in CG's coma we have decided to assume the spherical case in this first step. Our particles thus need to be interpreted as representing particles with the corresponding effective cross section and mass.

The gravitational acceleration has been calculated using the result of Section 4.3 by extracting the respective field strength at the dust particle position. Gravity affects mainly the liftability at the surface and the motion of large/slow moving particles. Inclusion of gravity is important. If we had a free radially out-flowing gas, its density and thus the drag force would drop with $1/r^2$ just as gravity does. In such a model gravity is to a large degree irrelevant to particles that are liftable. But for an accelerating gas flow that is also laterally expanding this is no longer true. In this case where the drag force drops faster than $1/r^2$ gravity can become a dominant factor. This is especially true for particles close to the terminator where lateral gas flow further decreases the gas number density. Thus we are essentially confronted with three dust dynamics regimes: 1) the escape regime where all particles of a certain size are lifted and escape the comets gravity field; 2) the ballistic or gravitational regime

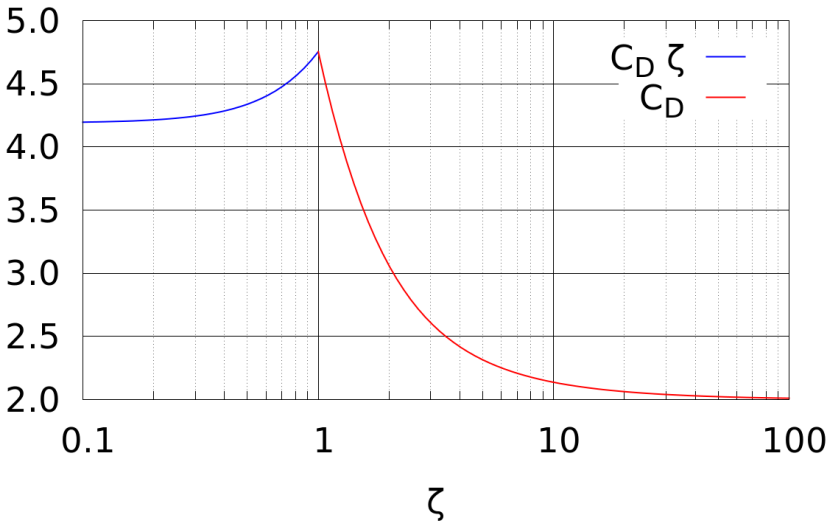

Figure 24: Drag coefficient according to Equation 23 as a function of ζ (Equation 24).

where most particles are lifted but not all escape the gravity field but rather are gravitationally bound and fall back to the surface; and 3) the un-liftable or inert regime where no particles are lifted. These regimes are schematically shown in Figure 25.

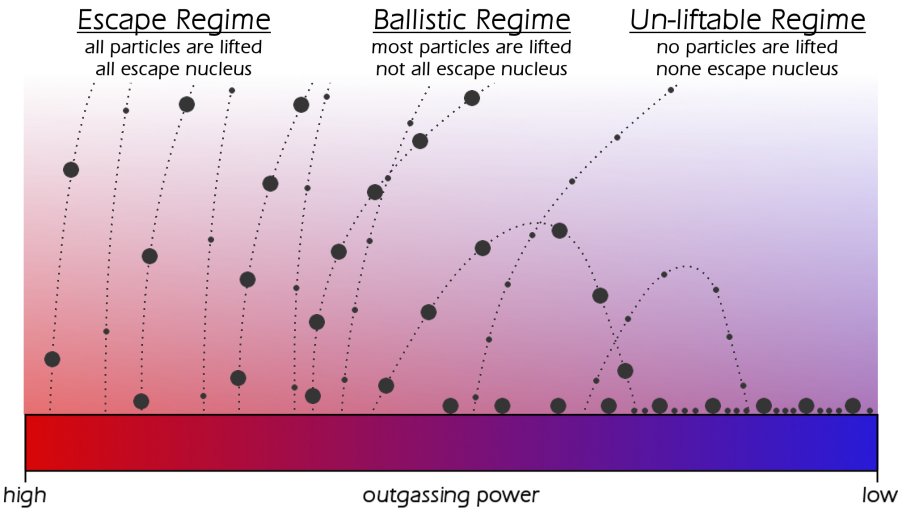

Figure 25: Schematic of the three dust dynamic regimes for different particle sizes.

Two further assumptions have been made. Firstly, as the drag force depends on the relative velocity, a non-Maxwellian velocity distribution may affect the result, an effect we have ignored. Skorov and Rickman, (1999) have derived more complex expressions for the drag force taking the non-LTE (local thermodynamic equilibrium) in the Knudsen layer into account. They have found that the difference

in grain speeds can be up to a factor of two. Secondly, concerning the liftability of dust grains, our model neglects surface cohesion. This may be justified for certain ejection processes but can also be accounted for by modifying the ejected size distribution. But without an appropriate surface model we rather not put any further constraints in the model.

The equation of motion is solved by means of a fourth-order Runge-Kutta method with an adaptive time step. For good statistics of the physical properties within the dust coma (number density, and dust speed) we want to sample the motion of the dust particle within one simulation cell during at least ten time steps. Also we need to ensure that the time is chosen such that the acceleration of the dust is correctly calculated, hence, in principle ensuring that our solution of the equation of motion is actually numerically solved. Finally, a time step that is too small just increases the computation time without improving substantially accuracy of the result. We therefore impose that the spatial displacement is either less than one tenth of the characteristic size, l_c, of the cell ($l_c = \sqrt[3]{V_c}$, where V_c is the cell volume), or the change in dust speed is less than 10% of the current speed, whichever is lower. Because of the unstructured grid contrary to a Cartesian grid the position of the particle does not hold any information on which simulation cell the particle is in. We must thus not only track the particles position but also which cell we are currently in. To avoid checking all cells at every time step to determine which cell our particle currently occupies we make use of the fact that we predetermine the four neighbouring cells of every tetrahedron. We therefore only need to check at every time step whether the particle is still in the current cell or to which neighbouring cell we have moved. This also explains why we need to choose a time step small enough such that we can ensure not to skip over neighbouring cells within one time step which would lead to us using the wrong gas field properties for the particle trajectory integration. The tracking of each particle is terminated in one of two cases. Either when its radial distance is larger than 10 km or when the particle is in an inlet cell and we have determined that the position of the particle has gone below the corresponding inlet facet. We check the latter by calculating the distance of the particle with respect to the surface facet normal.

In most simulations performed in this work we simulated 40 dust sizes in the range between 8 nm and 0.3 mm. The reason for this range will become apparent in Section 4.10. $4 - 10$ million test particles were simulated for each dust size depending on the setup. Each size is run independently from the others. Within each surface facet the particles are placed randomly on the surface with initial

velocity $\vec{v}_d|_{t=0} = 0$ and are subsequently tracked through the same unstructured grid of the simulation domain as in the gas dynamics model of Section 4.7. The tracking continues until the dust particle either reached the outlet surface at 10 km distance from the centre of the nucleus or «redeposited» on the cometary surface. We are mainly interested in the brighter day side of the comets coma. We therefore assign more simulation particles to surface facets with high production rates compared to ones with little to no gas activity.

Our final goal is not to see individual particles trajectories but to determine the macroscopic physical properties of the dust coma such as the dust number density and velocity in 3D space because we can use this to recreate artificial images of the dust coma to compare with OSIRIS using the models explained in Section 4.9 and Section 4.10. To acquire these properties from the tracking of the particles we employ the following scheme. A simulation particle i is weighted with w_i to represent the physical number of particles leaving the surface facet per second. On the one hand this depends on the number of test particles we actually want to simulate, thus a constant set in the simulation. On the other hand this weighting depends on the dust-to-gas production rate ratio, Q_d/Q_g, which is the actual physical property. We presume at this stage a dust-to-gas mass production rate ratio, Q_d/Q_g, of unity for each size. The dust number density behaves proportional to Q_d/Q_g and the result can thus be scaled - within a sensible range - to the desired value after the simulation. We will be scaling the result for a specific dust size distribution later on when we produce the artificial images (described in Section 4.10). This scaling breaks down when Q_d/Q_g is too large and dust-to-dust interactions and the back-reaction to the gas become important. We assume Q_d/Q_g globally and thus apply it to all surface facets equally. There is no regional scaling of Q_d/Q_g.

To calculate, for example, the number density, n_k, in a specific cell k with volume $V_{c,k}$, one simply has to measure the time t_k^i that each simulation particle i spends in that cell k. The total number density n_k of cell k can thus be calculated by

$$n_k = \frac{1}{V_{c,k}} \frac{Q_d}{Q_g} \sum_i t_k^i w_i \quad . \tag{25}$$

Similarly the mean velocity of the dust particles in cell k can be written as

$$\bar{\vec{v}}_k = \frac{\sum_i t_k^i w_i \vec{v}_k^i}{\sum_i t_k^i w_i} \quad , \tag{26}$$

and equally for any other dust parameter that one would want to track. Figure 26 illustrates the described procedure of determining

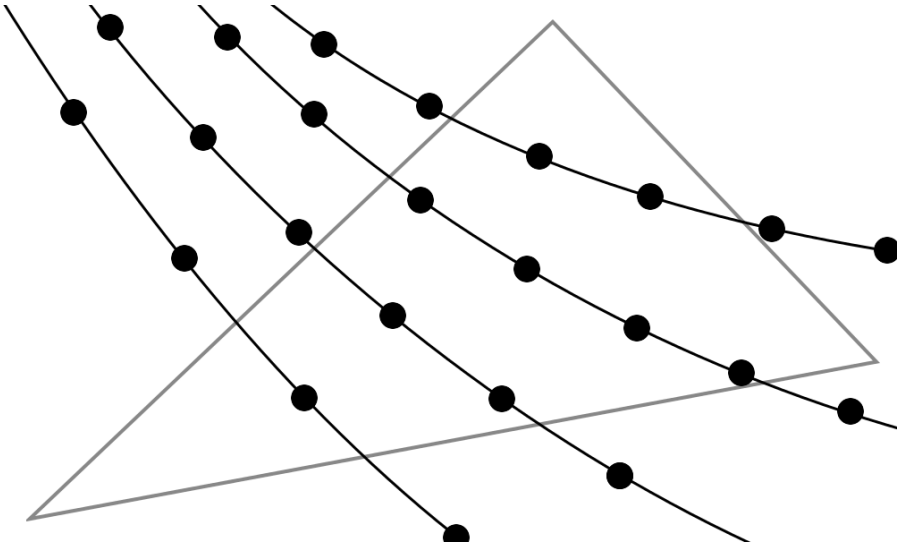

Figure 26: Illustration in 2D of the dust tracking trough a simulation cell. Each of the four lines represents a single dust particle and the circles show the position of the particle at each time step.

the number density from dust trajectories. Each of the four lines represents a single dust particle and the circles show the position of the particle at each time step. In general each of the particles represents a different number of actual particles emitted from the surface per second. Let us assume a constant time step of 1 s and each simulation particle representing one real dust particles emitted from the surface per second. In that case each of the drawn position would inhabit an actual particle and the number of particles in the cell is given directly. As described before this is equivalent to measuring the time of each test particle spent in the cell multiplied by the number of particles per second it represents.

The output of the dust dynamics code contains the dust number density, and velocity of each cell in the simulation domain as for the gas dynamics code. Furthermore, we also get the mean drag coefficient for each cell. In addition, a «surface file» is created containing the in- and out-flux of ballistic particles from each facet as well as the mean travel time, and mean distance of the destination cell to the origin cell.

4.9 COLUMN INTEGRATOR

To be able to compare the results of the dust simulation with OSIRIS we need to perform a line of sight integration through the dust coma as an intermediate step. The resulting dust column density, n_{col}, can then be converted to a predicted brightness for OSIRIS as we will describe in Section 4.10. It is at this point that we need to define the

respective illumination and viewing geometry as we explained in Section 4.7. For a specific OSIRIS image we must find the corresponding simulation that matches its solar illumination condition. Then the position of the spacecraft from the centre of the nucleus $\vec{x}_{s/c}$, the Euler rotation angles (α, β, γ) of the camera with respect to the spacecraft coordinates, and the pointing direction $\vec{p}$ of the spacecraft are all derived from calibration and the reconstructed spacecraft SPICE kernels. For calculating each pixel, we are using a planar projection onto the image plane compared to the actual angular field of view of the OSIRIS cameras. The artificial column density maps have a field of view equal to the field of view in the actual OSIRIS image plane (Section 3.2) and are usually comprised of 1024×1024 pixels - though the resolution can arbitrarily be in-/decreased. The depth of the line of sight integration extends 1'000 km beyond the nucleus centre. This is illustrated in Figure 27. Because of the quadratic footprint of our integration and the fact that we are integrating beyond our simulation domain of the gas-and-dust dynamics model, we need to extrapolate the dust number densities up to a distance of 1'000 km from the comet. We do this by interpolating the density values at the outlet surface at 10 km to a 2D longitudinal and latitudinal coordinate grid with a angular resolution of $0.2\,^\circ$, yielding more than 1.6 million grid points. The interpolation assumes a linear distance weighting. For the extrapolation to any point in 3D space, we assume that the number density falls off with $1/r^2$ just as we did for the gas. The density at a point $\vec{y} = \vec{y}(x, y, z) = \vec{y}(r, \theta, \phi)$ is thus calculated by

$$n_d(\vec{y}) = n_d(r, \theta, \phi) = n_d(10\,\text{km}, \theta, \phi) \left(\frac{r}{10\,\text{km}}\right)^2 \quad . \tag{27}$$

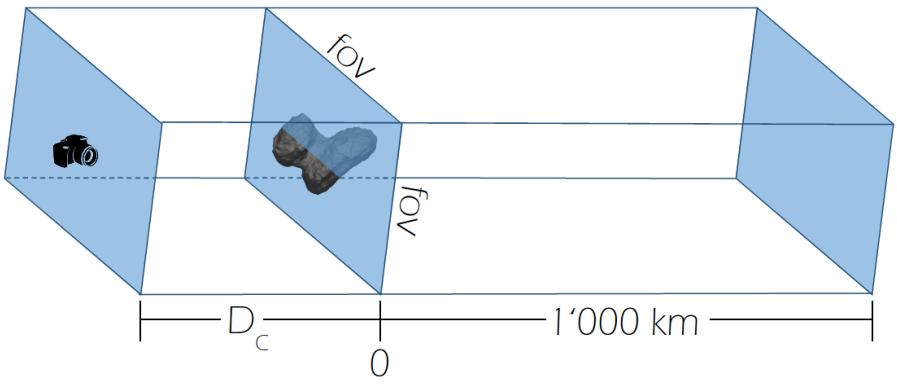

Figure 27: Schematic illustrating the column integration process. The image plane (plane in the centre) is at a distance D_c from the camera. The integration for all pixel extends 1'000 km beyond the image plane along parallel lines-of-sight.

The actual integral along the line of sight that needs to be numerically solved is

$$n_{col} = \int_{-D_c}^{1'000\ \mathrm{km}} n_d(\vec{y})\,dl \quad , \tag{28}$$

and becomes

$$n_{col} = \Sigma_i n_d(\vec{y})\Delta l_i \quad , \tag{29}$$

where Δl_i is the integration step such that finally $\Sigma_i \Delta l_i = D_c + 1'000$ km. The fact that the densities drop with $1/r^2$ can be used to decrease the computation time. We do this by employing a variable integration step, Δl_i. For large cometocentric distances, D_c, large integration steps can be used. As soon as we get within 10 km and thus enter the unstructured grid we need to ensure that we sample each cell without jumping over cells. We thus use the following formula to determine the integration step:

$$\Delta l_i = \begin{cases} r \cdot \sin(0.02°) & \forall\, r > 10\ \mathrm{km} \\ \frac{\sqrt[3]{V_c}}{10} & \forall\, r \leqslant 10\ \mathrm{km} \end{cases} \tag{30}$$

with V_c being the cell volume. Just as described in Section 4.8 the line of sight integration needs to be tracked through the unstructured grid and is stopped in case the cometary surface is hit before the full integration depth, $D_c + 1'000$ km, is reached.

This method only works well for dust that has reached terminal velocity and expands primarily radially. It does not perform well in situations with dust jets that have significant non-radial components, or comae dominated by gravitationally bound particles with scale heights on the scale of the domain itself. However, this appears to be a good approximation for most of the cases we have considered so far. In any case, for small impact parameters, b (the projected distance from the centre of the comet in the image plane), the column density is dominated by cells close to the nucleus and are hardly affected by the extrapolation. This line of sight integration is executed for each size bin individually assuming low optical depth. For bright outbursts optical depth needs to be accounted for in this step.

The explained method can just as well be used on the results from the gas dynamics model to produce single gas column densities, or gas column density maps. It can also be used to extract the local gas parameters (number density, speed, and temperature) along the line of sight. Such calculations can be used for comparisons with MIRO and VIRTIS and we will show predictions of our models for both of these instruments in Part iv and in Chapter 12.

4.10 DUST SCATTERING MODEL

The dust column densities, n_{col}, resulting from the line of sight integration of Section 4.9 can be used to produce an artificial image as could be seen by OSIRIS. To do this we need to determine how the light is scattered by the different particles. To do so, we use Mie theory for spherical particles and the algorithm of Bohren and Huffman, (1983). Mie theory and its application to comet observations have been extensively investigated by Fink and Rubin, (2012) and Fink and Rinaldi, (2015), who provide data for different values of the refractive index of the scattering efficiency versus the size parameter, x, defined as

$$x = \frac{2\pi r_d}{\lambda} \quad , \tag{31}$$

where λ is the wavelength and r_d the particle radius. The scattering efficiency typically shows a strong peak at values of $x = 1 - 3$. This is shown in Figure 28 were we can also see that the scattering efficiency drops sharply for $x < 1$ and on the other hand converges to ~ 1.2 for large size parameters. We compute the scattering functions for 40 discrete sizes, quasi-logarithmically distributed (10 linear bins per decade) between 8 nm to 0.3 mm. Larger particle sizes are computationally too time consuming for Mie theory, although their contribution to the total dust brightness from the inner coma is likely to be small (see Part iv). Our choice for this size range becomes clear now. We want to roughly cover the size range of $x \in [0.1, 100]$ to include all important scattering regimes (except for the geometrical regime at this point). The discretization can lead to oscillation in the scattering function in Mie calculations (see also Fink and Rubin, (2012)) and therefore, we avoid this by computing a mean scattering function over a size range that is $\pm 10\%$ of the nominal discrete size. As refractive index we have chosen that of astronomical silicate (Laor and Draine, 1993), which corresponds to $n = 1.81 + 0.1012i$ at $\lambda = 600\,\text{nm}$.
Under the assumption of zero optical depth, the observed radiance can be compared to the expected radiance of a column of dust with a specified size distribution, $n(r)$, of certain mass. When referring to the size distribution of the dust, we always refer to the distribution of dust sizes of the injected flux produced at the surface prior to any acceleration. This initial dust size distribution is altered due to unliftabitliy of certain particles and different relative acceleration of the respective sizes. Two approaches have been adopted. On the one hand a power law distribution for the size is set at the surface using

$$n(r) \sim r_d^{-b} \quad , \tag{32}$$

where b is referred to as the power law index. The resulting brightness images of the inner coma at the wavelength of the OSIRIS-WAC 18 filter is computed for direct comparison with the absolute calibrated

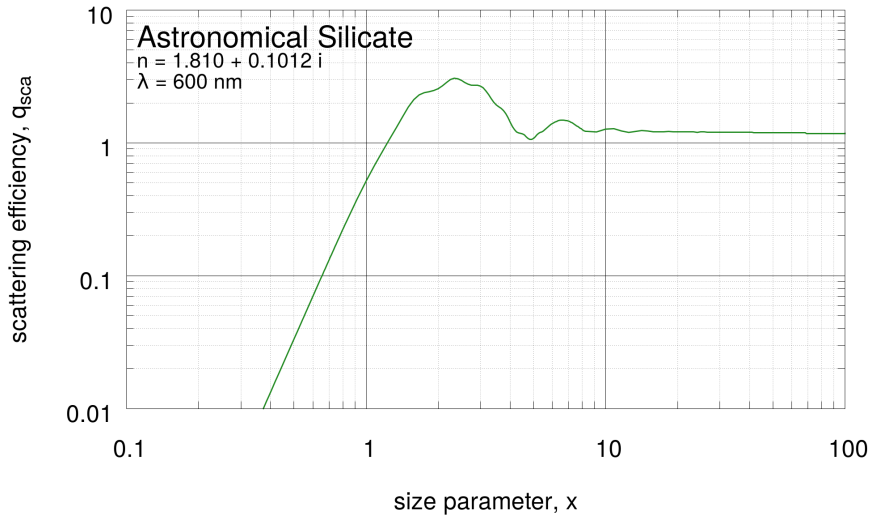

Figure 28: Scattering efficiency of astronomical silicate with complex refractive index of $n = 1.810 + 0.1012i$ (at $\lambda = 600$ nm) as a function of the size parameter.

OSIRIS data (Fornasier et al., 2015). Sometimes not the dust size distribution but the differential dust size distribution, $dn(r)/dr$, is used with b as the power law index. The differential power law index, b', and the power law index, b, we use in this work are connected with $b' = b + 1$.

On the other hand, we use a single dust size distribution

$$n(r) \sim \delta(r_d - r_d^i) \quad , \tag{33}$$

with r_d^i being the dust size that we want to study.

For a given dust size distribution and dust production rate, Q_d, the scaling of each size bin, $c(r_d)$ needs to be such that:

$$Q_d = \int_{r_{min}^{r_{max}}} c(r_d) \cdot n(r_d) \cdot m(r_d) dr_d \quad . \tag{34}$$

The weighting $c(r_d)$ will be used to scale the column densities of each dust size bin.
Following Fink and Rubin, (2012) and Fink and Rinaldi, (2015) the radiance (brightness) for each size bin is calculated according to

$$I(r_d) = \frac{F(\lambda)}{R_h^2} n_{col} \sigma_d q_{eff} \frac{p(\lambda, \phi)}{4\pi} \quad , \tag{35}$$

where F is the solar flux at 1 AU, n_{col} the dust column density, σ_{geo} the geometric cross-section of the dust grain, q_{eff} the scattering efficiency, and p the phase function for the scattering angle, ϕ. The

scattering angle is defined as the angle between direction of the incidence light and the direction of the scattered light. A scattering angle of 0° corresponds to the light being scattered along the direction of the incoming light (forward scattering). A scattering angle of 180° corresponds to the light being scattered in the opposite direction of the incoming light (backward scattering). Instead of comparing the dust coma radiance, I, which has the units of $Wm^{-2}nm^{-1}sr^{-1}$ it is often more convenient to compare the reflectance R which is

$$R(r_d) = \frac{I(r_d)R_h^2}{F} \quad , \tag{36}$$

and is unit-less. Figure 29 shows the phase function and phase function multiplied with the scattering efficiency of astronomical silicate at $\lambda = 600$ nm with a complex refractive index of $n = 1.810 + 0.1012i$ (Laor and Draine, 1993) for different dust sizes as a function of the scattering angle. We can observe the effect the scattering efficiency has on the brightness ($\sim p \cdot q_{sca}$) of the particles of different sizes. We especially see that the smallest dust size of 24 nm scatters quite uniformly but due to its low scattering efficiency its brightness is the lowest of all particles shown. It is also clear that the larger the particles are the more scattering we get in the forward direction. This of course is only true as long as we are not in the geometric scattering regime yet. When particles get very large back scattering will dominate. Figure 30 shows the phase function multiplied with the scattering efficiency at $\lambda = 600$ nm as a function of the scattering angle for a refractive index of $n = 1.65 + 0.002i$ (low absorption), $n = 1.810 + 0.1012i$ (astronomical silicate), and $n = 1.5502 + 0.4392i$ (carbon, high absorption). We can especially see the effect of the complex part of the refractive index on the phase curves. For low values (low absorbtion) we can see substantial back scattering especially for micron sized particles at this wavelength. For large values of the complex part of the refractive index - as for carbon - we observe hardly any back scattering but rather very pronounced forward scattering in all sizes. A very comprehensive description of scattering of light on small particles has been published in Mishchenko, Travis, and Lacis, (2002) and we will thus refrain from going into further details on this matter.

Individual images for each particle size can also be extracted to investigate the relative influence of each particle size on the result. It should be noted that we make no statement about how this initial power law is produced by the surface ejection mechanism. We recognise that many effects (e.g. charging or van der Waals forces) may lead to deviations from a simple power law distribution and, in particular, that there may be evidence that a population of larger particles is being ejected from the nucleus at the time of the observations used herein (Rotundi et al., 2015; Fulle et al., 2016a).

For comet 1P/Halley McDonnell et al., (1987) found a dust size distribution far from a power law. Also potential fragmentation of grains as well as sublimation of icy grains will certainly change the size distribution. Though to this point there is no evidence for these processes (Fulle et al., 2016b; Merouane et al., 2016).

The two parameters that have the strongest impact on the absolute value of the dust brightness are the dust size distribution and the dust to gas ratio. As long as the coma is optically thin a doubling of the dust to gas mass production rate ratio will result in a doubling of the dust brightness. On the other hand a change in the dust size distribution will change the brightness due to the very different scattering properties of different particle sizes as seen in Figure 29. A coma dominated by particles with size parameters $1 < x < 5$ will be much brighter than a coma dominated very small particles ($x << 1$). Inherently there is a degeneracy between the dust size distribution and the dust to gas ratio as we will show in Figure 82 of Section 9.3.1. As we run all individual dust sizes separate from each other we are able to re-scale the brightness of the individual dust sizes according to our desired dust size distribution and dust to gas ratio as a very last step without needing to make any assumptions at the beginning of the dust dynamics calculation which is the most computationally expensive. The only assumption we need to apply before the dust dynamics calculation is whether the dust to gas production rate ratio is globally constant - which we have assumed for this work. Any local or regional variation in either the dust size distribution of the dust to gas ratio would have to be applied before running the dust dynamics calculation.

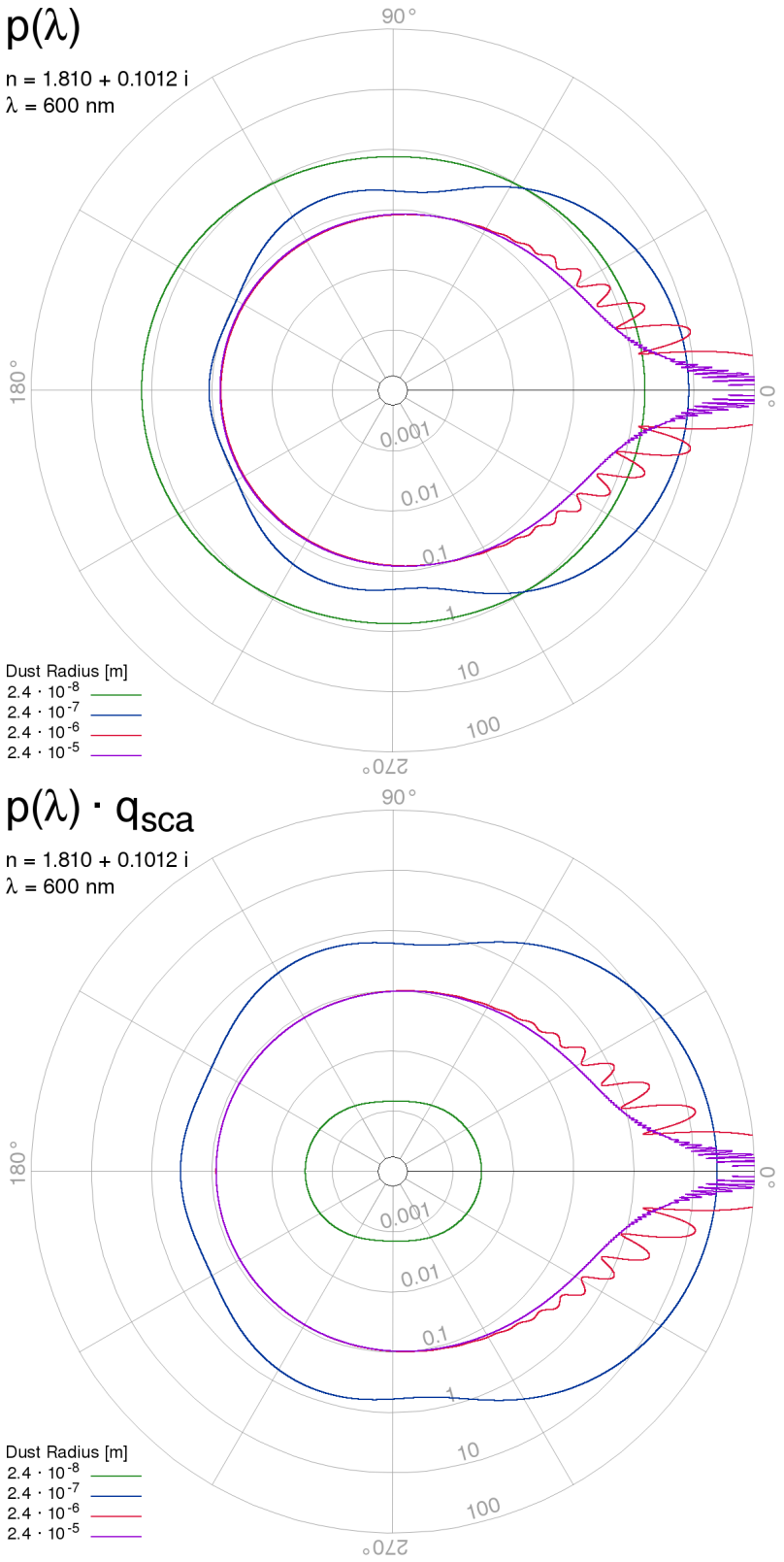

Figure 29: Phase function (top panel) and phase function multiplied with the scattering efficiency (bottom panel) of astronomical silicate at $\lambda = 600$ nm for different dust sizes as a function of the scattering angle.

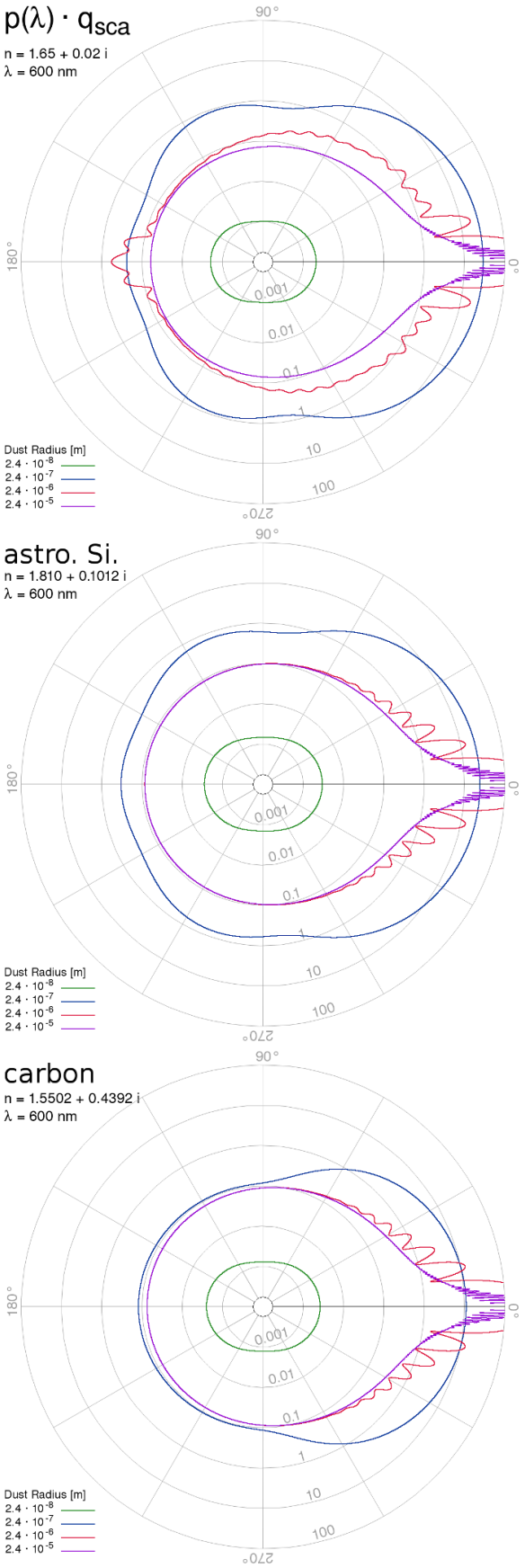

Figure 30: All three panels show the phase function multiplied with the scattering efficiency at $\lambda = 600$ nm as a function of the scattering angle for a refractive index of $n = 1.65 + 0.002i$ (low absorption, top panel), $n = 1.810 + 0.1012i$ (astronomical silicate, centre panel), and $n = 1.5502 + 0.4392$ (carbon, bottom panel).

4.11 SUMMARY OF CONSTANTS AND INPUT PARAMETERS

4.11.1 *Constants*

constant		**value**
solar constant at 1 AU	S	$1384\,\mathrm{W\,m^{-2}}$
IR emissivity	ϵ	0.9
Stefan-Boltzmann's constant	σ	$5.670367 \cdot 10^{-8}\ \mathrm{W\,m^{-2}\,K^{-4}}$
latent heat of sublimation of water ice[1]	L	$2.84\ \mathrm{MJ\,kg^{-1}}$
Boltzmann constant	k	$1.38065 \cdot 10^{-23}\ \mathrm{J\,K^{-1}}$
molecular mass of water	M_{H_2O}	$18.0153\ \mathrm{u}/2.99151 \cdot 10^{-26}\ \mathrm{kg}$
Gravitational constant	G	$6.67408 \cdot 10^{-11}\ \mathrm{m^3\,kg^{-1}\,s^{-2}}$
total mass of the comet[2/3]	M_C	$1.0 \cdot 10^{13}\ \mathrm{kg}/9.9 \cdot 10^{12}\ \mathrm{kg}$
volume of comet[2/4]	V_{comet}	$21.4 \pm 2.0\ \mathrm{km^3}/18.7 \pm 0.4\ \mathrm{km^3}$
bulk density of the comet[2/3]	ρ_C	$470 \pm 45\ \mathrm{kg\,m^{-3}}/533 \pm 6\ \mathrm{kg\,m^{-3}}$

Table 4: Table of constants used in our models.

1 Huebner et al., (2006)
2 Sierks et al., (2015) presented the first estimates which were mostly used in this work.
3 Pätzold et al., (2016)
4 Preusker et al., (2015)

4.11.2 *Parameters*

parameter		**value [possible range]**	**effect on result**
sublimation coefficient	α_s	1 [0.1, 1]	low[5]
directional–hemispheric albedo	A_H	0.04	low
incidence angle	i	$[0°, 90°]$	large
heliocentric distance	R_h	[1.24, 5.69 AU][6]	large
thermal inertia	I	$[0, 50\ J\ m^{-2}\ K^{-1}\ s^{-1/2}]$	low[7]
topographic heating		on/off	low[8]
equilibrium vapour pressure of water vapour	p_{evp}	Huebner et al., (2006)	
effective active fraction[9]	eaf	$[0, 1]$	large
reflectivity of surface		absorbing or reflecting (specular,diffuse)	medium
sub-solar latitude		$[-90°, 90°]$	large
sub-solar longitude		$[0°, 360°]$	large
bulk density of dust particles	ρ_d	440 kg m^{-3} [1 kg m^{-3}, 2300 kg m^{-3}][10]	large
dust particle radius	r_d	$[1 \cdot 10^{-8} m, 1 \cdot 10^{-1} m]$	large
dust size distribution	$n(r_d)$	power law/single dust size	large
dust to gas mass production rate ratio	Q_d/Q_g	[2, 5]	large
dust temperature	T_d	$T_d = T_g$	

parameter		**value [possible range]**	**effect on result**
fraction of specular reflection of gas particles on dust	ε	1 [0, 1]	
cometocentric distance	D_c	[10 km, 50 km][11]	large for gas/ medium for dust
depth of line of sight integration	T_d	$D_c + 1'000$ km	low when larger than this value
complex refractive index	n	$1.81 + 0.1012i$ for $\lambda = 600$ nm (astronomical silicate)[12]	large
phase angle	ϕ	[0°, 90°]	large
spacecraft position & pointing		extracted from SPICE kernels	large

Table 5: Table of input parameters used in our models.

5 Kossacki et al., (1999)
6 This is the range of heliocentric distances of comet CG but in this work we mainly present results for $2.8 < R_h < 3.4$.
7 Liao, (2017)
8 For our considered time span it has a low effect on the H_2O emission but can potentially have an influence on CO_2 emission.
9 In practice the eaf controls the production rate somewhat artificially and thus can have an equally large effect as the heliocentric distance.
10 Rotundi et al., (2015), Fulle et al., (2016b), and Pätzold et al., (2016)
11 For the time period of this work
12 The complex refractive index can effect the scattering efficiency and phase function strongly.

Part III

FROM SPHERICAL NUCLEI TO COMPLEX SHAPES

We will be studying how the global production rate, and its distribution on the surface affects the gas and dust flows. We will start with spherical cases and subsequently add complexity by introducing the actual shape of comet CG as described in Section 4.2. This approach is illustrated in Figure 31. Studying first uniform outgassing (Chapter 6) from a spherical nucleus eliminates any effects coming from variations in the emission on the surface and effects from surface topography. We will then add a first layer of complexity by introducing emission proportional to the incoming energy of the Sun in what we call purely-insolation-driven outgassing. In these models the outgassing power is primarily governed by the angle of incidence of the solar flux to the local surface normal. Such models exhibit new features such as redeposition of dust particles on the night side of the comet a process observed by Rosetta (Thomas et al., 2015a). We will conclude this part of the thesis with some considerations about the emission from the actual shape of comet CG in Chapter 7. We do this in preparation for our discussion in Chapter 9 on building models that can explain Rosetta data. But first we will discuss some fundamental considerations on our expectations of the flow results in Chapter 5

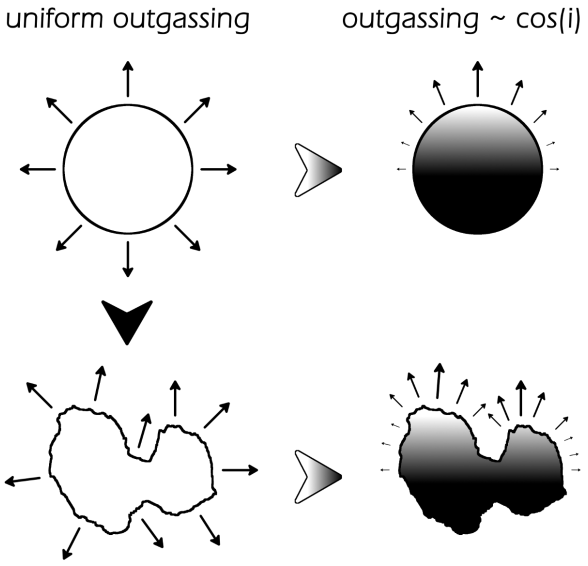

Figure 31: Schematic showing of our approach to studying the outgassing by going from a uniformly outgassing spherical nucleus to (top left) to purely-insolation-driven outgassing of the actual complex shape of comet CG (bottom right).

5

FUNDAMENTAL CONSIDERATIONS

Results can not only be compared with each other but we will frequently compare them to the most simple outgassing model, a force free radial outflow. We follow here the approach described by Thomas and Keller, (1990) who have to our knowledge first applied this kind of analysis in the cometary context for comet 1P/Halley. In the case of free radial outflow some quantities are conserved as a function of the distance from the comet. When there is no alteration of the gas or dust flow as a function of cometocentric distance - through e.g. dissociation, icy dust particle sublimation, or fragmentation - the mass flux is conserved for closed surface. More formally this means that

$$\int_{\Sigma} n m \vec{v} \, d\vec{A} = \text{const.} \quad , \tag{37}$$

where n is the number density of the gas or dust, m is the molecular mass of the gas or mass of the individual dust particle, $\vec{v}$ is the gas/-dust speed, $d\vec{A}$ the area through which the gas or dust flows, and Σ is a closed surface. The constant has the units kg s^{-1}. Although Σ can principally be chosen arbitrary, we have for simplicity chosen spheres of different radii enclosing the gas/dust source (i.e. the comet). If we were to not enclose the source the integral of Equation 37 would simply result in zero. The number density and speed are in general functions of time and the position in space.

In the case of force-free radial outflow $|\vec{v}|$ is constant and radial and thus Equation 37 reduces to

$$n \cdot r^2 = \text{const.} \quad , \tag{38}$$

where r is the radial distance to the centre of the comet. This law is often referred to the «$1/r^2$-law» because this implies that the number density drops with $1/r^2$.

There is a second important law that we will be making use of regularly. It is the so called «1/r-law». When integrating along a line of sight through the gas/dust coma we get gas/dust column densities. We thus effectively reduce the 3D coma number density to 2D column densities. Within this 2D domain we can integrated along closed curves (again enclosing the source) to find another conserved quantity which for free radial outflow results in

$$n_{col} \cdot b = \text{const.} \quad , \tag{39}$$

where b is called the impact parameter (i.e. the distance from the nucleus center). Mostly b is often interchangeably used with r although it is a projected distance and not the actual radial distance. Therefore it is called the «1/r-law». Hence for a free radial flow the column density (or for the dust also the brightness, see Section 4.10) drops with $1/b$.

There are a multitude of processes that can result in deviations from free radial outflow behaviour. Some of them are listed here.

For the gas:

- particle acceleration effects
- viewing geometry (non-point source, phases angle)
- non-radial flow
- optical depth effects
- photo dissociation
- molecular recombination

For the dust (especially when studying the dust brightness):

- particle acceleration effects
- viewing geometry (non-point source, phases angle)
- non-radial flow
- optical depth effects
- particle fragmentation (into either optically active or inactive daughters)
- sublimation of particles (reducing the effective scattering cross-section)
- condensation effects (increasing the scattering cross-section)
- gravitationally-bound particles.

In Gerig, Marschall, and Thomas, (2017) we discuss these phenomena in more detail in the context of a comprehensive study of the OSIRIS images over the entire escort phase of the Rosetta mission.

6 SPHERICAL MODELS

Let us consider a spherical nucleus with a radius of 2 km which results in approximately the surface area of comet CG. Models for spherical nuclei usually make use of this symmetry to reduce the posed problem from 3D to 2D or even 1D simulations. This is computationally favourable. But we are at this instance not interested in making the simulation as efficient as possible, mainly because we are no longer strongly constrained by the computational cost as in decades past. We thus perform all simulations in full 3D. This has the advantage that we can remain in one framework thought this work and will not be limited by any of the approximations that can occur when reducing the simulation to 2D or 1D. We will not have to consider whether or not any of the results can be expanded to the full 3D situation.

6.1 UNIFORM EMISSION

Considering a uniformly outgassing comet is somewhat artificial. Uniform outgassing would occur if at least one of the following physical properties of the considered comet is given. Either the thermal conductivity is so large that heat dissipates through the entire body quasi instantaneously (on time scales much smaller than the change in illumination). Or the comet is tumbling very fast that all surfaces are homogeneously supplied with energy. Regarding the first Prialnik, Benkhoff, and Podolak, (2004) have estimated the diurnal skin depth of comets to be of the order of 10 cm. For comet CG specifically, low values for the thermal inertia have been found (Gulkis et al., 2015; Schloerb et al., 2015; Choukroun et al., 2015). The second possibility of a fast tumbling comet is clearly not given in the case of comet CG because it has a very stable rotation axis with a rotation period on the order of 12 h[1]. Non the less uniform emission provides the next basic assumption one can make for a comet after force-free radial outflow.

The three cases of uniform emission we consider here differ only in their global gas production rate, Q_g. We have chosen Q_g to cover two orders of magnitude taking the values 4, 40, and 400 kg s^{-1}. The surface temperatures increase slightly from the low to high production rate case from 180 K, to 190 K, to 200 K, mimicking somewhat a change in heliocentric distance. All assume equal outgassing from

1 The rotation period of CG has decreased by roughly 4% in the escort phase of Rosetta.

each surface facet and result in only radial expansion being possible because lateral flow is inhibited due to the uniform emission. The gas is thus essentially accelerated radially outwards.

6.1.1 *Gas results*

We are interested in looking at the behaviour of the gas number density, gas speed, and the gas temperatures as a function of the radial distance from the centre of the comet. To do this we have averaged the respective quantities at different radial distances.

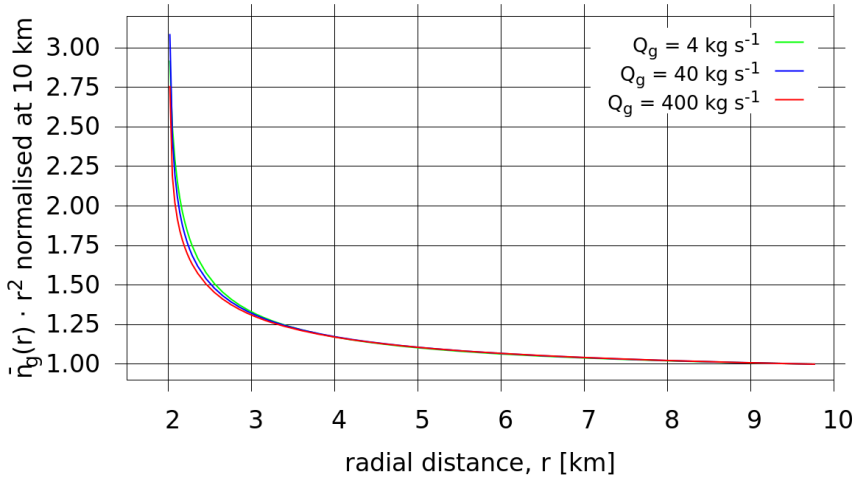

Figure 32: Gas number density multiplied by the square of the radial distance as a function of the radial distance for three global gas production rates of uniform outgassing. The three curves have been normalised to a value of unity at 10 km radial distance for relative comparison.

Figure 32 shows the gas number density multiplied by r^2 as a function of radial distance, r, for the three production rates probing the deviations from the «$1/r^2$—law ». To compare the behaviour of the different production rates we have normalised the results at the other edge of our simulation domain. We can see that in all three cases the number density drops steeply within the first kilometre above the surface, then continues a steady decline and finally becomes constant between 8 and 9 km indicating that the flow has gone over to the free radial outflow case. There is only a minor relative effect from the production rate. The higher it is the slightly stronger the number density curves fall in the first kilometre. This can be attributed to the marginally higher relative acceleration in the higher production rate cases, though this effect is very minor. Why this is the case will become apparent shortly.

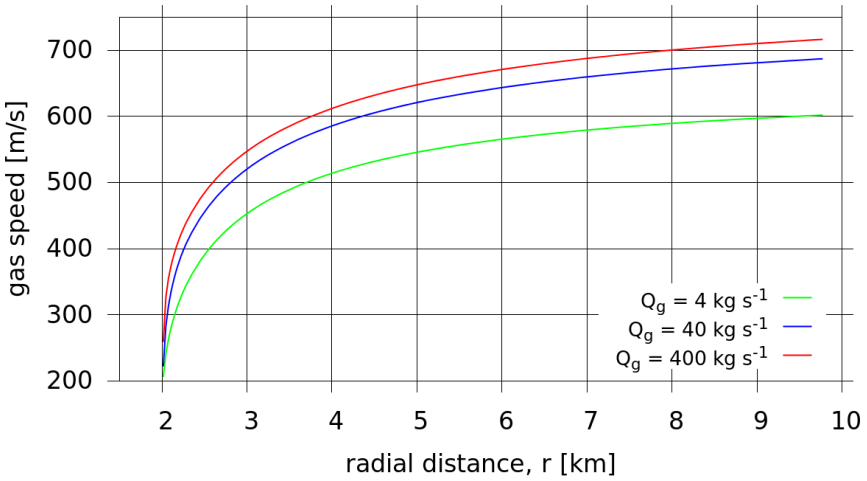

Figure 33: Gas speed as a function of the distance from the centre of the nucleus for three global gas production rates of uniform outgassing.

Figure 33 shows the gas speed as a function of radial distance for the three production rates. We can observe a large difference in the absolute values. We reach over 700 m s^{-1} for the highest production rate whereas the lowest production rate case just reaches 600 m s^{-1}. The gas is accelerated through two processes. On the one hand even in the free flow regime gas is accelerated from the surface outwards due to adiabatic expansion into vacuum. On the other hand in collisional flows the gas is additionally accelerated by energy transfer when a collision of two gas molecules occurs. In that case rotational temperature, T_{rot}, is transformed to translational temperature, T_{trans}. The more particle collisions the more efficient this process becomes and can lead the two temperatures to equilibrate. Different values for the two temperatures indicates non-local thermodynamic equilibrium (LTE) but the opposite is not true. Equal temperatures does not imply LTE. For this to be true we would also need to examine the local VDF which we will not be doing here.

Figure 34 shows the rotational and translational temperatures for the three production rates as a function of the radial distance. The overall trend of declining temperatures is due to the mentioned adiabatic expansion of the gas which even occurs in the free molecular flow regime. Additionally, we clearly see that in the lowest production rate case the two temperatures never equilibrate indicating a strongly non-LTE flow. It indicates that the acceleration due to molecular collisions is less efficient than in the high production rate case, where the two temperatures equilibrate. This explains the small effect in relative speeds leading to minor differences in number density behaviour seen in Figure 32.

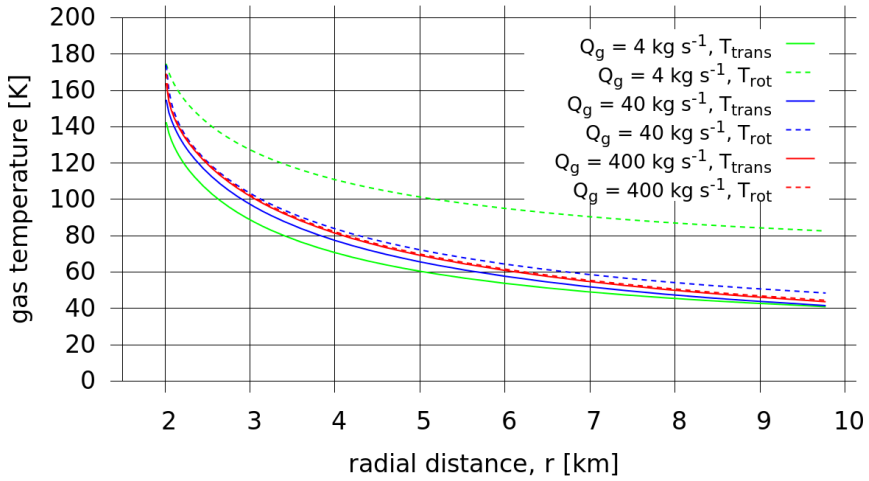

Figure 34: Translational (solid lines) and rotational (dashed lines) temperatures of the gas as a function of the radial distance for three global gas production rates of uniform outgassing.

6.1.2 *Dust results*

We have run our dust dynamics model (Section 4.8) on the three uniform emission gas flow fields for 64 dust particle radii, r_d, in the range from 10^{-8} m to 10^{-1} m. The dust sizes run are spaced semi logarithmically (nine linearly spaced dust sizes every decade).

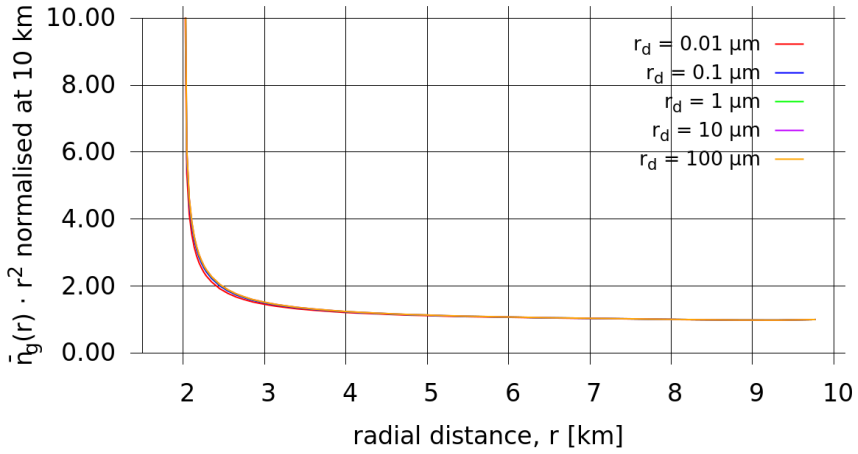

Figure 35: Dust number density multiplied by the square of the radial distance is shown as a function of the radial distance and five different dust sizes ranging from 0.01 µm to 100 µm for the 4 kg s^{-1} uniform outgassing model. The curves have been normalised to a value of unity at 10 km radial distance.

Figure 35 shows the dust number densities multiplied by r^2 as a function of the radial distance, r, for the lowest production rate case. All dust sizes show almost an identical behaviour but the overall

shape of the curves has two distinct differences to the curves of the gas in Figure 35. First the dust curves drop even faster than the gas curves do within the first kilometre above the surface and then goes over the expected behaviour of free radial outflow much earlier than the gas. This simply indicates that the dust decouples from the gas flow before the gas has reached its terminal velocity, mainly due to the gas densities dropping too fast for the gas flow to efficiently accelerate the dust particles any further. Second the curves not only drop faster to a constant value but also increase to higher values as we approach the surface. This is to some extent influenced by our setup of the dust simulation with dust particles on the surface having no initial velocity. The height of the curve at the surface is dominated by the speed ratio at the surface to the terminal speed. The gas is emitted from the surface at roughly 200 m s^{-1} and reaches speeds of up to 700 m s^{-1}. This ratio will always be lower than for that dust that has almost negligible speed close to the surface. Even though the curves of the different dust sizes are almost identical, we do see a trend that the smaller particles are the faster the curve decreases with increasing distance. This can be mainly attributed to the fact that smaller dust particles are more efficiently accelerated, not only due to their favourable mass to cross section ratio but also due to larger values of the drag coefficient as we will show later when we discuss the purely-insolation-driven cases in Section 6.2. Both will increase the acceleration of the dust particles as can be seen in Equation 22. For the low production rates this is only a minor effect.

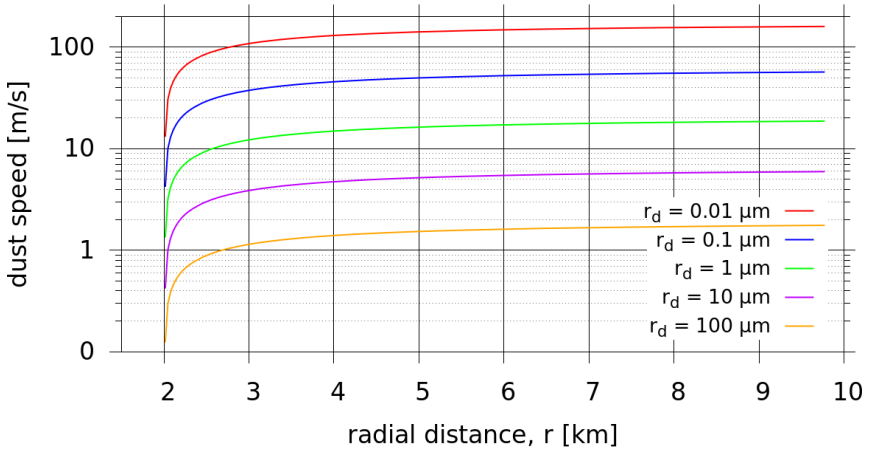

Figure 36: The dust speed is shown as a function of the radial distance and five different dust sizes ranging from 0.01 µm to 100 µm for the 4 kg s^{-1} uniform outgassing model.

Figure 36 shows the dust speed as a function of the radial distance for dust sizes covering four orders of magnitude from 10 nm to 0.1 mm. Assuming that the gas speed is much larger than the dust speed and we are dealing with a radial flow it follows from Equation 22 that the

dust speed should in first order increase with $\sqrt{r_d}$. This can be seen in Figure 36. As the dust size increases by factors of 100 from 0.01 µm to 1 µm to 100 µm the terminal speed increases by approximately factors of 10 from ~ 2 m s^{-1} to ~ 20 m s^{-1} to ~ 200 m s^{-1}. We can also see the reaching of a substantial fraction of the terminal velocity within the first three kilometres above the cometary surface. This mirrors what we have seen and discussed looking at Figure 35 showing the dust number density.

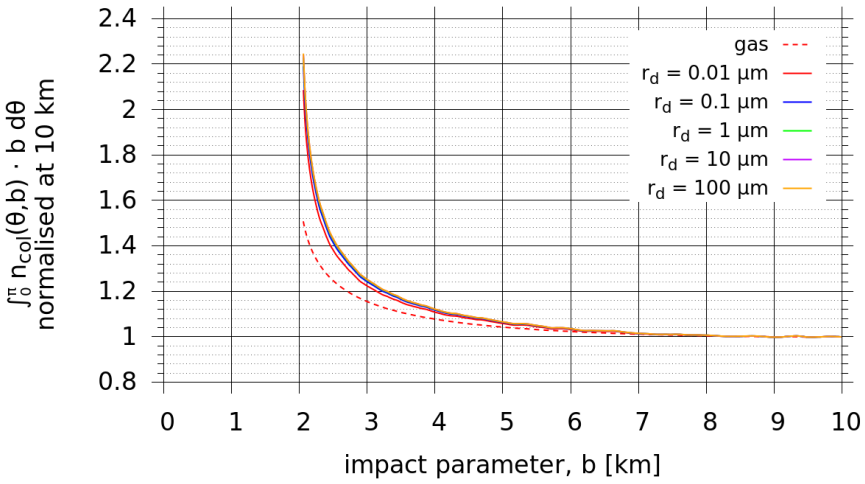

Figure 37: Azimuthally integrated dust column density multiplied by the impact parameter are shown as a function of the impact parameter and five different dust sizes ranging from 0.01 µm to 100 µm for the 4 kg s^{-1} uniform outgassing model. The curves have been normalised to a value of unity at 10 km radial distance. The dashed line shows the azimutally integrated gas column density multiplied by the impact parameter as a reference.

We would like to mention that as expected the dust flow shows no deviations from radial motion. As the gas flow is fully radial there is no physical mechanism to make the flow non-radial. Finally we will have a look at the behaviour and especially deviations from the «1/r-law» in the column density. Figure 37 and Figure 38 show the azimuthally integrated dust column density for the different dust sizes and for the lowest and highest gas production rate. While the relative behaviour of dust column densities in the lowest production rate case (Figure 37) are almost identical, which simply mirrors the behaviour seen in the number density behaviour seen in Figure 35, there are significant differences in the highest production rate case (Figure 38). The smaller the particles the closer their curves come to the behaviour of the gas up to the point where they effectively mimic the gas behaviour. This is simply due to the higher gas densities allowing for more efficient acceleration of the dust compared to the low production rate case.

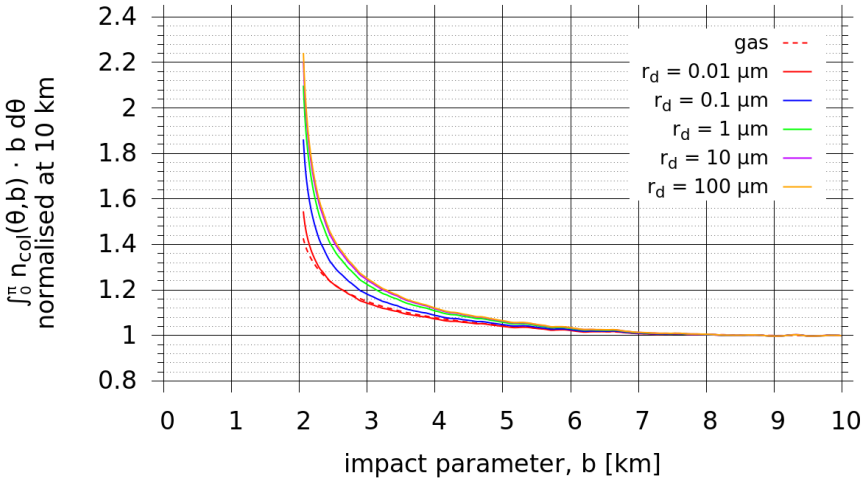

Figure 38: Azimuthally integrated dust column density multiplied by the impact parameter are shown as a function of the impact parameter and five different dust sizes ranging from 0.01 µm to 100 µm for the 400 kg s^{-1} uniform outgassing model. The curves have been normalised to a value of unity at 10 km radial distance. The dashed line shows the azimutally integrated gas column density multiplied by the impact parameter as a reference.

6.2 PURELY-INSOLATION-DRIVEN EMISSION

Going from a uniformly outgassing spherical comet we now add a first layer of complexity to what we call a purely-insolation-driven comet. Purely-insolation-driven means that the outgassing power is determined solely by the $\cos(i)$, where i is the angle of incidence of the Sun to the local surface normal. We define the position of the Sun and then proceed as described in Section 4.5 for the calculation of the incidence angles and then Section 4.6 for the thermal and sublimation related properties. Again we study three cases, this time linking them to a specific heliocentric distance. A low production rate case at 3 AU with $Q_g = 2$ kg s^{-1}, a mid production rate case at 2 AU with $Q_g = 20$ kg s^{-1}, and a high production rate case at CG's perihelion (1.25 AU) with $Q_g = 200$ kg s^{-1}. The heliocentric distance essentially determines the surface temperature and effective active fraction (eaf) have been adjusted to get the corresponding production rates. Their values are 0.81%, 2.11%, and 6.30% from lowest to highest production rate. Figure 39 shows the setup (production rate and surface temperature) of the low production rate case in a 0° and 90° phase angle view.

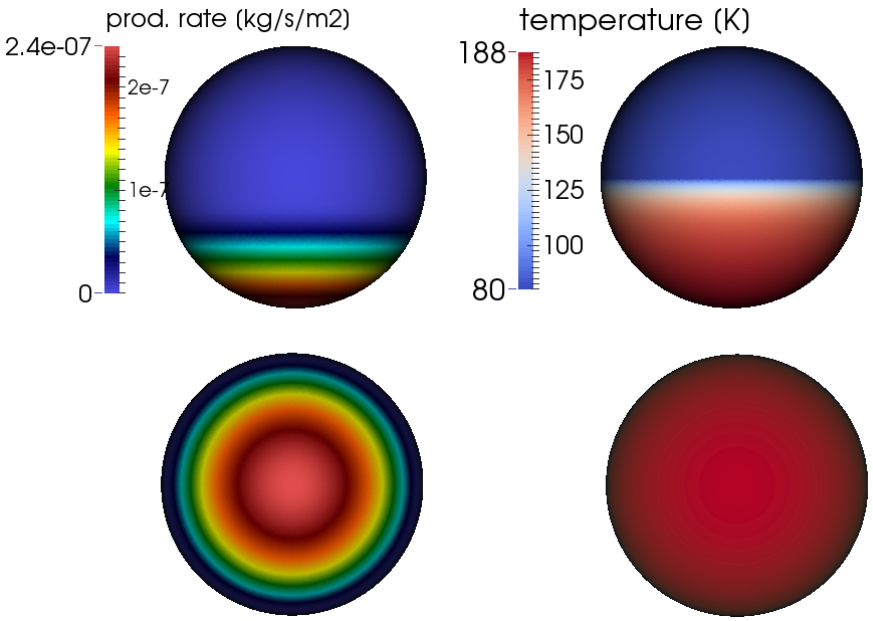

Figure 39: Gas production rate (right panels) and surface temperatures (left panels) are shown for the insolation driven model with a global production rate of 2 kg s^{-1}. The top panels show a 90° and the bottom panels a 0° phase angle viewing geometry

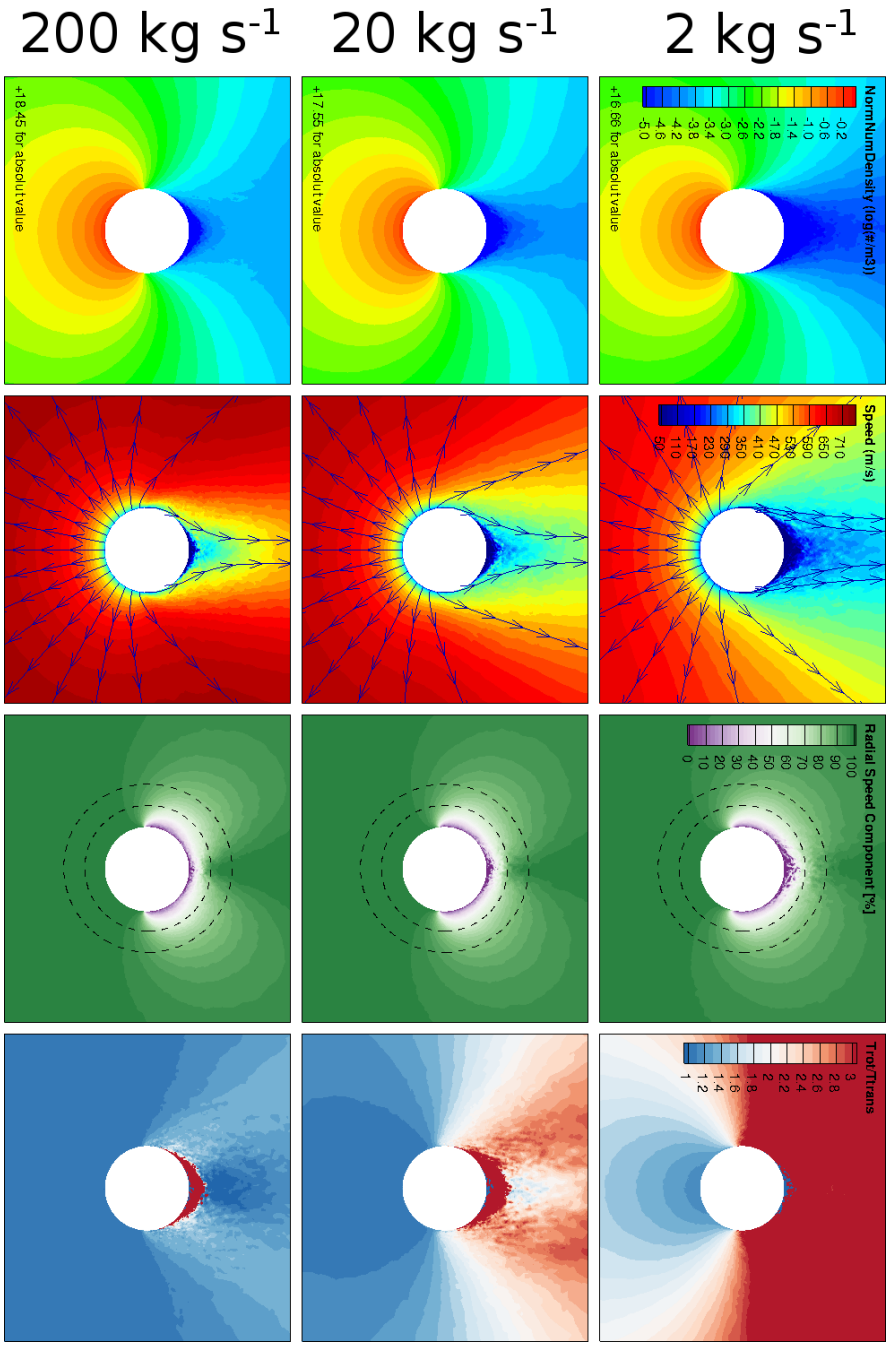

Figure 40: View of a slices (x = 0 m) through the 3D gas results for the three insolation driven cases with global production rates from 2 to 200 kg s^{-1} from top row to bottom. The left three panels show the local number density on a logarithmic scale and normalises for easier comparison. The second three panels from the left show the gas speed. The second three panels from the right show the radial fraction of the gas speed and the three right models show ratio between the rotational and translational gas temperatures.

6.2.1 *Gas results*

An overview of the 3D gas results of the purely-insolation-driven models is presented in Figure 40 showing a slice through the 3D flow solution at $x = 0$ m. The Sun comes from the bottom of the slice and we are viewing the coma with a phase angle of 90°. Therefore the terminator is a horizontal line in the centre of the sphere. The rows from top to bottom show the three production rate cases from low to high with the number density in the first column, the gas speed in the second column, the radial component of the gas speed in the third column, and finally the ratio between the rotational temperature and the translational temperature in the fourth column. Overlain on the gas speed field are stream traces that originate every 10° from the sub-solar point outwards towards the terminator and follow the velocity field assuming a particle with negligible mass. The higher the production rate the more radial the gas flow is. This is also mirrored in the three plots showing the fraction of the velocity vector that points along the radial direction. The ratio between the rotational and translational temperatures shows a trend we have already seen in the uniformly outgassing cases. The higher the production rate the more the temperatures equilibrate.

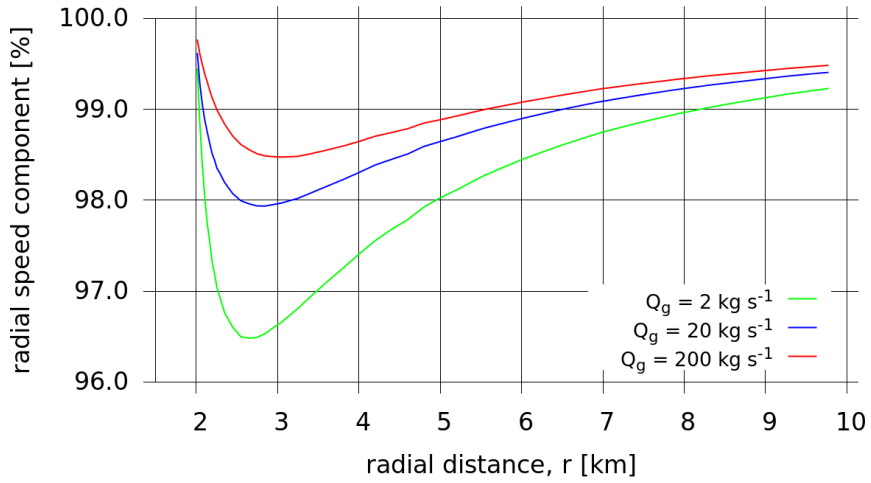

Figure 41: Average radial fraction of the gas velocity as a function of the radial distance for three purely-insolation-driven outgassing models.

For a more quantitative look of the gas properties we average the different gas properties as a function of the distance to the comet centre. The averaging is a number density weighted average and therefore represents the value of the average molecule at a certain distance. As can by seen in Figure 40 the range of the different values at a certain distance within the coma can be quite substantial.

Compared to the uniformly outgassing comet we have lateral flow in the insolation-driven cases. Due to the gradient in the surface emission from the sub-solar point towards the terminator lateral flow is induced including flow to the night side (i.e. non-illuminated and thus not outgassing) of the comet. Figure 41 shows the mean radiality of the flow field as a function of the distance. 100% represents fully radial flow away from the cometary surface, −100% fully radial flow towards the surface, and 0% flow horizontally to the surface. For all three production rate cases the flow starts out very radial (as we have set it up) then starts to expand laterally and then reverts to becoming a radial flow. The lower the production rate is the less radial the flow is overall (minimum value of radially at 96.5%). Though even in the most extreme case the flow is very radial. Furthermore, the higher the production rate the further away from the nucleus do we reach the regime of least radial flow. Both of these effects are directly explainable with the production rate. The higher it is the more efficiently the gas is accelerated radially outwards (suppressing lateral flow). In any case the maximum lateral flow is between 2.5 and 3.0 km from the nucleus centre.

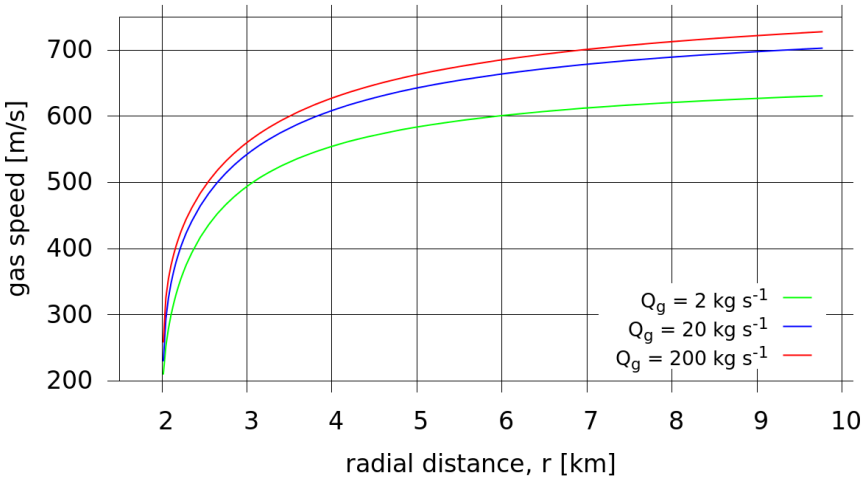

Figure 42: Average gas speed as a function of the radial distance for three purely-insolation-driven outgassing models.

Looking at the average gas speed in Figure 42 and comparing them to the results of the uniform emission case in Figure 33, we notice that the average gas molecule behaves almost identical in both cases. The gas speeds in the purely-insolation-driven case are slightly higher though, especially the lower the production rate is. The real difference is the large range in gas speeds at the same distance from the surface for different latitudes.

A very similar picture can be seen in the rotational and translational temperatures. Comparing the average temperatures of the insolation-

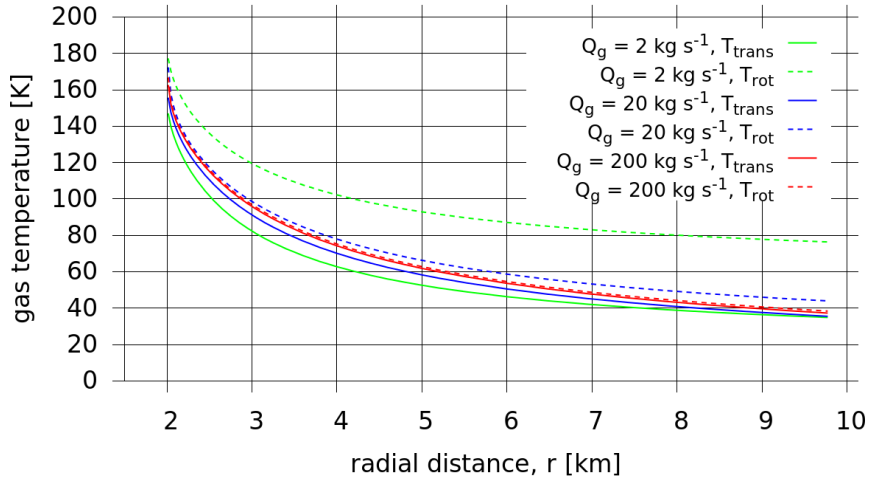

Figure 43: Average translational (solid lines) and rotational (dashed lines) gas temperatures as a function of the radial distance for three purely-insolation-driven outgassing models.

driven case in Figure 43 to the ones of uniform outgassing in Figure 34 shows almost identical behaviour. The temperature in the uniform emission cases are slightly higher than the temperature of the average molecule in the insolation-driven cases. This behaviour of both the gas speed and the gas temperatures shows that the average molecule in the purely-insolation-driven case can hardly be distinguished from its counterpart in the uniform emission cases. The details and especially the large range of values seen in Figure 40 as well as the presence of lateral flow is completely washed out by the averaging process as the dominant high production part of the coma behaves the same.

But we can make some analysis of the non-uniform emission effects. When we look at the gas column density at 90° phase angle as shown in Figure 44 and integrate not the full azimuthal range at each distance but split the integral into the day and night side part (splitting the coma at the terminator) we do find some interesting behaviour. For all three insolation driven cases we show these result in Figure 45. The integrated column densities are normalised at 10 km because of the different production rates and the much lower values on the night side. The day side behaviour looks very similar to the behaviour seen in the uniform case with the highest production rate case accelerating the most efficiently and thus showing the lowest values. On the night side the curves are almost a mirror image of the day side curves. The higher the production rate the smaller the values of the column densities are. This is intuitive as the higher production rate cases have higher speeds resulting in less lateral flow and thus it takes longer to reach the night side.

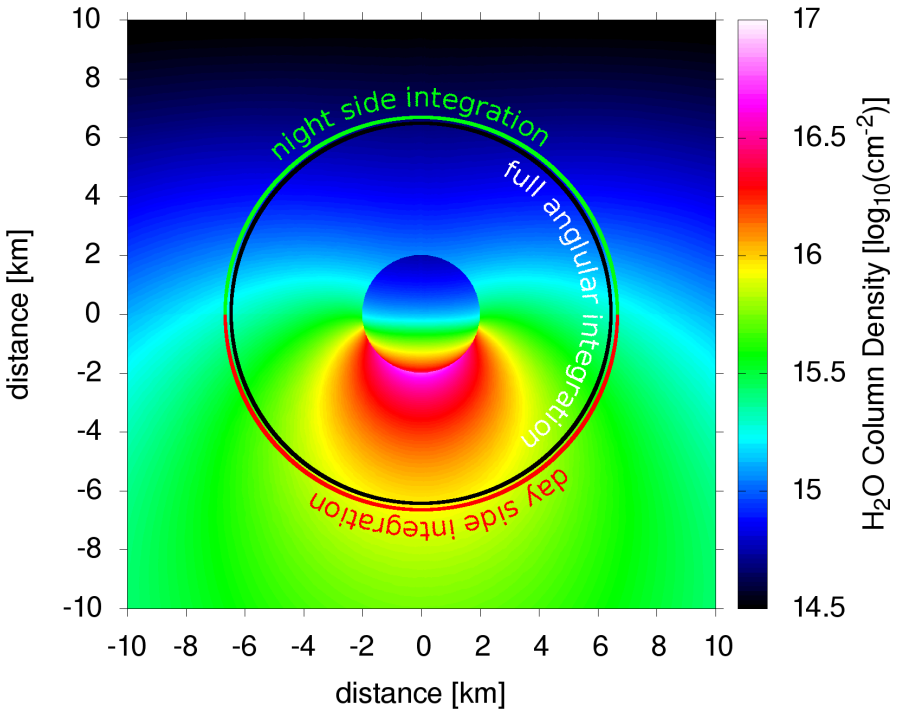

Figure 44: Gas column density of the 20 kg s^{-1} purely-insolation-driven model for a 90° viewing geometry. Furthermore, the definition of the full azimuthal angular integration (black circle), and the partial integration for the day (red semi circle) and night (green semi circle) side is illustrated. This definition will be used in subsequent plots.

Due to the non-uniformity of the emission column integrated values depend strongly on the viewing geometry. Setting aside non-point source effects - when the distance to the comet is too small ($<$ 100 km) - the phase angle has a substantial influence on the column integrated result. This is shown in Figure 46 where the two extreme cases of 0° and 90° phase angle are plotted. We have also included the result from the uniform case. The column integral is dominated by the effects in the image plane (point of closest proximity to the comet centre). In the case of 0° phase angle this is the terminator plane which has the least radial expansion because of the lateral flow going from the day side to the night side. Thus its column density drops very fast and then remains on the free radial outflow level. For a phase angle of 90° the results are dominated by the plane going though the sub-solar point. The results are influenced by a large gradient of acceleration and the lateral flow regimes from the sub-solar point to the terminator and we thus see a very long drop to the free radial flow level.

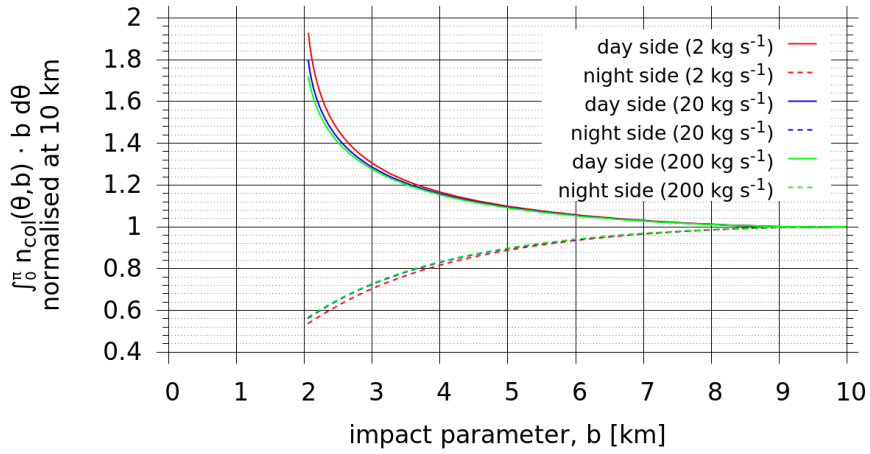

Figure 45: Azimuthally integrated gas column density multiplied with the impact parameter as a function of the impact parameter for the day (solid lines) and night (dashed lines) side (as defined in Figure 44) for three purely-insolation-driven outgassing models. The phase angle of the integration is 90°. The curves have been normalised to unity at 10 km.

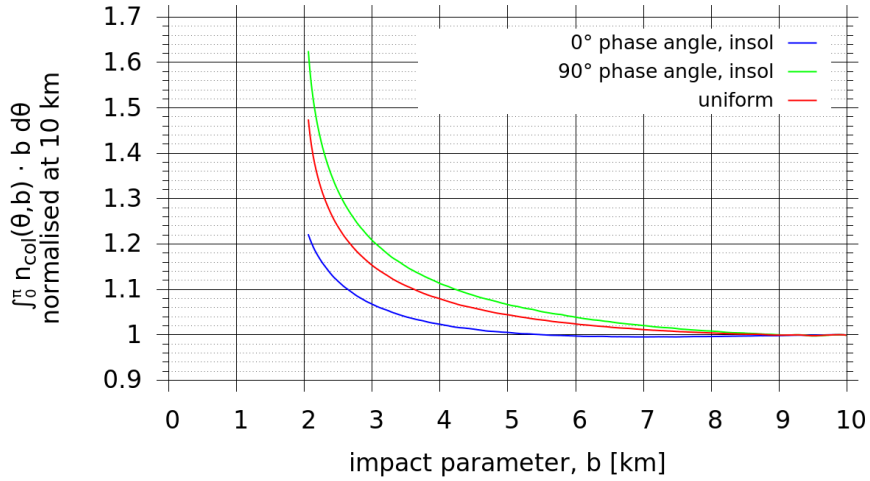

Figure 46: Comparison of azimuthally integrated gas column density multiplied with the impact parameter as a function of the impact parameter for two phase angles in the case of the purely-insolation-driven model with a production rate of 2 kg s^{-1} and the uniform emission model with a production rate of 4 kg s^{-1}. The phase angle of the integration is 90°. The curves have been normalised to unity at 10 km.

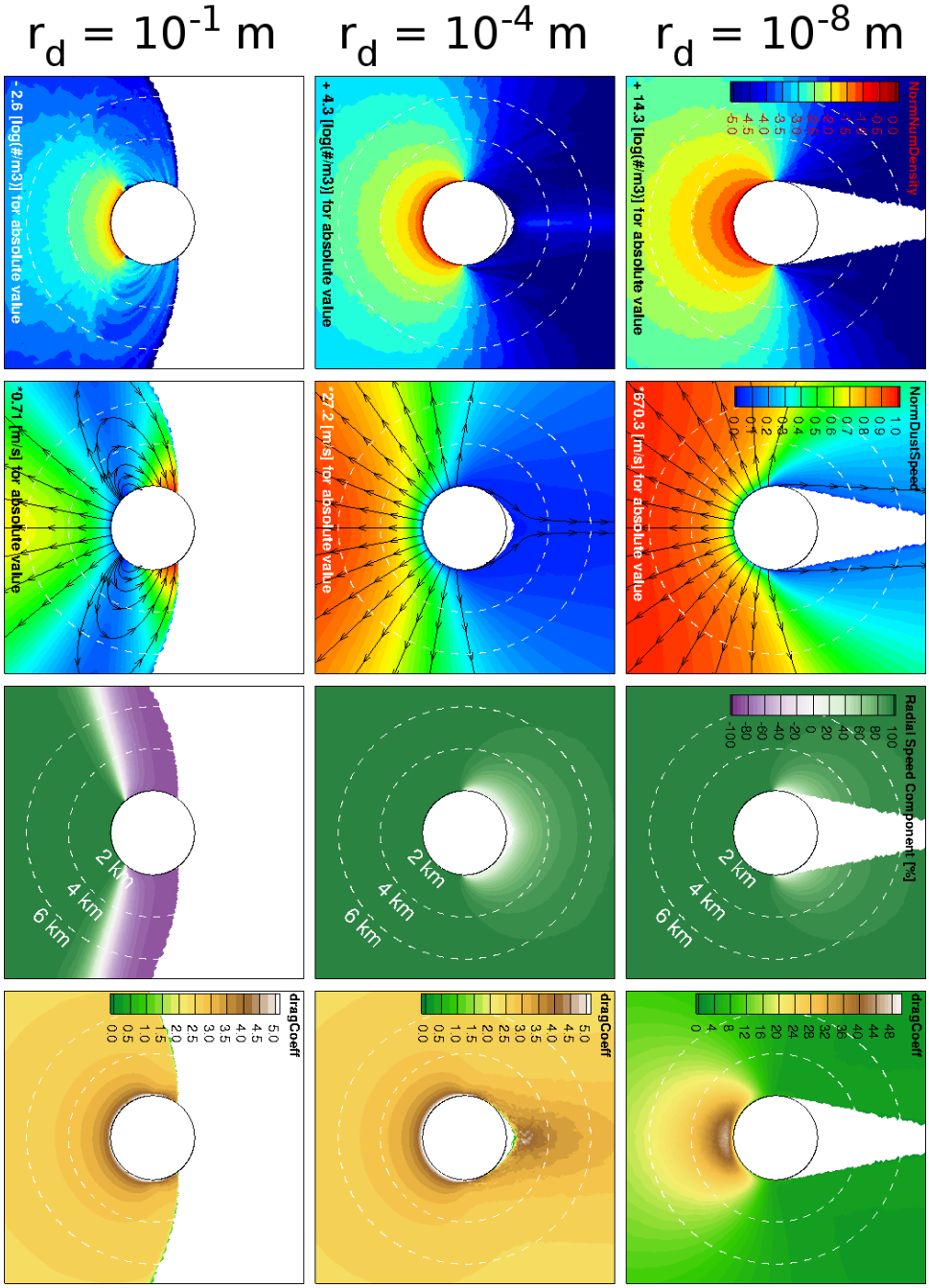

Figure 47: View of a slices through the 3D dust results for the insolation driven cases with global production rate of 200 kg s^{-1} for three different dust sizes from 10^{-8} m (top row) to 10^{-1} m (bottom row). The left three panels show the local dust density on a logarithmic scale and normalises for easier comparison. The second three panels from the left show dust speed. The second three panels from the right show the radial fraction of the dust speed and the three right models show the drag coefficient.

6.2.2 *Dust results*

As with the uniform emission cases we have run our dust model on the three purely-insolation-driven cases. Figure 47 gives an overview of the 3D results for three dust sizes for the 200 kg s^{-1} gas flow field showing a slice through the 3D flow solution at $x = 0$ m. The Sun comes from the bottom of the slice and we are viewing the coma with a phase angle of 90°. Therefore the terminator is a horizontal line in the centre of the sphere. The rows from top to bottom show the three dust sizes: 10 nm, 0.1 mm, and 10 cm. The dust number density is in the first column, the dust speed in the second column, the radial component of the dust speed in the third column, and the the drag coefficient in the fourth column. Overlain on the dust speed field are stream traces that originate every 10° from the sub-solar point outwards towards the terminator and follow the velocity field assuming a particle with negligible mass. Blank areas contain no dust particles. The number density plots show very different behaviour for these three dust sizes. For the smallest size the results look similar to that of the purely-insolation-driven gas result except for a part of the simulation domain on the night side that does not contain any dust particles because gravity and the gas drag are not strong enough to bring the particles all the way to the anti sub-solar point. This is also reflected in the stream traces. The dust particles reach terminal speeds on the day side fairly soon compared to the other two shown cases. The flow is radial to a high degree and hardly altered beyond the gas flow in this respect. For the sub millimetre particles the number density shows that dust particles flow all the way to the anti sub-solar point but there is no large scale redeposition of particles on the night side because the radiality of the flow does not turn negative. This is illustrated with all stream traces pointing outwards. For the largest particle size the situation is very different. A large part of the simulation domain is void of particles because they either escape (close to the sub-solar point) or are redeposited not far beyond the terminator. This can be seen very well in the stream traces. It also becomes apparent that on parts of the day side, particles are no longer lifted but rather deposited.

Often when performing dust dynamics it is assumed that the drag coefficient is equal to two, as e.g. in Fink and Rubin, (2012). The last column of Figure 47 shows that this is in some cases a bad approximation especially for small particles, where the drag coefficient can be very large. Even for the larger size we see deviations from a constant drag coefficient in particular close to the surface.

A new phenomena in the dust dynamics compared to the uniform emission cases is that we now have the possibility of particles

strongly affected by gravity and that may be redeposited on the surface. There are two reasons for this. Firstly acceleration and the non-uniform emission lead to a decline in the number density much stronger than $1/r^2$. Because gravity scales with $1/r^2$ it becomes the dominant force further out in the coma. Secondly the non-uniform emission of gas resulting in lateral flow (only minor lateral flow is sufficient) provides the dust with lateral motion. Stronger lateral motion leads particles to enter less dense areas of gas resulting in turn for the relative strength of gravity to increase. To understand this better we will come back to the concept of different dust dynamics regimes illustrated in Figure 25. We will have a look at the maximum dust speed as a function of gas production rate and dust size.

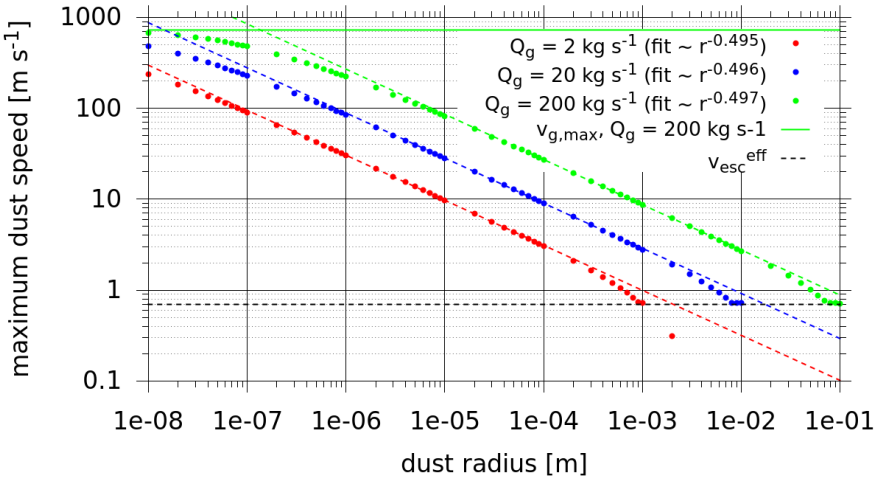

Figure 48: The maximum dust speed for each dust size (dots) and for the three different production rates of the purely-insolation-driven models are shown. The dashed lines are fits to the model values. Furthermore, the max gas speed of 200 km s^{-1} model and the escape velocity is plotted.

Figure 48 contains all important information about dust dynamics. First let us reiterate the expected behaviour of the maximum dust speed, v_d, as a function of the gas production rate, Q_g, and the dust size, r_d. Assuming the gas speed to be much larger than the dust speed and neglecting gravity Equation 22 can be reduced to

$$v_d \sim \sqrt{\frac{Q_g}{r_d}} \quad . \tag{40}$$

The fits to the dust speeds in the centre of the dust size range shows that this behaviour is reproduced. On the low and high end of the dust size range there are deviations to this behaviour. The reason is that in these size ranges one of our assumptions is no longer valid. What happens with very small dust sizes, in particular for the

highest gas production rate? When the dust size is smaller than 1 µm in the 200 kg s^{-1} flow field case the curve starts to deviate from the $r_d^{-1/2}$ behaviour and starts converging towards the maximum gas speed. When the dust speed becomes of the order of the gas speed the corresponding assumption is clearly no longer valid and the behaviour changes. Especially because the dust speed cannot exceed the gas speed. When the dust is small enough it behaves very similar to the gas, in a regime one might call the dust-gas-regime.

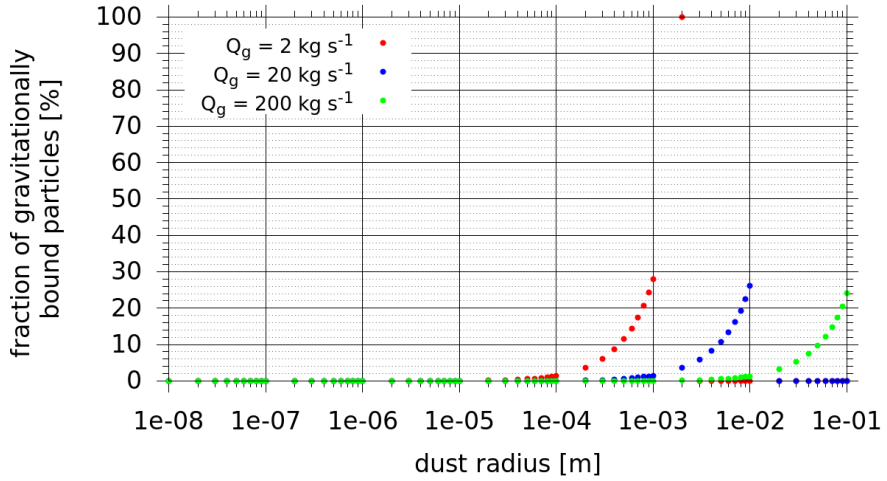

Figure 49: The fraction of gravitationally bound particles (particles that leave the surface but don't reach the outlet surface but rather redeposit on the nucleus surface) of each dust size is shown for the three purely-insolation-driven emission models.

When particles are very large, the assumption of neglecting gravity breaks down. The dynamics of these dust particles are significantly affected by gravity to the point that they no longer escape the gravity field and redeposit on the surface. The maximum dust speed will be less than the estimated value of Equation 40 due to the influence of gravity. At the point where dust particles are still lifted but gravitationally bound the maximum dust speed will be the escape velocity or less upon impact on the surface. This can be seen as the maximum dust speed curve hitting that threshold and remaining there for a small size range before the dust speed drops to zero when no particles are lifted anymore. As our simulation domain is not infinitely large, the escape velocity (we call it the effective escape velocity) reached here is smaller than the actual one and corresponds to a particle falling from a distance of 10 km onto the nucleus with no initial radial velocity at the 10 km boundary.

Besides the scaling of the dust speeds with $v_d \sim r_d^{-1/2}$, Figure 48 also shows that that maximum dust speeds scale as expected with $v_d \sim \sqrt{Q_g}$. Again this approximation is only valid in the regime where

both of our assumptions leading to the approximation in Equation 40 are valid.

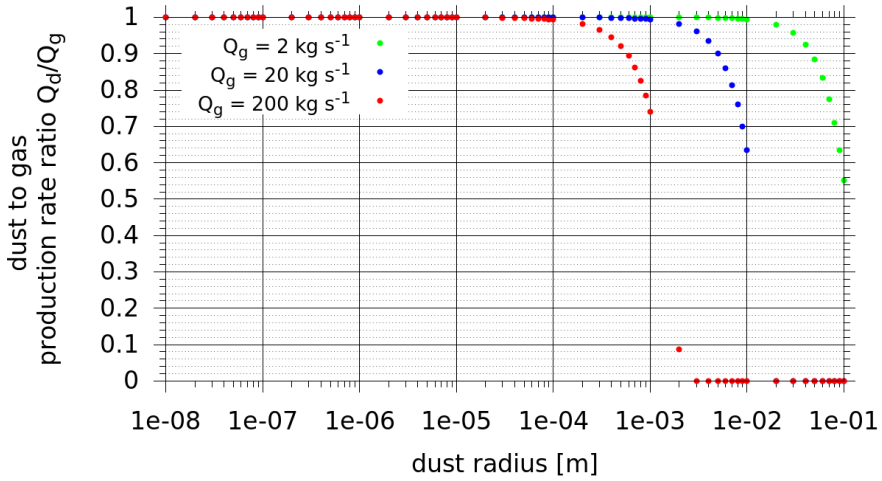

Figure 50: The dust to gas production rate ratio of each dust size is shown for the three purely-insolation-driven emission models under the assumption that each dust size starts with an initial dust to gas production rate ratio of unity at the surface.

The presence of gravity as a non-negligible force has consequences on the dust/gas coma composition. First of all the fraction of particles that are lifted is size dependent. Figure 49 shows this fraction as a function of the particle size and gas production rate. The transition from all particles being lifted to no particles being lifted covers only one order of magnitude in dust size, which is quite narrow. Depending on the initial surface dust size distribution this can dramatically alter the dust size distribution in the coma. This also manifest itself in the dust to gas production rate ratio as shown in Figure 50, which is almost the inverse of Figure 49. We assume at the surface a dust to gas production rate ratio of unity for each size bin. We will discuss in Chapter 9 how the actual dust to gas ratio is determined. Figure 50 corresponds to the actual dust to gas production rate ratio. Let us assume a coma with 2 kg s^{-1} gas production rate that is dominated by 1.5 mm sized particles. Half of these particles will not escape because they are either not lifted in the first place or redeposited on the surface. A dust to gas ratio in the coma of unity would thus require double that on the surface.

Observationally we usually deal with brightness or column densities. Gravitationally bound particles manifest primarily on the night side column density as a function of distance. Figure 51 shows the night side integrated column density for different dust sizes. As the dust particles flow around the comet from the day to the night side the column density increases with distance because particle need time to reach the night side while partially moving radially outwards.

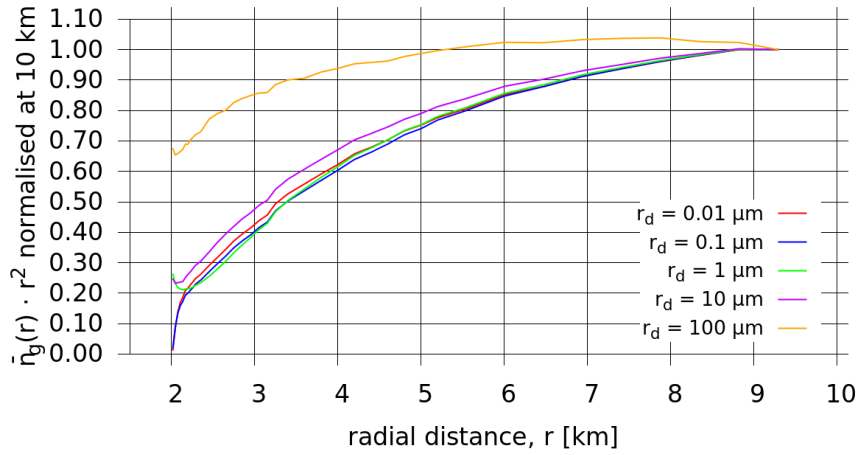

Figure 51: The average dust number density on the night side of the comet (phase angles larger than 90°) for different dust sizes of the 2 kg s^{-1} purely-insolation-driven model is shown as a function of radial distance to the nucleus centre.

This inertia of particles to move to the night side is larger for small particle resulting in lower values in the integrated column density. When particles fall back to the surface they reach a maximum altitude where the dust column will be maximal and beyond which the column density drops again. This can be seen nicely in the profile of the 100 µm particles.

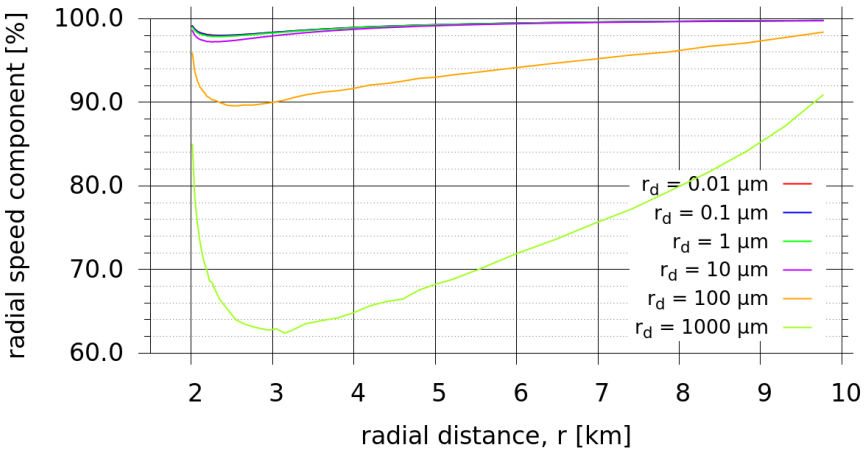

Figure 52: The average radial speed fraction of the dust velocity for different dust sizes of the 2 kg s^{-1} purely-insolation-driven model is shown as a function of radial distance to the nucleus centre.

We have already seen that the dust flow can become very lateral. This point is emphasised in Figure 52. For large particles the average radial component can become quite small, especially compared to anything we have seen until now in our gas results. Conversely the

smaller the dust the more radial it is.

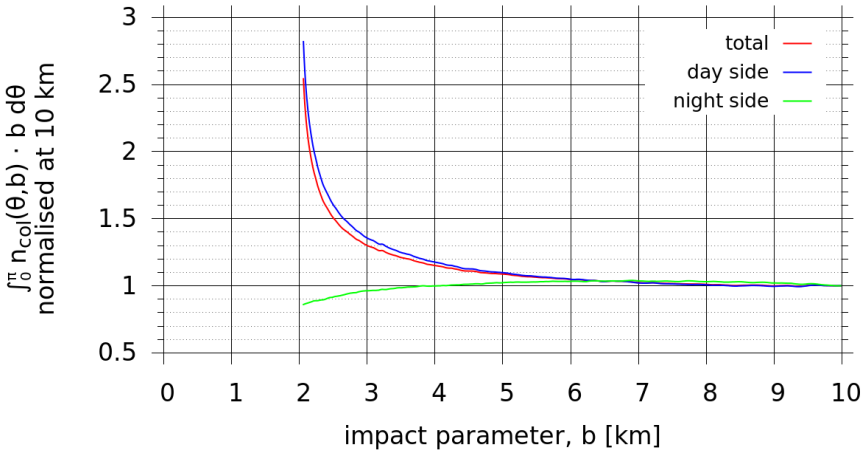

Figure 53: The azimutally integrated dust column density multiplied with the impact parameter for dust particles with $r_d = 100$ µm of the 2 kg s^{-1} purely-insolation-driven model is shown as a function of the impact parameter. The full angular integration (red) and the partial integration of the day (blue) and night (green) side are all normalised to unity at 10 km.

Finally let us look at the difference between day and night side behaviour of the azimuthally integrated dust column density. Figure 53 is an example of this for 100 µm particles in a 2 kg s^{-1} gas production rate coma. We can see that the column density on the day side drops as usual retaining a slightly falling slope even for large impact parameters. On the other hand the night side exhibits a rising slope. This behaviour has also been observed in OSIRIS images and is subject to a more detailed study in Gerig, Marschall, and Thomas, (2017).

7

SIMPLE MODELS FOR 67P/CG

Having understood some of the important processes for spherical cases we can now add complexity by replacing the spherical shape with the actual shape model of comet CG to study the effect of the irregular shape on the gas and dust flows. We will keep the discussion in this chapter to a minimum as much has already been mentioned in Chapter 6 and applies equally in the complex shape cases. We will thus attempt to highlight the similarities and differences to the spherical cases.

In Chapter 9 we will be discussing cases where parts of the surface are inert and others exhibit enhanced gas emission. We call this «inhomogeneous outgassing». We will examine here the degree to which this inhomogeneous outgassing distribution can be pushed without it being detected by Rosetta instruments in cases we call the «measles comet».

7.1 UNIFORM EMISSION

Again we start with the artificial case of a nucleus that is uniformly outgassing. The column density map (integration along the z-axis) in Figure 54 highlights nicely the effect of the complex shape of comet CG. The global production rate in this case is 40 kg s^{-1}. Even though we have equal production rate per unit area over the entire surface the density distribution is highly non-spherical. At a given impact parameter from the centre of the nucleus we find a large variation in the column density - a direct result of the large variation in local number density. Emission from the «Neck» regions is naturally enhanced due to the concave shape because of converging flows.

Another breaking of the spherical symmetry can be observed when azimuthally integrating the gas column density as a function of the impact parameter, b. We perform this for different viewing geometries as shown in Figure 55 along the primary Cartesian axes. In contrast to the spherical symmetric uniformly outgassing comet, where irrespectively of the viewing geometry these profiles are identical, they now differ substantially. The profiles are drawn only when the nucleus is not part of the integral and thus they begin at different impact parameters because the projected radius differs for different viewing geometries. The absolute values cover a relative range of $\sim$ 30% and are actually sorted by the degree of non-sphericallity

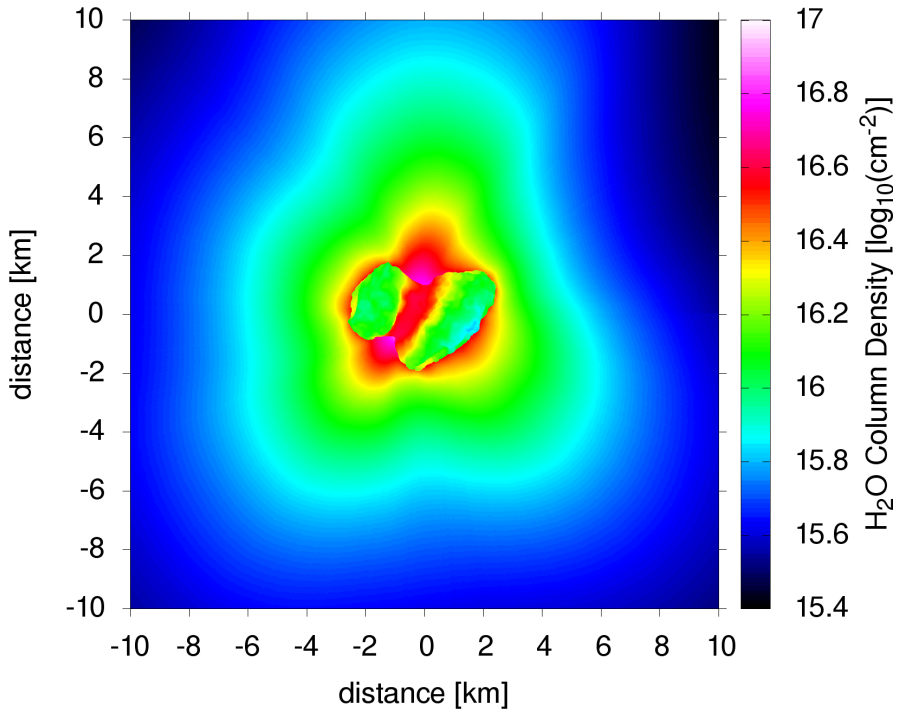

Figure 54: Gas column density of the 40 kg s^{-1} uniform emission model integrated along the z-axis.

of the projected nucleus and incidentally the projected size of the nucleus. For the integration along the x-axis the nucleus looks the most spherical and also has the smallest projected size. This leads to the least enhancements due to converging flows and thus to lower number and column densities which is reflected in the profile. The enhancement in number density in the viewing geometry of the integration along the z-axis (as seen in Figure 54) was just discussed and leads to higher values of the azimuthally integrated column densities.

The dust simulation also shows some interesting effects that can be attributed to the shape and topographic variations of the surface. Figure 56 shows the dust column density of the uniformly outgassing comet with a production rate of 40 kg s^{-1} for two different viewing geometries. Compared to the spherical case clear dust filaments can be seen and the dust coma does not look uniform at all. This is caused by the topographic irregularities of the surface. Strong changes in the orientation of facets with respect to each other - on the small but also the larger scale - give rise to the irregular distribution of the dust within the coma. Furthermore, this figure illustrates possible deceptions caused by the viewing geometry. The left panel shows what seem to be two jets originating in the northern and southern part of the «Neck». We should briefly specify what we mean by jet. We consider something a jet if it originates from a rather confined space

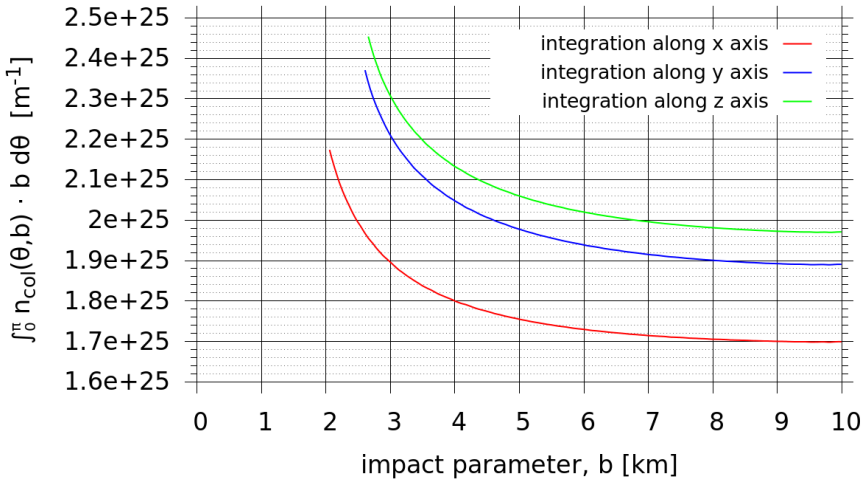

Figure 55: Azimuthally integrated gas column density multiplied with the impact parameter as a function of the impact parameter for integration directions along the three primary axes of 40 kg s^{-1} uniform emission model.

on the surface. But as the right panel with a head on view of the comet shows, this is just a result of the viewing geometry. The dust structures originating in the concave parts of the «Neck» are to some part collimated but extend laterally for what would rather be called a «fan» structure than a «jet». In the correct viewing geometry these fans appear like jets even though they are clearly not. This needs to be kept in mind when viewing column density images as e.g. images of OSIRIS. Additionally, this figure also shows that dust filaments can be curved, caused purely by the interaction with the gas flow and not gravity. It cannot be gravity in theses cases as the shown plots are dominated by smaller fast moving particles as we have used a power law size distribution with a power law index of 3.

7.2 PURELY-INSOLATION-DRIVEN EMISSION

We will not go into too much detail regarding purely-insolation-driven emission from the complex shape as we will be discussing various cases in Chapter 9. But we do want to discuss results supporting our extrapolation of the results beyond the extent of our simulation domain of 10 km from the nucleus centre.

When using the 3D gas number density distribution within the first 10 km of the nucleus centre to extract the flow properties (in particular the gas number density) and compare them with the in-situ measurements performed on-board Rosetta by especially ROSINA/COPS we need to extrapolate our results to the spacecraft position when it is farther away than 10 km from the nucleus centre. We have already discussed our extrapolation in Section 4.9 but not shown that the con-

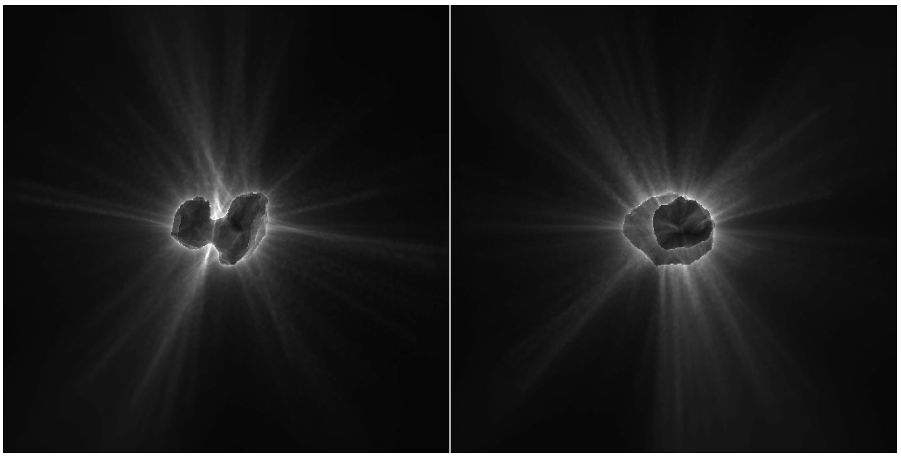

Figure 56: Artificial dust brightness images for two different integration directions with the spacecraft at a sub-spacecraft latitude of 0° and a sub-spacecraft longitude of 60° (left panel) and 150° (right panel). The scaling is arbitrary but the same for both panels.

ditions are fulfilled in the cases we consider. We can only use the method described in Equation 27 to extrapolate or results to larger cometocentric distances than our simulation domain covers for a free radial outflow. We therefore need to confirm that the the gas speed does not increase beyond 10 km and that the direction of the flow is radially outwards. To validate this we have performed a test with purely-insolation-driven emission in a grid with a radius of 20 km. The Sun is at a sub-solar latitude of 42.5° and a sub-solar longitude of 140°. Figure 57 shows the significant results of this simulation. We have found that the radial component of the gas velocity on the day side is larger than 99% of the total gas velocity at the 10 km boundary. Even on the night side, the radial component accounts for 95% of the direction of the gas flow. This is illustrated in the right-hand panel of Figure 57. We can thus safely consider the flow to be radial. Furthermore, the increase in the gas speed beyond 10 km from the nucleus centre as seen in the left-hand panel of Figure 57 is only minor. This is in line with the findings of Tenishev, Combi, and Davidsson, (2008) (see Fig. 7 in Tenishev, Combi, and Davidsson, (2008)), and the subsequent comparison with the ROSINA/COPS data in Chapter 9 also shows that a constant radial outflow beyond 10 km is a fair assumption to make for a comet such as CG.

7.3 INHOMOGENEITY OF EMISSION

Before we compare our simulations to actual data of Rosetta there is a more theoretical question as to the spacial distribution of the activity that we can address. The most basic assumption of activity - be it gas or dust - that one can imagine is that the emission is proportional to

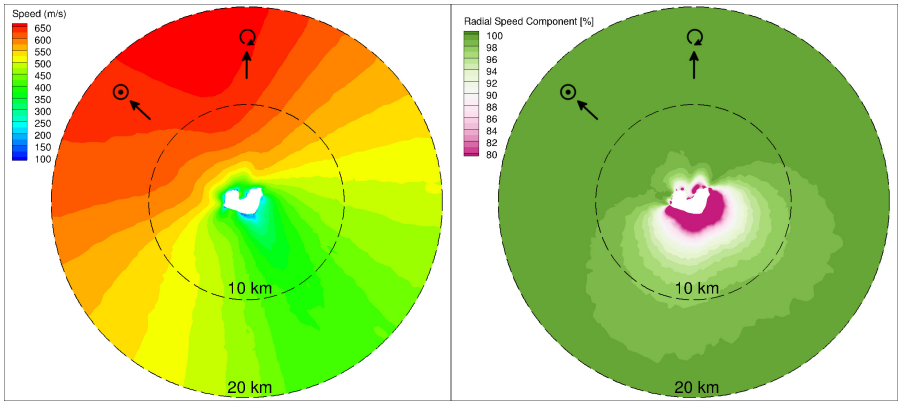

Figure 57: Both panels show a cut through the 20 km simulation domain though the long axis of the comet of the purely-insolation-driven outgassing case with an absorbing surface where the Sun is at a sub-solar latitude of 42.5° and sub-solar longitude of 140°. The left panel shows the total gas speed and the right panel the radial component of the gas velocity relative to the total speed.

the energy input to the surface. We have mentioned in Section 4.6 that the eaf of comet CG is around 1% if the entire surface had the equal potential of outgassing (i.e. equal ice content of the surface over the entire surface). If effectively only ~ 1% of the surface is outgassing this begs the question as to how this activity is distributed spatially. We have therefore set up three scenarios with different spacial outgassing distributions to test whether the different outgassing patterns can be detected by ROSINA/COPS and OSIRIS. The three cases are:

- 100% of the surface has the potential of outgassing with an eaf of 1.2%.
- 10% of the surface has the potential of outgassing and the rest is completely inert. The active areas have an eaf of 12%.
- 1.2% of the surface has the potential of outgassing and the rest is completely inert. The active areas have an eaf of 100% (i.e. are pure ice surfaces).

In the two cases where we set large portions of the surface to be inert the active facets are chosen randomly. The gas production rate on the surface of the three cases is shown in Figure 58. The Sun is at a sub-solar latitude of 42.5°, sub-solar longitude of 140°, and the comet a heliocentric distance of 3.4 AU. Due to the emission pattern we refer to this kind of emission as a «measles distribution». The global gas production rates of the three cases are identical due to the way the cases were set up.

Figure 59 shows a cut through the 3D gas solutions. In the gas number density it is very difficult to see any qualitative difference

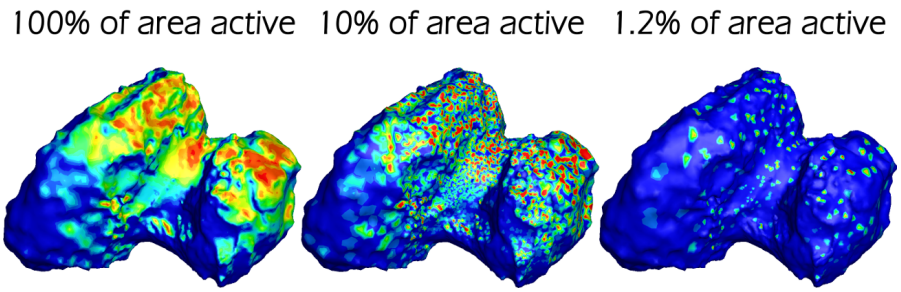

Figure 58: Gas production rate setups of the three measles cases with the 100% active surface on the left, the 10% active surface in the middle, and 1.2% active surface on the right. The Sun is at a sub-solar latitude of 42.5°, sub-solar longitude of 140°.

between the three models. It is only very close to the surface and only for the case where 1.2% of the surface area is active where we see the effect of the smaller active areas. The two cases of 100% and 10% active surface area are qualitatively almost identical in number density and speed. For the model with 1.2% of the active surface the gas speed can be significantly larger. This is especially pronounced in the area above the Ash region.

The important question is whether this kind of inhomogeneities can be detected by instruments on board Rosetta. To study what ROSINA/COPS would measure we have defined an artificial trajectory for Rosetta, where for different constant cometocentric distances we «fly» though the gas coma. We start the spacecraft trajectory at a phase angle of 0° then subsequently increasing the phase angle by 5°. At each phase angle we take multiple measurements ensuring approximately equal spacing between measurements. The points at which we take measurements along the trajectory is illustrated in Figure 60. This way we ensure a relative equal spatial sampling of the coma at different cometocentric distances. The local number densities along the trajectory are shown in Figure 61 for a cometocentric distance of 3 km and 10 km. We only focus on phase angles up to 90° because we are interested in the variations in close vicinity to the source of the emission. The local number densities of the 10% and 100% active surface models are very similar for both cometocentric distances. But the 1.2% active area model shows much more variation on the 3 km trajectory. Theses differences are smoothed out substantially by the time the gas reaches 10 km and the model becomes more similar to the other two. This is of course what we would expect. The variations due to the inhomogeneous emission will influence the measured number densities when we are close to the surface. As we move away these differences are smoothed out. To get a quantitative analysis of how close the different models are to each other we have calculated the PPMCC taking the 100% active

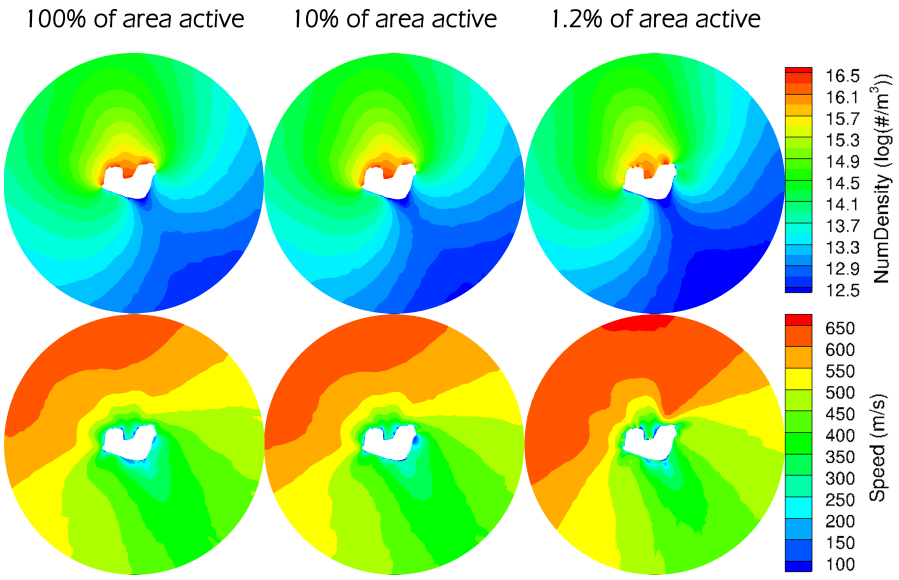

Figure 59: Slices ($y = 0$) through the gas results of the three measles cases. The 100% active surface is shown in the two panels on the left, the 10% active surface is shown in the two middle panels, and 1.2% active surface is shown in the two right panels. The top row shows the local gas number density on a logarithmic scale and the bottom row shows the local gas speed. The Sun is at a sub-solar latitude of 42.5°, sub-solar longitude of 140°

surface as the reference model and then comparing the other two to it. Figure 62 shows the results as a function of cometocentric distance. The 10% active area model with a PPMCC > 0.9975 correlates almost perfectly with the 100% active area model and can thus be considered indistinguishable for ROSINA/COPS at all cometocentric distances. Even the 1% active surface model has a very high correlation to the 100% active area model, though the correlation is slightly lower. As seen qualitatively in Figure 61 the correlation increases with cometocentric distance because the structures are washed out. There would be a chance for ROSINA/COPS to recognise a 1% active surface comet on a 3 km orbit. Unfortunately we never observed the comet in such close proximity for a longer time span. Though a closer inspection of the data from the close fly-bys and the end of mission descent could constrain such emission. But at this point it must be concluded that ROSINA/COPS has no way of distinguishing even the most extreme randomly inhomogeneous emission as assumed here. Inhomogeneous outgassing can only be detected if the outgassing direction is altered as in models we will show in Chapter 9. Because of the random distribution of sources the main direction of the emission is conserved.

The situation changes when looking at the dust. Figure 63 shows artificial OSIRIS images for the three models for the same viewing

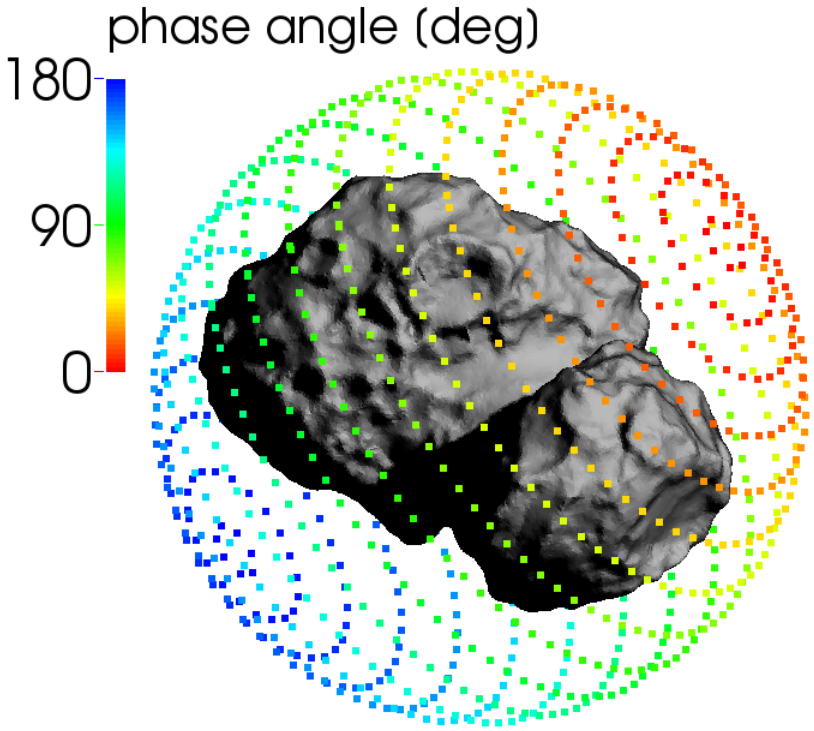

Figure 60: Artificial orbit as described in the text in relation to the shape of the nucleus. We only show the phase angle steps ever 10° instead of the ever 5° we have run to make the figure more easily readable.

geometry. We assume here a power law dust size distribution with a power law index of 3. The dust dynamics is much more sensitive to the initial conditions of the gas and we therefore see differences even in the 10% active surface model when comparing it to the 100% active surface model. The contrast is even stronger in the case of only 1% active surface area. Hence even if ROSINA/COPS is not sensitive to this kind of variation in the emission distribution the OSIRIS data should be able resolve this. This illustrates the power of multi-instrument constraints.

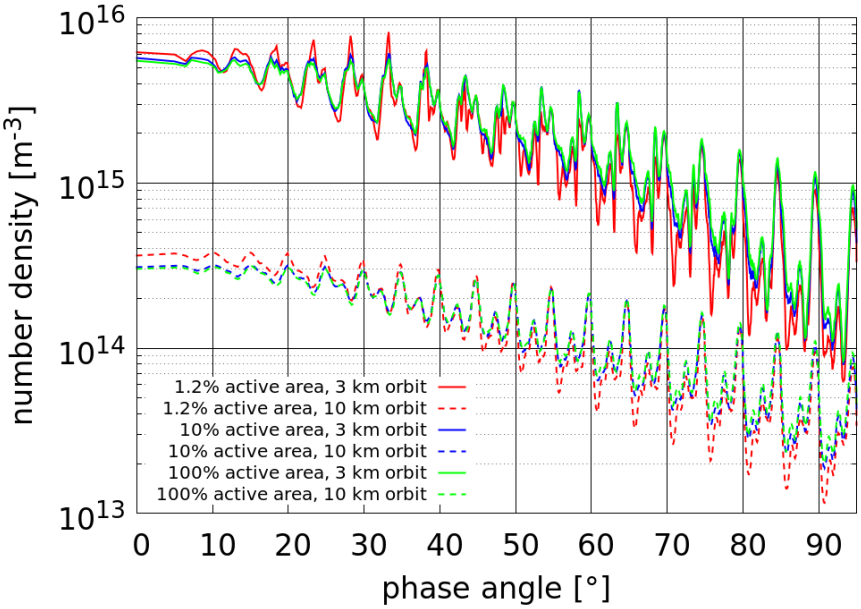

Figure 61: Number density for the three measles cases along the artificial orbit of Figure 60 up to a phase angle of 90°. Only the results of the orbits at a cometocentric of 3 km (solid lines) and at 10 km (dashed lines) are shown here.

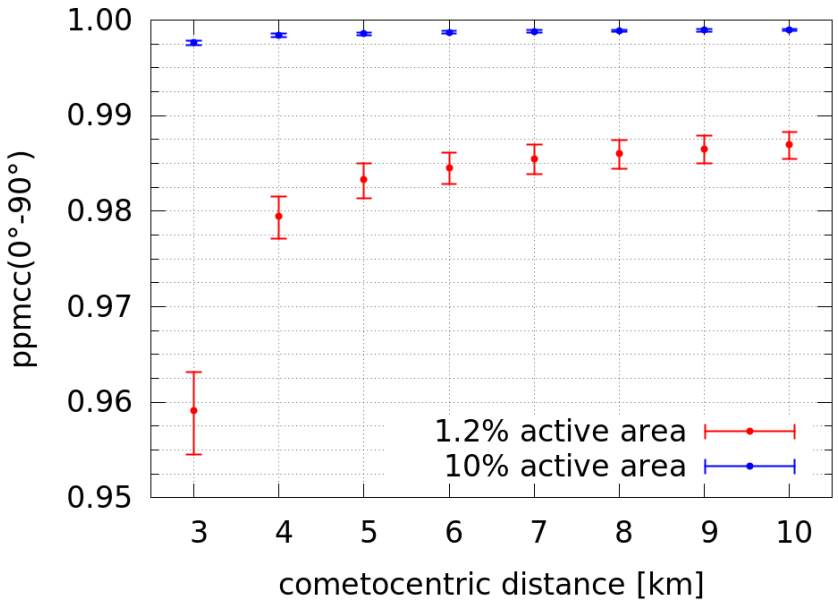

Figure 62: The PPMCC as a function of the cometocentric distance for the 10% (blue) and 1.2% (red) active surface models with respect to the 100% active surface model is shown. The error bars correspond to a 2σ confidence interval.

Figure 63: Artificial dust brightness images for two three measles cases are shown. The scaling of the images is arbitrary but the same for the three panels.

Part IV

UNDERSTANDING ROSETTA GAS AND DUST MEASUREMENTS

8

ROSINA DATA

This chapter is intended to give a brief overview of the data set of ROSINA that was available to us and which we want to understand through the application of our models in Chapter 9. Because the data from OSIRIS is much more straight forward we will be discuss it directly in Section 9.3 when we describe our simulation results.

We have introduced the ROSINA instrument suite and especially the COPS instrument in Section 3.1. First we will discuss the data and how it relates to illumination, orbital, and viewing geometries. Then we will present the illumination geometries that are the basis of all our models in this work. ROSINA/COPS/NG measures gas pressure/gas number density at the location of the spacecraft. To understand the COPS measurements better we will first take look at a short time span to understand daily variations before taking a more macroscopic view and the longer scale trends. The time span covered with this work is August 2014 to January 2015 and the main orbital parameters can be seen in Figure 12. Hansen et al., (2016) have used ROSINA, MIRO, and VIRTIS to make estimates for the gas production rate over the course of the entire mission. For the beginning of the period we consider they estimate a global H_2O production rate of ~ 1 kg s^{-1}.

First we look at the small time span from 2014-09-20 to 2014-09-25 thus covering roughly nine cometary days. The COPS number density, heliocentric distance, phase angle, sub-solar latitude and longitude, and sub-spacecraft latitude are displayed for this period in Figure 64. In all these plots data within 30 minutes of thruster firings for attitude changes, and other orbital manoeuvres of the spacecraft have been omitted because they can influence the measurements strongly. The main point to be made here is that the number density varies strongly on the very short time scale ($<$ 1 comet day (cd)). In fact we see a repeating daily pattern of two peaks and two minima insync with the sub-solar longitude (red line in the bottom most panel). This pattern of two maxima per cd can be seen during most of the mission and as we will see is mainly due to the bi-lobate shape of the comet. Often this pattern in the data is referred to as the diurnal variation of the density. But the word «diurnal»can be a bit misleading because the variations seen in the data are not due to the change of illumination condition of a specific point or area on the surface (the diurnal cycle on the surface) that the spacecraft follows. Rather the spacecraft is almost stationary with respect

to the comet and the observed variation is due to the rotation of the comet beneath the spacecraft. We are therefore observing the change in density due to the varying surface at a constant local time on the surface. As time progresses we are sampling different parts of the surface. The variation is thus strictly speaking more of positional/cometographical nature than a temporal one. As the variation is usually presented as a function of time we do remain to using a temporal term but prefer the term «daily variation»and reserve the term of «diurnal variations»for variations at a specific location in the course of a day. The daily variation can thus be assigned to specific areas on the comet. Having said that the more pronounced peak in the considered time span usually corresponds to the spacecraft observing the «Neck»from the Anuket side of Hapi. The lower maximum corresponds to the spacecraft being on the Aker side of Hapi. The minimum after the higher peak corresponds to when the spacecraft is observing the comet from the Imhotep side, and the second minimum corresponds to a spacecraft location above the Hatmehit side.

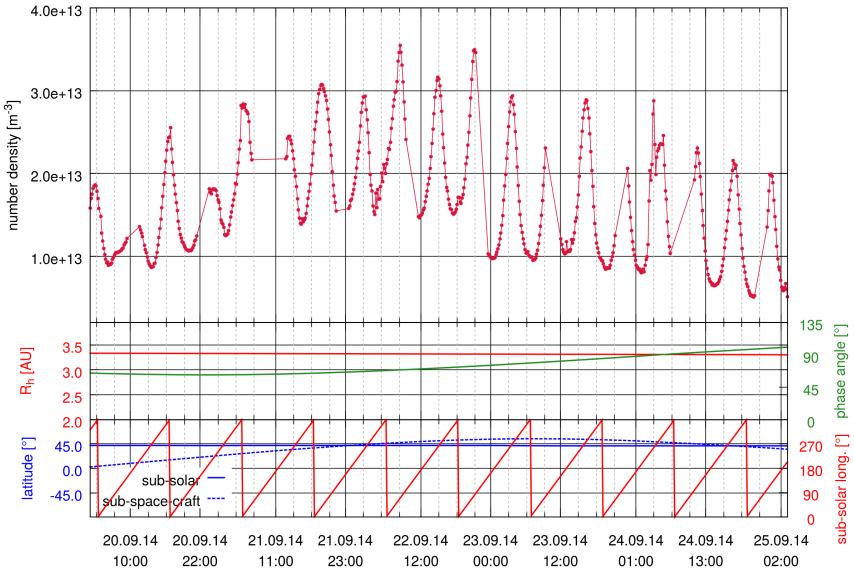

Figure 64: In-situ gas number density (top panel) are shown for the time period of 2014-09-20 to 2014-09-25 as measured by ROSINA/ COPS. The centre panel shows the heliocentric distance and the phase angle. The bottom panel shows the sub-solar and sub-spacecraft latitude as well as the sub-solar longitude.

Figure 65 gives a macroscopic overview of the entire period considered in this work. The data points seem to be smeared but this is simply due to the daily variations due to the rotation as seen in before in Figure 64. The long term trends in the data give first insights as to the activity on the comet. First, the density is clearly increasing as the distance to the comet decreases. Secondly the

density seems to vary more strongly with the sub-spacecraft latitude compared to the phases angle. This can be clearly seen in areas where the phase angle is constant over a longer period. In those cases the density increases as the sub-spacecraft latitude increases. This indicates that the emission might be more inhomogeneously distributed on the surface because with emission proportional to the incident light, the number density would be mainly influenced by the phase angle. The increase of density with sub-spacecraft latitude hints at enhanced emission from the north polar region, something we will return to in Chapter 9. This change in magnitude due to the sub-spacecraft latitude was also identified by Bieler et al., (2015). The shown time span is too short though to see effects from the heliocentric distance and sub-solar latitude. These effects can be seen when looking at the data on very large time scales. Of course the decrease in heliocentric distance will manifest itself with an increase in gas densities. The sub-solar longitude impacts the structure of the daily variation.

The illumination geometries considered in this work have been selected for the time when the comet was between heliocentric distances of 3.4 and 2.8 AU pre-perihelion. The Sun was at northern sub-solar latitudes between 42° and 34°. We ran two sets of models at the edges of this range fixing the heliocentric distance/sub-solar latitude pair to (3.4 AU, 42°) and (2.8 AU, 34°). Steady state gas solutions at each of these heliocentric distance/sub-solar latitude were run for sub-solar longitudes of 0°, 50°, 90°, 140°, 180°, 230°, 270°, and 320°. This corresponds to a time resolution of ~ 1.5 h. We presumed the models to be valid for variations in the heliocentric distance of ±10 %, and changes in the the Sun direction within a 4 ° cone. This results in the two sets of models overlapping and the results roughly covering the time span from beginning of August 2014 to the end of January 2015. Usually though we have applied the model to time spans smaller than the one resulting with the mentioned criteria here.

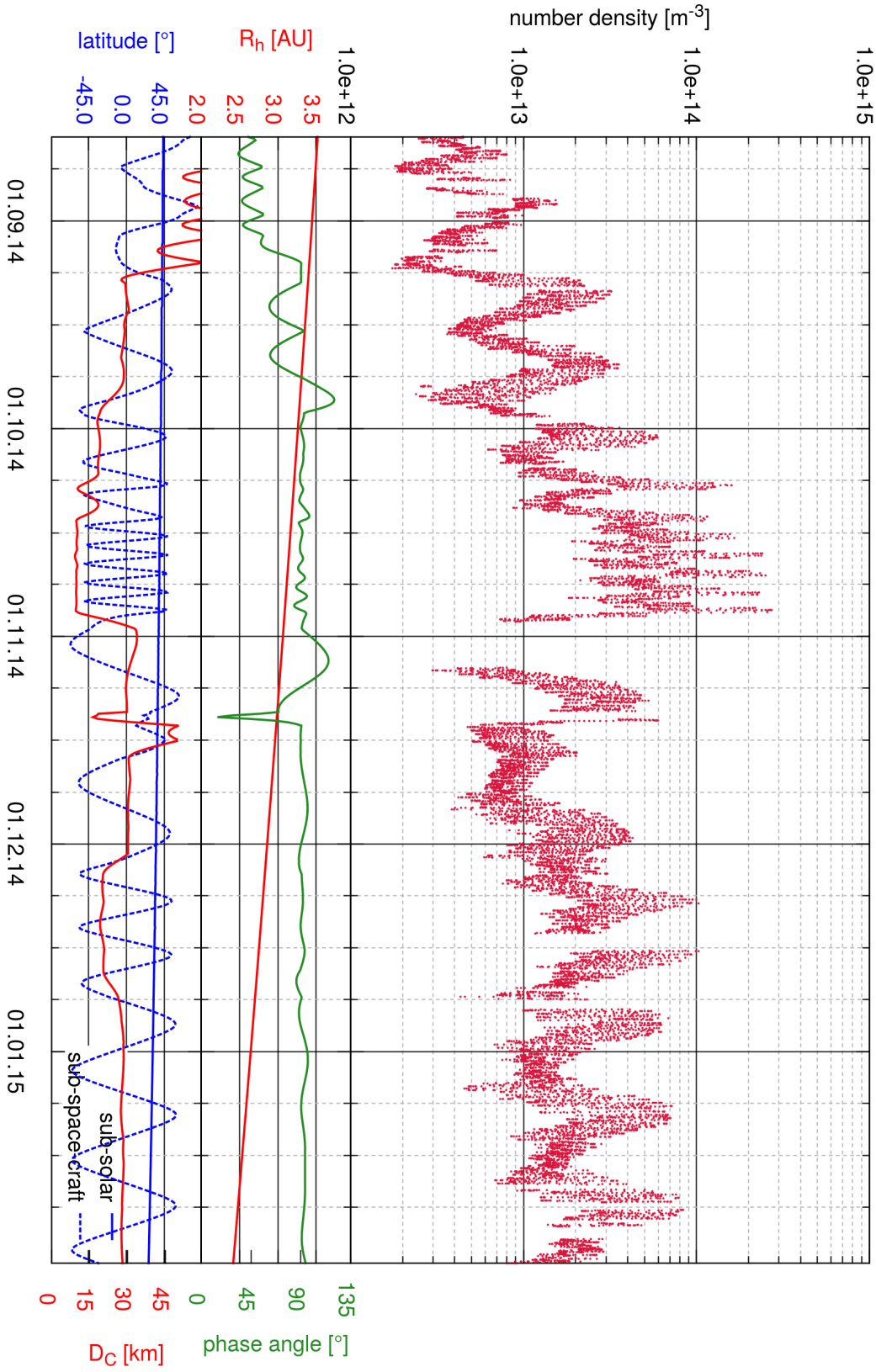

Figure 65: In-situ gas number density (top panel) are shown for the time period of 2014-08-20 to 2015-01-31 as measured by ROSINA/ COPS. The bottom two panels are as described in Figure 64

9 SIMULATION RESULTS

This chapter brings together in one document our results presented in Marschall et al., (2016) and Marschall et al., (2017). We thus follow closely the discussion presented in these two papers.

It is our aim to understand the constraints that Rosetta data, especially ROSINA and OSIRIS, put on the distribution of the gas and dust emission on the surface of comet CG. Furthermore we have built tools into our modelling pipeline to include in the near future constraining data from other instruments such as, MIRO, VIRTIS, and GIADA. What can we learn about gas and dust activity, the distribution within the comae, or the dust size distribution and dust to gas ratio? These are just some of the questions driving this scientific effort.

In a first step we shall attempt to start with the most simple model of purely-insolation-driven outgassing and to what extent this kind of emission can explain the data gathered by ROSINA and OSIRIS in August to October 2014. We will see that a more elaborate emission distribution (regional inhomogeneous emission model) is needed to reproduce the most important features of the data, something the purely-insolation-driven model fails to do. In our search for a model explaining the data we will also examining how certain boundary conditions - such as reflecting vs. absorbing surfaces - impact the results. In a second step we turn our attention to examine whether emission can be correlated with surface morphology which, in our opinion, is an essential step towards understanding the emission processes occurring at the surface.

9.1 GAS SIMULATIONS AND COMPARISON WITH ROSINA/COPS

9.1.1 *Purely-insolation-driven vs. inhomogeneous emission*

Or initial approach is to study two different emission distributions. The first is purely-insolation-driven emission. As described in Section 4.6, we scale the inlet number density by a fixed factor in order to meet the observational constraint and to match the variation in the ROSINA/COPS measurements as the spacecraft moves and the comet rotates. The global scaling constant is typically of the order of 0.01 (i.e. 1% of the sublimation from a pure water ice surface at the given albedo) and was applied to all facets to provide a number density at the spacecraft that roughly agrees with the ROSINA/COPS

data. This model can also be viewed as a globally uniform dust-ice surface layer. Such models are sometimes also referred to as uniform models as their scaling is globally uniform (i.e. constant).

The second inlet condition we use is what we refer to as regional inhomogeneous outgassing. In contrast to the first case, the scaling constant is now regionally defined and not globally defined. Each region has an independent scaling. But within each region the outgassing is still insolation driven. In this sense inhomogeneous outgassing is simply a regionally varying enhancement superimposed on the purely-insolation-driven outgassing case.

For each of the models we will additionally vary the type of cometary surface. One will be a purely absorbing surface and the other a purely diffusely reflecting surface, where gas back flux is thermally equilibrated and re-emitted. The absorbing surface results are presented in Section 9.1.1.1 and those of the reflecting surface in Section 9.1.1.2. The viewing geometries are defined by the respective OSIRIS images for which we extracted the necessary geometrical parameters from the SPICE kernels (Acton, 1996) provided by the European Space Operations Centre (ESOC)

All our PDSC^{++} simulations were run successfully and resulted in the mcs to mfp ratio being less than 1 at most points in the simulation domain and therefore acceptable according to recognised criteria (Bird, 1994). Only for some cells in the inhomogeneous outgassing cases did mcs/mfp exceed 1 but was well below 10 which we still consider to be reliable.

9.1.1.1 *Absorbing surface models*

We discuss first our results of the models with an absorbing surface. Any gas back flux to the cometary surface will be absorbed fully. The solid lines in Figure 66 show the global production rates for a full revolution of the nucleus with the purely-insolation-driven (red) and inhomogeneous (blue) outgassing condition. For the insolation driven model, the global eaf of 0.014 (corresponds to 1.4% active are) has been applied to all surface facets. In contrast to the purely-insolation-driven case, the scaling constant for the inhomogeneous model is regionally defined. The fluxes have been adjusted such that we have higher activity (10% eaf) in the Hapi and Hathor regions. This was identified as a location of a potentially strong source region by Lin et al., (2015) for the dust and Bieler et al., (2015) for the gas. Low emission (0.5% eaf) has been set in the Hatmehit, Maftet, Nut, and parts of Ma'at and Bastet regions on the «Head» of the nucleus. Similarly very low values have been assigned to the Imhotep region, and parts of Khepry, Aten, and Ash on the «Body». Medium

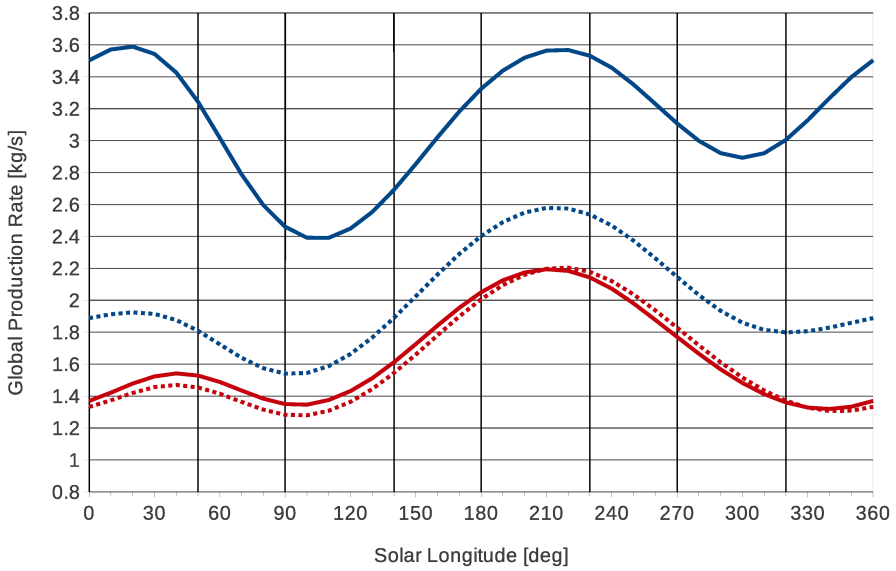

Figure 66: Global gas production rates Q_g in kg s^{-1} for the insolation-driven (red) and inhomogeneous (blue) outgassing models with an absorbing (solid) and reflecting (dashed) surface and the eight solar geometries run that we modelled (vertical lines).

activity (1.5% eaf) has been assigned to the rest of the comet. Within these regions the outgassing is still driven by the incidence power of the solar light. The injected gas production rates, Q_g, for these two models range from 1.32 to 2.19 kg s^{-1} ($3.94 \cdot 10^{26}$ to $6.56 \cdot 10^{26}$ molecules s^{-1}) for the insolation-driven and 2.39 to 3.59 kg s^{-1} ($7.15 \cdot 10^{26}$ to $1.07 \cdot 10^{25}$ molecules s^{-1}) for the inhomogeneous case. The modulation in the production rate seen in Figure 66 is a direct consequence of the shape of the nucleus and thus the variation and orientation in the cross section of the comet exposed to the Sun. For the inhomogeneous models, the differences in active areas modify the modulation further. We have tried other distributions for the inhomogeneous model, but we show here only the best result obtained so far. The criterion for setting the eaf, influencing strongly the gas production rate, was to match the ROSINA/COPS data as well as possible while modulating the outgassing within the morphological regions of Thomas et al., (2015a) and Thomas et al., (2015b) only.

Figure 67 shows the comparison of the number density measured insitu by ROSINA/COPS and the two models. The drawn line in our simulated data is solely for the purpose of readability and is not an interpolation of the model results. This must be kept in mind especially when we have no simulated data point at the centre of a peak, and thus the line will not show the actual maximum for when our simulation had been run at the exact geometry of the peak. We estimate the error to be ±10% which corresponds to our estimate for

the accuracy of our DSMC code and the applied extrapolation from the 10 km simulation domain boundary. We have also truncated the time axis to show only the main time intervals of interest that are, to the greatest extent, representative of the entire time interval. We have omitted data with high southern spacecraft latitudes where CO_2 was a significant contributor (Hässig et al., 2015) to the measured COPS density.

When we compare the data with the models, we can see that for time span A, both models fit fairly well. The purely-insolation-driven model fits the data almost perfectly, while the inhomogeneous model is slightly inferior with the density systematically overestimated in this case. In time span B we can see that the purely-insolation-driven model underestimates the magnitude of the rotational oscillation with the minima very weak. This is an indication of low activity in the larger surroundings of Hatmehit. This is confirmed by our inhomogeneous model that is in fact reproducing this feature to higher accuracy.
Time span C shows three interesting trends in the purely-insolation-driven model. First, this model is systematically underestimating the number density by around 30 %. Second, while we should see two peaks per cometary day, we only see one. Third, the peaks seem to be shifted by approximately minus one hour. The inhomogeneous model shows improvement in the magnitude of the measurements but primarily in the shape of the curve that now exhibits the expected frequency over the nucleus rotation. There is no improvement in the shift already observed in the purely-insolation-driven case. The shift in time span C is most likely linked to the viewing geometry. The spacecraft is just in the process of crossing over the north pole, so this shift may be an indication that the structure of the more active polar region that we have placed in the Hapi region is not yet defined accurately enough. Thermal inertia or topographic re-radiation effects may also be relevant. This will need to be resolved in further studies.

The purely-insolation-driven model exhibits two trends in time span D. As in time span C the model underestimates the actual data, but especially in this case the minima are low. In the ROSINA/COPS data we see two peaks during one revolution of the nucleus with one being more pronounced than the other. The more pronounced peak corresponds to geometries where Hathor is illuminated and additionally in the field of view. In our purely-insolation-driven model, what should be the higher peak is the lower one and vice versa. This inversion of peaks is an indicator of stronger activity from the Hathor region. The inhomogeneous model shows that this is indeed a viable explanation because the relative size of the maxima

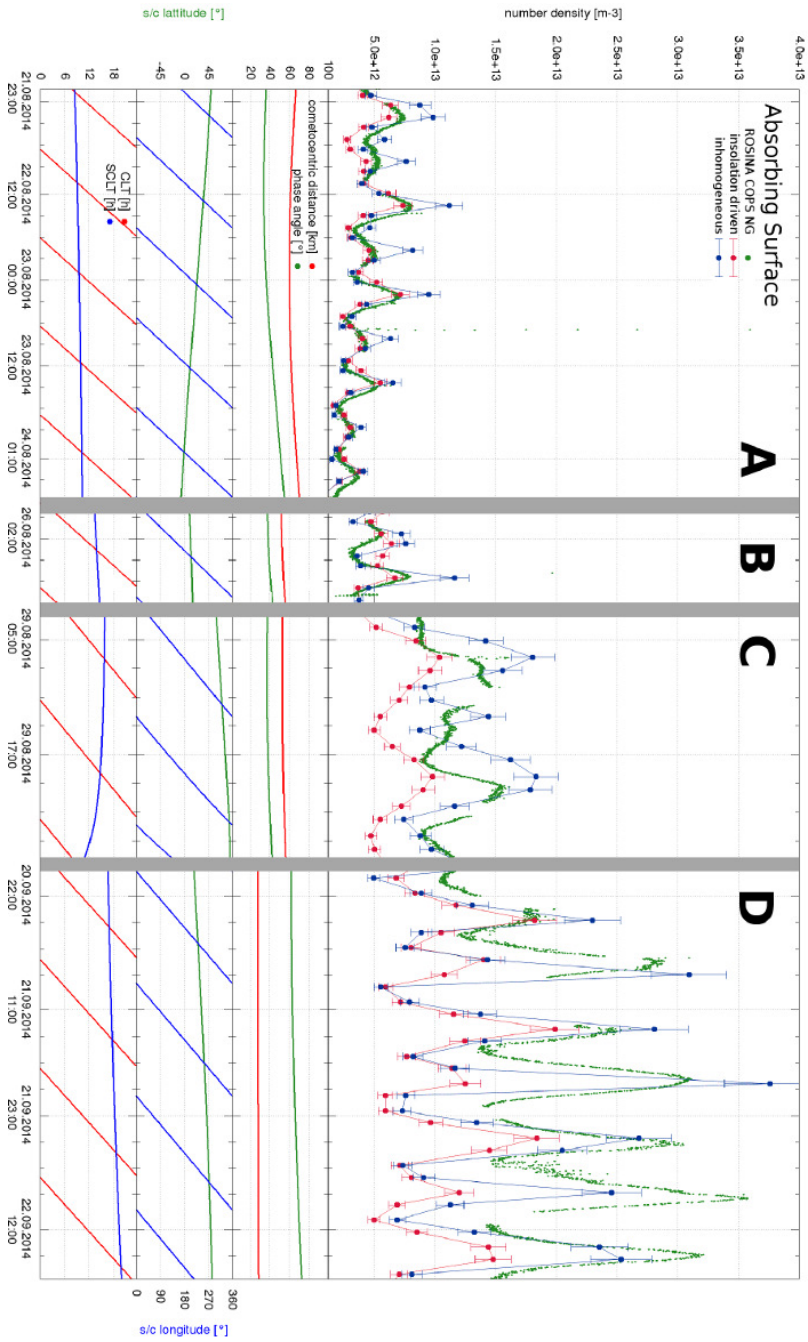

Figure 67: Top panel: Comparison of the COPS NG data with our insolation driven and inhomogeneous outgassing models with an absorbing nucleus surface over the period from the 2014-08-21 to 2014-09-23. Middle up panel: The cometocentric distance and the phase angle of the observations shown on the same scale showing how the spacecraft approached the comet towards time span D but at relatively high phase. Middle lower panel: The sub-spacecraft latitude (left axis) and longitude (right axis) showing how in time span D the spacecraft was moving towards the northern pole which is located in the Hapi region. Bottom panel: The sub-spacecraft local time (SCLT) and the local time at the position of the zero longitude meridian (CLT) which runs through Imhotep.

is correctly modelled in the inhomogeneous case.

In general, there is significant improvement in the fit to the data with the inhomogeneous model and especially the form of the curve matches the actual data considerably better.

Neither the purely-insolation-driven nor the inhomogeneous models fit the minima in time span D. This presumably indicates night-side outgassing, which our thermal model cannot fit under the assumptions adopted. Bieler et al., (2015) use an ad hoc assumption of $7-10\,\%$ of activity relative to the maximum flux coming from the night side and shadowed areas.

The downside of these models with an absorbing surface is that strictly speaking, we lose self consistency with Equation 15 since we are effectively reducing the total flux from the inlet surface. Increased back flux is observed in geometries where either the Hathor or the Seth regions are not illuminated, which shows that a part of the absorbed flux is due to the concave shape of the nucleus around the Hapi region and not to immediate reabsorption after sublimation on the original facet. When both Seth and Hathor are illuminated simultaneously, the outgassing prevents additional back flux from other regions and thus we see lower back flux rates in these illumination geometries. Because of the fairly high back flux in the inhomogeneous case, it becomes clear that the production rate must be higher than in the purely-insolation-driven case to produce equivalent number densities at the spacecraft position, especially for the absorbing case. This is the main motivation for us to investigate whether reflecting surfaces can achieve similar results and at the same time fulfil self-consistency.

9.1.1.2 *Reflecting surface models*

As we have just seen in section 9.1.1.1, high gas fluxes back to the cometary surface warrant the examination of reflecting surfaces. With a reflecting surface, none of the gas is absorbed when hitting the cometary surface so that compared to the absorbing surface models with identical setups, all subliming gas reaches the outlet surface. To reproduce the insitu measurements of the gas number density by ROSINA/COPS less gas needs to be produced, and consequently the eaf is lower compared to the absorbing surface models. In the purely-insolation-driven case, we used an eaf of 0.012 compared to 0.014 with the absorbing surface. Unilluminated surfaces were set to a nominal temperature of 100 K. We can see in Figure 68 the effect of the reflecting surface in a cut through the coma comparing the purely-insolation-driven absorbing case with the diffusely reflecting case. The Sun is at 230° sub-solar longitude so that Hathor is in

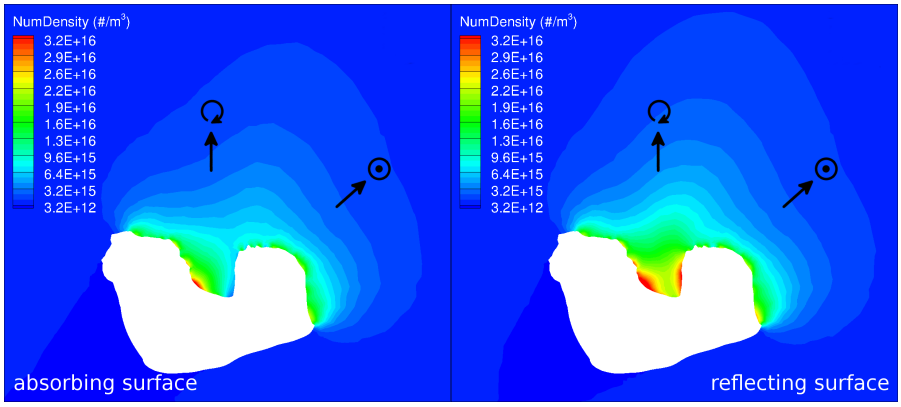

Figure 68: Cuts though the long axis of the comet with a solar longitude of 230° comparing the gas number density [m^{-3}] of the insolation driven model with an absorbing surface (left column) and a diffuse reflecting surface (right column).

shadow and Seth is illuminated. One can see that the coma is distorted in the absorbing case. The reflecting surface means we see higher densities at the surface and the coma being pushed back towards the «Body» lobe.

The comparison of the ROSINA/COPS data with the purely-insolation-driven outgassing model with a diffusely reflecting surface shows that in some regions such as time spans A and C, the results are similar to the purely-insolation-driven outgassing model with an absorbing surface. Figure 69 shows that the purely-insolation-driven reflecting surface models exhibit similar problems to those with the absorbing surface (e.g. the missing peaks in time span C). As in section 9.1.1.1, we have adopted the approach of improving the shortcomings of the purely-insolation-driven model by introducing regional heterogeneity. Figure 70 shows the eaf for the purely-insolation-driven model, the inhomogeneous model and the cliffs + Hapi model (which will be introduced later). The figure illustrates how the fluxes were adjusted such that we have higher activity in the Hapi (0.075) and Hathor (0.04) regions. Low emission (0.005) were set in the Hatmehit, Maftet, Nut, and parts of Ma'at and Bastet regions on the «Head» of the nucleus. Similarly very low values were assigned to the Imhotep region and parts of Khepry, Aten, and Ash on the «Body». Medium activity (0.0095) was assigned to the rest of the comet. Within these regions the outgassing is still purely-insolation-driven though the outgassing power varies regionally. Compared to the absorbing surface, the Hathor region's activity is weaker than the one in Hapi. The gas production rates Q_g for these two models range from 1.28 to 2.20 $kg\,s^{-1}$ ($3.82 \cdot 10^{26}$ to $6.59 \cdot 10^{26}$ molecules s^{-1}) for the purely-insolation-driven and 1.54 to 2.58 $kg\,s^{-1}$ ($4.61 \cdot 10^{26}$ to $7.71 \cdot 10^{26}$ molecules s^{-1}) for the

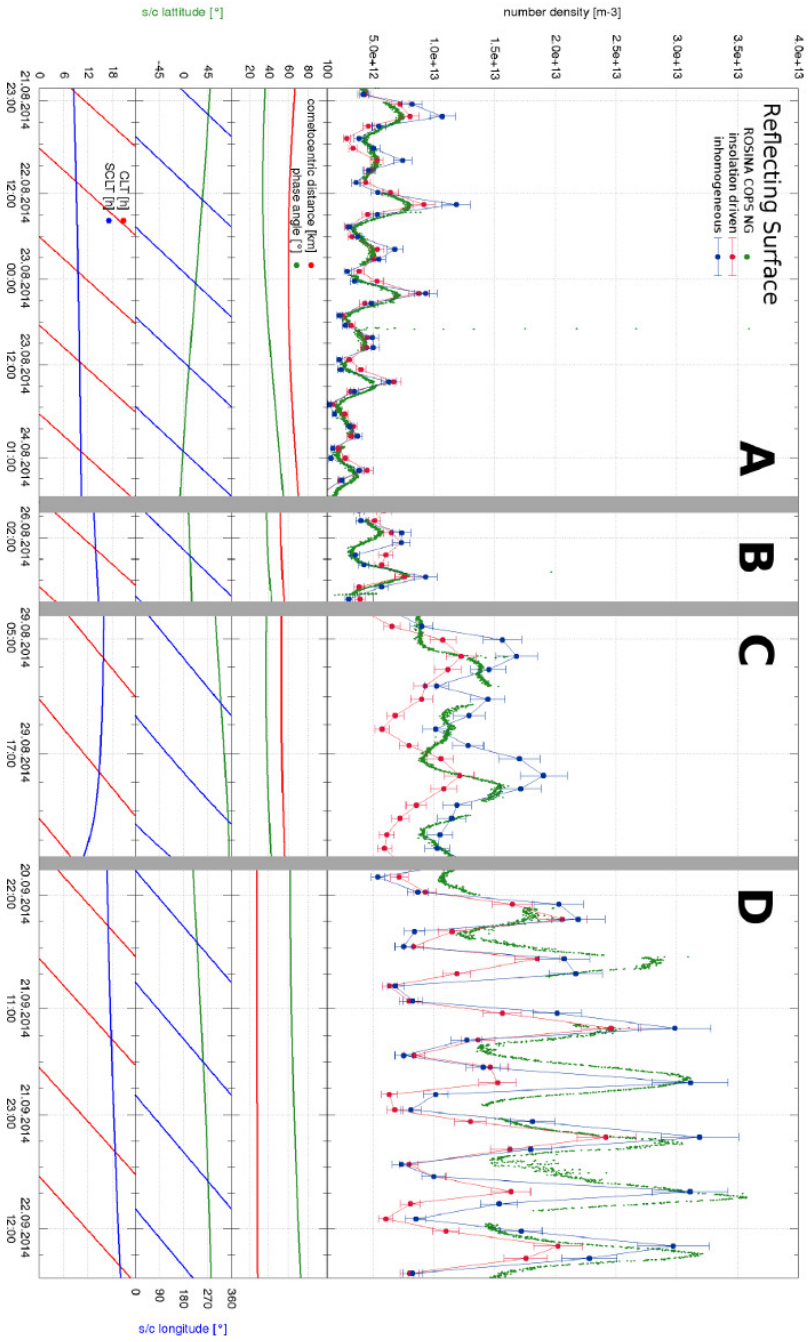

Figure 69: Top panel: Comparison of the COPS NG data with our purely-insolation-driven and inhomogeneous outgassing models with an absorbing and a diffusely reflecting nucleus surface over the period from the 2014-08-29 to 2014-09-23. Upper middle panel: The cometocentric distance and the phase angle of the observations shown on the same scale showing how the spacecraft approached the comet towards time span D but at relatively high phase. Middle lower panel: The sub-spacecraft latitude (left axis) and longitude (right axis) showing how in time span D the spacecraft was moving towards the northern pole, which is located in the Hapi region. Bottom panel: The sub-spacecraft local time (SCLT) and the local time at the position of the zero longitude meridian (CLT) that runs through Imhotep.

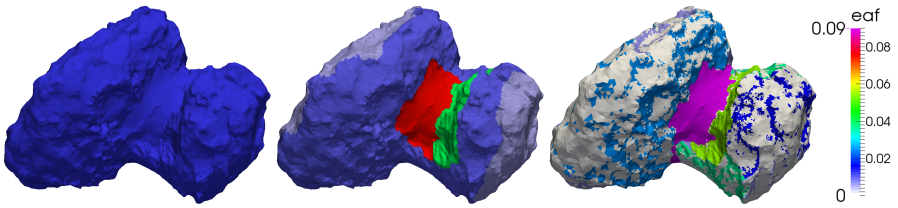

Figure 70: Regional effective active fraction on the comet as seen from a north polar view used for the purely-insolation-driven model (left), the inhomogeneous outgassing model (centre), and the cliffs + Hapi model (right, see Section 9.1.2). All of the shown models have a diffusely reflecting boundary condition.

inhomogeneous case over the entire revolution of the nucleus. The global production rates for the entire nucleus rotation can be seen in Figure 66. As with the absorbing surface, this inhomogeneous model improves the fit to the ROSINA/COPS data in all regions.

To summarise at this point: We ran purely-insolation-driven and regionally inhomogeneous outgassing models with absorbing and diffusely reflecting nucleus surface boundary conditions and compared the simulations with the in situ gas number density measurements of the COPS-Nude Gauge (NG). For both surface behaviours, we have seen that insolation driven outgassing does not reproduce the data to a satisfactory degree. The shape of the ROSINA/COPS curves in particular indicate the inadequacy of the model. Regionally inhomogeneous outgassing models have, both in the absorbing and the reflecting cases, improved the fit to the data and overcome most shortcomings of the purely-insolation-driven outgassing.

To place this on a more objective footing, we use the approach of Bieler et al., (2015) and use the PPMCC which shows that the inhomogeneous models (PPMCC $= 0.87$) are statistically better fits to the data than the purely-insolation-driven models (PPMCC $= 0.816/0.834$ for the absorbing/reflecting surface) and compare well to the values in Bieler et al., (2015). We must stress, though, that compared to Bieler et al., (2015), we do not need any post simulation correction of the simulation results to achieve these fits. Additionally, we do not consider any artificially introduced night-side activity, which leads to underestimating the number density over lower latitudes where CO_2 emission becomes relevant. The physical process of the CO_2 production, especially in the southern hemisphere, has not been tackled and understood yet so certainly warrants further study.

That we can achieve a good correlation with both the absorbing and reflecting surfaces shows that ROSINA/COPS alone cannot distinguish between these two types of surface properties. On the other hand,

line-of-sight instruments, such as MIRO or VIRTIS, should be able to see such a difference in surface reflectance, as can be suspected from Figure 68. We look at this in more detail in Section 9.2.

One further point in need of attention is that we have only looked at heterogeneities on a regional scale. The results shown can be seen as a hint of more local inhomogeneities than assumed in our models. The measured gas densities in viewing geometries that are at high northern latitudes, especially directly over the pole, seem to indicate this. Thus locally inhomogeneous models may need to be studied.

9.1.2 *Linking activity to topography*

A study by Vincent et al., 2016 proposed that the cometary dust jets in the northern hemisphere of comet CG arise mainly from rough cliff-like terrain. Using our 3D gas and dust dynamics coma model we have run simulations targeting the question whether areas with high gravitational slopes alone can account for both the ROSINA/COPS and the OSIRIS data obtained in the mid August to end October 2014 time frame, hence the identical time frame as discussed in Section 9.1.1. Linking gas and dust emission to morphology on the surface can help understand the mechanisms involved in cometary activity.
We have used our gravity model (Section 4.3) to separated the surface facets into two categories - one with gravitational slopes larger than 30° which we call «cliffs» and one with slopes less than 30° which we shall call «plains». Figure 71 shows the northern hemisphere of the shape model SHAP4S. The surface is coloured according to our cliff/plains criterion. We have chosen 30° as it is close to the angle of repose for granular material - the minimum angle of an inclined plane which causes an object to slide down the plane. This value is consistent with the range of 20°-30° found by Vincent et al., 2016.

We are adding three models the ones already discussed in Section 9.1.1. The setups of these three additional models focused on gravitational slopes can be summarised as follows:

1. **Plains-only model:** Only surface areas with gravitational slopes less than 30° are active with an eaf of 4.95%.

2. **Cliffs-only model:** Only surface areas with gravitational slopes larger than 30° are active with an eaf of 7.5%.

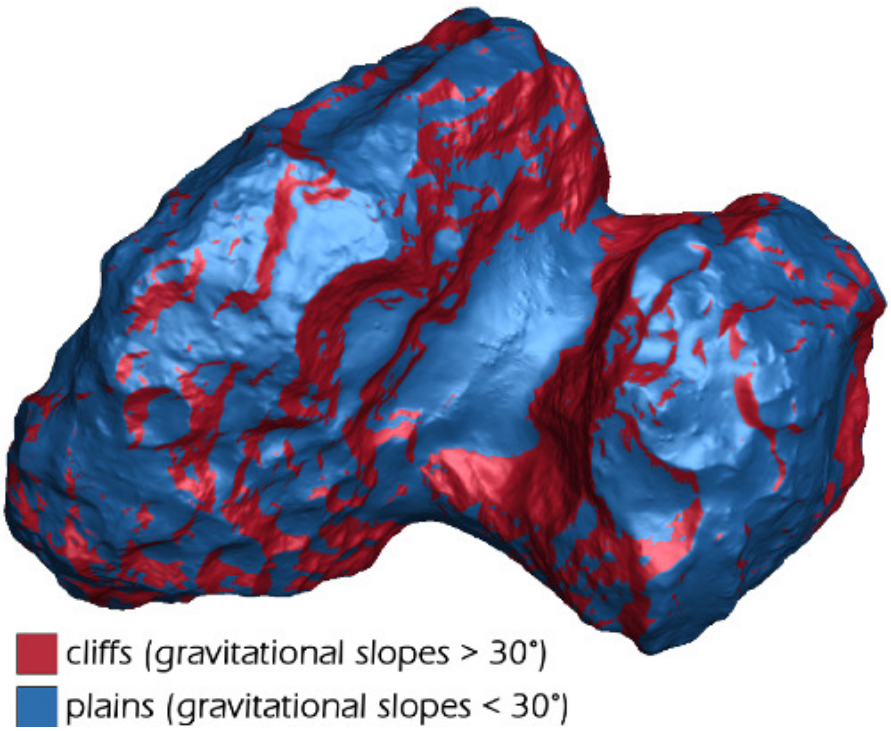

Figure 71: Shape model SHAP4S with surface coloured according to gravitational slopes: cliffs (gravitational slopes $> 30°$) in red and plains (gravitational slopes $< 30°$) in blue. This view shows the northern hemisphere.

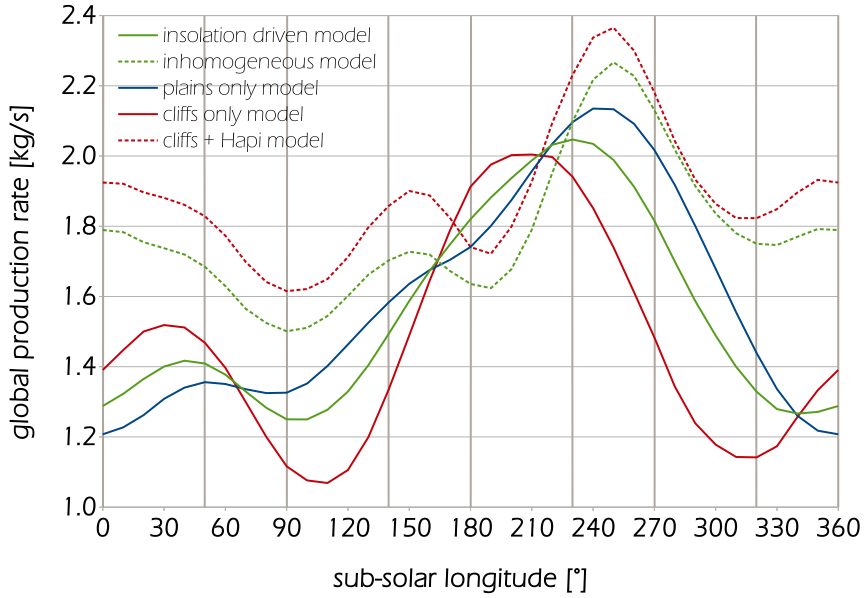

Figure 72: Global gas production rates Q_g in kg s^{-1} on 2014-09-09 for the different models as a function of the sub-solar longitude (vertical lines at 0°, 50°, 90°, 140°, 180°, 230°, 270°, 320° indicate the sub-solar longitudes that were run with our gas dynamics code). The Sun is at a sub-solar latitude of 42.5° and the comet is at a heliocentric distance of 3.4 AU pre-perihelion.

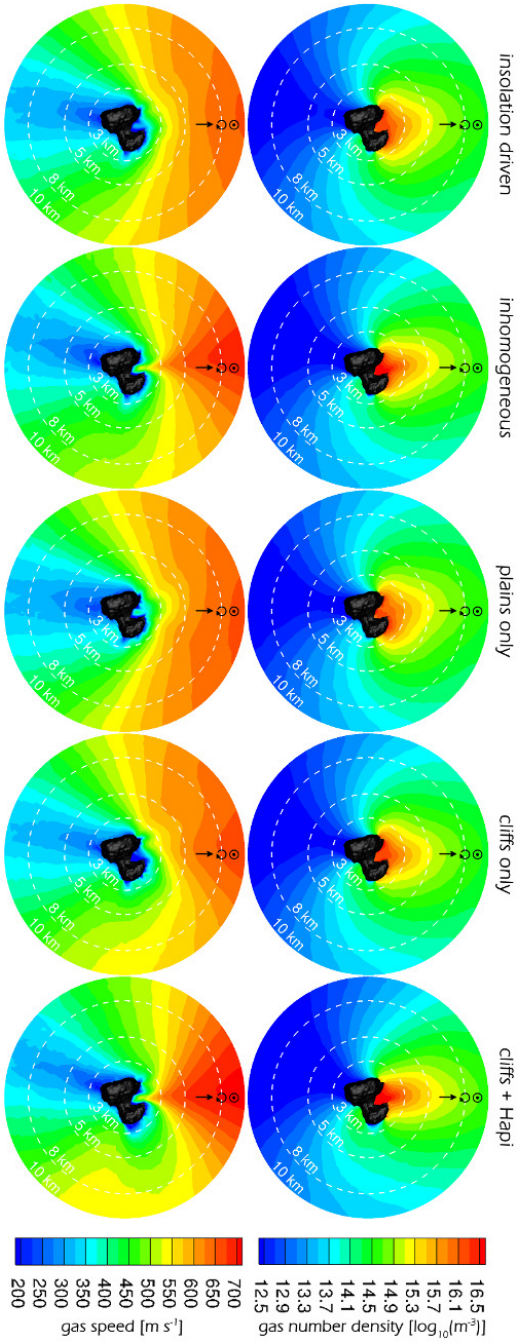

Figure 73: View of a slice through the 3D gas solutions for the sub-solar longitude of 140°. The shown plane is normal to the terminator plane. The direction of the Sun is in the shown plane, the rotation axis of the comet comes out of the plane but has the same projected direction as the Sun direction in this view. The top row shows the gas number density [$\log_{10}(\mathrm{m}^{-3})$] for the five models (columns). The bottom row shows the gas speeds [$\mathrm{m\ s}^{-1}$] for the five models (columns). The 3D shape of the comet is also displayed.

3. **Cliffs + Hapi model[1]:** Only surface areas with gravitational slopes larger than 30° are active. In addition Hapi (a region with a low gravitational slope) is added as an active area. Both Hapi and Hathor - a cliff area - have been assigned higher eaf. The following eaf (illustrated in Figure 70) have been used in this model:
   a) Hapi: 22.50%
   b) Hathor: 13.50%
   c) Cliffs in Anuket, and Bastet: 9.00%
   d) Cliffs in Ash, Babi, and Seth: 6.00%
   e) Cliffs in Hatmehit, and Ma'at: 3.75%
   f) remaining cliffs: 1.50%

Figure 72 shows the global gas production rate as a result of the illuminated hemisphere of the comet as a function of sub-solar longitude. The values were calculated for the 2014-09-09 when the comet was at a heliocentric distance of 3.4 AU and the Sun was at a sub-solar latitude of 42.5°. For the inhomogeneous and the cliffs + Hapi models, the eaf have been adapted to optimize the fits to the data. In the other three cases, a single effective active fraction has been used but again scaled to match to the best extent possible, the observed gas densities at Rosetta.

Figure 73 shows a view of a slice through the 3D gas solutions for a sub-solar longitude of 140° plotting gas number densities and speeds. The plane that is shown is normal to the terminator plane and contains the direction of the Sun. Looking at the gas number density we can observe that the direction of the coma is generally in the direction of the Sun but does vary depending on the model. In the cliffs + Hapi model the coma direction is skewed the strongest towards the nucleus' «Head» lobe. The inhomogeneous model on the other hand exhibits a coma with the largest bend towards the «Body» lobe of the nucleus. The plains-only and cliffs-only models mainly differ in the direction of the gas coma. When looking at the gas speeds we can see that the inhomogeneous and cliffs + Hapi models differ very strongly from the other three models. Due to their higher activity in the Hapi region these two models also produce higher gas speeds of over $700\,\mathrm{m\,s^{-1}}$. Furthermore, the high gas speeds are reached very close to the surface.

1 To complete the full set of models we have also made several simulations of regionally inhomogeneous outgassing using only plains (in contrast to the regionally inhomogeneous cliffs + Hapi model) but not found any good fit. This by itself does of course not rule out that there is a good solution with emissions only from plains, but we have not found any.

So how do these models compare to the data collected by ROSINA/COPS? Figure 74 shows the comparison of the insolation-driven and inhomogeneous models with the in situ measured number density by ROSINA/COPS over the period from the 2014-08-29 to 2014-09-22. This figure is an updated version of that shown in Section 9.1.1.2 because of the improved self shadowing algorithm compared to the one used in Marschall et al., (2016). Compared to Section 9.1.1 we see that the time shift in time span C is now resolved and we get a very high agreement of the inhomogeneous model with the data.

Figure 75 is an equivalent figure to the previous one but comparing the plains-only (red circles), cliffs-only (orange triangles), and cliffs + Hapi (green squares) outgassing models with the in situ measured number density by ROSINA/COPS. We can see that the plains-only model falls short especially in time spans B, C, and D where the daily structure is not reproduced at all. The cliffs-only model is an improvement with respect to reproducing the daily periodicity of the data. But we also see that this model falls short especially in time span E by not reproducing the correct relative peak height. The cliffs + Hapi model on the other hand reproduces the data substantially better. Not only the daily structure of the data is reproduced (seen especially in time spans B, and C) but also the relative height of the peaks (seen especially in time spans D, and E).

To get a more objective view on how well each of the models performs, we extend our initial statistical approach and apply two measures of the PPMCC. The first one considers the entire period from 2014-08-20 through to 2014-10-31 as a whole, and we call this the «total PPMCC». It does factor in daily variations but is mainly dominated by long term variations in the data. The second metric we have chosen should give an understanding of how well we match the daily variations. To do this we have calculated the PPMCC for all intervals where we have a full cometary day of data and then averaged over all days. We call this metric the «diurnal PPMCC». The results are presented in Figure 76. The error bars represent a 2σ (or 95%) confidence interval. We can see that our five models split into three groups. These are in ascending order of the goodness of fit:

1. **Worst fit:** The plains-only model is statistically inferior to all other models.

2. **Intermediate fit:** The purely-insolation-driven and cliffs-only models are statistically indistinguishable and fit the data better than the plains-only model. Hence the ROSINA/COPS data cannot differentiate between the two.

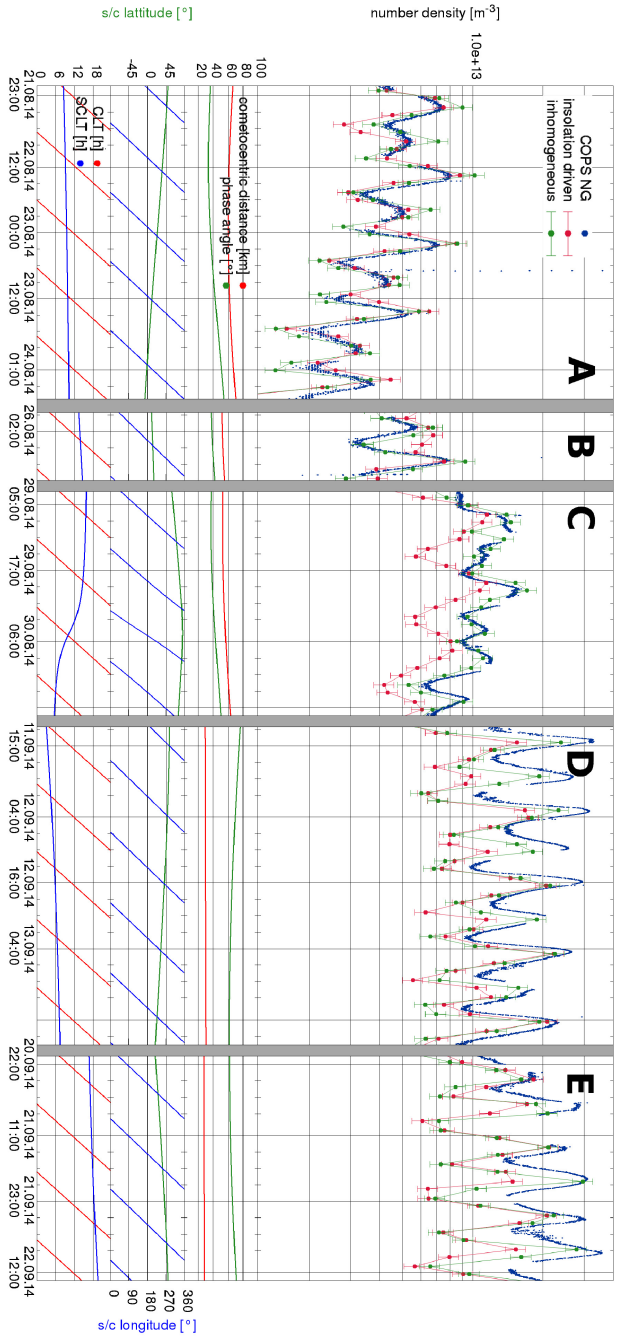

Figure 74: Top panel: Comparison of the COPS NG (blue points) data with our insolation-driven (red points), and inhomogeneous (green points) outgassing models over the period from the 2014-08-29 to 2014-09-22. Upper middle panel: The cometocentric distance and the phase angle of the observations on the same scale showing how the spacecraft approached the comet towards time span D but at relatively high phase. Middle lower panel: The sub-spacecraft latitude (left axis) and longitude (right axis) showing how in time span C the spacecraft was moving towards the northern pole, which is located in the Hapi region. Bottom panel: The sub-spacecraft local time (SCLT) and the local time at the position of the zero longitude meridian (CLT) that runs through Imhotep.

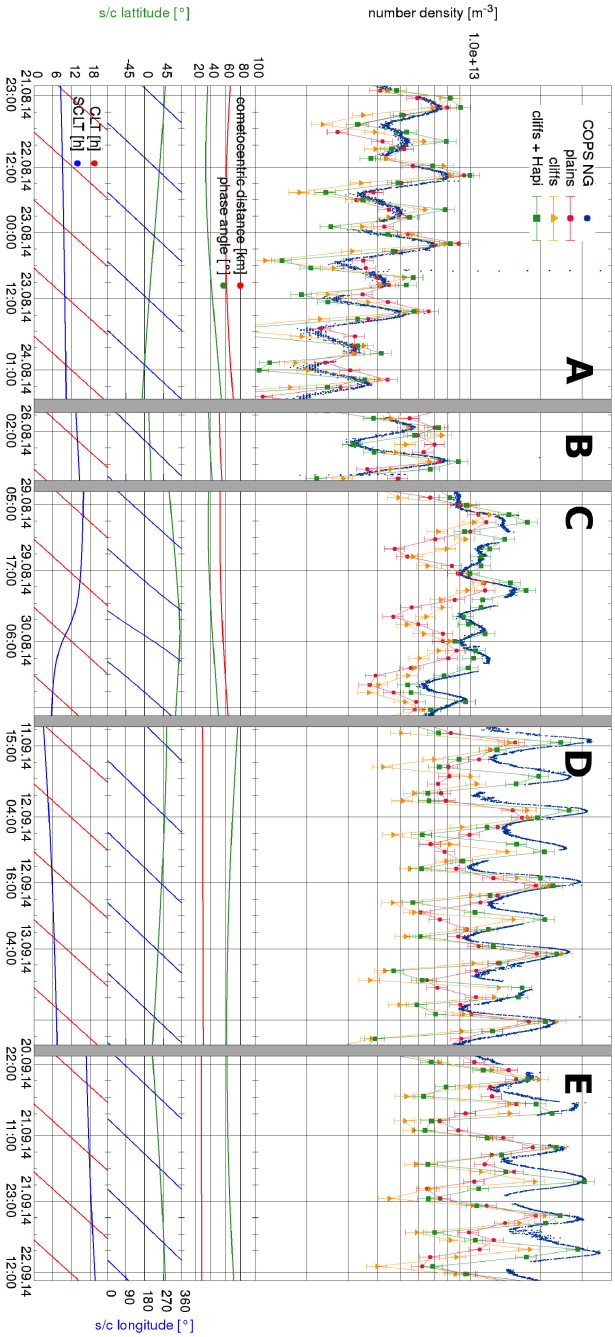

Figure 75: Top panel: Comparison of the COPS NG (blue points) data with our plains-only (red circles), cliffs-only (orange triangles), and cliffs + Hapi (green squares) outgassing models over the period from the 2014-08-29 to 2014-09-22. Lower three panels are the same as in Figure 74.

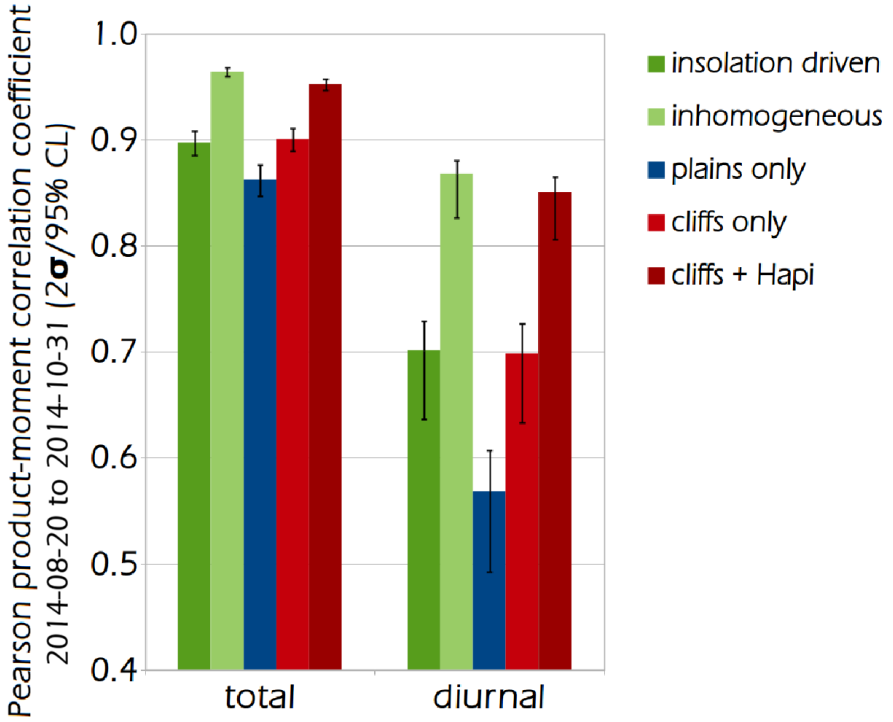

Figure 76: The «total » and «diurnal» PPMCC for the period 2014-08-20 through to 2014-10-31 for the five models is shown. The error bars represent a 2σ confidence interval.

3. **Best fit:** The inhomogeneous and the cliffs + Hapi models are statistically indistinguishable and fit the data the best. ROSINA/COPS cannot differentiate between these two either.

We have also see that the cliffs + Hapi model fits the ROSINA/COPS data equally well as the inhomogeneous one and better than any of the other models. In addition, the cliffs-only model is statistically equally good as our purely-insolation-driven model. It is not surprising that the models with more free parameters perform better than the ones with less. But the important point is that the models with fewer free parameters do not seem to capture the complexity of this problem to a satisfying degree thus requiring more variation in the outgassing distribution over the surface. This of course leads to the solutions possibly being even more degenerate. We have thus seen that eliminating all plains surfaces except for Hapi from an inhomogeneous model does not worsen the fit to the ROSINA/COPS data in our considered time span. It is thus plausible that cliffs play an important role in the gas emission from the stand point of ROSINA/COPS.

9.1.3 *The role of topographic re-radiation*

In our simple thermal model we neglect not only thermal conductivity, which seems well justified by the measurements (Gulkis et al., 2015; Schloerb et al., 2015), but also possible topographic re-radiation effects in concave areas of the comet. The motivation for having a look at the influence of topographic re-radiation comes from analysis we will show later in Section 9.3.3. In Rosetta literature this has often also been referred to «self heating», though this term can be misleading. Self heating could be understood as some additional internal heating source.

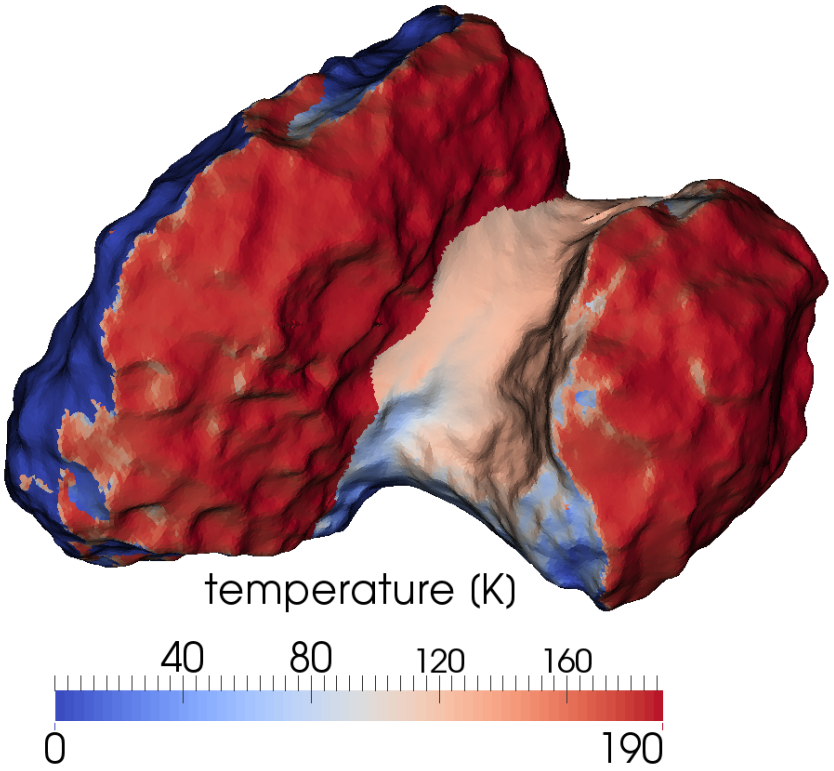

Figure 77: Surface temperature including topographic re-radiation in the thermal model for 2.87 AU pre perihelion. The Sun in the figure is at 185° longitude.

Non illuminated surfaces can be heated by illuminated surfaces that are facing them as shown by Keller et al., 2015. Calculating the surface temperature taking this into consideration (according to Keller et al., 2015) has shown that we do not reach the sublimation regime of water ice in shadowed areas of the comet. In our simple thermal model neglecting topographic re-radiation and heat conduction, shadowed surface areas receive no energy input and thus no temperature can be calculated and thus do not lead to sublimation. Including topographic re-radiation into the thermal model for a

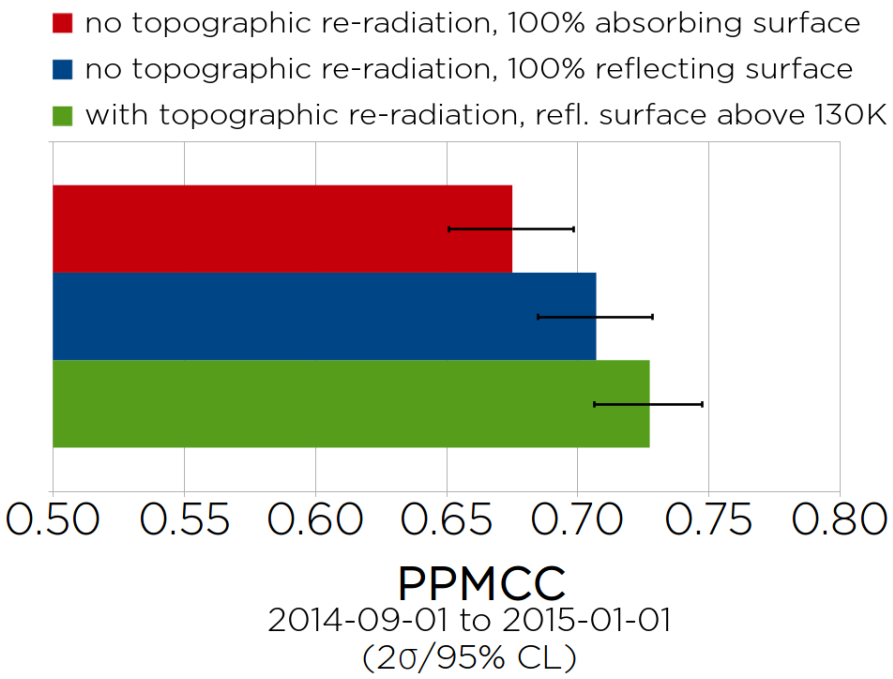

Figure 78: PPMCC for ROSINA/COPS data for three insolation-driven models for 2.87 AU pre perihelion in the period 2014-09-01 to 2015-01-01. The three models only differ in the thermal model and surface reflectivity applied. In red no topographic re-radiation is included and the surface is assumed to be absorbing. In blue no topographic re-radiation was assumed but the surface was set to be diffusely reflecting. Lastly in green topographic re-radiation is included and all surfaces above 120 K are assumed to be diffusely reflecting.

2.87 AU pre-perihelion model shows that the temperatures in shadowed areas in the «Neck» reach temperatures between 120 to 140 K and thus do not lead to additional water sublimation. This is shown in Figure 77. The resulting global production rates are within 2% of the model neglecting topographic re-radiation. Locally production rates close to the terminator especially with proximity to illuminated facets that are vis-à-vis are as expected boosted more strongly.

Even though topographic re-radiation is not significant for water sublimation at theses heliocentric distances there is an advantage to including it in a thermal model. Topographic re-radiation is important for understanding the behaviour of the surface with respect to the back flux of gas. When a surface is cold enough, gas is adsorbed to it, and thus such surfaces act like a vacuum boundary in our model. Previously we have set the entire cometary surface as a diffusely reflecting boundary without giving a physical justification for that choice other than it fitting the data (especially OSIRIS, see Section 9.3). As illustrated in Figure 78 where we have compared three insolation-

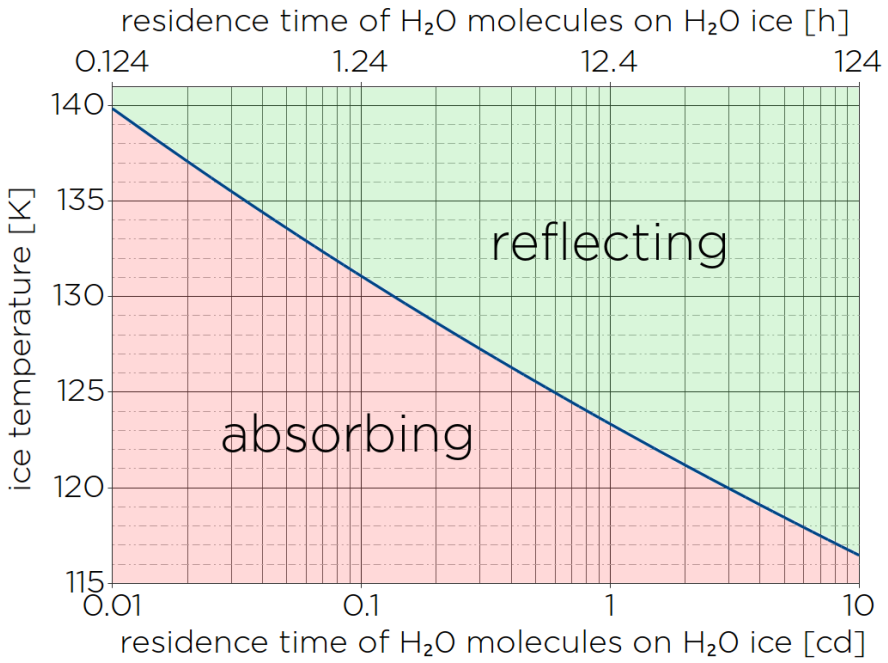

Figure 79: Residence time (blue line) in hours or comet days (cd) as a function of the ice temperature according to the formula and date from Sandford and Allamandola, 1993. When for a given residence time the temperatures is above the blue line we can consider a surface to reflect gas particles (green area) and conversely when temperatures are lower than the blue line we should consider the surface to be absorbing (red area).

driven models to the ROSINA/COPS data in the time span from 2014-09-01 to 2015-01-01. This assumption provides a slightly better fit to the data. The red and blue models both do not account for topographic re-radiation and differ only in the reflectivity of the surface. In the red model the entire nucleus surface is absorbing and in the blue one the entire surface reflects gas back flux diffusely. The green model on the other hand takes topographic re-radiation into account. Additionally, surface facets with temperatures above 130 K are set to reflect and those below 130 K absorb any gas back flux. This threshold has been chosen according to a study by Sandford and Allamandola, 1993 who have determined residence times for different molecules on various icy surfaces for different temperatures. Figure 79 shows the residence time according to the values taken from Sandford and Allamandola, 1993. At 130 K water molecules will be trapped on a water ice surface for no longer than 1.7 hours (i.e. $< \frac{1}{8}$ of a rotation period). Figure 78 shows that the fit to the ROSINA/COPS data is improved when going from an absorbing to a reflecting surface even without taking topographic re-radiation into account, though the correlation coefficients are within the margin of error of each other. The fit further improves when we include topographic re-radiation, and

is statistically better than the absorbing model without topographic re-radiation. Thus topographic re-radiation does not only provide for better fits to the ROSINA/COPS data but more importantly provides a stable frame work with a solid physical foundation for setting the surface boundary condition. In our previous models without topographic re-radiation no temperature could be determined for shadowed surfaces and thus their reflectivity could not be determined physically.
Even though the water production rate is not altered by the inclusion of topographic re-radiation effects the considered heliocentric distances this needs to be re-evalueted for smaller heliocentric distances. It is well imaginable that for simulations close to perihelion topographic re-radiation can push even shadowed areas to the free sublimation temperature of water. For the larger heliocentric distances considered here another effect might warrant further study. Though we don't reach the free sublimation temperature of water ice we do reach the free sublimation temperature of CO_2 ice ($\sim$ 125 K, Huebner et al., (2006)) in large parts of the non illuminated surface. These areas could thus be subject to CO_2 sublimation instead. In illuminated areas it has been shown that H_2O emission is dominant (Hässig et al., 2015).

9.2 GAS SIMULATIONS AND COMPARISONS WITH MIRO AND VIRTIS

There are also two other instruments on board Rosetta that can help constrain the gas emission. These are the MIRO (described in Section 3.3) and VIRTIS (described in Section 3.4) instruments. Both instruments measure the emission and absorption spectrum of different gas species in various wavelengths. In Marschall et al., (2016) we have made a first comparison with published MIRO water column densities in Biver et al., (2015). We will present this here too. There are in principle three things we can compare:

1. **Single water column densities:** Using the 3D gas number density distribution within the first 10 km we can produce a water column density within the field of view using a line-of-sight integration.

2. **Water column density maps:** In some cases MIRO and VIRTIS are able to produce maps of column densities, which are in some sense the equivalent of the gas to the brightness measured by OSIRIS for the dust. In practice they are simply many executions of the point above for multiple lines-of-sight.

3. **Gas parameters along a line-of-sight:** Instead of integrating the local gas number density along a line-of-sight we can also simply extract the local gas parameters along a specific line-of-sight.

We are particularly interested in the number density, the speed component along the line of sight, and the temperature.

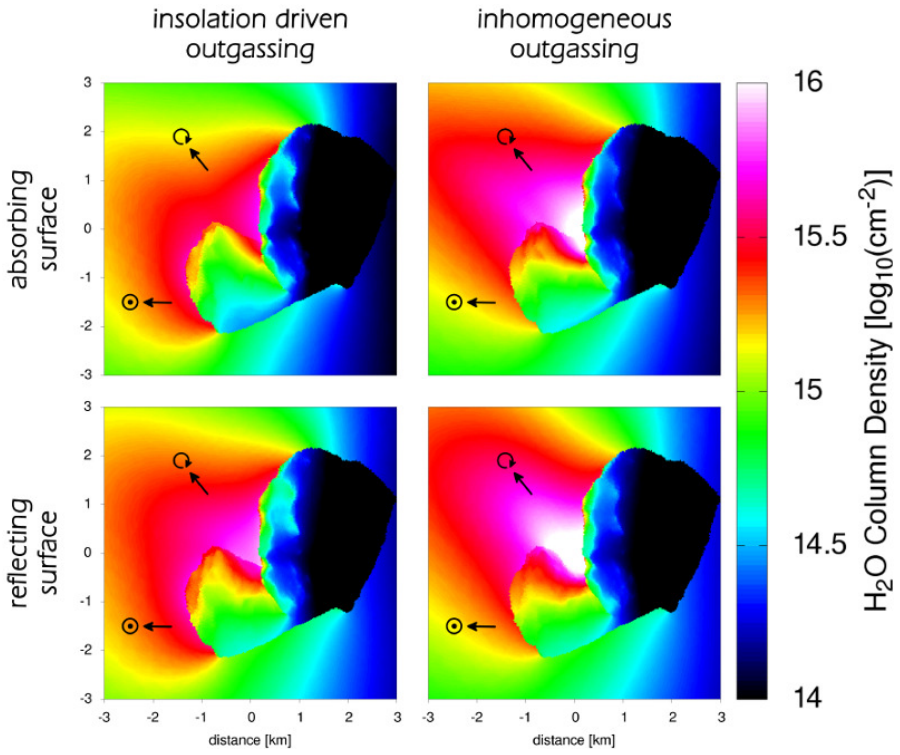

Figure 80: Comparison view of the water column density in $\log_{10}(\mathrm{cm}^{-2})$ for the insolation-driven (left) and inhomogeneous (right) outgassing cases with an absorbing (top) and a reflecting (bottom) surface using the viewing geometry on 2014-09-07 at 12:30:00 UTC. The Sun is at a sub-solar longitude of 180°.

To produce all three of the above end products we use a slight variation of the code described in Section 4.9 applying the same extrapolation. All of this sounds quite straight forward. But there can arise some challenges due to the way the observations of MIRO and VIRTIS are executed. For a good signal to noise ratio both instruments must in some cases expose for a long time or average data acquired over a long period. As MIRO is not a mapping spectrometer column density maps as e.g. in Biver et al., (2015) are composed of measurements taken of long periods of time (~ hours) during which the comet has rotated substantially. The same is true for VIRTIS-H that needs to average its data acquired over the time span of tens of minutes to hours. For averages over time spans of tens of minutes this is not a big issue but for longer averaging periods the rotation of the comet again becomes something in need of consideration. There are two ways of getting around this issue. Either we perform a time integration which requires multiple simulations on our side, or we try to pick data that was acquired using a relatively short exposure time, or a combination of the both. Short exposure times are

given (mostly) for single acquisitions of MIRO that can be converted into local gas properties along the line of sight, and for VIRTIS-M data.

We will start with a comparison with MIRO. The results shown in Figure 80 corresponds to an observation taken on 2014-09-07 at 12:30:00 UTC (identical viewing geometry as in Fig. 6 in Biver et al., (2015)). We clearly see the influence in the case of inhomogeneous outgassing boosting the column density by at least a factor of 2. The influence of the reflecting surface can be seen especially in the inhomogeneous case where the coma is pushed away from the «Head» lobe towards the «Body» lobe (top of the image), and thus the main direction of the gas flow is clearly deflected by approximately 15 °. The inhomogeneous outgassing models with increased activity from the «Neck» structurally agree with the conclusion of Biver et al., (2015). However, our column densities are roughly one order of magnitude higher even though our production rates are in general agreement with their derived production rate of $1.46 \pm 0.75\,\mathrm{kg\,s^{-1}}$. (Our values are within that interval for the purely-insolation-driven outgassing and slightly higher for the inhomogeneous outgassing models as seen in Figure 66.) These observations of MIRO were performed during a time period of 4 h (or 116° of comet rotation) compared to our steady state solution in Figure 80. A first comparison with VIRTIS column densities has shown that our column densities resemble the ones reported in Bockelée-Morvan et al., (2015). In Chapter 12 we will present some preliminary work as an outlook on our future work with MIRO and VIRTIS data.

9.3 DUST SIMULATIONS AND COMPARISON WITH OSIRIS

Although we have made considerable effort to fit the ROSINA/COPS data, our main objective was to take this a step further and fit the OSIRIS dust brightness measurements. The dust results shown here have been created in an attempt to reproduce the OSIRIS-WAC image WAC_2014-09-05T09.19.13.810Z_ID30_1397549700_F18 taken on 2014-09-05 at 9:20:23 UTC with filter 18 from a distance of 42.5 km to the nucleus centre, a phase angle of 59°, and an exposure time of 0.469 s. In this image, seen in Figure 89, the Sun is at 140° sub-solar longitude located in the top of the image. The data have been absolute-calibrated (Fornasier et al., 2015) and are in physical units of spectral radiance. This processed form of the image clearly shows a fan-like structure of the dust brightness. Other than this feature, we do not see any other major dust activity.
The coma brightness depends on the dust size distribution. We have thus included two types of distribution in our analysis: (1) a power law distribution over a large interval of dust sizes from tens of nanometres to tenths of millimetres favouring a coma dominated by small particles and (2) a single-size coma dominated by large particles of tens or hundreds of micrometres.

9.3.1 *Coma with a power law size distribution*

To compare the dust results a dust size distribution needs to be defined. We start with a power law distribution where the number production rate $n(r)$ is proportional to r^{-b} at the inlet boundary, with b being the power law index and not the impact parameter. For different values of the power law index we calculated the dust brightness for the purely-insolation-driven and inhomogeneous outgassing solutions each for the two surface types presented in Section 9.1.1. A power law of $b = 3$ amounts to an constant mass distribution for any dust size and $b = 4$ an equal mass distribution over each dust size decade. Figure 81 shows the spectral brightness with the purely-insolation-driven outgassing and the reflecting surface of the individual dust size bin run with $b = 4.5$. The final image will be composed by simply summing up these 40 partial brightness images.
The main contribution to the total coma brightness for such a coma with $b = 4.5$ comes from the size bins in tenths of µm range, and the small and large dust sizes only provide a small contribution. This is a combined effect of the power law and the scattering efficiency (see Figure 28). The brightness of large particles is suppressed mainly due to the effect of the power law. For very small particles, the situation is slightly different. Because of to the power law, they are much more numerous, which might suggest a high brightness. But

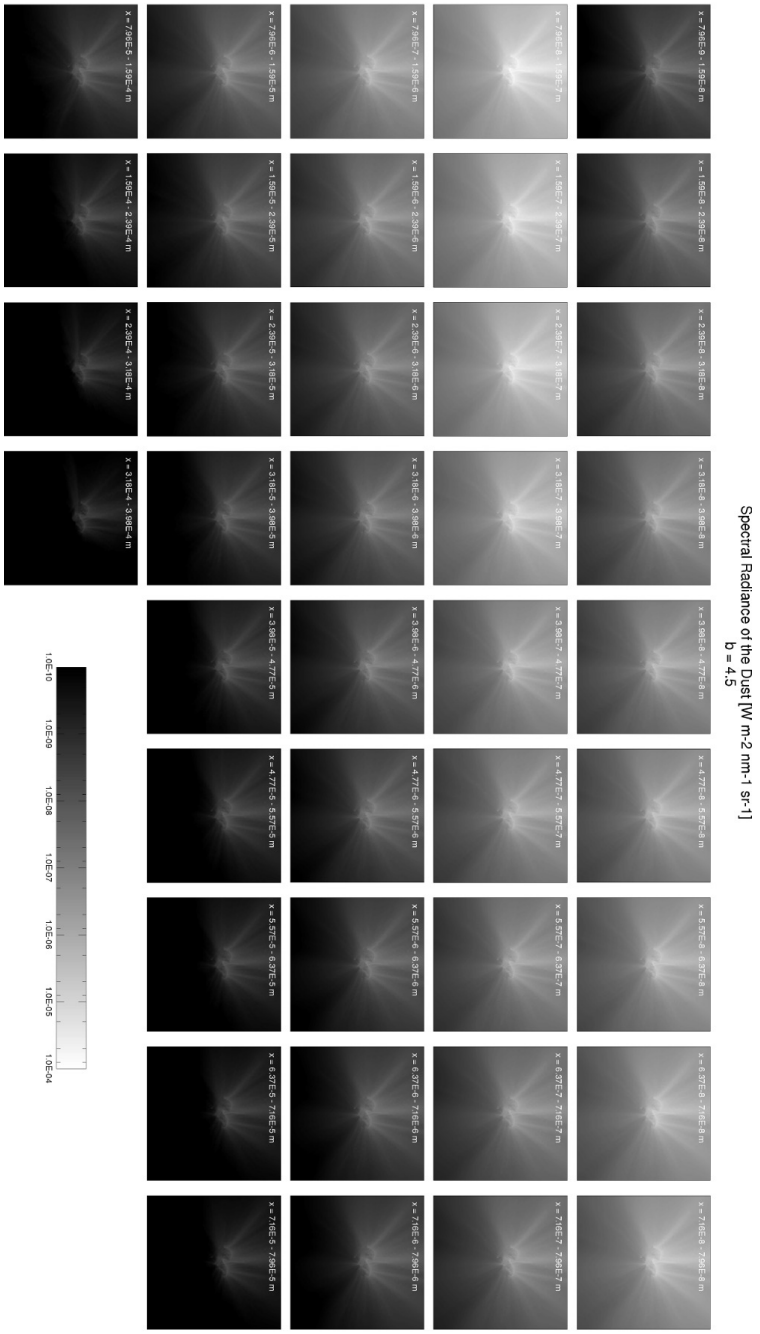

Figure 81: Spectral radiance in [W m^{-2} nm^{-1} sr^{-1}] for all the 40 dust size bins between $8 \cdot 10^{-8}$ and $3 \cdot 10^{-4}$ m for the power law exponent $b = 4.5$ of the insolation driven outgassing case with a reflecting surface. The individual size ranges are indicated in each plate.

because they are much smaller than the observation wavelength, their scattering efficiency drops to almost zero, which results in a small contribution to the total radiance from these sizes. This was previously illustrated in Figure 28 and Figure 29, which shows for one the scattering efficiency as a function of dust size and the phase function, p, multiplied by the scattering efficiency, q_{sca}, of spherical particles as a function of scattering angle in a polar diagram. Small particles are very much fainter than all other sizes because their scattering efficiency is so low, and they scatter uniformly in all directions. For these very small particles to contribute significantly a very large power law index would be required pushing most of the mass into the inefficient scattering regime.

When the power law exponent increases from low values up to 4, we have an increasing number of particles in the efficient scattering regime for the same dust mass, so the total spectral radiance increases. When the power law exponent goes beyond 4, most of the particles are found in the very small size bins, which have an almost negligible scattering efficiency, resulting in a drop in the total brightness. We can put this differently by saying that for a constant (measured) brightness of the coma, the dust-to-gas mass production rate ratio Q_d/Q_g must decrease because the power law exponent increases in the range of low values up to 4 (i.e. there is degeneracy between b and Q_d/Q_g). This is illustrated in Figure 82 where we can see Q_d/Q_g as a function of the power law exponent, and the blue line shows a coma of constant brightness (in this case the one of the OSIRIS image WAC_2014-09-05T09.19.13.810Z_ID30_1397549700_F18 we have chosen). This figure furthermore shows the degeneracy we have just described. For a given Q_d/Q_g, up to two power law exponents will produce the desired brightness. Recent results (Rotundi et al., 2015; Fulle et al., 2016b; Merouane et al., 2016) suggest that $b \sim 3$ for large particles (> mm) and closer to 2 for sub-millimetre particles and that $Q_d/Q_g = 4 \pm 2$, which would, however, constrain this result and lift the degeneracy (light red area in Figure 82). Our models are able to reproduce results within these constraints, though we are at the lower end of the constraining interval. It must be stressed, however, that for $b < 3.5$ the brightness is dominated by the large size bins, hence the upper limit of our considered size interval, such that the size of the interval can become important by influencing the trend of the curve in Figure 82. We have therefore also studied single-size comae in Section 9.3.2 to circumvent this problem. A further problem can arise when the power law exponent becomes to small and large particles dominate the coma. These large particle move slowly and thus stay within the inner coma for a long time during which the nucleus can rotate substantially changing the illumination condi-

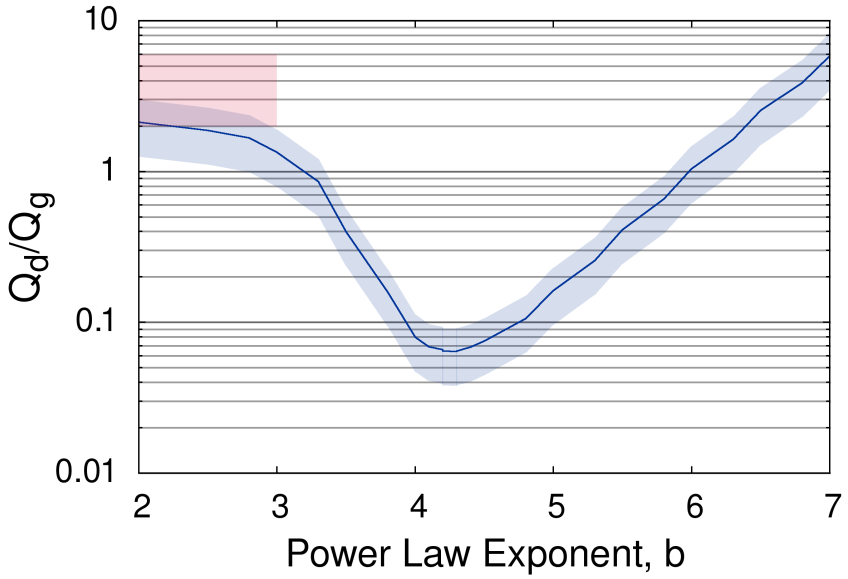

Figure 82: Dust-to-gas mass production rate ratio as a function of the power law exponent, b. The solid blue line represents the mean value of the four models run (insolation-driven/inhomogeneous outgassing and reflecting/absorbing surface), and the blue band indicates the maximum and minimum values obtained. The red area shows the constrained area by Rotundi et al., (2015).

tions and with that the gas flow field. For very large particles a time dependent solution would be needed.

We should highlight at this point that the power law exponent is set at the surface. As the different dust sizes accelerate at different rates, i.e. the small particles undergo higher acceleration close to the surface compared to the smaller ones, the small particles are diluted compared to the large particles, thereby changing the power law. The effective or mean power-law exponent of the total coma will thus always be lower than the one at the surface (McDonnell et al., 1987) because the dust speeds as a function of the dust size, r_d, typically scale with $r_d^{-0.5}$, as we have seen in Equation 40.

The outgassing distribution also affects the dust distribution. Figure 83 shows a comparison of the total brightness of the dust coma for the purely-insolation-driven and inhomogeneous outgassing flow fields. By comparing with the actual image, we can see immediately that there is considerably more dust visible in our models on the entire illuminated part of the comet. The dust filaments seen are a direct product of the nucleus shape (as also shown in Chapter 7), including the varying illumination conditions across the surface and not of any manually introduced jet sources.

None of these models reproduces the data well. This indicates that we either (1) are dealing with very locally varying outgassing rather than the broad regional inhomogeneities we were considering in Sec-

tion 9.1.1 (this could also include small scale shadowing effects below the currently used resolution), (2) have regionally or locally varying Q_d/Q_g, or (3) have regionally or locally varying power law exponents, b. Comparing the purely-insolation-driven and inhomogeneous solutions, we note that the structure of the coma varies substantially.Since the dust is following to a high degree the motion of the gas, we immediately see the differences caused by the inhomogeneous outgassing and thus higher activities in the Hapi and Hathor regions. The coma filaments have clearly shifted to the Seth side of the comet from the purely-insolation-driven to the inhomogeneous outgassing case. The inhomogeneous models come closer to the data because they show a more pronounced main dust feature originating in the Hapi region and more faint emission everywhere else. Additionally, the influence of the reflecting surface can be seen especially with the main filament turning towards the «Body» lobe.
Of the four models shown here, the inhomogeneous model with a reflecting surface resembles the actual data the closest, particularly since the main dust feature coming from the Hapi region has almost the correct direction. We must stress that dust filaments coming from the Hatmehit region on the «Head» lobe and the Seth, Ash, Aten, and Babi regions on the «Body» lobe can still be seen even though they are not observed in our specific OSIRIS image. We can also see bent jet filaments near the surface in the «Neck» part of the comet, especially in the purely-insolation-driven outgassing models. Because the dust speeds are too high (see Table 6), this bending cannot be not caused by gravity but rather by the gas drag.

Table 6: Maximum dust speed at 10 km for the insolation-driven and inhomogeneous outgassing models with an absorbing surface for specific dust radii r_d.

r_d [m]	$\lvert v_{d,\,max}^{hom}\rvert$ [m s^{-1}]	$\lvert v_{d,\,max}^{inhom}\rvert$ [m s^{-1}]
$1.6 \cdot 10^{-8}$	201	335
$1.6 \cdot 10^{-7}$	75	139
$1.6 \cdot 10^{-6}$	25	48
$1.6 \cdot 10^{-5}$	8.0	15.7
$1.6 \cdot 10^{-4}$	2.3	4.7

9.3.2 *Coma dominated by large particles*

As mentioned in Section 9.3.1 we will also examined a coma dominated by large particles in contrast to a power law dust size distribution. This was motivated by the inferred dominance of large particles from the GIADA and COSIMA experiments (Rotundi et al.,

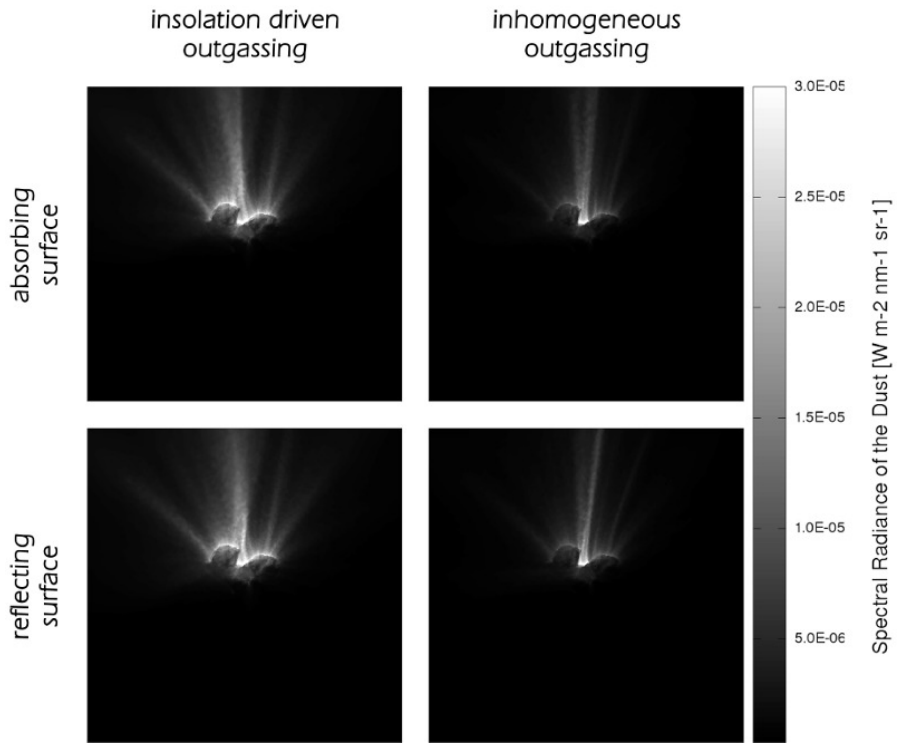

Figure 83: Spectral brightness of a power law dust coma for insolation-driven (left column) and inhomogeneous (right column) outgassing for the absorbing (top row), and reflecting (bottom row) surface with a power law exponent of $b = 4.5$ and dust to gas mass production rate ratios $Q_d/Q_g = 0.075$.

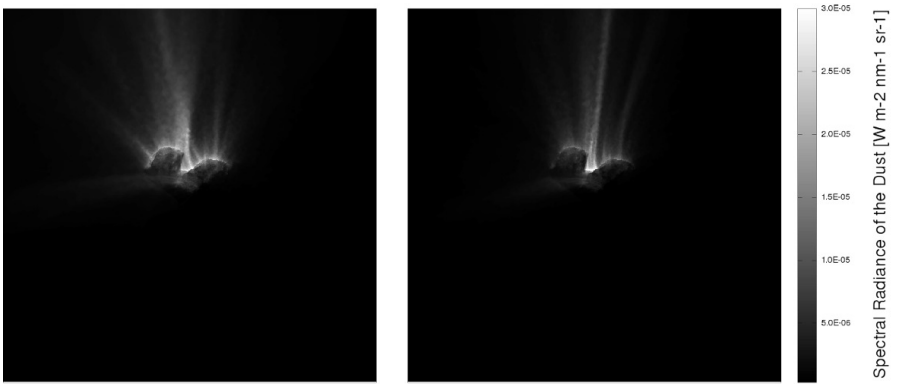

Figure 84: Spectral brightness of the dust for insolation-driven (left) and inhomogeneous (right) outgassing for a coma consisting only of 318 µm sized particles.

(2015); Langevin presentation at SWT 2015). We looked especially at a coma consisting solely of particles with radii of $3.18 \cdot 10^{-4}$ m. Figure 84 shows the results for a reflecting surface with purely-insolation-driven and inhomogeneous outgassing.

What immediately stands out is that the purely-insolation-driven model in no way resembles the real coma. The inhomogeneous outgassing model is a much better approximation and structurally resembles the actual coma quite well. In particular, the inhomogeneous coma dominated by 0.318 mm particles no longer shows the filament from Hatmehit and only retains a few excess jets coming from the Seth, Ash, Aten, and Babi regions. This case structurally resembles the observed coma most closely. The dust-to-gas mass production rate ratio in this case is $Q_d/Q_g = 2.2$, so it is within the expected range. A coma dominated by large particles thus seems plausible but is unlikely to be a unique solution.

We would like though to reiterate a point as to the limits of our models. The travel time needed to reach the edge of the domain for the large particles is not negligible (90 min in the worst case for 318 µm radius particles in the purely-insolation-driven flow field), so that ultimately a time-dependent solution will be required to account for the rotation of the comet. Figure 85 shows the amount of dust mass reaching the outlet surface for different dust sizes in the range of 1 µm to 1 cm. Approximately 27 % of the particles do not reach the outlet surface regardless of the size. These are the particles that mainly get reabsorbed in the concave shape of the comet's «Neck» region. Additionally, some of these particles are on ballistic trajectories because they originate near the terminator. Since the dust size increases beyond 0.1 mm, the number of particles reaching the outlet surface decreases further as areas with lower activity can no longer lift the dust particles. For the purely-insolation-driven

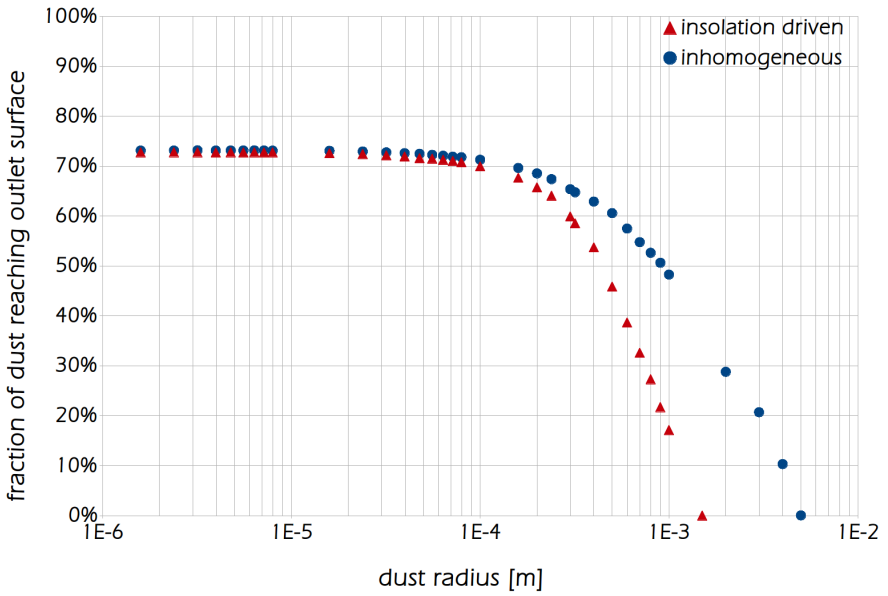

Figure 85: Mass fraction of dust reaching the outlet boundary as a function of the dust size in the size range of 1 µm to 1 cm for the insolation driven (red triangles) and inhomogeneous (blue circles) outgassing model with an absorbing surface. The dust density is 440 kg m^{-3} for all sizes.

outgassing model with an absorbing surface, the maximum liftable mass of our particles with a density of 440 kg m^{-3} lies at 1.5 mm. For the inhomogeneous case, the largest liftable size is 5 mm. It is higher because we have stronger gas emission from the «Neck» region compared to the purely-insolation-driven case. It needs to be stressed that localized activity within the facet leaves the possibility open of even larger particles being lifted.

For a free radial flow (as explained in Chapter 5) the brightness drops off according to the "1/r-law ". In all of our simulations we have observed deviations from this behaviour when studying profiles along jets and the total radial brightness behaviour, especially close to the nucleus. As a result, the observation of deviations from this "1/r-law "(Lin et al., 2015; Gerig, Marschall, and Thomas, 2017) can be explained by a combination of non-point source geometry, acceleration (e.g. Thomas and Keller, (1990)), and the non-spherical shape of CG although a detailed comparison must still be performed. The signal-to-noise in the August-September 2014 observation is, however, low in the data and not optimal. Extension of this work to times of higher activity (near perihelion) would offer better prospects for evaluation and comparison. The deviation from a "1/r-law "of the brightness in our simulations is illustrated in Figure 86. The lefthand panel shows a polar transform of the dust brightness of the smallest size bin of the insolation-driven outgassing model with an absorbing surface. The

righthand panel shows the integrated brightness multiplied by the radial distance to the nucleus centre, $I(r) \cdot b$, as a function of the impact parameter, b, given by

$$I(r)\ b = \int_0^{2\pi} I(b, \phi)\ b\ d\phi \quad , \tag{41}$$

with $I(r, \phi)$ being the spectral radiance at the respective point in the image plane given in polar coordinates, (b, ϕ).

The two curves shown correspond to the smallest (8 nm, green line) and largest bins (0.32 mm, dashed red line) we ran for theses simulations. The values have been scaled relative to each other at a radial distance of 4000 m from the comet centre. For free radial outflow we would expect a constant line in the righthand panel of Figure 86. But we observe a drop in brightness that is steeper than $\frac{1}{b}$. This deviation indicates that our flow is non-radial and accelerating. For radial distances larger than four kilometres the brightness drops comparably for the large and small particles and starts to flatten out towards the edge of our simulation domain. Two factors are the main cause for the curves not flattening out perfectly both of which are viewing geometry related: (1) non-point source viewing geometry produces a negative slope at larger impact parameters (the distance to the comet for this image is 42.5 km), and (2) larger phase angles (maximum effect at 90°) introduce a further decline in the slope (the phase angle is 59° in this image). That This indicates that the coma indeed goes over to a radial flow with constant dust speed when our particles start reaching their terminal velocity. More interesting is the regime between 2.5 and 4.0 km. The drop in brightness for the small particles is slightly less than the one of larger particles. Our analysis has shown that this is most likely caused by the fact that the small particles go over to a radial outflow faster than the large particles. Additionally, the large particles have a more significant non-negligible non-radial motion close to the surface and thus providing higher relative brightness. This non-radial motion close to the surface is primarily driven by the non-spherical shape of the nucleus itself as we have seen in Chapter 7.

9.3.3 *Comparison of the cliff vs. plains results*

For the comparison of our three gravitational slope related models we add a second OSIRIS image to the analysis. The image presented above in Section 9.3.1 and Section 9.3.2 will be referred to as 'image A'. The second image ('image B') we will be presenting in this section is WAC_2014-12-02T09.19.03.915Z_IDB0_1397549800_F18 taken with the WAC on 2014-12-02 at 9:19:04 UTC with filter 18 with a cometocentric distance of 30.2 km, a phase angle of 89°, and an exposure

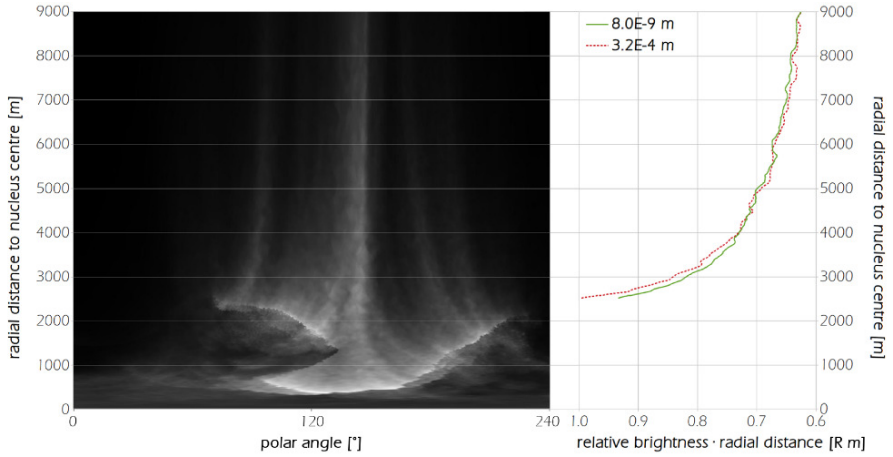

Figure 86: Left panel: polar transform of the spectral brightness of the smallest dust size bin of the insolation-driven outgassing model with an absorbing surface. Right panel: integrated brightness at a given radial distance multiplied by the radial distance, $I(r)r$, as a function of the radial distance, r, calculated according to eq. 41. The two curves shown correspond to the smallest (8 nm, green line) and largest size bins (0.32 mm, dashed red line) that we ran. The values have been scaled relative to each other at a radial distance of 4000 m from the comet's centre

time of 0.648 s. The Sun in this image is at a longitude of 218°. Both of these images represent well our considered time span and show the prominent dust feature originating from the Hapi region. In addition, image B shows a second dust feature originating around the Hatmehit and Ma'at region on the «Head» lobe (see Figure 89 at polar angle 250°). But the peak intensity of that feature is 40% less than the peak intensity of the dust feature originating in the Hapi region.
Figure 87 shows a view of a slice through the 3D dust solutions for sub-solar longitude of 140° plotting dust number densities and speeds for dust with radius $r_d = 1.6\,\mu m$ and assuming a dust to gas production rate ratio of $Q_d/Q_g = 1$. The latter only affects the number density values and thus the overall dust brightness. Because we are only interested in the relative brightness - which is proportional to the number density - at this point, assuming an optically thin coma, this assumption is well justified. Comparing especially the plains-only and cliffs-only models we see that the main coma structure in the plains-only model is in the sunward direction whereas in the cliffs-only model the main direction of the dust coma is clearly skewed towards the «Head» lobe of the comet and thus slightly away from the Sun direction. Also the cliffs-only and cliffs + Hapi models are missing the prominent feature originating around the Aten regions (this feature can be very clearly seen in the purely-insolation-driven case). Also the emission (or lack of it) from the Hatmehit (primarily plains) region can be clearly seen when comparing the plains-

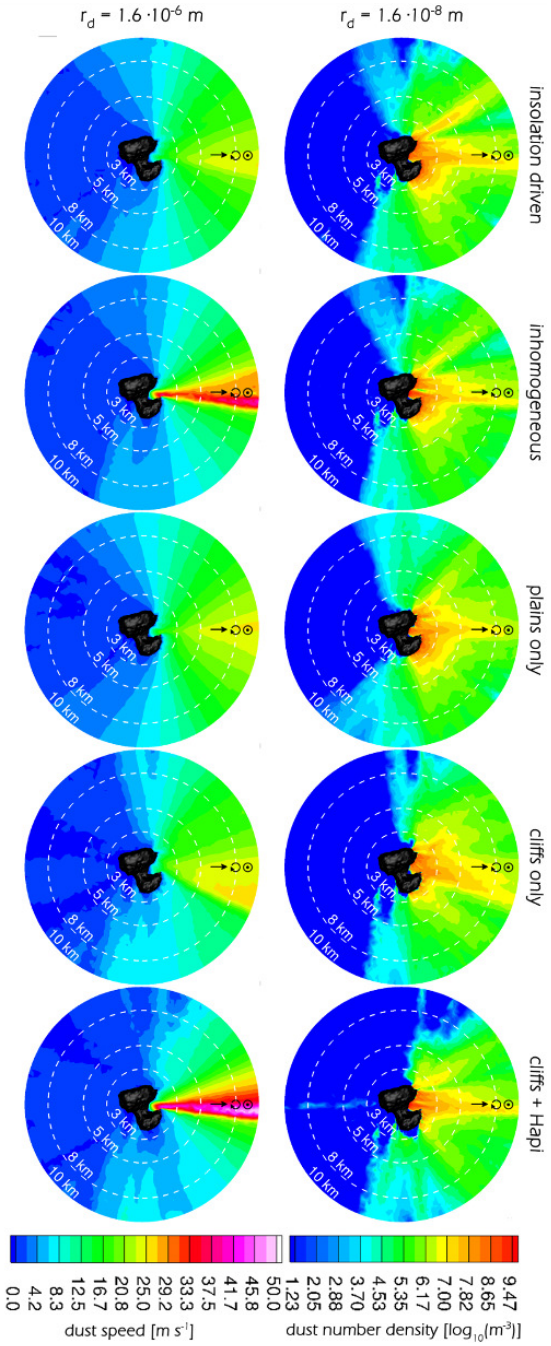

Figure 87: View of a slice through the 3D dust solutions for the sub-solar longitude of 140° for different dust size radii, starting from 1.6E−8 to 1.6E−4 m. The shown plane is normal to the terminator plane. The direction to the Sun is in the shown plane, the rotation axis of the comet comes out of the plane but has the same projected direction as the Sun direction in this view. The top row shows the dust number density [$\log_{10}(m^{-3})$] for the five models (columns). The bottom row shows the dust speeds [m s^{-1}] for the five models (columns). The results are given for a dust radius of $r_d = 1.6\,\mu m$ and assuming a dust to gas production rate ratio of $Q_d/Q_g = 1$. The latter only affects the number density values. The 3D shape of the comet is also displayed.

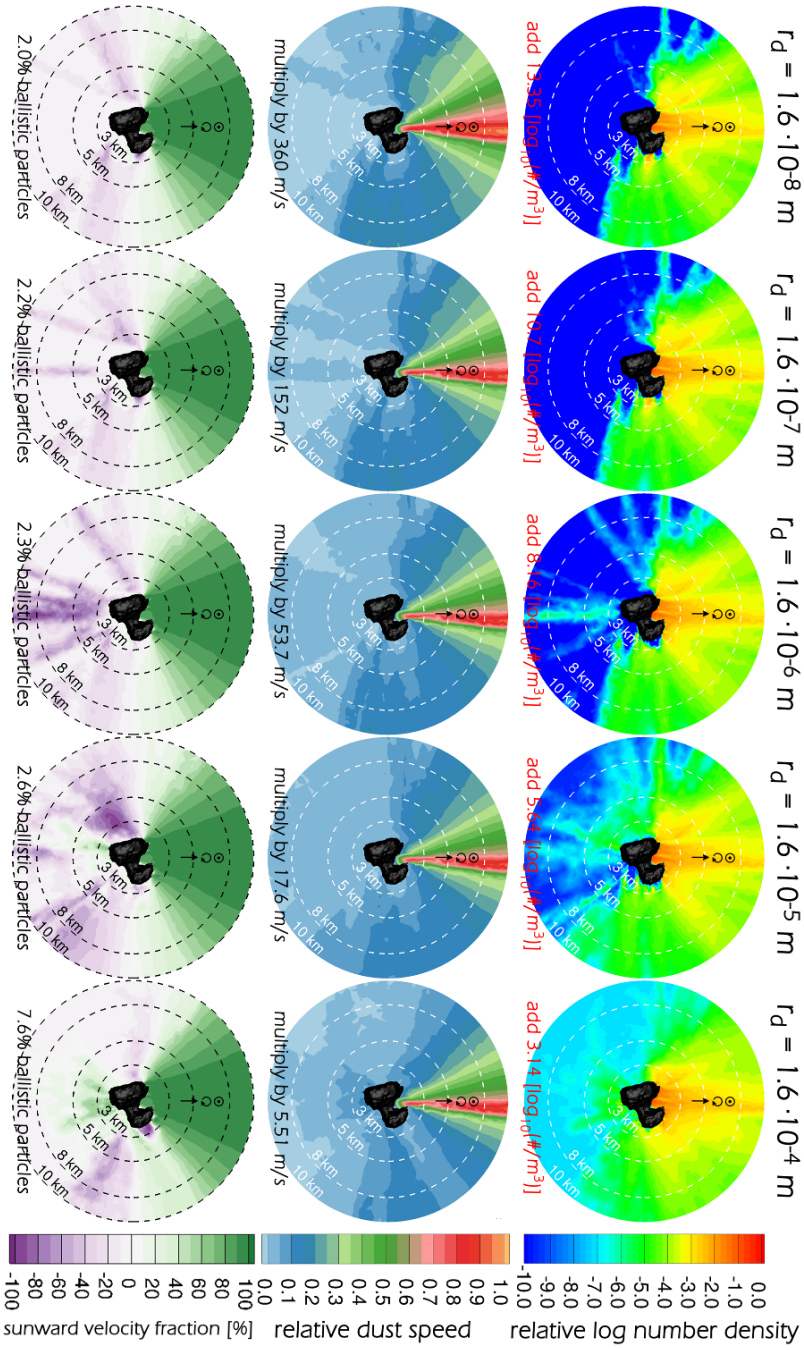

Figure 88: View of a slice through the 3D dust solutions for the sub-solar longitude of 140° for different dust size radii, starting from 1.6E−8 to 1.6E−4 m. The shown plane is normal to the terminator plane. The direction of the Sun is in the shown plane, the rotation axis of the comet comes out of the plane but has the same projected direction as the Sun direction in this view. All results assume the gas solution of the cliffs + Hapi model as an input for the dust model. The top row shows the logarithmic relative dust number density for each dust size. The convert to absolute units of $\log(\mathrm{m}^{-3})$ the corresponding value needs to be added. For each size dust size a dust to gas ratio of unity was assumed for these plots. The centre row shows the relative dust speeds of each dust size. For the absolute values the corresponding values need to be multiplied by the given scaling. The bottom row show the fraction of the dust velocity that is in the direction of the Sun with 100% being sunward and −100% anti sunward. Also the fraction of ballistic particles is given. The 3D shape of the comet is also displayed.

only to the cliffs-only model. There are also stark differences in the dust speeds. As with the gas, the inhomogeneous and cliffs + Hapi models exhibit the largest speeds. This can be mainly attributed to the higher gas production rates and hence gas drag on the dust in the Hapi. The maximum dust speed of the inhomogeneous and cliffs + Hapi models is almost double that of the other three models. Additionally, the inhomogeneous and cliffs + Hapi models illustrate nicely how in this geometry the dust coma is blocked from expansion by the Hathor cliff. As the dust size increases, the dust speeds decrease and gradually particles start falling back to the night side of comet. This is illustrated in Figure 88. For increasing dust sizes from left to right this figure shows in the bottom row the fraction of the dust velocity that is in the direction of the Sun with 100% being sunward and −100% anti sunward. Not surprisingly the main direction of the dust is sunwards for the main dust activity. Particles close to the terminator are emitted primarily normal to the surface which in that case is transverse to the direction of the Sun. When the gas density drops enough gravity will redirect the dust into the anti-sunward direction and if the dust was not accelerated past escape speed it will finally be redeposited on the surface. As the dust size increases this process becomes favoured. This can especially be seen for the $1.6 \cdot 10^{-4}$m particles where 7.6% of ejected particles return to the surface, thus being on ballistic trajectories. Most particles on ballistic trajectories are gravitationally bound particle. The rest of ballistic particles are emitted in the «Neck» regions and collide with the opposing region. For e.g. a sub-solar longitude of 140° as shown in the figure, some particles emitted in the Hapi region collide shortly afterwards with the Hathor region. When particles redeposit on the southern hemisphere their velocity is towards the surface and thus in that specific case also sunwards. Figure 88 also shows the relative dust number densities and relative dust speed for the different dust sizes. The smaller the dust particles are the higher is the relative speed is in a larger part of the domain. This is mainly due to the fact that for small particles gravity is a significant force thus reducing the speed. For the largest dust size shown values of 0.15 (dark blue) corresponds to the escape speed of 0.8 m s^{-1}. Thus in a large part of the simulation domain particles are on ballistic trajectories. This can also be seen in the relative number densities. Whereas the night side is almost void of small particles the largest dust size shows non negligible dust densities. In this case there is dust mass transport from the northern to the southern hemisphere.

Again we want to compare our modles to the OSIRIS images and we have thus produced the respective artificial dust brightness images. The results for our five models can be seen in Figure 89. There are large differences in the structure of the dust coma that can be observed qualitatively by comparing the artificial images to the

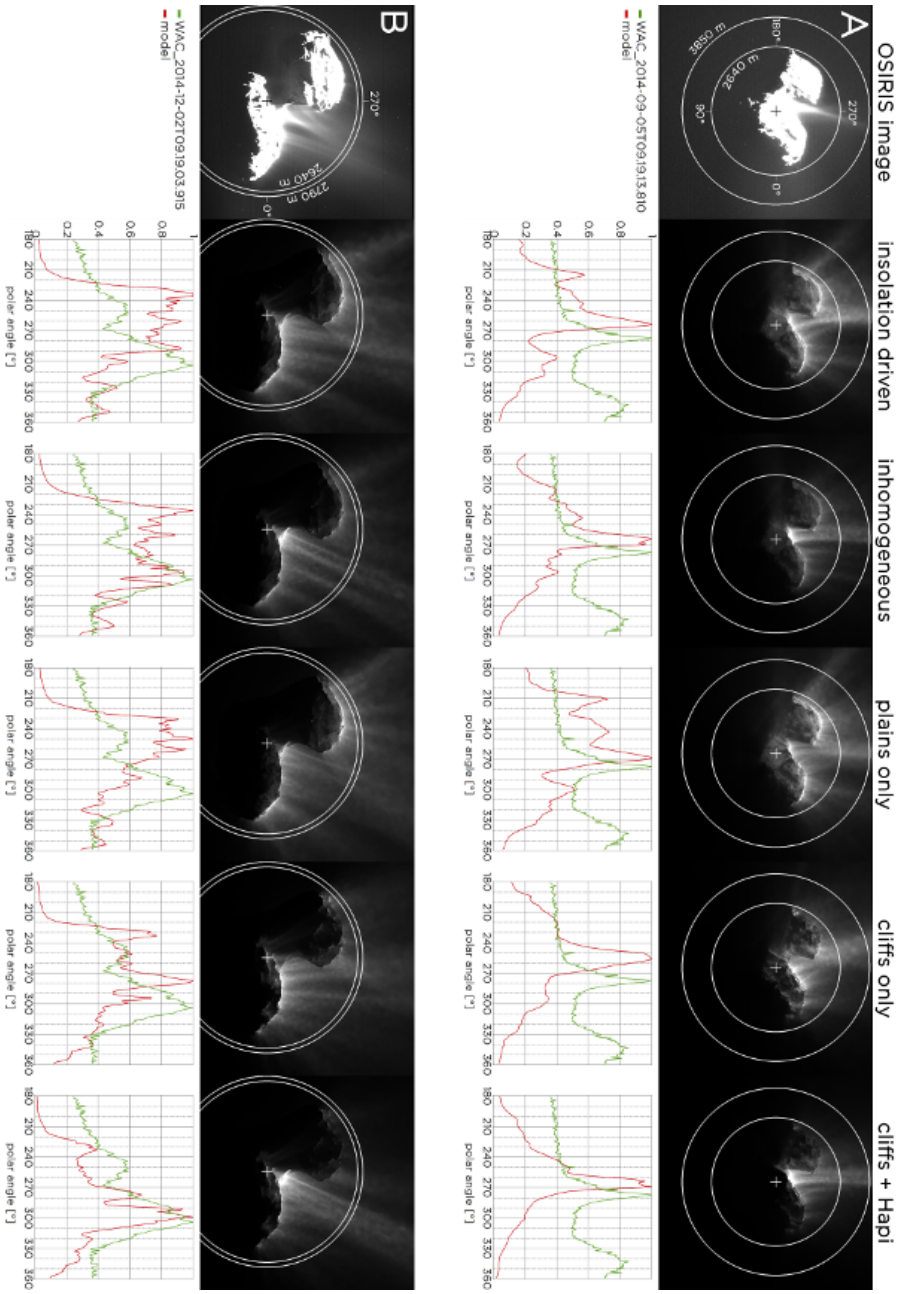

Figure 89: Artificial dust brightness images of our five models compared to the OSIRIS images WAC_2014-09-05T09.19.13.810Z (image A) with a sub-solar longitude of 140° and WAC_2014-12-02T09.19.03.915Z (image B) with a sub-solar longitude of 218°. The second and fourth rows show polar profiles of the relative dust brightness radially integrated from the inner to the outer circles drawn multiplied by the radial distance for the OSIRIS images and the respective model. The profile of image A show an increase starting at a polar angle of 320° and maximum at 345°. This increase is due to a ghost image as described in Tubiana et al., (2015). The crosses in the images mark the centre of the nucleus.

OSIRIS images. What stands out immediately is that the insolation and plains-only models both exhibit the most dust filaments across the entire day side of the comet in both image A and B. Especially a pronounced dust feature originating in the Hatmehit and Ma'at region on the «Head» lobe seen in the models is not seen in image A at all. Considering this we can exclude these two models as a match for the OSIRIS data and hence confirm the conclusion we had already seen in Section 9.1.2 regarding these models. In the cliffs-only model we clearly see the suppression of the dust feature coming from Hatmehit and Ma'at as this region mainly has low gravitational slopes. More predominantly this model exhibits a very different direction of the dust structure. It is originating primarily from the Seth region rather than Hapi and is directed very clearly away from the «Body» lobe. The direction is almost normal to the projected surface of Seth. Based on this we can exclude the cliffs-only model as a viable candidate.

To get a more qualitative view on the fit of the models to the data we have performed polar profiles as shown in the graphs of Figure 89 to study the brightness as a function of the polar angle in a specific distance interval. As the OSIRIS images are quite noisy we have decided to radially integrate the brightness for each polar angle to get a clearer signal. The minimum distance is given by the comet's nucleus not being within the integration interval and the maximum distance by the field of view of the OSIRIS image itself. For an easier comparison with the data all profiles have been scaled such that the main peak takes the value of 1. Image A shows only one peak and the rest of the profile shows no features. However the peak is not much above the noise level. In principle there could be more features that are simply hidden in the noise. The profile of image A also show an increase starting at a polar angle of 320° and maximum at 345°. This increase is due to a ghost image as described in Tubiana et al., (2015). We can clearly see what we were already able to observe qualitatively in Figure 89. The plains-only model exhibits at least four very pronounced peaks for image A and a very pronounced feature on the «Head» lobe for image B. The cliffs-only model does indeed only have one dust peak for image A but the direction is off by approximately 20°. For image B the model profile is very far from the one of the data. The insolation-driven model also produces too many dust peaks which are not observed at this stage of the mission. For the inhomogeneous and cliffs + Hapi models the main peak is close to the one in the data of image A. The main difference of these two models is that only the cliffs + Hapi model produces only the main peak and is featureless along the rest of the profile. For image B the profile of the cliffs + Hapi model comes very close to that actual profile compared to the inhomogeneous model that does not. The

cliffs + Hapi model is hence a very plausible candidate.

However even the cliffs + Hapi model's peak is shifted by approximately 7° and the Hatmehit and Ma'at dust feature is not well reproduced. The latter indicates some emission from the Hatmehit and Ma'at regions. Regarding the direction of the Hapi jet there are three possible explanations for this. First: Due to the fact that we are using a decimated shape model it is possible that the actual surface and the model surface facets are inclined to each other by just a few degrees. Second: We could be dealing with non-orthogonal emission from the surface. In our model the dust leaves the surface primarily normal to the respective surface and subsequently goes over to a radial flow. Third: Additional gas emission from Hathor during local night would push the gas and thus the dust coma away from the «Head»lobe. Such night time activity is conceivable when considering topographic re-radiation. A test with night activity from Hathor has shown that this can indeed push the jet in the right direction but does not account for the full shift. This result had motivated us to study the effect of topographic re-radiation in Section 9.1.3 which has unfortunately shown that topographic re-radiation cannot increase the gas production rate in the Hathor region. This is of course true for water, which is the only species considered in this work. On the other hand CO_2 sublimation would be triggered in the topographic re-radiation cases studied and could contribute to the dynamics of the dust in the «Neck».

There are several possibilities as to why we do not reproduce the dust data perfectly. For one we are assuming the dust production rate to proportional to the gas production rate using a globally defined dust to gas ratio. Furthermore, we have used the same dust size distribution across the entire surface only letting it change naturally due to particles not being lifted. But the dust activity might also vary regionally or locally as we have seen for the gas activity distribution. The dust activity would in that case not be directly correlated with the gas activity which has been suggested by Tenishev et al., (2016).

Part V

SUMMARY, CONCLUSIONS, & OUTLOOK

10

SUMMARY

We have presented in this work our pipeline for modelling the inner gas and dust comae in Part ii. Our approach is illustrated in Figure 8 and we explain how our simulation results can be compared to Rosetta data and by doing that how our models can be constrained and in turn help understand the data. We focus primarily on ROSINA/COPS and OSIRIS measurements. In Part iii we presented first simulations for a spherical nucleus and subsequently added layers of complexity. In particular we show the deviations from force free radial outflow. Deviations from the «$1/r^2$-law» cannot only be caused by acceleration but also more complex emission distributions and effects due to the complex surface topography. The fact that we do not include e.g. dust fragmentation in our model allows us to test whether the observed deviations from free-radial outflow is consistent with the data in the absence of such effects. Results from a purely-insolation-driven spherical nucleus have shown the different dust dynamics regimes including the highly interesting regime of gravitationally bound particles which eventually redeposit on the cometary surface. Our considerations on spherical cases and cases with a complex shape model were an important step in preparation for our work to interpret ROSINA/COPS and OSIRIS data from the early escort phase of the Rosetta mission (Part iv).

Given the number of free parameters (Section 4.11) implied by the complete scheme, combined with the resolution of the simulation and the physical limitations arising from the measurements (as seen in the «measles» cases of Section 7.3), many assumptions are needed to obtain tractable and useful results at this stage of the analysis. We have deliberately used the simplest thermal model for setting the initial boundary conditions in this first work. This is in part because the model we used has essentially no free parameters. Only the hemispherical albedo and the emissivity can be chosen, the albedo having very little influence within the expected range. The low thermal inertia shown by MIRO measurements does indicate that the approximation is suitable. However, the assumption of direct surface sublimation provides considerably more uncertainty. Conductivity provides heat for the sub-surface, which would lead to sublimation and gas transport through a porous surface layer. We have assumed initial LTE at the source. This might be envisaged as gas equilibrating while flowing through the porous surface layer. However, if there is direct ejection, then there will be less energy for the expansion

because the rotational degrees of freedom will not have had time to equilibrate. On the other hand, the gas will be warmer than the free sublimation temperature of water ice if there is sub-surface sublimation followed by interaction with the porous hot inert surface layer. These processes affect the total energy of the gas and thus influences the final gas speed and the lateral expansion. Hence any effects from a different thermal model will impact the gas flow and thus the dust flow. These effect on the solutions presented will need to be assessed.

The outgassing distribution on the surface has been assumed, even in the inhomogeneous case, to be purely-insolation-driven on a regional scale. The morphological evidence from OSIRIS (Thomas et al., (2015a) and Thomas et al., (2015b)) suggests that redeposition of larger particles back onto the surface has produced a coating of «airfall» in several regions. There is no strong evidence for dust and/or gas emission from these coated areas - except for the Hapi region as we have shown in Section 9.1.2. We have discussed how our modelling approach is well suited to test hypothesis linking activity to morphological/topographical variations of the surface. Furthermore, outgassing may be inhomogeneous on a more local scale. This would affect the properties of the gas flow in several ways. For example, local activity will result in lateral expansion close to the source, reducing the energy available for radial expansion and lowering the final gas speed. The interaction between the molecules will have raised their temperature relative to a single source. It remains to be assessed whether the resolution of the grid and the description of active areas can be adapted to provide a realistic simulation of the varying surface outgassing properties.

We have at this stage assumed a single gas species (H_2O) only. But we are aware that CO_2 has a high mixing ratio above the southern hemisphere (Hässig et al., 2015) during our considered time frame. Introducing CO_2 and even CO would result in adding more free parameters which can influence the results. It was our goal to build a modelling pipeline with the least number of free parameters needed to capture the dominant physical processes. We have studied absorbing and reflecting surfaces for the gas dynamics and seen an influence of this choice that cannot be distinguished by the ROSINA/COPS but is seen in the structure of the dust coma. Additionally, we have seen that certain types of activity variations on the surface cannot be differentiated by certain instruments but by others. Hence a multi-instrument approach to understanding Rosetta data is paramount.

We also assumed two extremes for the dust with a specific refractive index (that of astronomical silicate (Laor and Draine, 1993)), a power law distribution and a single fixed size. Although these are common assumptions, they may be violated for numerous reasons in order to match the integrated brightness seen by OSIRIS. Perhaps more critical is that we have assumed as an input condition that the local dust to gas production ratio at the surface is a global constant only modified naturally by means of dust not being liftable depending on the illumination. Given the remarkably diverse surface morphology, this appears to be unjustifiable, but we have no clear evidence to the contrary at this point in time. Local variations in either the dust to gas production rate ratio or the size distribution will make the interpretation of the data much more challenging.

11

CONCLUSIONS

We have set out to examine the neutral gas coma for the autumn 2014 time frame when the comet was at a heliocentric distance of 3.4 AU pre-perihelion. This was done for a wide range of initial conditions ranging from different surface properties (absorbing to reflecting) to different outgassing distributions on the surface (purely-insolation-driven to regionally inhomogeneous). Our analysis has shown that in the considered time span, the most straightforward assumption of purely-insolation-driven emission does not fit the in-situ ROSINA/COPS measurements regardless of the possible surface properties (absorbing/reflecting). This conclusion is strengthened by the fact that the resulting dust coma based on purely-insolation-driven emission does not reproduce the observed structures seen by OSIRIS. The two instruments come to the same consistent conclusion that purely-insolation-driven outgassing cannot be considered a viable solution and thus explanation of the data.

As a next logical step we had introduced regionally varying emission, where the emission within each region was still driven by the insolation but the relative strength of the emission from the individual regions was decreased or boosted. In particular we have found models using an absorbing and reflecting surface with increased activity from the Hapi and Hathor regions will reproduce the ROSINA/COPS remarkably well. This regionally inhomogeneous model is in line with measurements presented by the MIRO (Biver et al., 2015) and VIRTIS (Bockelée-Morvan et al., 2015) teams. Also this conclusion of increased activity from the «Neck» regions is consistent with the independent findings of Bieler et al., (2015). They have found an improvement in their fits to the ROSINA/COPS data with an aposteriori skew of the activity in higher northern latitudes.

We have also set out to test the hypothesis whether activity originating solely from cliff areas on comet CG can account for the measurements seen in the ROSINA/COPS and OSIRIS data sets in the early phase of the Rosetta mission. We have furthermore included the opposite assumption of activity solely from plains. From the analysis of the gas and dust model results we can clearly conclude that a plains-only model of cometary activity is not a feasible option. Regarding the gas, the cliffs-only model performs equally well as the purely-insolation-driven model and can statistically not be differentiated by ROSINA from such a model. Contrarily the cliffs-only

model does not reproduce the dust coma structure and can, on these grounds, be discarded as a valid model. We have also seen that a cliffs + Hapi model performs equally well with respect to the ROSINA/COPS data as the regionally inhomogeneous model. It is not possible to differentiate between them solely with the ROSINA/COPS observations. When looking at the OSIRIS images we give a slight edge to the cliffs + Hapi model over the inhomogeneous model as the latter still exhibits too many dust features as shown in Figure 89. We must stress at this point though that this only means that a cliffs + Hapi model is plausible. We have clearly seen that the solutions are non-unique. Also we need to address the fact that it might not be surprising that models with more free parameters (cliffs + Hapi or inhomogeneous vs. purely-insolation-driven) fit the data better. That is not the striking thing. What needs to be understood is that purely-insolation-driven emission - even though having less degrees of freedom - is insufficient as a model implying directly that more degrees of freedom are needed address the issue of reproducing the data. Nevertheless, it is remarkable that we can reduce the activity of large parts of the cometary surface (all plains except for Hapi) to zero and yet still get good agreement with OSIRIS and ROSINA/COPS data. It must also be noted that these results should only be understood for the studied epoch. The relative contributions of the different areas might change with time, as heliocentric distance and seasons change.

Both our best fit models (cliffs + Hapi and inhomogeneous) require strong emission from the Hapi regions. This indicates that Hapi is distinctly different from other regions with dust layer deposits from «airfall». The reason as to why that is is beyond the scope of this work but warrants further investigation.

The shortcomings of our fits point to stronger locally varying outgassing especially in the northern polar region. This and the fact that multiple inputs can lead to equally good fits (see also Section 7.3) to the data show the importance of including data from other instruments, such as MIRO and VIRTIS, and other data from ROSINA to further constrain some of the free parameters. We have already seen the power of multi-instrument analysis and adding more date will be helpful in the search for a fully consistent model.

Regarding the dust coma we have learnt that for a dust to gas mass production rate ratio, Q_d/Q_g, in the range of $1-10$, we require a power law exponent, b, in the range of $2-3$ to match the observed dust coma brightness. This is consistent with the findings of Rotundi et al., 2015 from GIADA and Merouane et al., 2016 from COSIMA. However these power law models exhibit too many dust filaments

and thus do not match the observed coma structure particularly well. This implies either a locally varying Q_d/Q_g or a locally varying dust size distribution. Furthermore, we have seen that single-sized comae with large particles ($r_d \sim 100$ μm) and dust densities of 440 kg m^{-3} fit the OSIRIS data rather well. As a by-product, we showed how the assumed surface boundary condition (i.e. absorbing vs. reflecting) can change the direction of the dust jet originating in the Hapi region. Including data from dust instruments such as GIADA and COSIMA should be used to check our models and help constrain some of the dust parameters.

Finally we have found that topographic re-radiation provides a solid physical frame work to determine the surface boundary condition regarding reflectivity which leads to an improvement of the fits. Also topographic re-radial could be a source of CO_2 activity in shadowed areas - especially in the concave parts of the nucleus - which might contribute to eliminating the shift in the dust jet we observe in our models.

12

OUTLOOK

Our modelling pipeline has been well tested and provides us with a powerful tool for multi-instrument analysis. First let us mention some general considerations before giving two concrete examples of where we are currently making progress in extending our work.

Determining the global and moreover the local gas production rates is of great importance for the understanding of cometary activity. Especially to the point where it can be linked to surface morphology and thus help understanding erosional processes and mass transport. As we have seen, this is not an easy task. Different models can reproduce fairly well the overall measurements of ROSINA/COPS but differ substantially in their respective global and local gas production rates. Often a simple Haser model (Haser, 1957) assuming uniform spherically symmetric emission is used to estimate the global gas production rate. Even the second most simple model - a purely-insolation-driven one - will not be sufficient in explaining the activity of comet CG. Our work and that of others (Bieler et al., 2015; Fougere et al., 2016b; Fougere et al., 2016a) clearly shows that especially with the complex shape of comet CG these kinds of simple models will not produce any sufficiently accurate value for the gas production rate. This is especially true for the local emission rate. The global production rate will be less affected by a «bad» model. Hansen et al., (2016) have applied a more elaborate approach by using activity maps from Fougere et al., (2016a) produced by approximating the gas densities from ROSINA/COPS with spherical harmonics. With this method they estimate the global gas production rate for the entirety of the escort phase of Rosetta and compare the results to published results by the MIRO and VIRTIS teams. Due to the non-spherical shape of the comet we would propose that a spherical harmonics approach might not be sufficient and should be extended. It must be our goal to produce activity maps for the entirety of the escort phase of the mission. Knowing the local gas production rate as a function of time will help to understand processes linked to the sublimation of $H_2O$and other volatiles. Some of the processes we would like to understand are: The link between surface morphology and activity; estimating and understanding the dust mass transport («airfall») which in the current orbital and rotational state is presumably dominated by south to north mass transport (Lai et al., 2016); determining the non-gravitational forces acting on the orbit; and ultimately converging on a self-consistent model of the

processes at and below the surface that result in the observed activity.

Regarding the dust specifically we have in a work by Selina-Barbara Gerig (Gerig, Marschall, and Thomas, 2017) begun to examine systematically the deviations of the dust brightness from the «1/r-law» in the OSIRIS data set. Using our models we have the ability to differentiate between deviations caused by the shape of the comet, the viewing geometry (non-point source effects, phase angle effects), gravitationally bound particles, and others (see Chapter 5). The absence of e.g. fragmentation in our model could exclude this process as a possibility in the case where we are able to fit the data within the framework of our current model.

Throughout this work we have not mentioned the topic of gas and dust outbursts. Outbursts defined as transient events were observed quite frequently especially during the time close to perihelion. Outbursts are distinctly different from the «normal» activity that is reproduced to a very high precision every day. We have not attempted to model these kinds of events. The main reason for that is the implications of their brightness. Contrary to the «normal» dust activity the brightness of outbursts has easily reached or surpassed the brightness of the cometary surface. This indicates that the dust is optically thick and that therefore dust-dust and dust-gas interactions are likely to be important. At this point though, our models are not set up to deal with these kinds of interactions.

Another important prospect for this work is expanding our analysis by including data from more instruments. With regards to the dust we are particularly interested in performing an integration through the dust coma results collecting the respective number of particles along the Rosetta orbit and comparing the resulting dust size distribution and dust speeds to GIADA and COSIMA measurements. For the gas we have made first rudimentary comparisons with MIRO and VIRTIS data (see Section 9.2) but are preparing more in depth analysis within the next months. In the following, we will explain in more detail the direction we have taken for comparing data from these two instruments with our models. Both instruments will help further constrain the model.

As part of the MiARD project we are currently in the process of expanding the gas analysis in different ways. The work on MIRO data is in close collaboration with Ladislav Rezac and David Marshall from MPS. We expand our analysis of MIRO data by not primarily comparing gas column densities along the line-of-sight but rather local gas parameters along a line-of-sight or conversely converting the local gas parameters of our simulations along the line-of-sight

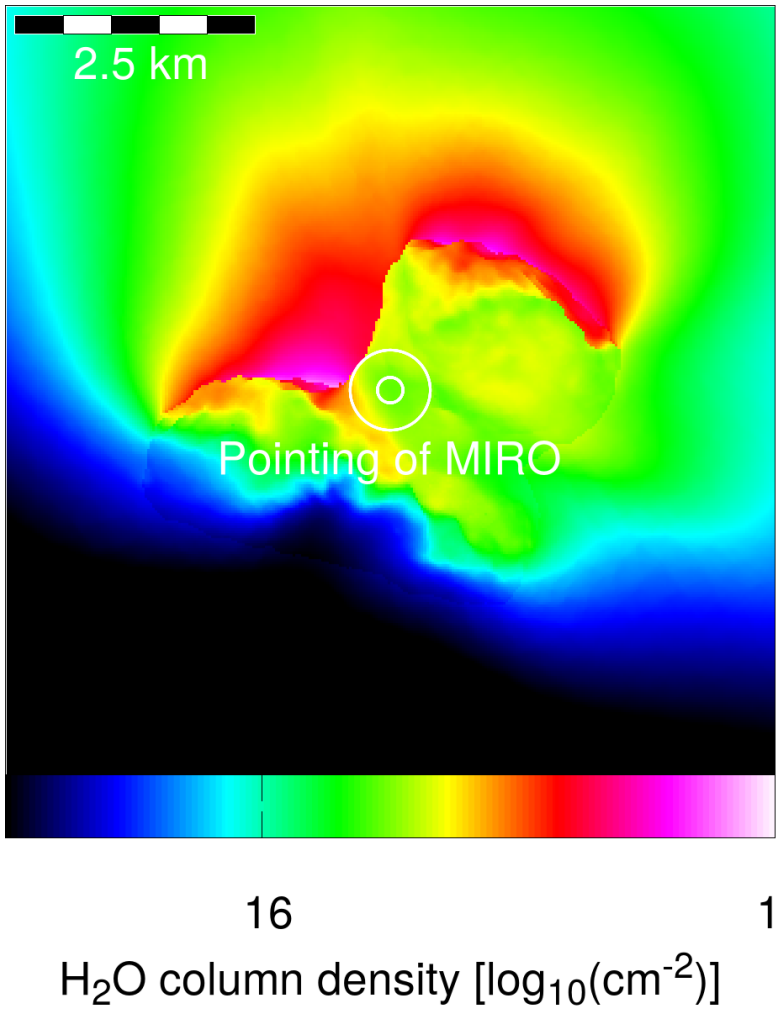

Figure 90: The gas column density for the MIRO observation on 2015-05-03 at 12:30 UTC is shown on log scale. The Sun is at a sub-solar longitude of 228° and sub-solar latitude of 3°. The spacecraft was at time at a cometocentric distance of 130 km and observing the comet at a phase angle of 60°. The MIRO beam of the mm- (large circle) and sub-mm-channel (small circle) are also plotted.

into a predicted MIRO absorption spectrum. In this context we have performed profile extractions along the corresponding lines-of-sight using SPICE for 52 MIRO observations between the 2015-05-02 and 2015-05-18. The model we are using is a purely-insolation-driven emission model with an eaf of 2%. One example showing the water column density and the pointing of MIRO is presented in Figure 90. The field of view of the column density map in this example is arbitrarily set to 8 km to give the context of where the profile has been extracted. The large number of observations provide for a wide range in observation and illumination geometries.

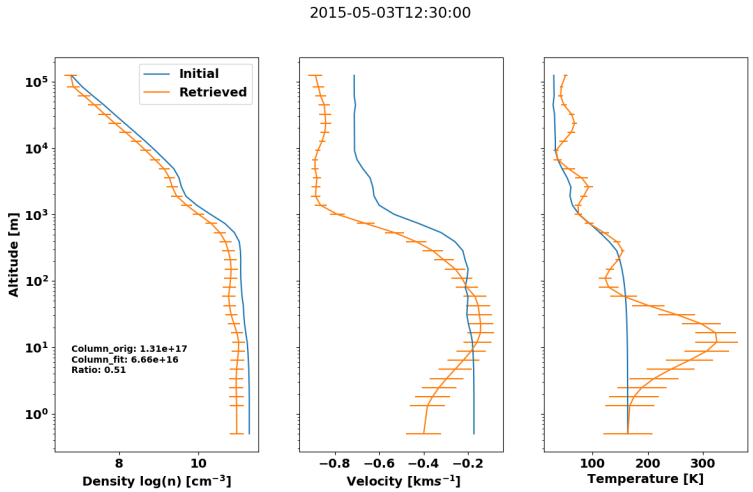

Figure 91: Here we show the local gas number density (left panel), the gas speed along the line-of-sight (centre panel), and the gas temperature (right panel) along the line-of-sight of the observation shown in Figure 90. The blue lines are the extracted values from our model and the orange lines are direct retrievals from the fitting of the spectral lines. Figure courtesy of Ladislav Rezac

Figure 91 shows the local gas number density, the component of the velocities along the line-of-sight, as well as the temperature as a function of the altitude from the surface along the line-of-sight for the observation on 2015-05-03 at 12 : 30. Ladislav Rezac has used these extracted profiles to produce an artificial absorption spectrum for the direct comparison with the spectrum acquired by MIRO. The result (blue line) is shown in Figure 92. The spectrum from our model does not fit the actual spectrum well. Ladislav Rezac has used an inversion algorithm taking into account non-LTE effects to invert the spectrum to local gas properties. The result of this is shown as the orange lines in Figure 91 and Figure 92. The error bars are due to the noise of the data. We see that the retrieved spectrum fits the actual measurement very well and we can get first conclusion from the comparison of the model profiles to the retrieved ones. First the local number densities of the model seem too high, resulting in a gas column density roughly a factor of two too high. Additionally, the gas speeds as well as the temperatures in the model are too low. When the gas is hotter at the surface this would result in higher temperatures in the coma but also higher gas speeds. We should stress here though that these are just preliminary results for one MIRO spectrum and more work needs to be done to find solid conclusions and constraints for the model. But this first comparison does show how MIRO data can constrain our models.

For VIRTIS we are focusing on gas column densities derived from VIRTIS-M-IR. This work is being done in close collaboration with

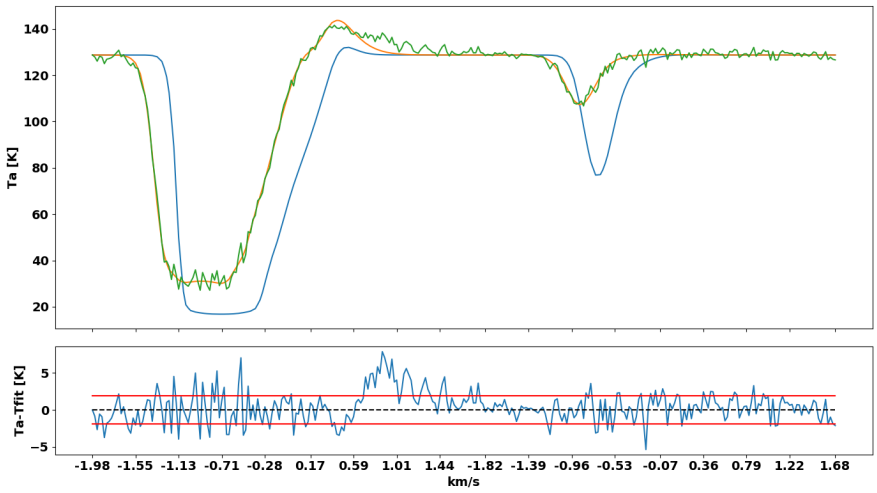

Figure 92: The top panel shows the MIRO spectrum (green line) from the 2015-05-03 at 12:30 UTC observation. The blue line shows the artificial spectra using the local gas properties from our model. The orange line represents the retrieved spectrum resulting in the local gas properties seen in Figure 91. The bottom panel shows the difference of the measured antenna temperature, T_a, and the retrieved spectrum. Figure courtesy of Ladislav Rezac.

David Kappel from DLR, Berlin. The VIRTIS-M-IR instrument acquired spectrally resolved images (i.e. «cubes») of the coma. Using the algorithm described by Migliorini et al., (2016) (continuum subtraction and emission band integration) David Kappel has determined the H_2O gas column densities for each pixel of each cube recorded by the instrument. To increase the signal-to-noise ratio (SNR), some additional preprocessing steps had to be applied, including a median smoothing and a 2×2 pixel binning of the cubes. We focus primarily on the time span where the nucleus activity is noticeable uptil cryocooler failure in May 2015. Furthermore we concentrate on cubes with a significant number of pixels sampling the coma giving us sufficient context for the comparisons. Although the SNR is significantly lower than for VIRTIS-H coma measurements, the latter provide gas column densities only for a single line-of-sight at a time, whereas the VIRTIS-M-IR data has the great advantage that it is capable to map the spatial distribution of the gas coma. Because the different lines of a VIRTIS-M-IR cube were acquired by scanning the scene with the movable mirror and were thus acquired at different times we computed the viewing geometry for each pixel individually. We compare here the two cubes a) and g) from Fig. 6 of Migliorini et al., (2016) with the same model as for the MIRO comparison above. Cube a) was acquired on 2015-04-11 between 13:18:05 and 14:03:21, and cube g) was acquired on 2015-04-12 between 07:52:57 and 08:16:16. Figure 93 shows for the two cubes the radiance and H_2O column density from VIRTIS-M-IR (left and centre columns) and

the results from the column integration of our model (right column). The model fits fairly well for cube g) and a pixel for pixel comparison has shown that the model number densities are roughly 30% too high, which, considering that the data was taken roughly one month earlier than the model was built for, this result is consistent with the rough estimate from the first MIRO comparison. The result for cube a) is quite different. Although we match the emission coming from the «Neck» regions we see no emission from the Imhotep area in the data whereas the model clearly shows exactly that. This illustrates that we can use VIRTIS-M-IR to help constrain not only the rough level of emission but also its distribution. Complementing this analysis we will also include data from VIRTIS-H which has a much higher SNR but will require time integration.

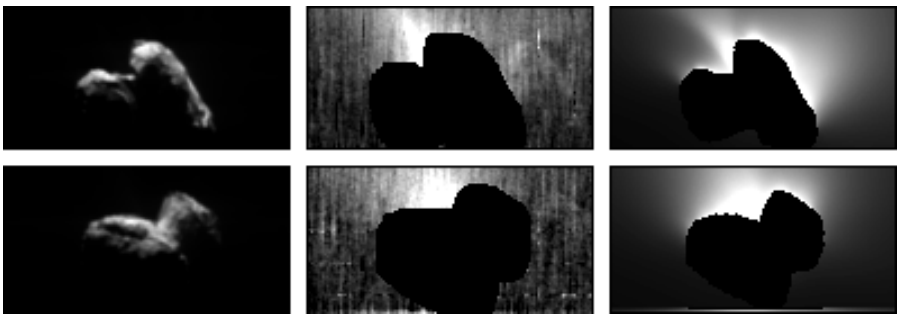

Figure 93: Cubes a) and g) from Fig. 6 of Migliorini et al., (2016) are compared to our model. The top row shows cube a), and the bottom row shows cube g). The right left column shows the VIRTIS-M-IR radiance, the centre column shows the VIRTIS-M-IR H_2O column density with the nucleus blacked out and the right column shows the H_2O column density from our model. We are only interested in a qualitative comparison and thus the scales are not shown but are the same within each of the columns. Figures from VIRTIS-M-IR were produced by David Kappel.

Part VI

APPENDIX

The five appendices collected here represent smaller projects as part of the work done in the past years. They only indirectly relate to the main work of this theses. Some of them are still work in progress and thus do not contain fully fleshed out results.

A

SPHERICAL NUCLEUS WITH A JET

As part of this theses we have not looked at the influence of jets (high emission from very limited spacial region). In Part iii we have studies, amongst other things, purely-insolation-driven outgassing from a sphere. Here we want to expand theses spherical cases with cases that contain a single jet. The three cases set up all contain one single jet at the sub-solar point. The eaf at the sub-solar point is 20% and drops with a cosine ($\sim \cos(\alpha \frac{90^\circ}{1.5^\circ})$) from the sub-solar point to the edge of the jet at 1.5° from the sub-solar point. The value at the edge of the jet is scaled to the respective background eaf. Three backgrounds have been considered:

1. No background: The eaf outside of the jet area is 0%. The global production rate for this case is 0.14 kg s^{-1}.
2. Low background (1% background): The eaf outside of the jet area is 0.2%. The global production rate for this case is 2.13 kg s^{-1}.
3. High background (10% background): The eaf outside of the jet area is 2%. The global production rate for this case is 20.12 kg s^{-1}.

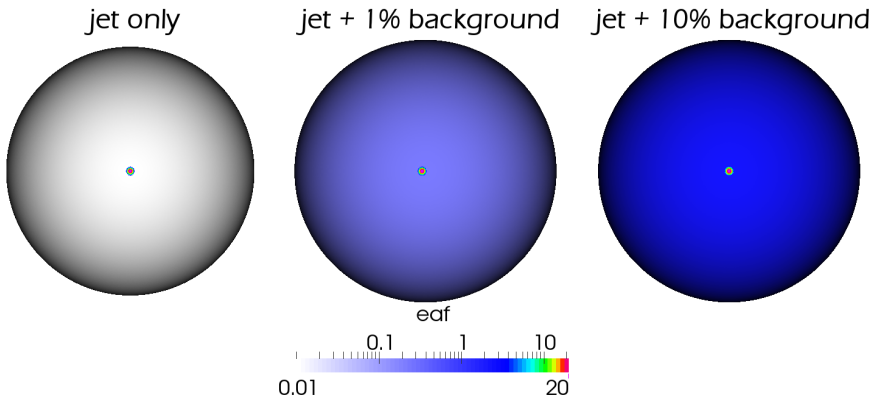

Figure 94: The three panels show the eaf [%] of the three cases with a jet. The phase angle in this view is 0°. The left panel corresponds to the set-up of the case with only a jet, the centre panel to the jet + 1% background case, and the right panel to the jet + 10% background case.

The eaf of theses three cases is shown in Figure 94. The value of 2% in the high background cases also corresponds to the eaf of the mid activity purely-insolation-driven case of Chapter 6. From

the global production rates we can clearly see that in the two cases with the background this kind of jet contributes only a small fraction of the gas emission. But the emission is concentrated to a rather small surface area. Theses cases with an equally strong jet but varying background allow us to study the jet-background interaction.

Figure 95 shows cuts through the 3D gas solutions showing only the x-z-plane. The rows show from top to bottom the purely-insolation-driven case, the jet + 10% background case, the jet + 1% background case, and the jet-only case. The gas number density (left panels) shows that we only see a minor influence of the jet in the 10% background case. A clear influence of the jet can be seen in the 1% background case. The jet only case shows how lateral expansion fills much of the simulation domain with gas even though the emission comes from a very small active area only. The differences to the purely-insolation-driven case are more pronounced in the gas speeds (second column from the left) where in all cases including the jet the gas speeds above the jet region show very high speeds very close to the surface. We also see that the opening angle of the jet gets narrower the higher the background. This is due to the fact that gas from the background is producing a pressure inhibiting the lateral expansion of the jet. In the radial speed component (second column from the right) we only see minor differences between the jet cases with background and the purely-insolation-driven case. It is only in the jet-only case where we see the signature of the strong lateral expansion towards the night side. Finally there are big differences between all cases when looking at the ratio of the rotational and translational gas temperatures (right panels). In the jet-only case the gas is in equilibrium solely very close to the source and then quickly the temperatures diverge. This is due to the flow going over to collision-less radial outflow much faster than in the other cases «freezing» the non equilibrium temperatures into the flow. The more background we add to the system the larger the volume of the simulation domain with equilibrated gas. Again the case with the jet + 10% background can hardly be differentiated from the purely-insolation-driven case.

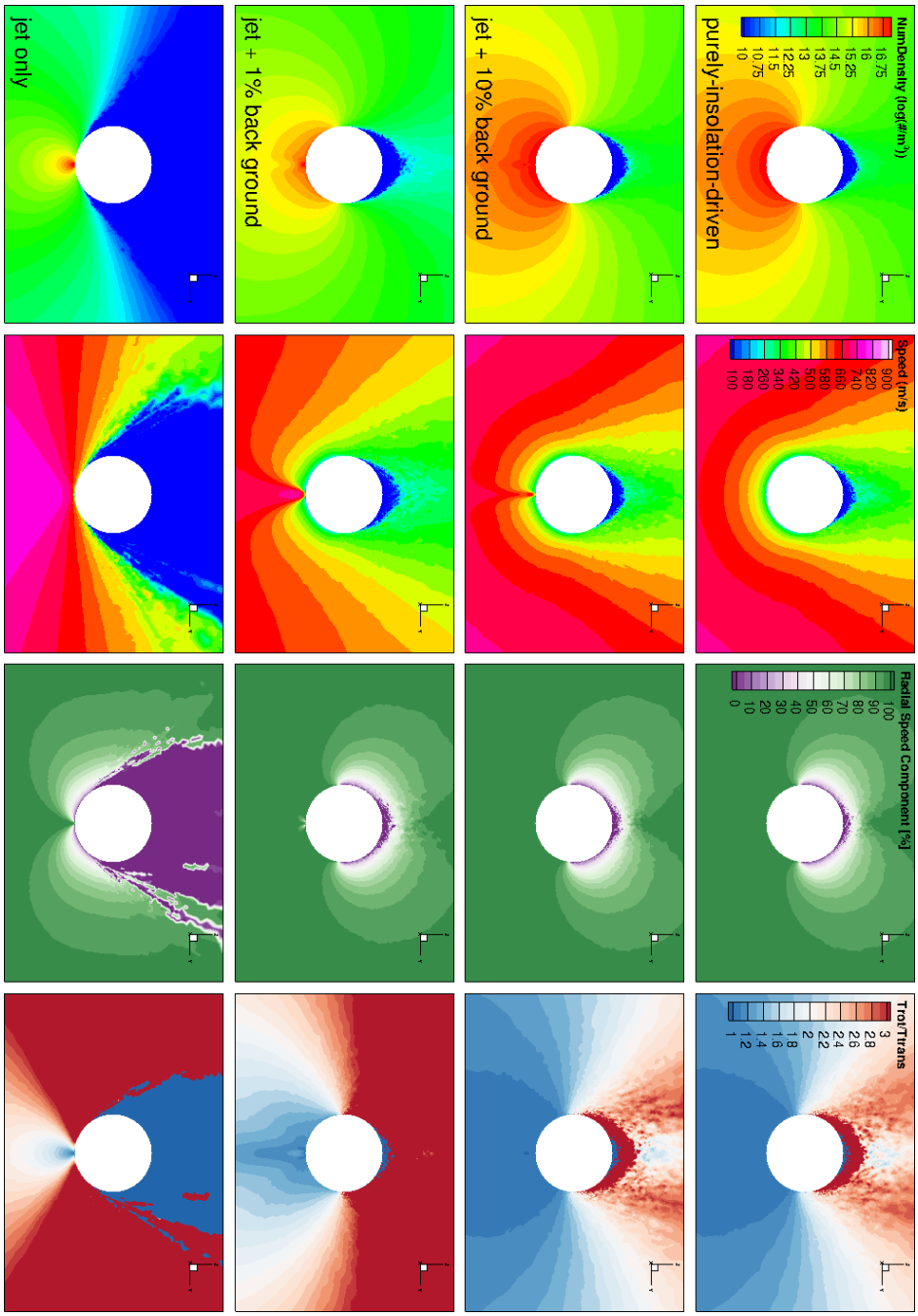

Figure 95: We show here cuts through the 3D gas solutions showing only the x-z-plane. The rows show from top to bottom the purely-insolation-driven case, the jet + 10% background case, the jet + 1% background case, and the jet-only case. The columns show from left to right the gas number density [$\log(m^{-3})$], the gas speed [$m\ s^{-1}$], the fraction of the speed in radial direction [%], and the ratio between the rotational and translational temperatures.

We have also produced the azimutally integrated gas column densities multiplied by the impact parameter as a function of the impact parameter as shown in Figure 96. As explained in Chapter 5 the deviations from the «1/r-law» are mainly due to acceleration and lateral expansion of the gas. There is hardly any difference in the two cases with a background. The case with only the jet shows a much steeper decline within the first two kilometres above the surface compared to the background cases. Beyond four kilometres a flatter behaviour of the jet-only case is observed. This is indicative of the much higher acceleration in the jet-only case which then goes over to an almost free radial outflow much earlier than the cases including a background.

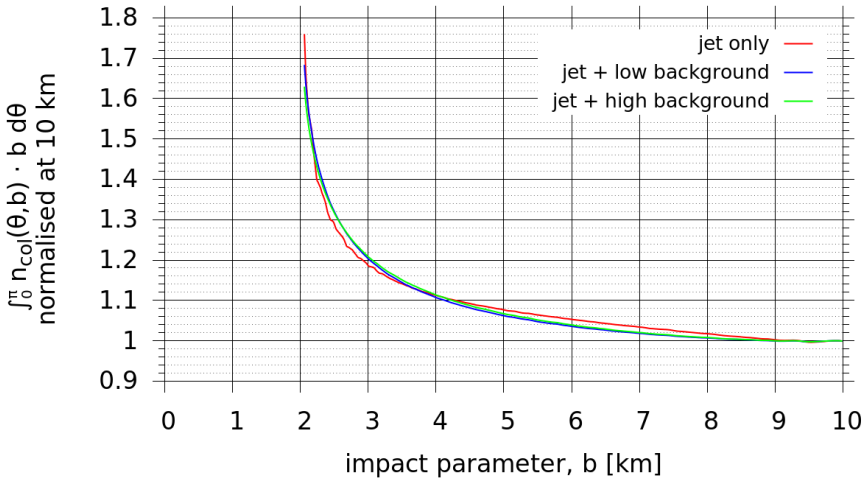

Figure 96: The azimutally integrated gas column density multiplied by the impact parameter as a function of the impact parameter is shown here for the three models with a jet.

Finally we have also looked at the behaviour of the dust in a jet environment. Figure 97 shows the dust column density of 500 µm particles in the jet-only flow field. The dust coma clearly expands laterally less than the gas coma. The two more interesting cases are the ones with a background. Figure 98 and Figure 99 show the dust column density for 500 µm particles in the jet + background cases. We can clearly see the influence of the jet on the dust distribution with a «build up» along the interface between the jet and the background flow. Particles coming from the background regions are picked up by the faster flow at the jet boundary. Inside the volume influenced by the jet directly - this can be seen especially well in the low background case - the dust density drops faster than in the background regions. This is due to the higher relative acceleration of the dust originating in the jet area of the surface. The largest difference between the two background cases is the opening angle of the jet. In the low background case this angle is much larger than in the high background case. The jet can more easily expand laterally in a low background

environment. We can also observe in both of these cases that there is dust transport from the day to the night side. In the low background case this is even more pronounced because we can see a clear «fountain like» structure on the night side produced by the graviationally bound particles. How the fraction of gravitationally bound particles is influenced by a jet is shown in Figure 100. In the low background case the fraction of particles that is being re-deposited on the surface rises to 30% between 0.1 and 1 mm and then drops to almost zero again before rising to 100% for 2 cm particles. Hence no particles larger than 2 cm escape. The drop is causes by the fact that beyond 1 mm particles are no longer lifted from the background emission region. The fraction of gravitationally bound particles below 1 mm comes purely from the background emission region. Particles up to 1 mm size that originate in the jet emission area all escape and do not fall back to the surface.

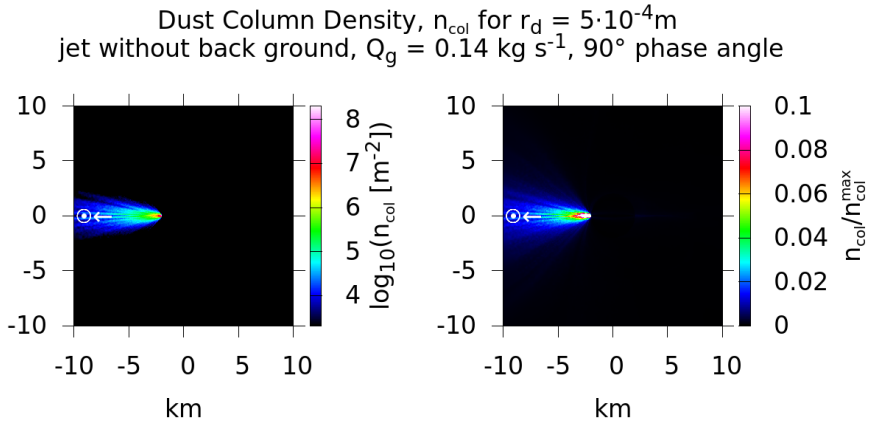

Figure 97: The dust column density for the jet-only case is shown in absolute units (left panel) and relative units (right panel) for a dust size of 500 µm. A dust to gas production rate ratio of unity is assumed.

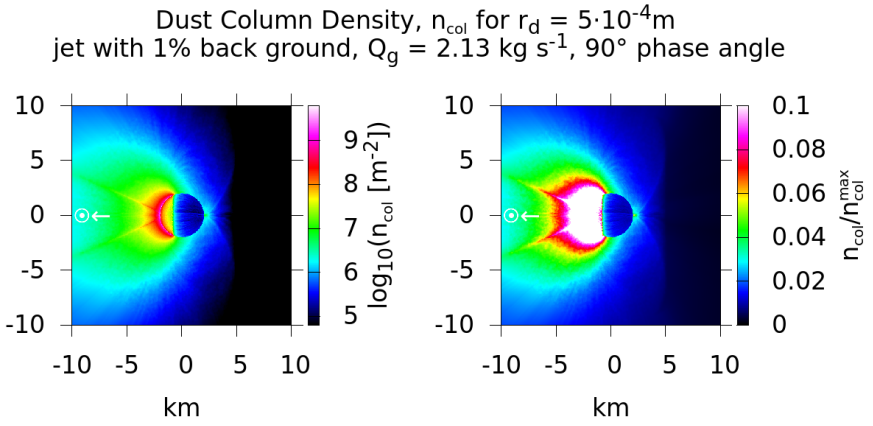

Figure 98: The dust column density for the jet + 1% background case is shown in absolute units (left panel) and relative units (right panel) for a dust size of 500 µm. A dust to gas production rate ratio of unity is assumed.

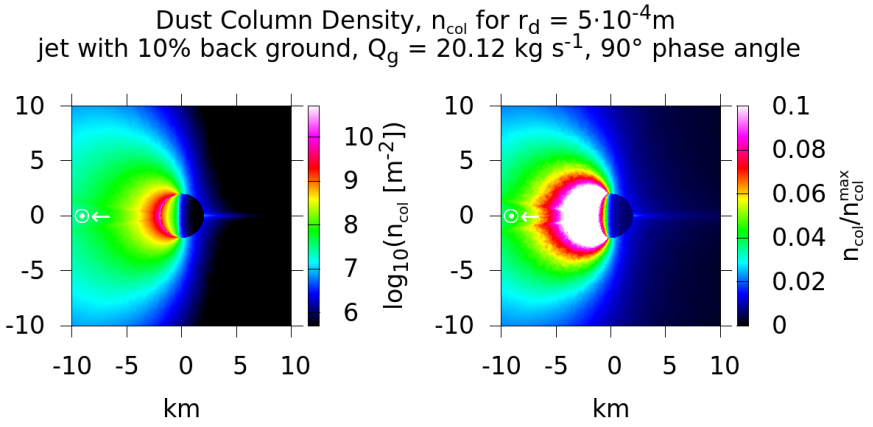

Figure 99: The dust column density for the jet + 10% background case is shown in absolute units (left panel) and relative units (right panel) for a dust size of 500 µm. A dust to gas production rate ratio of unity is assumed.

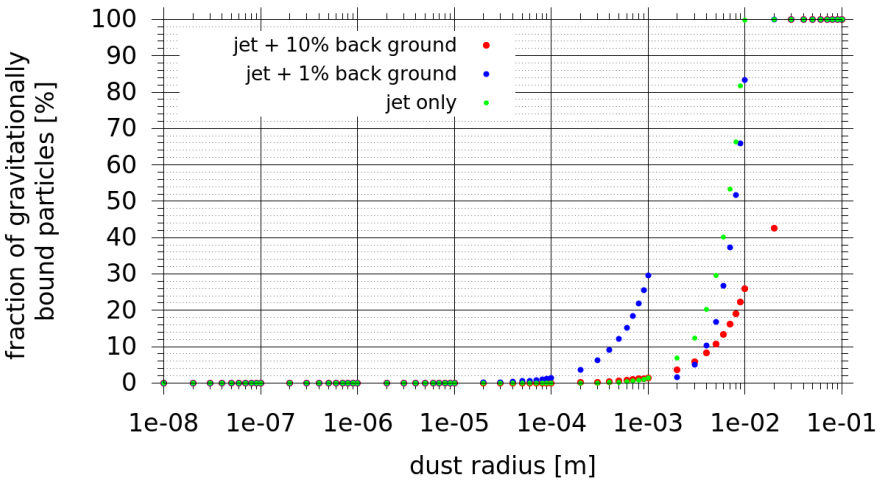

Figure 100: For the three jet models the fraction of particles that leave the surface but do not reach the escape speed are shown here as a function of the dust size.

B

GRAVITATIONAL DUST TRANSPORT

This chapter is based on work done as part of Thomas et al., (2015a) where we have studied the effect of the unusual gravity field on the trajectory of large/slow moving dust particles. Understanding dust transport is vital in understanding the large dust covered areas in the northern hemisphere of comet CG. Such dusty deposits can be explained by airfall - re-deposition of ejected particles from other regions. We consider here particles that are mainly undisturbed by the gas drag and thus neglect it as we are only interested in the gravitational effects. Because the particles we seek to study will have speeds below the escape speed and thus are also much slower than the rotation rate of the comet we need to take into account the Coriolis and centrifugal accelerations. In this specific case the equation of motion is independent of the mass. To determine the trajectory of particles with speed, $\vec{v}$, we solve numerically the equation of motion

$$\frac{d\vec{v}}{dt} = \vec{a}_G + \vec{a}_C \tag{42}$$

$$= \vec{a}_G - 2(\vec{\omega} \times \vec{v}) - \vec{\omega} \times (\vec{\omega} \times \vec{x}) \quad , \tag{43}$$

where $\vec{a}_G$ is the gravitational acceleration according to the calculation in Section 4.3, a_C are the Coriolis and centrifugal acceleration, $\vec{\omega}$ is the direction of the rotation axis of the comet and its magnitude equals the angular speed of the comets' rotation. The rotation period is set to 12.4 hours and we assume a pure spin.

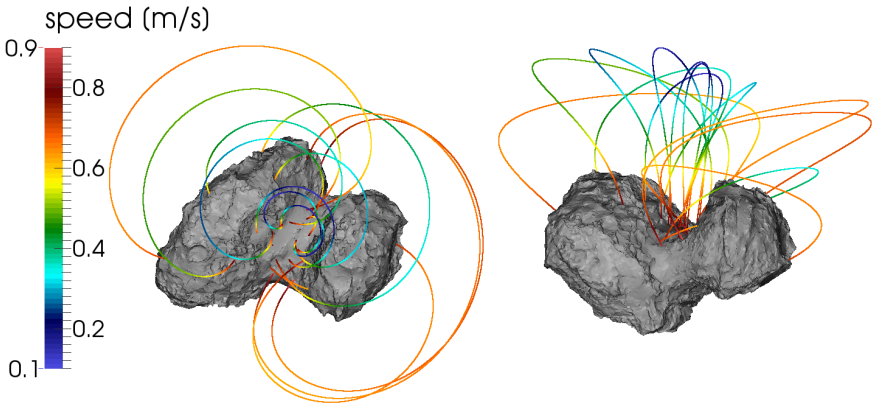

Figure 101: Trajectories of particles in 3D originating in the «Neck» region are shown in two views with the corresponding local speed colour coded. The particle trajectories are shown in in the comet frame, the frame co-rotating with the nucleus.

We assume that particles have an initial velocity at the surface, $\vec{v}_i$, that varies between 0.1 and 0.9 m s^{-1} and is directed randomly within a 3° cone of the respective surface normal. An illustration of what particle trajectories look like is shown in Figure 101. The trajectories are shown in the co-rotating frame of the comet and are thus bent due to the rotation of the comet. The effect of the rotation is stronger the further away particles are from the rotation axis. For the different initial speeds we calculate the location at which 100′000 test particles impact the surface. In this way we can study the deposition range of a certain initial region of dust emission. As our initial dust emission region (seed region) we have chosen a part of the Hapi region where strong dust activity was observed in the early part of Rosetta's escort phase (Section 9.3). Figure 102 shows the result of this calculation for different initial particle speeds. At low speeds particles remain close to or within the seed region. At an initial speed of 0.7 m s^{-1} we reach almost the entire northern hemisphere. Relatively few particles reach the southern hemisphere as e.g. Khepry and Imhotep. For lower speeds than 0.7 m s^{-1} the dust cover on the northern hemisphere is greatly reduced as particles with initial speeds of less than 0.5 m s^{-1} barely escape the «Neck» region. For higher speeds dust particles also reach the southern hemisphere or escape the gravity field (reach the 10 km boundary of our simulation domain). Airfall deposits on the northern hemisphere can thus not only be built up from dust transport from the southern hemisphere during the time of highest activity close to perihelion but also from re-deposition of particles originating from the «Neck» and covering the northern dusty regions. The relative contributions of south-to-north and north-to-north re-deposition will need further investigation. Understanding dust re-deposition is an important part of understanding cometary activity because a dry dust cover can insulate the ice rich layers and thus lead to reduction or termination of activity.

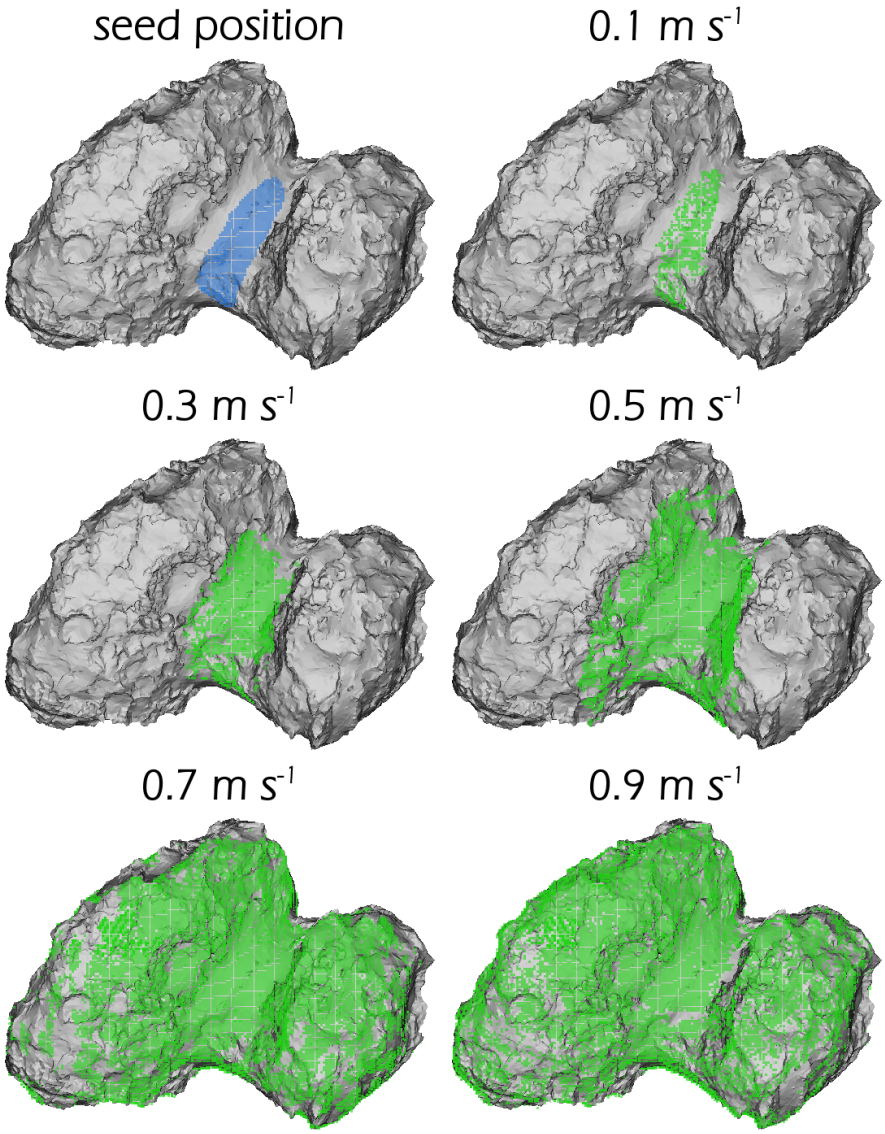

Figure 102: The impact locations (green areas) of particles originating in the seed area (top left, blue) are shown for different initial particle speeds.

C

SPECTRAL ALTERATIONS OF THE COMETARY SURFACE DUE TO THE DUST COMA

Colour variations on the cometary surface has been observed by Fornasier et al., (2015) for comet CG. The surface of comets is more red than the solar spectrum. Additionally for comet Halley the Halley Multicolour Camera (HMC) (Schmidt et al., 1986) observed that the surface was less red than the dust coma (Thomas and Keller, 1989). Why is the surface bluer than the dust coma? The fact that the surface is less red can be caused by multiple processes. Firstly the surface - as the source of the cometary activity - could contain a larger amount of ices than the ejected dust. While the ice is mixed with the dust on the surface it appears bluer than when the dust is lifted by the sublimated ice. Secondly water could re-condensate in shadowed parts of the comet (Rubin et al., 2014) which can make the surface appear more blue when it re-enters the Sun light. This process is time dependent because the exposed ice sublimates when heated by the Sun light. Thirdly the presence of dust particles between the sun and the surface and subsequently between the surface and the spacecraft can alter the solar spectrum by means of scattering of the light. Especially scattering on large particles will result in a bluing of the spectrum. Such alterations of the surface colour has also been observed e.g. on Mars (Thomas et al., 1999). We will explore this last option to determine whether the presence of dust can account for all or parts of the observed change in surface colour.

We use the same scattering model as described in Section 4.10 to calculate the scattering properties of astronomical silicate for different sized spherical particles. We then apply a variety of dust size distributions, examples of which are shown in Figure 103. Especially we also use the size distribution measured by McDonnell et al., (1987) for comet Halley and the one by Markiewicz et al., (1999) for Martian aerosols. The dust emission is mainly in the sunward direction and thus the spectral alteration is primarily influenced by this part of the coma. To mimic the dust enhancement in the sunward direction we have assumed three different cases. Firstly that the main dust features are dominated by a $1°/10°$ cone in the sunward direction. Secondly we have assumed the full $90°$ cone from which the surface receives light but scaled the contribution from the different phase angles, α, from which the incoming light strikes the surface with $\cos^2(\alpha)$. This mimics the diminished emission of dust in the α direction and the diminished light flux from that direction. We refer to these scalings

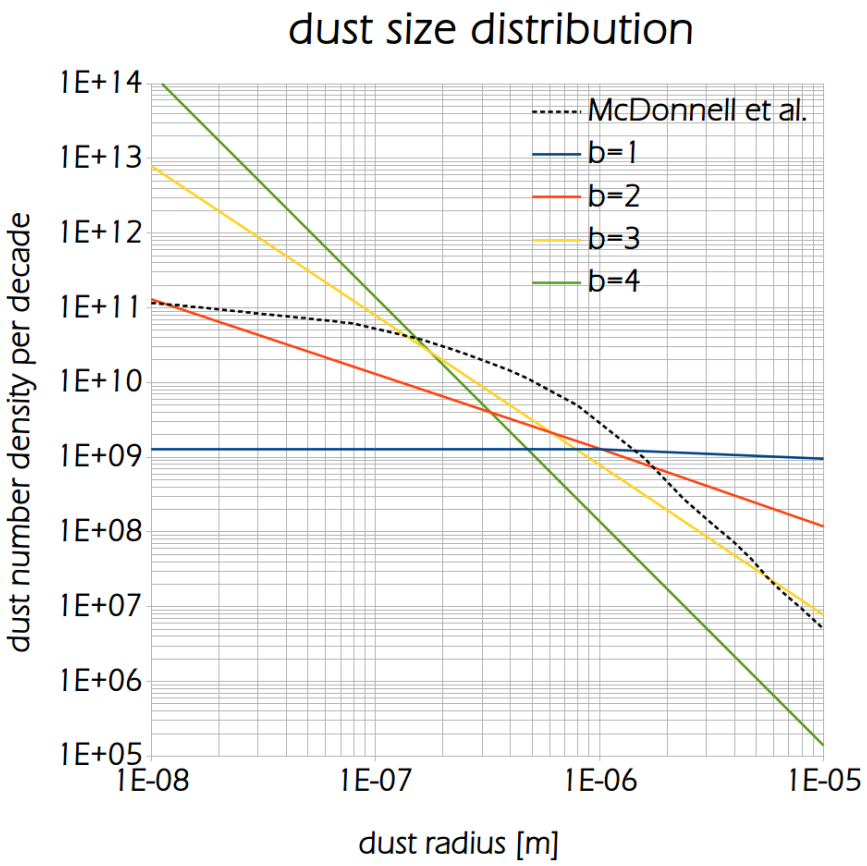

Figure 103: The number of particles per decade is shown for different dust size distributions. For the power law distributions the number of particles is proportional to r_d^{-b}, where r_d is the radius of the dust particles and b is the power index.

as different spacial dust distributions. Figure 104 shows the spectral slope for the different size distributions, different optical depths and spacial dust distributions. The spectral slope, s, is calculated by evaluating

$$s = \frac{F_c(\lambda_2) - F_c(\lambda_2)}{F_c((\lambda_2 - \lambda_1)/2)} \frac{100}{\lambda_2 - \lambda_1} 100\% \quad , \tag{44}$$

where F_c is the colour flux compared to the solar flux, and we have chosen $\lambda_1 = 400$ nm and $\lambda_2 = 800$ nm. The spectral slope has units of percent per one hundred nanometres. A negative spectral slope indicates that the spectrum is becoming more blue. The shown results only account for the spectral alteration between the Sun and the surface and neglect any effect between the surface and the spacecraft. We can see that for both non power law distributions we have slight blue slopes for all spacial dust distributions and optical depths. The higher the optical depth the stronger the bluing effect. For the power law distributions the spectral slope is negative in all cases up to a power index of $\sim$ 2.8 after which the spectral slope becomes

red. Again the higher the optical depth the stronger the spectral alteration. The strongest blue slope is achieved with the highest shown optical depth and lowest shown power index. For this distribution the scattering cross section is dominated by large particles, as can be understood from Figure 103.

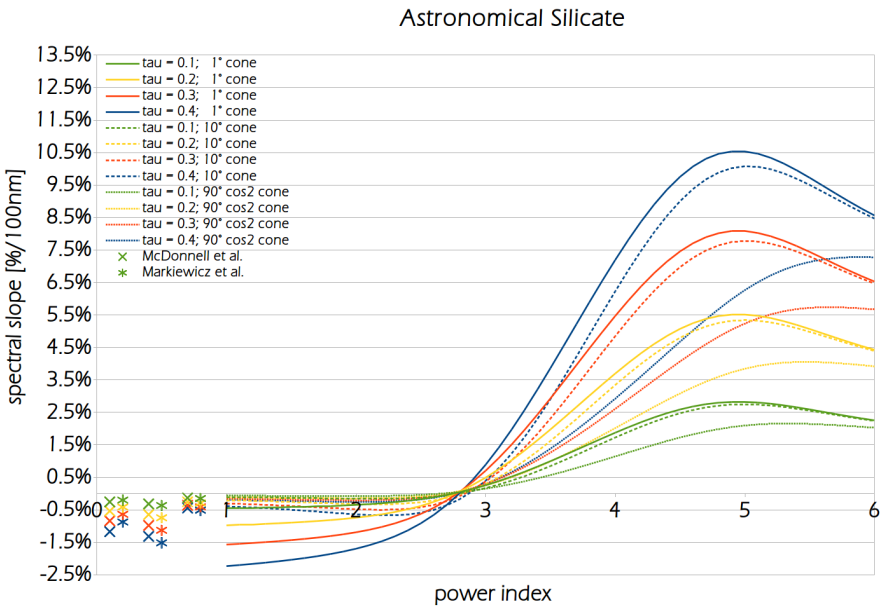

Figure 104: The spectral slope is shown for different optical depths, spacial dust distributions, and dust size distributions. A negative spectral slope indicates that the spectrum is becoming more blue.

As we have seen the light coming from the Sun is spectrally altered by the dust between it and the cometary surface but then the reflected light is further altered on its way from the surface to the spacecraft. This second alteration can in some cases be even stronger than the first because it is influenced by a much smaller solid angle. The 1° cone results hint at this behaviour. Additionally the spectral slope can be more blue if the dust size distribution is dominated or has an enhancement at ~ 0.5 µm. In conclusion this analysis shows that the dust coma can alter the surface colour significantly.

D

DETECTION AND SIZE DISTRIBUTION OF LARGE PARTICLES USING OSIRIS

This chapter is based on an exploratory analysis as to whether the dust size distribution of large dust particles can be derived from OSIRIS data. In some OSIRIS images we can not only see the brightness of the non resolved (diffuse) dust coma (as studied in Part iv) but rather a large number of individual large dust particles can be seen. We attempt to detected and characterised such particles.

We have taken the approach to automatically detect the dust particles within a certain region of interest of an OSIRIS image, measure the brightness of theses particles and convert the brightness into a dust radius. This allows us to determine the number of particles within the column of the respective line-of-sight as a function of dust size. By probing different regions of interest we can determine variations in the dust distribution. To make these calculation we make two assumptions. Firstly, we assume that the detected particles are close to the surface of the nucleus and can thus be considered to be at the distance from the spacecraft to the comet centre. When fitting the brightness of the particles in the images with a two dimensional Gaussian, the full width at half maximum was determined to be less than one pixel. This indicates that the particles are not resolved and cannot be too close to the camera as they would go out of focus and have a larger full width at half maximum (Drolshagen et al., 2017) and additionally for longer exposure times would produce tracks (Cremonese et al., 2016). Secondly, we assume the particles to be spherical and their surface to be scattering the light like a Lambertian surface.

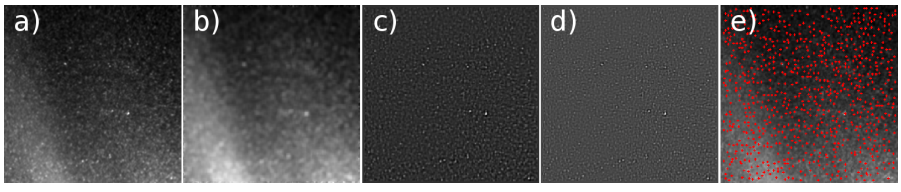

Figure 105: The process of automatic particle detection is shown in this sequence of images. Image a) shows the original unprocessed OSIRIS image, image b) is after smoothing, image c) is the subtraction of image b) from a), image d) is after contrast enhancement, and finally image e) depicts the original with red crosses where particles have been detected.

To detect and characterise particles we perform the following steps. Firstly, the image (or part of it, when we only consider a region of interest) is smoothed as shown in image b) of Figure 105. Secondly, the smoothed image is then subtracted from the original image removing most of the diffuse dust coma background. This is shown in image c) of Figure 105. Thirdly, we apply a Sobel filter for edge detection and then enhance the contrast of the image. This is shown in image d) of Figure 105. Fourthly, to detect particles we calculate in the high contrast image of the previous step for every pixel with coordinates $[i, j]$ the standard deviation, σ, within a box of $[i-3 : i+3, j-3 : j+3]$ around that pixel. If the value of that pixel is 2.5σ higher than the mean value of the box, we flag this pixel as containing a particle. This is shown in image e) of Figure 105. Fifthly, we fit a two dimensional Gaussian to the original image within the box around the respective pixel described above. From the fit we calculate the brightness beneath the fit subtracting the diffuse coma background. Finally, this brightness of the dust particle, F_d, can be used to determine the dust radius using a scattering model.

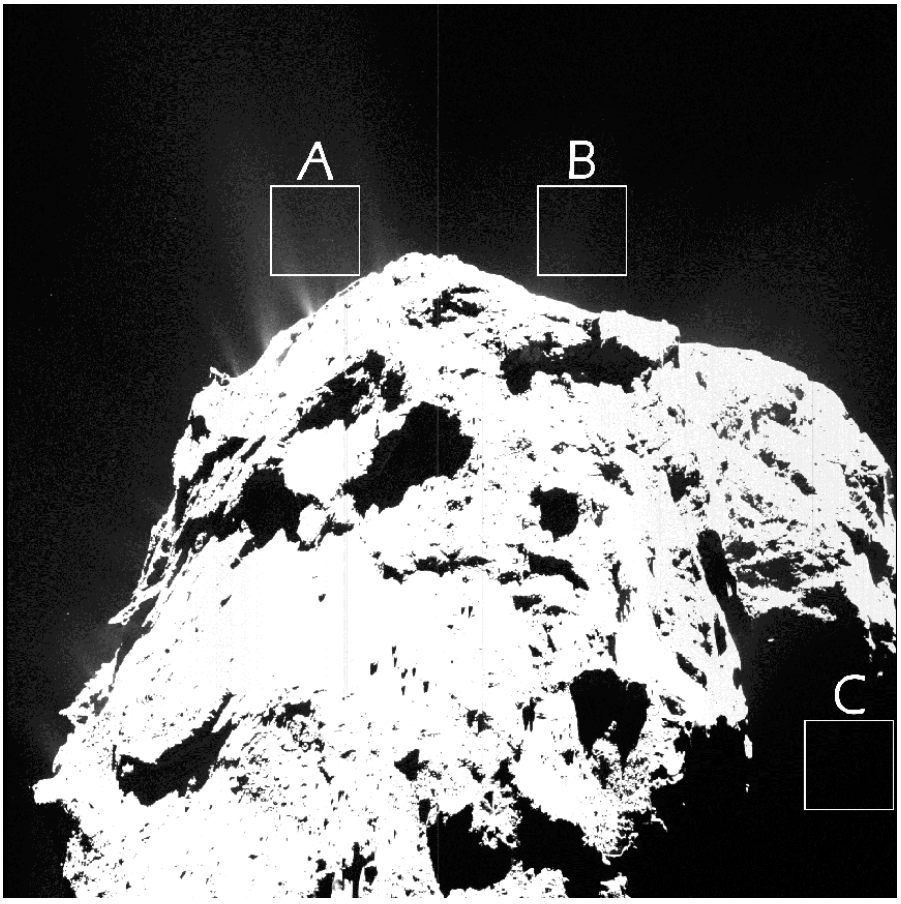

Figure 106: OSIRIS image WAC_2015-12-06T21.12.56.009Z_ID30_1397549000_F22 and three regions of interest (A, B, C) which are considered here.

For the final step of converting the dust particle brightness to a dust radius we assume that the particles are Lambertian spheres. In that case the scattering phase function, ϕ, is defined as

$$\phi(\alpha) = \frac{1}{\pi}\left[\sin(\alpha) + (\pi - \alpha)\cos(\alpha)\right] \quad , \tag{45}$$

where α is the phase angle. A particle of radius, r_d, will then have the brightness

$$F_d = A\frac{\phi(\alpha)}{q}\frac{\pi r_d^2}{d_c^2}\frac{F_{sol}}{R_h^2} \quad , \tag{46}$$

where A is the albedo (set to 0.04), q is the phase integral ($= 3/2$ for a Lambertian surface), F_{sol} is the solar flux at 1 AU, d_c is the distance to the comet, and R_h is the heliocentric distance in AU.

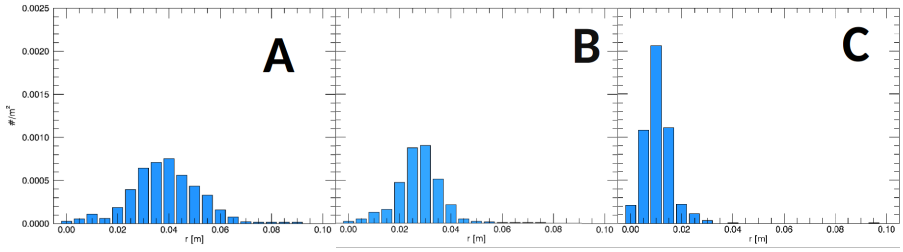

Figure 107: Dust size distribution [m^{-2}] for the three regions of interest of Figure 106.

As a test case we have chosen to look at the OSIRIS-WAC image WAC_2015-12-06T21.12.56.009Z_ID30_1397549000_F22 shown in Figure 106. In particular we have chosen three regions of interest (marked in the image with A, B, and C). Region A is above clearly visible dust activity, whereas region B is located on the day side of the comet but at a place where no clear dust emission can be seen. Finally region C was chosen towards the night side of the comet. For all three regions we have calculated the dust size distribution (number of particles per square meter) as shown in Figure 107. First of all it becomes clear that the observed dust particles are quite numerous and large (several centimetres). We also observe that the dust sizes are largest where we observe the highest activity. From there the dust sizes decrease and the distribution becomes narrower as we go to region B and then to region C which is towards the night side. The size distribution of theses large particles in clearly not at all uniform and varies depending on the location over the nucleus. We should stress though that these are very preliminary results and this analysis needs to be extended such that robust conclusions can be drawn.

E

MAP PROJECTIONS

We have seen in Section 4.2 (illustrated in Figure 10) that the definition of the common longitude/latitude coordinate system does not uniquely describe the surface of comet CG. This can be very clearly seen when showing the regions on a projection map as in Figure 108 and Figure 109. The overlaps produced by the definition of the longitude and latitude in conjunction with the concave shape can be very large. Different regions can hide large portions of other regions. Theses overlaps are particularly pronounce for «Hathor» , «Ma'at» , and «Serqet».

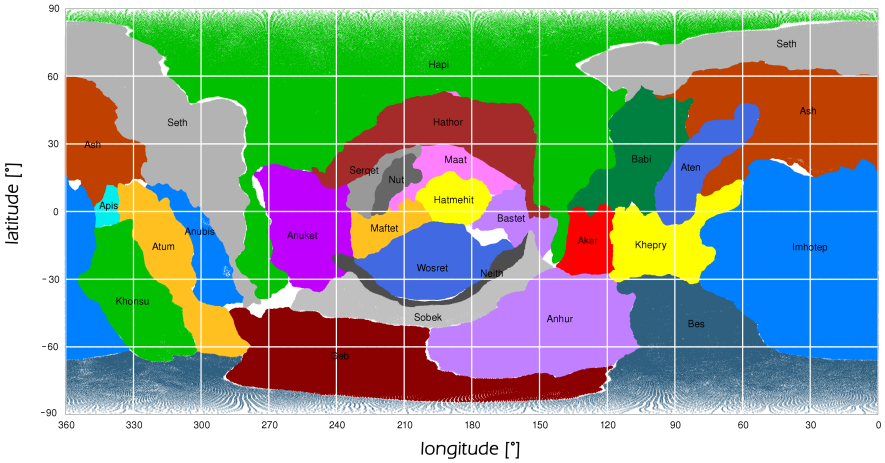

Figure 108: Regional map using the standard longitudinal/latitudinal projection.

To lift this degeneracy we have defined a spherical projection for each of the two lobes dividing the comet through the «Neck» regions. We call this a bi-spherical coordinate system (BCS). The centre of each of the two spherical projections is located within the «head» and «body» lobe respectively. To avoid adding a third coordinate component (in addition to a longitude and latitude) that would differentiate on which lobe we are, we have chosen to encode this information in the latitude. To determine the BCS longitude and BCS latitude the following transformation needs to be performed for a point $\vec{x} = (x, y, z)$ on the surface:

$$x' = x - 512\ \mathrm{m} \tag{47}$$

$$y' = y + 103\ \mathrm{m} \tag{48}$$

$$z' = z \tag{49}$$

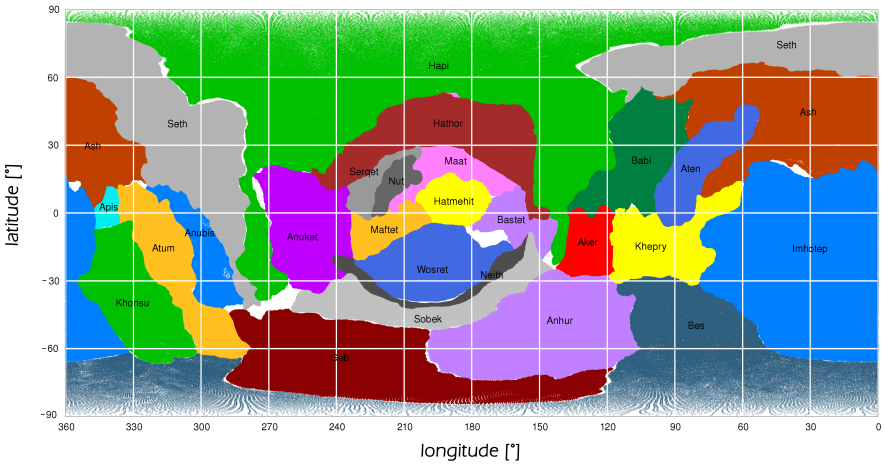

Figure 109: Regional map using the standard longitudinal/latitudinal projection. The regions have been plotted in a different order than in Figure 108 and thus show a different overlap of regions.

This moves the comet slightly before a subsequent rotation about the z-axis by 30° is performed:

$$x'' = \cos(30°)x' - \sin(30°)y' \tag{50}$$

$$y'' = \sin(30°)x' + \cos(30°)y' \tag{51}$$

$$z'' = z' \tag{52}$$

Finally, the two lobes need to be re-centred to their respective new origin that will be used for the spherical projection. Coordinates with $x'' > 0$ correspond to points on the «head» lobe. Coordinates with $x'' \leqslant 0$ correspond to points on the «body» lobe:

$$x''' = \begin{cases} x'' - 1126\ \mathrm{m} & \forall\, x'' > 0 \\ x'' + 1560\ \mathrm{m} & \forall\, x'' \leqslant 0 \end{cases} \tag{53}$$

$$y''' = y'' \tag{54}$$

$$z''' = z'' \tag{55}$$

These coordinates are then converted to longitudes and latitudes as usual except for the fact that we add 180° to all latitudes on the «body» lobe. This results in the coordinate system as shown on the surface of the 3D shape in Figure 110

This kind of BCS projection still has slight degeneracies in particular in the southern hemisphere of the «body» lobe because this lobe is still very much non-spherical by itself. The resulting map projection is shown in Figure 111. The empty space in the middle of this projection arises from the separation of the two lobes which leads to two surfaces that are no longer closed. The BCS projection has the advantage of reducing the overlap of regions and lifts to a large extent the degeneracy of the simple spherical projection.

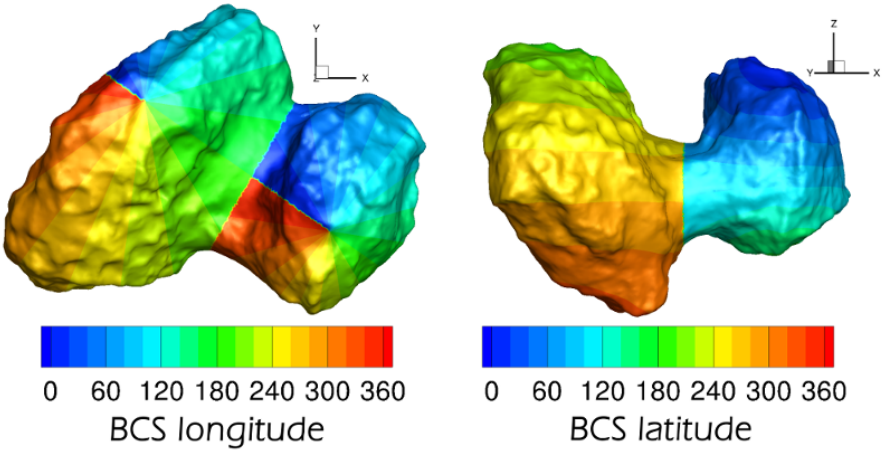

Figure 110: View of the 3D surface of CG from two views with the BCS longitude (left) and latitude (right).

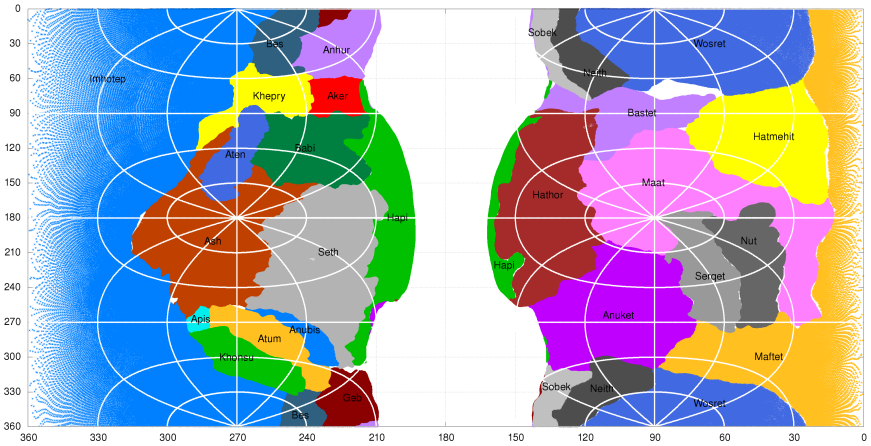

Figure 111: Regional map using the BCS projection.

BIBLIOGRAPHY

Acton, C. H. (1996). "Ancillary data services of NASA's Navigation and Ancillary Information Facility." In: Planet. Space Sci. 44, pp. 65–70. DOI: 10.1016/0032-0633(95)00107-7.

Agarwal, J., M. Müller, and E. Grün (2007). "Dust Environment Modelling of Comet 67P/Churyumov-Gerasimenko." In: Space Sci. Rev. 128, pp. 79–131. DOI: 10.1007/s11214-006-9139-1.

Agarwal, J., M. Müller, H. Böhnhardt, and E. Grün (2006). "Modelling the large particle environment of comet 67P/Churyumov Gerasimenko." In: *Advances in Space Research* 38, pp. 2049–2053. DOI: 10.1016/j.asr.2005.04.046.

Ahearn, M. F., S. Hoban, P. V. Birch, C. Bowers, R. Martin, and D. A. Klinglesmith III (1986). "Gaseous jets in Comet P/Halley." In: *ESLAB Symposium on the Exploration of Halley's Comet*. Ed. by B. Battrick, E. J. Rolfe, and R. Reinhard. Vol. 250. ESA Special Publication.

Bentley, M. S. et al. (2016). "Aggregate dust particles at comet 67P/Churyumov-Gerasimenko." In: Nature 537, pp. 73–75. DOI: 10.1038/nature19091. arXiv: 1704.00526 [astro-ph.EP].

Bieler, A. et al. (2015). "Comparison of 3D kinetic and hydrodynamic models to ROSINA-COPS measurements of the neutral coma of 67P/Churyumov-Gerasimenko." In: A&A 583, A7, A7. DOI: 10.1051/0004-6361/201526178.

Bird, G. A. (1994). *Molecular Gas Dynamics and the Direct Simulation of Gas Flows*.

Biver, N. et al. (2015). "Distribution of water around the nucleus of comet 67P/Churyumov-Gerasimenko at 3.4 AU from the Sun as seen by the MIRO instrument on Rosetta." In: A&A 583, A3, A3. DOI: 10.1051/0004-6361/201526094.

Bockelée-Morvan, D. et al. (2015). "First observations of H_2O and CO_2 vapor in comet 67P/Churyumov-Gerasimenko made by VIRTIS onboard Rosetta." In: A&A 583, A6, A6. DOI: 10.1051/0004-6361/201526303.

Bohren, C. F. and D. R. Huffman (1983). *Absorption and scattering of light by small particles*.

Choukroun, M. et al. (2015). "Dark side of comet 67P/Churyumov-Gerasimenko in Aug.-Oct. 2014. MIRO/Rosetta continuum observations of polar night in the southern regions." In: A&A 583, A28, A28. DOI: 10.1051/0004-6361/201526181.

Combi, M. R. (1996). "Time-Dependent Gas Kinetics in Tenuous Planetary Atmospheres: The Cometary Coma." In: Icarus 123, pp. 207–226. DOI: 10.1006/icar.1996.0150.

Combi, M. R. and A. H. Delsemme (1980). "Neutral cometary atmospheres. I - an average random walk model for photodissociation in comets." In: ApJ 237, pp. 633–640. DOI: 10.1086/157909.

Combi, M. R., W. M. Harris, and W. H. Smyth (2004). "Gas dynamics and kinetics in the cometary coma: theory and observations." In: *Comets II*. Ed. by M. C. Festou, H. U. Keller, and H. A. Weaver, pp. 523–552.

Combi, M. R. and W. H. Smyth (1988). "Monte Carlo particle-trajectory models for neutral cometary gases. I - Models and equations." In: ApJ 327, pp. 1026–1059. DOI: 10.1086/166260.

Coradini, A., F. Capaccioni, P. Drossart, A. Semery, G. Arnold, and U. Schade (1999). "VIRTIS: The imaging spectrometer of the Rosetta mission." In: *Advances in Space Research* 24.9, pp. 1095 –1104. ISSN: 0273-1177. DOI: http://dx.doi.org/10.1016/S0273-1177(99)80203-8. URL: http://www.sciencedirect.com/science/article/pii/S0273117799802038.

Coradini, A. et al. (2007). "Virtis: An Imaging Spectrometer for the Rosetta Mission." In: Space Sci. Rev. 128, pp. 529–559. DOI: 10.1007/s11214-006-9127-5.

Cremonese, G. et al. (2016). "Photometry of dust grains of comet 67P and connection with nucleus regions." In: A&A 588, A59, A59. DOI: 10.1051/0004-6361/201527307.

Crifo, J. F. and A. V. Rodionov (1997a). "The Dependence of the Circumnuclear Coma Structure on the Properties of the Nucleus." In: Icarus 127, pp. 319–353. DOI: 10.1006/icar.1997.5690.

— (1997b). "The Dependence of the Circumnuclear Coma Structure on the Properties of the Nucleus." In: Icarus 129, pp. 72–93. DOI: 10.1006/icar.1997.5714.

Crifo, J. F., G. A. Lukianov, A. V. Rodionov, G. O. Khanlarov, and V. V. Zakharov (2002). "Comparison between Navier-Stokes and Direct Monte-Carlo Simulations of the Circumnuclear Coma. I. Homogeneous, Spherical Source." In: Icarus 156, pp. 249–268. DOI: 10.1006/icar.2001.6769.

Crifo, J. F., G. A. Loukianov, A. V. Rodionov, and V. V. Zakharov (2003). "Navier-Stokes and direct Monte Carlo simulations of the circumnuclear coma II. Homogeneous, aspherical sources." In: Icarus 163, pp. 479–503. DOI: 10.1016/S0019-1035(03)00041-1.

Crovisier, J. (1989). "The photodissociation of water in cometary atmospheres." In: A&A 213, pp. 459–464.

Davidsson, B. J. R. (2008). "Comet Knudsen Layers." In: Space Sci. Rev. 138, pp. 207–223. DOI: 10.1007/s11214-008-9305-8.

Divine, N. et al. (1986). "The Comet Halley dust and gas environment." In: Space Sci. Rev. 43, pp. 1–104. DOI: 10.1007/BF00175326.

Drolshagen, E. et al. (2017). "Distance determination method of dust particles using Rosetta OSIRIS NAC and WAC data." In: Planet. Space Sci. 143, pp. 256–264. DOI: 10.1016/j.pss.2017.04.018. arXiv: 1705.03740 [astro-ph.EP].

Eberhardt, P. et al. (1987). "To CO and N_2 Abundance in Comet p/ Halley." In: A&A 187, p. 481.

Eddington, A. S. (1910). "c 1908 (Morehouse), the envelopes of." In: MNRAS 70, pp. 442–458. DOI: 10.1093/mnras/70.5.442.

El-Maarry, M. R. et al. (2015). "Regional surface morphology of comet 67P/Churyumov-Gerasimenko from Rosetta/OSIRIS images." In: A&A 583, A26. DOI: 10.1051/0004-6361/201525723. URL: http://dx.doi.org/10.1051/0004-6361/201525723.

El-Maarry, M. R. et al. (2016). "Regional surface morphology of comet 67P/Churyumov-Gerasimenko from Rosetta/OSIRIS images: The southern hemisphere." In: A&A 593, A110, A110. DOI: 10.1051/0004-6361/201628634.

— (2017). "Regional surface morphology of comet 67P/Churyumov-Gerasimenko from Rosetta/OSIRIS images: The southern hemisphere (Corrigendum)." In: A&A 598, C2, p. C2. DOI: 10.1051/0004-6361/201628634e.

Emerich, C. et al. (1987). "Temperature and Size of the Nucleus of Comet p/ Halley Deduced from IKS Infrared VEGA-1 Measurements." In: A&A 187, p. 839.

Feldman, P. D. et al. (2015). "Measurements of the near-nucleus coma of comet 67P/Churyumov-Gerasimenko with the Alice far-ultraviolet spectrograph on Rosetta." In: A&A 583, A8, A8. DOI: 10.1051/0004-6361/201525925. arXiv: 1506.01203 [astro-ph.EP].

Fink, U. and G. Rinaldi (2015). "Coma dust scattering concepts applied to the Rosetta mission." In: Icarus 257, pp. 9–22. DOI: 10.1016/j.icarus.2015.04.005.

Fink, U. and M. Rubin (2012). "The calculation of Afρ and mass loss rate for comets." In: Icarus 221, pp. 721–734. DOI: 10.1016/j.icarus.2012.09.001.

Finklenburg, S. (2014). "Investigations of the Near Nucleus Gas and Dust Coma of Comets." PhD thesis. Universität Bern, Switzerland.

Finklenburg, S., N. Thomas, C. C. Su, and J.-S. Wu (2014). "The spatial distribution of water in the inner coma of Comet 9P/Tempel 1: Comparison between models and observations." In: Icarus 236, pp. 9–23. DOI: 10.1016/j.icarus.2014.03.032.

Finson, M. J. and R. F. Probstein (1968). "A theory of dust comets. I. Model and equations." In: ApJ 154, pp. 327–352. DOI: 10.1086/149761.

Fornasier, S. et al. (2015). "Spectrophotometric properties of the nucleus of comet 67P/Churyumov-Gerasimenko from the OSIRIS

instrument onboard the ROSETTA spacecraft." In: *ArXiv e-prints*. arXiv: 1505.06888 [astro-ph.EP].

Fougere, N., M. R. Combi, M. Rubin, and V. Tenishev (2013). "Modeling the heterogeneous ice and gas coma of Comet 103P/Hartley 2." In: Icarus 225, pp. 688–702. DOI: 10.1016/j.icarus.2013.04.031.

Fougere, N. et al. (2016a). "Direct Simulation Monte Carlo modelling of the major species in the coma of comet 67P/Churyumov-Gerasimenko." In: MNRAS 462, S156–S169. DOI: 10.1093/mnras/stw2388.

— (2016b). "Three-dimensional direct simulation Monte-Carlo modeling of the coma of comet 67P/Churyumov-Gerasimenko observed by the VIRTIS and ROSINA instruments on board Rosetta." In: A&A 588, A134, A134. DOI: 10.1051/0004-6361/201527889.

Fulle, M. et al. (2015). "Density and Charge of Pristine Fluffy Particles from Comet 67P/Churyumov-Gerasimenko." In: ApJ 802, L12, p. L12. DOI: 10.1088/2041-8205/802/1/L12.

Fulle, M. et al. (2016a). "Evolution of the Dust Size Distribution of Comet 67P/Churyumov-Gerasimenko from 2.2 au to Perihelion." In: ApJ 821, 19, p. 19. DOI: 10.3847/0004-637X/821/1/19.

Fulle, M., N. Altobelli, B. Buratti, M. Choukroun, M. Fulchignoni, E. Grün, M. G. G. T. Taylor, and P. Weissman (2016b). "Unexpected and significant findings in comet 67P/Churyumov-Gerasimenko: an interdisciplinary view." In: MNRAS 462, S2–S8. DOI: 10.1093/mnras/stw1663.

Gerig, S.-B., R. Marschall, and N. Thomas (2017). "Deviations from free-radial outflow in the inner dust coma of comet 67P/Churyumov-Gerasimenko using OSIRIS data." In: in prep.

Glassmeier, K.-H., H. Boehnhardt, D. Koschny, E. Kührt, and I. Richter (2007). "The Rosetta Mission: Flying Towards the Origin of the Solar System." In: Space Sci. Rev. 128, pp. 1–21. DOI: 10.1007/s11214-006-9140-8.

Gombosi, T. I. (1987). "Dusty cometary atmospheres." In: *Advances in Space Research* 7, pp. 137–145. DOI: 10.1016/0273-1177(87)90211-0.

Gombosi, T. I., T. E. Cravens, and A. F. Nagy (1985). "Time-dependent dusty gasdynamical flow near cometary nuclei." In: ApJ 293, pp. 328–341. DOI: 10.1086/163240.

Gombosi, T. I., A. F. Nagy, and T. E. Cravens (1986). "Dust and neutral gas modeling of the inner atmospheres of comets." In: *Reviews of Geophysics* 24.3, pp. 667–700. ISSN: 1944-9208. DOI: 10.1029/RG024i003p00667. URL: http://dx.doi.org/10.1029/RG024i003p00667.

Gulkis, S. et al. (2007). "MIRO: Microwave Instrument for Rosetta Orbiter." In: *Space Science Reviews* 128.1, pp. 561–597. ISSN: 1572-

9672. DOI: 10.1007/s11214-006-9032-y. URL: http://dx.doi.org/10.1007/s11214-006-9032-y.

Gulkis, S. et al. (2015). "Subsurface properties and early activity of comet 67P/Churyumov-Gerasimenko." In: *Science* 347, aaa0709, p. 709. DOI: 10.1126/science.aaa0709.

Halley, Edmond (1705). *Synopsis Astronomia Cometicae*.

Hansen, K. C. et al. (2016). "Evolution of water production of 67P/Churyumov-Gerasimenko: An empirical model and a multi-instrument study." In: MNRAS 462, S491–S506. DOI: 10.1093/mnras/stw2413.

Haser, L. (1957). "Distribution d'intensité dans la tête d'une comète." In: *Bulletin de la Societe Royale des Sciences de Liege* 43, pp. 740–750.

Hässig, M. et al. (2015). "Time variability and heterogeneity in the coma of 67P/Churyumov-Gerasimenko." In: *Science* 347, aaa0276, p. 276. DOI: 10.1126/science.aaa0276.

Hodges, R. R. (1990). "Monte Carlo simulation of nonadiabatic expansion in cometary atmospheres - Halley." In: Icarus 83, pp. 410–433. DOI: 10.1016/0019-1035(90)90076-L.

Huebner, W. F., J. Benkhoff, M.-T. Capria, A. Coradini, C. De Sanctis, R. Orosei, and D. Prialnik, eds. (2006). *Heat and Gas Diffusion in Comet Nuclei*.

Ivanovski, S. L., V. V. Zakharov, V. Della Corte, J.-F. Crifo, A. Rotundi, and M. Fulle (2017). "Dynamics of aspherical dust grains in a cometary atmosphere: I. axially symmetric grains in a spherically symmetric atmosphere." In: Icarus 282, pp. 333–350. DOI: 10.1016/j.icarus.2016.09.024.

Keller, H. U., Mottola, S., Skorov, Y., and Jorda, L. (2015). "The changing rotation period of comet 67P/Churyumov-Gerasimenko controlled by its activity." In: A&A 579, p. L5. DOI: 10.1051/0004-6361/201526421. URL: https://doi.org/10.1051/0004-6361/201526421.

Keller, H. U. et al. (1987). "Comet P/Halley's nucleus and its activity." In: A&A 187, pp. 807–823.

Keller, H. U. et al. (2007). "OSIRIS The Scientific Camera System Onboard Rosetta." In: Space Sci. Rev. 128, pp. 433–506. DOI: 10.1007/s11214-006-9128-4.

Keller, H. U. et al. (2015). "Insolation, erosion, and morphology of comet 67P/Churyumov-Gerasimenko." In: A&A 583, A34, A34. DOI: 10.1051/0004-6361/201525964.

Kepler, J. (1609). *Astronomia nova ..., seu physica coelestis, tradita commentariis de motibus stellae martis*. DOI: 10.3931/e-rara-558.

— (1622). *Epitome astronomiae copernicanae usitata forma quaestionum responsionum conscripta, inque VII. libros digesta*. DOI: 10.3931/e-rara-3122.

Kitamura, Y. (1986). "Axisymmetric dusty gas jet in the inner coma of a comet." In: Icarus 66, pp. 241–257. DOI: 10.1016/0019-1035(86)90155-7.

— (1987). "Axisymmetric dusty gas jet in the inner coma of a comet. II - The case of isolated jets." In: Icarus 72, pp. 555–567. DOI: 10.1016/0019-1035(87)90052-2.

Kolokolova, L. and H. Kimura (2010). "Comet dust as a mixture of aggregates and solid particles: model consistent with ground-based and space-mission results." In: *Earth, Planets, and Space* 62, pp. 17–21. DOI: 10.5047/eps.2008.12.001. arXiv: 0910.4755 [astro-ph.EP].

Kossacki, Konrad J., Wojciech J. Markiewicz, Yuri Skorov, and Norbert.I. Kömle (1999). "Sublimation coefficient of water ice under simulated cometary-like conditions." In: *Planetary and Space Science* 47.12, pp. 1521 –1530. ISSN: 0032-0633. DOI: http://doi.org/10.1016/S0032-0633(99)00037-9. URL: http://www.sciencedirect.com/science/article/pii/S0032063399000379.

Lai, I.-L. et al. (2016). "Gas outflow and dust transport of comet 67P/Churyumov-Gerasimenko." In: MNRAS 462, S533–S546. DOI: 10.1093/mnras/stx332.

Langevin, Y., M. Hilchenbach, N. Ligier, S. Merouane, K. Hornung, C. Engrand, R. Schulz, J. Kissel, J. Rynö, and P. Eng (2016). "Typology of dust particles collected by the COSIMA mass spectrometer in the inner coma of 67P/Churyumov Gerasimenko." In: Icarus 271, pp. 76–97. DOI: 10.1016/j.icarus.2016.01.027.

Laor, A. and B.T. Draine (1993). "Spectroscopic Constraints on the Properties of Dust in Active Galactic Nuclei." In: *The Astrophysical Journal 402, 441*.

Lara, L. M. et al. (2015). "Large-scale dust jets in the coma of 67P/Churyumov-Gerasimenko as seen by the OSIRIS instrument onboard Rosetta." In: A&A 583, A9, A9. DOI: 10.1051/0004-6361/201526103.

Lee, S. et al. (2015). "Spatial and diurnal variation of water outgassing on comet 67P/Churyumov-Gerasimenko observed from Rosetta/MIRO in August 2014." In: A&A 583, A5, A5. DOI: 10.1051/0004-6361/201526155.

Liao, Y. (2017). "Global Explorations of Inner Neutral Gas Coma of Comet 67P/Churyumov-Gerasimenko with DSMC Approach." PhD thesis. Universität Bern, Switzerland.

Liao, Y. et al. (2016). "3D Direct Simulation Monte Carlo Modelling of the Inner Gas Coma of Comet 67P/Churyumov-Gerasimenko: A Parameter Study." In: *Earth Moon and Planets* 117, pp. 41–64. DOI: 10.1007/s11038-016-9486-1.

Lin, Z.-Y. et al. (2015). "Morphology and dynamics of the jets of comet 67P/Churyumov-Gerasimenko: Early-phase development." In: A&A 583, A11, A11. DOI: 10.1051/0004-6361/201525961.

Mannel, T., M. S. Bentley, R. Schmied, H. Jeszenszky, A. C. Levasseur-Regourd, J. Romstedt, and K. Torkar (2016). "Fractal cometary dust - a window into the early Solar system." In: MNRAS 462, S304–S311. DOI: 10.1093/mnras/stw2898.

Marconi, M. L. and D. A. Mendis (1982). "A multi-fluid model of an H2O-dominated dusty cometary atmosphere." In: *Moon and Planets* 27, pp. 431–452. DOI: 10.1007/BF00929997.

— (1983). "The atmosphere of a dirty-clathrate cometary nucleus - A two-phase, multifluid model." In: ApJ 273, pp. 381–396. DOI: 10.1086/161377.

Markiewicz, W. J., R. M. Sablotny, H. U. Keller, N. Thomas, D. Titov, and P. H. Smith (1999). "Optical properties of the Martian aerosols as derived from Imager for Mars Pathfinder midday sky brightness data." In: J. Geophys. Res. 104, pp. 9009–9018. DOI: 10.1029/1998JE900033.

Marschall, R. et al. (2016). "Modelling observations of the inner gas and dust coma of comet 67P/Churyumov-Gerasimenko using ROSINA/COPS and OSIRIS data: First results." In: A&A 589, A90, A90. DOI: 10.1051/0004-6361/201628085.

Marschall, R. et al. (2017). "Cliffs versus plains: Can ROSINA/COPS and OSIRIS data of comet 67P/Churyumov-Gerasimenko in autumn 2014 constrain inhomogeneous outgassing?" In: A&A 605, A112, A112. DOI: 10.1051/0004-6361/201730849.

McDonnell, J. A. M., G. C. Evans, S. T. Evans, W. M. Alexander, W. M. Burton, J. G. Firth, E. Bussoletti, R. J. L. Grard, M. S. Hanner, and Z. Sekanina (1987). "The dust distribution within the inner coma of comet P/Halley 1982i - Encounter by Giotto's impact detectors." In: A&A 187, pp. 719–741.

Merouane, S. et al. (2016). "Dust particle flux and size distribution in the coma of 67P/Churyumov-Gerasimenko measured in situ by the COSIMA instrument on board Rosetta." In: A&A 596, A87, A87. DOI: 10.1051/0004-6361/201527958.

Migliorini, A. et al. (2016). "Water and carbon dioxide distribution in the 67P/Churyumov-Gerasimenko coma from VIRTIS-M infrared observations." In: A&A 589, A45, A45. DOI: 10.1051/0004-6361/201527661.

Mishchenko, M. L., L. D. Travis, and A. A. Lacis (2002). *Scattering, absorption, and emission of light by small particles / Cambridge University Press, 2002*.

Moreno, F. et al. (2016). "The dust environment of comet 67P/Churyumov-Gerasimenko from Rosetta OSIRIS and VLT observations in the 4.5 to 2.9 AU heliocentric distance range inbound." In: A&A 587, A155, A155. DOI: 10.1051/0004-6361/201527564. arXiv: 1602.01965 [astro-ph.EP].

Mottola, S. et al. (2014). "The rotation state of 67P/Churyumov-Gerasimenko from approach observations with the OSIRIS

cameras on Rosetta." In: A&A 569, L2, p. L2. DOI: 10.1051/0004-6361/201424590.

Pätzold, M. et al. (2016). "A homogeneous nucleus for comet 67P/Churyumov-Gerasimenko from its gravity field." In: Nature 530, pp. 63–65. DOI: 10.1038/nature16535.

Pommerol, A. et al. (2015). "OSIRIS observations of meter-sized exposures of H_2O ice at the surface of 67P/Churyumov-Gerasimenko and interpretation using laboratory experiments." In: A&A 583, A25, A25. DOI: 10.1051/0004-6361/201525977.

Preusker, F. et al. (2015). "Shape model, reference system definition, and cartographic mapping standards for comet 67P/Churyumov-Gerasimenko - Stereo-photogrammetric analysis of Rosetta/OSIRIS image data." In: A&A 583, A33, A33. DOI: 10.1051/0004-6361/201526349.

Prialnik, D., J. Benkhoff, and M. Podolak (2004). "Modeling the structure and activity of comet nuclei." In: *Comets II*. Ed. by M. C. Festou, H. U. Keller, and H. A. Weaver, pp. 359–387.

Rotundi, A. et al. (2015). "Dust measurements in the coma of comet 67P/Churyumov-Gerasimenko inbound to the Sun." In: *Science* 347, aaa3905, p. 3905. DOI: 10.1126/science.aaa3905.

Rubin, M., N. Fougere, K. Altwegg, M. R. Combi, L. Le Roy, V. M. Tenishev, and N. Thomas (2014). "Mass Transport around Comets and its Impact on the Seasonal Differences in Water Production Rates." In: ApJ 788, 168, p. 168. DOI: 10.1088/0004-637X/788/2/168.

Sandford, S. A. and L. J. Allamandola (1993). "The condensation and vaporization behavior of ices containing SO2, H2S, and CO2 - Implications for Io." In: Icarus 106, p. 478. DOI: 10.1006/icar.1993.1186.

Schloerb, F. P. et al. (2015). "MIRO observations of subsurface temperatures of the nucleus of 67P/Churyumov-Gerasimenko." In: A&A 583, A29, A29. DOI: 10.1051/0004-6361/201526152.

Schmidt, W. K. H. et al. (1986). "The Giotto Halley Multicolour Camera." In: *ESA Special Publication*. Vol. 1070. ESA Special Publication, pp. 149–172.

Schulz, R. (2010). "The Rosetta Mission: Comet and Asteroid Exploration." In: *IAU Symposium*. Ed. by J. A. Fernandez, D. Lazzaro, D. Prialnik, and R. Schulz. Vol. 263. IAU Symposium, pp. 312–316. DOI: 10.1017/S1743921310001997.

Schulz, R. et al. (2015). "Comet 67P/Churyumov-Gerasimenko sheds dust coat accumulated over the past four years." In: Nature 518, pp. 216–218. DOI: 10.1038/nature14159.

Sengers, J. V., Y.-Y. Lin Wang, B. Kamgar-Parsi, and J. R. Dorfman (2014). "Kinetic theory of drag on objects in nearly free molecular flow." In: *Physica A Statistical Mechanics and its Applications* 413,

pp. 409–425. DOI: 10.1016/j.physa.2014.06.026. arXiv: 1404.7826 [cond-mat.stat-mech].

Shou, Y. et al. (2016). "A New 3D Multi-fluid Model: A Study of Kinetic Effects and Variations of Physical Conditions in the Cometary Coma." In: ApJ 833, 160, p. 160. DOI: 10.3847/1538-4357/833/2/160.

Sierks, H. et al. (2015). "On the nucleus structure and activity of comet 67P/Churyumov-Gerasimenko." In: *Science* 347, aaa1044, p. 1044. DOI: 10.1126/science.aaa1044.

Skorov, Y. V. and H. Rickman (1999). "Gas flow and dust acceleration in a cometary Knudsen layer." In: Planet. Space Sci. 47, pp. 935–949. DOI: 10.1016/S0032-0633(99)00008-2.

Skorov, Y., V. Reshetnyk, P. Lacerda, P. Hartogh, and J. Blum (2016). "Acceleration of cometary dust near the nucleus: application to 67P/Churyumov-Gerasimenko." In: MNRAS 461, pp. 3410–3420. DOI: 10.1093/mnras/stw1470. arXiv: 1606.08461 [astro-ph.EP].

Su, C. C. (2013). "" PhD thesis. National Chiao Tung Univ., Taiwan.

Szegö, K., J.-F. Crifo, A. V. Rodionov, and M. Fulle (2002). "The Near-Nuclear Coma of Comet Halley in March 1986." In: *Earth Moon and Planets* 90, pp. 435–443.

Tenishev, V., M. R. Combi, and M. Rubin (2011). "Numerical Simulation of Dust in a Cometary Coma: Application to Comet 67P/Churyumov-Gerasimenko." In: ApJ 732, 104, p. 104. DOI: 10.1088/0004-637X/732/2/104.

Tenishev, V., M. Combi, and B. Davidsson (2008). "A Global Kinetic Model for Cometary Comae: The Evolution of the Coma of the Rosetta Target Comet Churyumov-Gerasimenko throughout the Mission." In: ApJ 685, pp. 659–677. DOI: 10.1086/590376.

Tenishev, V. et al. (2016). "Analysis of the dust jet imaged by Rosetta VIRTIS-M in the coma of comet 67P/Churyumov-Gerasimenko on 2015 April 12." In: MNRAS 462, S370–S375. DOI: 10.1093/mnras/stw2793.

Thomas, N. and H. U. Keller (1989). "The colour of Comet P/Halley's nucleus and dust." In: A&A 213, pp. 487–494.

— (1990). "Interpretation of the inner coma observations of comet P/Halley by the Halley Multicolor Camera." In: *Annales Geophysicae* 8, pp. 147–165.

Thomas, N., W. J. Markiewicz, R. M. Sablotny, M. W. Wuttke, H. U. Keller, J. R. Johnson, R. J. Reid, and P. H. Smith (1999). "The color of the Martian sky and its influence on the illumination of the Martian surface." In: J. Geophys. Res. 104, pp. 8795–8808. DOI: 10.1029/98JE02556.

Thomas, N. et al. (2015a). "Redistribution of particles across the nucleus of comet 67P/Churyumov-Gerasimenko." In: A&A 583, A17, A17. DOI: 10.1051/0004-6361/201526049.

Thomas, N. et al. (2015b). "The morphological diversity of comet 67P/Churyumov-Gerasimenko." In: *Science* 347, aaa0440, p. 440. DOI: 10.1126/science.aaa0440.

Tubiana, C. et al. (2015). "Scientific assessment of the quality of OSIRIS images." In: A&A 583, A46, A46. DOI: 10.1051/0004-6361/201525985.

Vaisberg, O., V. Smirnov, and A. Omelchenko (1986). "Spatial distribution of low-mass dust particles (m less than or = 10 to the minus 10th power g) in Comet Halley coma." In: *ESLAB Symposium on the Exploration of Halley's Comet*. Ed. by B. Battrick, E. J. Rolfe, and R. Reinhard. Vol. 250. ESA Special Publication.

Vincent, J.-B. et al. (2016). "Are fractured cliffs the source of cometary dust jets? Insights from OSIRIS/Rosetta at 67P/Churyumov-Gerasimenko." In: A&A 587, A14, A14. DOI: 10.1051/0004-6361/201527159. arXiv: 1512.03193 [astro-ph.EP].

Wallace, L. V., I. Miller, and D. Freeman (1958). "Isophote configurations for model comets." In: AJ 63, p. 213. DOI: 10.1086/107729.

Wu, J.-S. and Y.Y. Lian (2003). "Parallel three-dimensional Direct Simulation Monte Carlo method and its applications." In: *Computers & Fluids* 32, pp. 1133–1160.

Wu, J.-S. and K.-C. Tseng (2005). "Parallel DSMC method using dynamic domain decomposition." In: *International Journal for Numerical Methods in Engineering* 63, pp. 37–76. DOI: 10.1002/nme.1232.

Wu, J.-S., K.-C. Tseng, and F.-Y. Wu (2004). "Parallel three-dimensional DSMC method using mesh refinement and variable time-step scheme." In: *Computer Physics Communications* 162, pp. 166–187. DOI: 10.1016/j.cpc.2004.07.004.

Xie, X. and M. J. Mumma (1996a). "Monte Carlo Simulation of Cometary Atmospheres: Application to Comet P/Halley at the Time of the Giotto Spacecraft Encounter. I. Isotropic Model." In: ApJ 464, p. 442. DOI: 10.1086/177335.

— (1996b). "Monte Carlo Simulation of Cometary Atmospheres: Application to Comet P/Halley at the Time of the Giotto Spacecraft Encounter. II. Axisymmetric Model." In: ApJ 464, p. 457. DOI: 10.1086/177336.

Yoldi, Z., A. Pommerol, B. Jost, O. Poch, J. Gouman, and N. Thomas (2015). "VIS-NIR reflectance of water ice/regolith analogue mixtures and implications for the detectability of ice mixed within planetary regoliths." In: Geophys. Res. Lett. 42, pp. 6205–6212. DOI: 10.1002/2015GL064780.

Ytrehus, T. (1975). "Kinetic theory description and experimental results for vapor motion in arbitrary strong evaporation." In: *NASA STI/Recon Technical Report N* 76.

Zakharov, V. V., A. V. Rodionov, G. A. Lukianov, and J. F. Crifo (2009). "Monte-Carlo and multifluid modelling of the circumnuclear dust coma II. Aspherical-homogeneous, and

spherical-inhomogeneous nuclei." In: Icarus 201, pp. 358–380. DOI: 10.1016/j.icarus.2008.12.022.

CURRICULUM VITAE

Name	Raphael Marschall
Date of birth	22.04.1987
Nationality	Switzerland
Contact	marschall@cosmoculus.net

May 2013 - July 2017	**Doctoral dissertation in Physics** University of Bern, Physics Institute, Space Research & Planetary Sciences Division, Planetary Imaging Group, Bern, Switzerland *Thesis:* Inner gas and dust comae of comets: Building a 3D simulation pipeline to understand multi-instrument results from the Rosetta mission to comet 67P/Churyumov-Gerasimenko *Advisor:* Prof. Dr. Nicolas Thomas
February 2011 - November 2012	**Master of Science in Physics with special qualifications in «Theoretical Physics»** University of Bern, Albert Einstein Center for Fundamental Physics, Institute for Theoretical Physics, Bern, Switzerland *Thesis:* «Observer Dependence of Hawking Radiation» *Advisor:* Prof. Dr. Matthias Blau
September 2007 - January 2011	**Bachelor of Science in Physics** University of Bern, Albert Einstein Center for Fundamental Physics, Institute for Theoretical Physics, Bern, Switzerland *Thesis:* «The Hydrogen Atom in Dirac Theory» *Advisor:* Prof. Dr. Christoph Greub
August 2003 – May 2006	**Matura with special qualifications in biology and chemistry** Gymnasium Bern Kirchenfeld, Bern, Switzerland

COLOPHON

This document was typeset using the typographical look-and-feel `classicthesis` developed by André Miede. The style was inspired by Robert Bringhurst's seminal book on typography "*The Elements of Typographic Style*". `classicthesis` is available for both LaTeX and LyX:

https://bitbucket.org/amiede/classicthesis/